

Een uitgebreid ontwerp van stabiele aldolreactiekatalysatoren
door afstemming van actiefcentrum-, drager-, en solventeigenschappen

A Comprehensive Design of Stable Aldol Reaction Catalysts
by Tuning Active Site, Support, and Solvent Properties

Anton De Vylder

Promotoren: prof. dr. ir. J. W. Thybaut, prof. dr. P. Van Der Voort, dr. ir. J. Lauwaert
Proefschrift ingediend tot het behalen van de graad van
Doctor in de ingenieurswetenschappen: chemische technologie



Vakgroep Materialen, Textiel en Chemische Proceskunde
Voorzitter: prof. dr. P. Kiekens
Faculteit Ingenieurswetenschappen en Architectuur
Academiejaar 2018 - 2019

ISBN 978-94-6355-278-3
NUR 913, 952
Wettelijk depot: D/2019/10.500/86

Examencommissie:

Prof. Dr. Ir. Filip De Turck, voorzitter	Universiteit Gent
Prof. Dr. Ir. Christophe Walgraeve*	Universiteit Gent
Prof. Dr. Ir. Maarten K. Sabbe*, secretaris	Universiteit Gent
Prof. Dr. Igor I. Slowing*	Iowa State University
Prof. Dr. Christine Kirschhock*	Katholieke Universiteit Leuven

Prof. Dr. Ir. Joris W. Thybaut, promotor	Universiteit Gent
Prof. Dr. Pascal Van Der Voort promotor	Universiteit Gent
Dr. Ir. Jeroen Lauwaert, promotor	Universiteit Gent

* leescommissie

Universiteit Gent

Faculteit Ingenieurswetenschappen en Architectuur

Vakgroep Materialen, Textiel en Chemische Proceskunde

Laboratorium voor Chemische Technologie

Technologiepark 125

B-9052 Gent

België

Tel.: +32 (0)9 331 17 57

<http://www.lct.ugent.be>

This work was funded by the Fund for Scientific Research Flanders (FWO) through Grant Number 3G006813, and the European Research Council under the European Union's Seventh Framework Programme (FP7/2007-2013), ERC grant agreement number 615456. Part of this work was carried out using the STEVIN Supercomputer Infrastructure at Ghent University, funded by Ghent University, the Flemish Supercomputer Center (VSC), the Hercules Foundation and the Flemish Government – department EWI.

Dankwoord

Acknowledgement

Vier jaar lang onderzoek mogen doen aan het Laboratorium voor Chemische Technologie (LCT) aan de Universiteit Gent was een uniek voorrecht, maar ook een immense uitdaging. Een uitdaging die ik nooit succesvol had kunnen afwerken zonder de rechtstreekse en onrechtstreekse hulp van verschillende mensen. Daarom is een woord van dank op zijn plaats.

Op de eerste plaats wil ik prof. Joris Thybaut bedanken voor de kans die hij mij geboden hebt om aan dit doctoraat te beginnen. Bedankt ook voor uw begeleiding, voor de vele wetenschappelijke discussies die we gevoerd hebben, en uw geduld en sereniteit tijdens de moeilijkere momenten.

Bedankt prof. Pascal Van Der Voort om als copromotor op te treden. Uw kennis van heterogene katalysatorsynthese en de samenwerking met uw onderzoeksgroep COMOC was van onschatbare waarde voor dit werk. In het bijzonder wil ik daarbij dr. Judith Ouwehand bedanken voor de inzichten in de PMO synthese en Funda Aliç voor de aanzienlijke hoeveelheid elementaire analyses die u voor mij uitgevoerd heeft.

Dr. Jeroen Lauwaert, jouw doctoraat rond aldol reacties eindigde op het moment dat het mijne startte. Door je uitgebreide kennis rond dit onderwerp en intensieve begeleiding ben ik vlot van start kunnen gaan. Onze wekelijkse voortgangvergaderingen waren bepalend voor de richting van dit doctoraat en zorgden er telkens voor dat ik vol goede moed opnieuw aan de slag ging. Bedankt ook om altijd je duidelijke en terechte kritische mening te geven, alsook telkens mogelijke oplossingsstrategieën aan te reiken. Ik wens je het aller beste toe, zowel in je academische carrière als met je gezin.

Een woord van dank gaat ook uit naar Prof. Jeriffa De Clercq om de apparatuur in uw labo ter beschikking te stellen voor dit onderzoek en ook telkens feedback te geven op mijn conferentiebijdragen en manuscripten.

Prof. Maarten Sabbe en Prof. Marie-Françoise Reyniers, bedankt om mij de nodige inzichten in de fundamentele, en de mogelijke valkuilen, van de computationele chemie bij te brengen. Jullie grondige en scherpe feedback hebben mijn werk telkens sterker gemaakt.

I would like to thank prof. Christopher W. Jones for accepting me as a visitor in his research group at the Georgia Institute of Technology. Working in your lab and collaborating

with the people from your group was intellectually stimulating and a lot of fun! A special thanks goes to Nathan, Akshay, Cornelia, Claudia, Qandeel, Sang Jae, Jacob, Nima, Taylor and Dharam for making me feel welcome in the group and helping me out in the lab.

Bedankt aan alle thesisstudenten die rechtstreeks en onrechtstreeks een bijdrage geleverd hebben aan dit werk: Handan Nalli, Stijn Van Auwenis, Aster Onderbeke, Eli Moens, Bert Biesemans, Laurent Cantillon en Kevin Van Der Plas.

Mijn oprechte dankbaarheid gaat uit naar het technisch personeel van het LCT. Wim, Michaël, Brecht, Bert, Tom, Georges, Lambert, Hans en Erwin, bedankt voor alle hulp wanneer ik weer eens jullie bureau kwam binnenvallen met een probleem. Ook het secretariaat, met in het bijzonder Paulien en Kim, bedankt om mij te helpen met kleine en grote administratieve problemen die eigen zijn aan een universitaire omgeving.

Bedankt prof. Geraldine Heynderickx voor de geslaagde samenwerking voor de oefenlessen van het vak Stoftransport en de toffe babbels tussendoor.

Vier jaar lang heb ik aan dezelfde bureau gezeten en zag ik rondom mij telkens collega's komen en gaan. Hoewel we altijd consciëntieus de niet wetenschappelijke discussies voor de koffiepauze gehouden hebben, was het toch telkens bijzonder fijn om samen te werken. Een woord van dank dus aan Brigitte, voor het samen opfleuren van ons bureau met planten en kerstversiering; Jonas, Kristof en Luis, de toenmalige "anciens" naar wie ik opkeek en wiens raad ik volgde; en Bert, voor de interessante discussies rond aldol reacties. *A word of thanks also goes to Nebojsa and Carlos, my two non-Dutch speaking officemates.*

Ik had het geluk om mijn onderzoek te mogen uitvoeren in de tofste onderzoeksgroep van het LCT: de CaRE groep. *I would like to thank all the previous and current members of the CaRE group for the many interesting lunch meetings and the fun events.* Een speciaal woord van dank gaat naar Alexandra, voor je immense hulp bij het voorbereiden en geven van workshops en de ontelbare fijne koffiepauzes samen; Jolien, om me telkens goede moed en vooruitzichten te geven; Jeroen P., om samen te lachen met de absurditeiten in het leven; Maëli, om altijd bereid te zijn voor een babbel; *Laura, for teaching me about the dos and don'ts of Italian food; Pedro, for always showing us the bright side of things; Chanakya, for the great times together in Minneapolis and Rita, for always being there for a chat and a coffee.*

Een woord van dank aan de medestudenten van mijn afstudeerjaar 2015 die samen met mij een doctoraat gestart zijn aan het LCT, maar in een andere onderzoeksgroep: Florence, Jens, Alexander, Steffen, Yoshi, Jenoff en Lies. Hoewel we allemaal andere richtingen zijn uitgegaan, hebben we toch steeds contact gehouden en onze zotte en ook minder zotte ervaringen met elkaar gedeeld.

Verder wil ik graag alle andere fantastische mensen bedanken die ik in het LCT heb ontmoet gedurende de afgelopen vier jaar, waardoor het een plezier was om elke dag naar het labo te komen!

Natuurlijk zijn er ook een hoop mensen buiten de universiteit die me aangemoedigd en gesteund hebben in dit doctoraat. Samuel, Alexander, Jolien, Jirka en Tim, als we samen afspreken dan is het voor mij altijd opnieuw duidelijk wat écht telt in het leven. Timur, jij was één van de eersten aan wie ik vertelde dat ik een doctoraat ging doen. Je was direct enthousiast dat je dan “een echte doctor gaat kennen, net zoals in *The Big Bang Theory!*”. Het is nu bijna zo ver, en we hadden nog zoveel samen te beleven, maar jij bent veel te vroeg heengegaan. Slaap zacht maatje.

Tot slot wens ik mijn familie en de familie van Anke te bedanken voor hun aanhoudende steun en aanwezigheid. En *last but not least*, liefste Anke, bedankt om er altijd voor mij te zijn en mij te steunen. Bedankt om mij op te beuren wanneer het eens wat minder ging en om mij aan te moedigen om de successen te vieren. Zonder jou zou dit doctoraat er niet geweest zijn.

Anton

Gent, zomer 2019

Table of Contents

DANKWOORD / ACKNOWLEDGEMENT	I
TABLE OF CONTENTS	V
LIST OF FIGURES	XI
LIST OF SCHEMES	XIX
LIST OF TABLES	XXIII
LIST OF SYMBOLS	XXV
LIST OF STRUCTURES	XXXI
GLOSSARY OF TERMS	XXXV
SUMMARY	XLI
REFERENCES	XLIX
SAMENVATTING	L
REFERENTIES	LX
CHAPTER 1 INTRODUCTION	1
1.1 SUSTAINABLE DEVELOPMENT AND GREEN CHEMISTRY	1
1.1.1 CATALYSIS	1
1.1.2 SAFER SOLVENTS	2
1.1.3 RENEWABLE FEEDSTOCKS	3
1.2 ALDOL REACTIONS	4
1.2.1 BRØNSTED ACID CATALYZED REACTION MECHANISM	6
1.2.2 BRØNSTED BASE CATALYZED REACTION MECHANISM	7

1.2.3	LEWIS BASIC AMINE CATALYZED REACTION MECHANISM	8
1.3	HETEROGENEOUS CATALYSTS FOR THE ALDOL REACTION	9
1.3.1	ZEOLITES	9
1.3.2	LAYERED DOUBLE HYDROXIDES	10
1.3.3	FUNCTIONALIZED SILICA	10
1.3.4	FUNCTIONALIZED ORGANOSILICAS	16
1.3.5	FUNCTIONALIZED POLYMER RESINS	19
1.4	SOLVENT EFFECTS IN THE AMINE CATALYZED ALDOL REACTION	21
1.4.1	THE HOMOGENEOUS ALDOL REACTION CATALYZED BY L-PROLINE	21
1.4.2	THE HETEROGENEOUS ALDOL REACTION CATALYZED BY AMINATED SILICA	21
1.4.3	TUNING HYDROPHOBICITY IN THE SUPPORT MATERIAL	23
1.5	SCOPE AND OUTLINE OF THIS WORK	24
1.6	REFERENCES	25
 CHAPTER 2 COMPUTATIONAL PROCEDURES		 33
2.1	FUNDAMENTALS OF QUANTUM CHEMISTRY	33
2.2	MOLECULAR ORBITAL THEORY	34
2.2.1	HARTREE-FOCK THEORY	35
2.2.2	DENSITY FUNCTIONAL THEORY	37
2.2.3	BASIS SETS	39
2.2.4	QUANTUM CHEMICAL COMPOSITE METHODS	40
2.3	REINTRODUCING NUCLEAR MOTION IN THE HAMILTONIAN	40
2.3.1	TRANSLATION	41
2.3.2	ROTATION	41
2.3.3	VIBRATION	42
2.4	STATISTICAL MECHANICS	42
2.5	CONVENTIONAL TRANSITION STATE THEORY	44
2.6	SOLVATION EFFECTS	46
2.6.1	POLARIZABLE CONTINUUM MODELS	47
2.6.2	COSMO-RS	48
2.7	REFERENCES	52
 CHAPTER 3 THEORETICAL ASSESSMENT OF STERIC AND ELECTRONIC EFFECTS IN AMINES		 55

3.1 COMPUTATIONAL METHODS	57
3.2 RESULTS AND DISCUSSION	58
3.2.1 VALIDATION OF THE COMPUTATIONAL METHOD	58
3.2.2 CORRELATING THE TRIMETHYLBORANE BASICITY OF AMINE-BASED CATALYSTS TO THEIR EXPERIMENTAL ACTIVITY IN THE ALDOL REACTION	59
3.2.3 DESIGN OF A NEW MONOFUNCTIONAL AMINE AND BIFUNCTIONAL AMINE-HYDROXYL SITE WITH A HIGH TMB BASICITY	66
3.3 CONCLUSIONS	68
3.4 REFERENCES	69

CHAPTER 4 THE ROLE OF WATER IN THE REUSABILITY OF AMINATED SILICA CATALYSTS FOR ALDOL REACTIONS **73**

4.1 EXPERIMENTAL PROCEDURES	74
4.1.1 SYNTHESIS OF THE COOPERATIVE ACID-BASE CATALYST AND THE MONOFUNCTIONAL BASE CATALYST	74
4.1.2 CHARACTERIZATION OF THE FRESH AND SPENT CATALYSTS	75
4.1.3 DETERMINATION OF THE WATER CONTENT IN STOCK ORGANIC SOLVENTS	75
4.1.4 DRYING OF STOCK ACETONE	76
4.1.5 CATALYTIC PERFORMANCE EVALUATION OF THE FRESH AND SPENT CATALYSTS IN THE BATCH REACTOR	76
4.1.6 SAMPLE ANALYSIS AND DEFINING THE CATALYST ACTIVITY	77
4.2 RESULTS AND DISCUSSION	78
4.2.1 CATALYST CHARACTERIZATION AND VALIDATION OF THE SYNTHESIS PROCEDURE	78
4.2.2 CATALYTIC PERFORMANCE IN THE ALDOL REACTION OF ACETONE WITH 4-NITROBENZALDEHYDE	79
4.2.3 EFFECT OF WATER ON THE REUSABILITY OF AMINATED SILICA CATALYSTS FOR ALDOL REACTIONS IN THE BATCH REACTOR	84
4.3 CONCLUSIONS	89
4.4 REFERENCES	90

CHAPTER 5 WATER AND SILANOL ASSISTED PATHWAYS IN THE AMINE CATALYZED ALDOL REACTION **107**

5.1 INTRODUCTION	91
5.2 COMPUTATIONAL DETAILS	93
5.2.1 COMPUTATIONAL MODEL CONSTRUCTION	93
5.2.2 GAS-PHASE CALCULATIONS	93

5.2.3	LIQUID-PHASE CORRECTIONS	94
5.3	RESULTS AND DISCUSSION	95
5.3.1	AMINE-CATALYZED ALDOL REACTION ASSISTED BY WATER	95
5.3.2	AMINE-CATALYZED ALDOL REACTION ASSISTED BY SILANOL GROUPS	103
5.3.3	ALDOL PRODUCT DEHYDRATION TO THE ENONE PRODUCT AND READSORPTION	108
5.3.4	EFFECT OF SOLVENT ON REACTION BARRIERS AND INTERMEDIATES	112
5.4	CONCLUSIONS	113
5.5	REFERENCES	114
 CHAPTER 6		
CONTINUOUS-FLOW ALDOL REACTIONS		117
<hr/>		
6.1	DESIGN OF A LIQUID-SOLID LAB-SCALE (LS)² PLUG FLOW REACTOR	117
6.1.1	FEED SECTION	118
6.1.2	REACTION SECTION	120
6.1.3	OUTLET COLLECTION AND SAMPLING	121
6.1.4	SAFETY CONSIDERATIONS	122
6.2	PROCEDURE FOR CATALYST STABILITY ASSESSMENT	122
6.3	CATALYST STABILITY WITH TIME ON STREAM	123
6.3.1	HEXANE AS SOLVENT	123
6.3.2	ACETONE AS SOLVENT	124
6.3.3	DMSO AS SOLVENT	125
6.4	EXPERIMENTAL INTRINSIC KINETICS ASSESSMENT	128
6.4.1	REACTION RATE EQUIVALENCE WITH A BATCH-TYPE REACTOR	128
6.4.2	EXPERIMENTAL VERIFICATION OF HEAT AND MASS TRANSFER LIMITATIONS	129
6.5	CONCLUSIONS	130
6.6	REFERENCES	131
 CHAPTER 7		
CHITOSAN AS A SUSTAINABLE CATALYST IN THE AQUEOUS ALDOL REACTION		133
<hr/>		
7.1	INTRODUCTION	133
7.2	PROCEDURES	136
7.2.1	CATALYST SYNTHESIS	136
7.2.2	CATALYST CHARACTERIZATION	137
7.2.3	PERFORMANCE EVALUATION	138
7.3	RESULTS AND DISCUSSION	140

7.3.1	KINETIC INVESTIGATION OF CHITOSAN IN A BATCH REACTOR	140
7.3.2	CONTINUOUS-FLOW STABILITY OF CRUDE CHITOSAN	145
7.3.3	AMINE ACTIVITY AS A FUNCTION OF THE DEGREE-OF-DEACETYLATION	146
7.4	CONCLUSIONS	148
7.5	REFERENCES	149
CHAPTER 8 STABLE ALDOL REACTION CATALYSTS UNDER CONTINUOUS-FLOW		153
8.1	INTRODUCTION AND GOAL	153
8.1.1	PMO SUPPORTED AMINE CATALYSTS	154
8.1.2	PEGMA CATALYSTS	155
8.2	PROCEDURES	157
8.2.1	PERIODIC MESOPOROUS ORGANOSILICA (PMO) CATALYST SYNTHESIS	157
8.2.2	SYNTHESIS AND CHARACTERIZATION OF PEGMA CATALYSTS	160
8.2.3	PERFORMANCE EVALUATION	161
8.3	RESULTS AND DISCUSSION	161
8.3.1	CHARACTERIZATION RESULTS	161
8.3.2	CATALYTIC PERFORMANCE EVALUATION	168
8.4	CONCLUSIONS	172
8.5	REFERENCES	173
CHAPTER 9 CONCLUSIONS AND PERSPECTIVES		175
9.1	CONCLUSIONS	175
9.2	PERSPECTIVES	177
APPENDIX A		179
A.1	EXPERIMENTAL NUCLEOPHILICITY OF AMINES	179
A.2	TMB COMPLEXATION GEOMETRY	182
A.3	REFERENCES	183
APPENDIX B		185
B.1	ADDITIONAL CHARACTERIZATION FIGURES AND DATA	185

APPENDIX C	189
C.1 REACTIONS TOWARDS (S,S) DIASTEREOMER	189
C.2 TRANSITION STATES TS1 AND TS2 WITH ZERO, ONE OR TWO ASSISTING WATER MOLECULES	192
C.3 REACTION COORDINATE SCAN IN GAS PHASE AND DMSO	195
C.4 COMPARISON OF MINIMAL CLUSTER MODEL WITH PERIODIC SILICA SURFACE MODEL	196
C.4.1 ISOLATED SILANOLS	196
C.4.2 VICINAL SILANOLS	201
C.5 MECHANISM OF THE ALDOL REACTION PROMOTED BY TWO VICINAL SILANOL GROUPS	206
C.6 ACTIVITY COEFFICIENTS IN KINETIC RATE COEFFICIENTS	206
C.7 REFERENCES	208
APPENDIX D	209
D.1 THEORETICAL BACKGROUND	209
D.1.1 PLUG FLOW CRITERION AND MAXIMAL BED DILUTION	210
D.1.2 MASS TRANSFER LIMITATIONS	212
D.1.3 HEAT TRANSFER LIMITATIONS	214
D.2 EVALUATION OF CRITERIA	216
D.2.1 HEXANE AS SOLVENT	217
D.2.2 DMSO AS SOLVENT	219
D.2.3 ACETONE AS SOLVENT	221
D.3 REFERENCES	222
APPENDIX E	223
APPENDIX F	227
F.1.1 PMO MATERIALS	227
F.1.2 PEGMA MATERIALS	228

List of Figures

Figure 1. ^{13}C CP/MAS NMR spectrum of the spent cooperative acid-base catalyst. The grafted secondary amine can be identified in the spectrum, as well as the carbon atoms originating from the aromatic ring with a nitro substituent.

Figure 2: Reusability of the cooperative acid-base MAP catalyst (◆) and monofunctional MAP catalyst (●) in a second batch experiment, using DMSO as solvent and varying water contents.

Figure 3. Stability of the cooperative acid-base MAP catalyst (◆) and monofunctional MAP catalyst (●) as a function of time on stream in the aldol reaction using DMSO + 2.19 wt% water as solvent.

Figure 4: Gibbs free energy diagram calculated with CBS-QB3 for the aldol reaction of acetone with 4-nitrobenzaldehyde, according to the mechanism displayed in Scheme 1, with 50 vol% DMSO as solvent and 50% acetone as excess reagent at 328.15 K.

Figure 5: Conversion as a function of time on stream for the PEGMA-EDA catalyst (■) in the aqueous aldol reaction of acetone with 4-nitrobenzaldehyde.

Figuur 1. ^{13}C CP/MAS NMR van de gebruikte coöperatieve zuur-base katalysator. Het geënte secundaire amine kan in het spectrum worden geïdentificeerd, evenals de koolstofatomen die afkomstig zijn van de aromatische ring met een nitrogroep.

Figuur 2. Herbruikbaarheid van de coöperatieve zuur-base MAP-katalysator (◆) en monofunctionele MAP-katalysator (●) in een tweede batch-experiment, met DMSO als solvent en een variërend watergehalte.

Figuur 3. Stabiliteit van de coöperatieve zuur-base MAP-katalysator (◆) en de monofunctionele MAP-katalysator (●) als functie van de bedrijfstijd in de aldolreactie met DMSO + 2.19 m% water als solvent.

Figuur 4. Gibbs-vrije energiediagram berekend met CBS-QB3 voor de aldolreactie van aceton met 4-nitrobenzaldehyde, volgens het mechanisme weergegeven in Schema 1, met 50 vol% DMSO als solvent en 50% aceton als overmaat reagens bij 328.15 K.

Figuur 5. Conversie als een functie van de bedrijfstijd voor de PEGMA-EDA-katalysator (■) in de aldolreactie van aceton met 4-nitrobenzaldehyde met water als solvent.

Figure 1-1: Burning fuels from eons old fossil resources produces a net increase in CO_2 (left), while the CO_2 emitted by burning biomass is again taken up by the biomass in the course of a few years (right).

Figure 1-2: Conversion of lignocellulose into liquid hydrocarbon fuels. Scheme based on ref 37.

Figure 1-3: Surface silanol types: isolated (a), geminal (b) and vicinal (c), adapted from Van Der Voort et al.⁷⁶

- Figure 1-4: Silanol type distribution as a function of calcination temperature (■, green, vicinal silanols, ▲, blue, isolated silanols, ◆, yellow, geminal silanols, ●, black, total silanols). Figure adapted from Van Der Voort et al.⁷⁶
- Figure 1-5: Currently the most active secondary amine site for the aldol reaction using hexane as solvent, as determined by Lauwaert et al.⁸⁷.
- Figure 1-6: Unfavorable protonation/deprotonation equilibrium when a strong carboxylic acid is employed as promoting group, figure adapted from Brunelli et al.⁴⁷
- Figure 1-7: Promotion of silanol groups on primary amines (◆) and secondary amines (■) for the aldol reaction. Figure from Lauwaert et al.⁴⁶
- Figure 1-8: Inter- and intramolecularly promoted amine catalysts evaluated by Lauwaert et al.⁹⁴
- Figure 1-9: Non-exhaustive list of example organosilica precursors that have been successfully condensed into a PMO material. Terminal Si(OR) with R = CH₃ or C₂H₅. Figure adapted from Hoffmann et al.¹⁰⁷
- Figure 1-10: Example organosilica material with an ethylene bridge
- Figure 1-11: Swelling of a cross-linked polymer resin in a compatible solvent.
- Figure 2-1: Gibbs free energy as function of the reaction coordinate for the reaction $A + B \rightarrow C$. Subscript *r* refers to the thermodynamic Gibbs free energy, superscript ‡ refers to the transition state Gibbs free energy.
- Figure 2-2: Schematic representation of moving a molecule from the gas phase to the liquid phase using the polarizable continuum model. Step 4 is iterated until self-consistency is obtained.
- Figure 2-3: Multiple ways to construct the solvent cavity in polarizable continuum models
- Figure 2-4: Screening charge density (σ -surface) of acetone as calculated by the COSMO method
- Figure 2-5: Example σ -profile for hexane (blue), acetone (green) and water (red).
- Figure 3-1: L-proline derivatives evaluated by Sakthivel et al.³⁷ in the aldol reaction of 4-nitrobenzaldehyde with acetone, ranked according to their TMB basicity (TMBB) and proton basicity (PB). Catalysts 9 to 12 (red) are too sterically hindered to form a stable complex with TMB and are also reported to be inactive in the aldol reaction³⁷.
- Figure 3-2: Effect of ring and ring size in (cyclic) amino acids on the TMB basicity (TMBB) and the proton basicity (PB). Catalysts 13, 14 and 16 have been evaluated by Sakthivel et al.³⁷ for the amine catalyzed aldol reaction of acetone with 4-nitrobenzaldehyde.
- Figure 3-3: Monofunctional amine active sites (top, 18-21) evaluated by Lauwaert et al.³⁶ for the aldol reaction of acetone with 4-nitrobenzaldehyde, ranked along their TMB basicity (TMBB) and proton basicity (PB). Active site 17 (green) is suggested as a new optimal monofunctional amine that can be attached to mesoporous silica via a propyl linker.

- Figure 3-4: Bifunctional amine-hydroxyl functions that can be grafted on mesoporous silica ranked along their TMB basicity (TMBB) and proton basicity (PB). Groups 22, 24 and 25 (green) are new amine-hydroxyl functions proposed for the aldol reaction, group 23 has already been experimentally tested by Lauwaert et al.⁴⁴
- Figure 4-1. Raman spectrum of the spent cooperative acid-base catalyst (a) and spent monofunctional base catalyst (b).
- Figure 4-2. ¹³C CP/MAS NMR spectrum of the spent cooperative acid-base catalyst. The grafted secondary amine can be identified in the spectrum, as well as the carbon atoms originating from the aromatic ring with a nitro substituent.
- Figure 4-3. Turnover frequency (TOF – s⁻¹) for the aldol reaction of acetone with 4-nitrobenzaldehyde, using a cooperative acid-base catalyst (a, red) and a monofunctional base catalyst (b, blue) as a function of the amount of water in the reactor. Full bars represent the first run, empty bars the second run, and the right axis indicates the ratio between the TOF observed in the second and the first run. Lines are a guide for the eye. Absolute water content in the reactor has been determined with Karl-Fischer titrations. Error bars indicate a 95% confidence interval. (T = 55 °C, 0.45 g 4-nitrobenzaldehyde, 45 g acetone, 52 g – 55 g DMSO, 0.20 g methyl 4-nitrobenzoate, 0.5 g to 3.0 g water added, 0.31 wt% water in stock acetone, 0.09 wt% water in dried acetone, 0.09 wt% water in stock DMSO)
- Figure 4-4. Raman spectrum of the spent cooperative acid-base catalyst (left) and the spent monofunctional base catalyst (right) (a: 0.09 wt% water, b: 0.19 wt% water, c: 0.69 wt% water, d: 1.19 wt% water, e: 2.19 wt% water and f: 3.19 wt% water).
- Figure 4-5 ¹³C-NMR result of a cooperative acid-base catalyst, spent in the aldol reaction of 4-nitrobenzaldehyde with acetone, using 1.19 wt% water in the reactor.
- Figure 4-6. Spent catalyst color as a function of the water amount in the reactor. (a) Cooperative acid-base, (b) monofunctional base catalyst
- Figure 4-7: Percentage UV-Vis reflection as a function of wavelength of the spent cooperative acid-base catalysts, relative to a fresh catalyst (a: 0.09 wt% water, b: 0.19 wt% water, c: 0.69 wt% water, d: 1.19 wt% water, e: 2.19 wt% water and f: 3.19 wt% water).
- Figure 5-1: Gibbs free energy diagram for the aldol reaction of acetone with 4-nitrobenzaldehyde at 328.15 K catalyzed by an N-methylpropylamine catalyst (black pathway, no subscript) and catalyzed by N-methylpropylamine, assisted by one water molecule (green pathway, H₂O subscript). The numbers indicate the $\Delta^\ddagger G_{\text{forward}}$ for the considered reaction. The Gibbs free energy includes a correction term for a 50/50 vol% DMSO/acetone liquid phase, as experimentally employed in Chapter 4.
- Figure 5-2: Gibbs free energy diagram and reaction barriers of the aldol reaction of acetone with 4-nitrobenzaldehyde at 328.15 K catalyzed by N-methylpropylamine, assisted by two water molecules (red, subscript 2H₂O). The dashed green line indicates the promotion by one water molecule, as reported in Figure 6-1. The numbers indicate

the $\Delta^\ddagger G_{\text{forward}}$ for the considered reaction. The Gibbs free energy includes a correction term for a 50/50 vol% DMSO/acetone liquid phase, as experimentally employed in Chapter 4.

Figure 5-3: Gibbs free energy diagram for the aldol reaction of acetone with 4-nitrobenzaldehyde at 328.15 K catalyzed by N-methylpropylamine, assisted by one isolated silanol group (subscript s). The numbers indicate the $\Delta^\ddagger G_{\text{forward}}$ for the considered reaction. The Gibbs free energy includes a correction term for a 50/50 vol% DMSO/acetone liquid phase, as experimentally employed¹.

Figure 5-4: Gibbs free energy diagram for the aldol reaction of acetone with 4-nitrobenzaldehyde catalyzed by N-methylpropylamine, assisted by two vicinal silanols (subscript 2s). The numbers indicate the $\Delta^\ddagger G_{\text{forward}}$ for the considered reaction. The Gibbs free energy includes a correction term for a 50/50 vol% DMSO and acetone liquid phase, as experimentally employed¹.

Figure 5-5: Gibbs free energy reaction barriers for the aldol product dehydration to the enone product, readsorption on the N-methylpropylamine site, and dehydration, assisted by one isolated silanol (grey, subscript s) or two vicinal silanols (black, subscript 2s). The numbers indicate the $\Delta^\ddagger G_{\text{forward}}$ for the considered reaction. The Gibbs free energy includes a correction term for a 50/50 vol% DMSO/acetone liquid phase, as experimentally employed¹.

Figure 6-1: Schematic representation of the (LS)² reactor with the feed vessel (1), the positive displacement pump (2) with pulsation damper (3), the pre-heating (4), the reactor heating (5) and insulation (6), the outlet pressure gauge (7), the check valve (8) and three-way valve (9)

Figure 6-2: Continuously stirred reagent vessel (1), plunger pump Eldex 2SMP (2) with pulsation damper (3).

Figure 6-3: Heating element (4) of 125 W to pre-heat the feed before it enters the reactor. The green arrow indicates the direction of flow.

Figure 6-4: Heating cone for the reactor tube (5), surrounded by insulation (6). Indication 'F' is the mesh location at 50 mm from the bottom of the heating coat, indication 'T' is the height of the internal thermocouple at 103 mm from the bottom of the heating coat. The green arrow indicates the direction of flow.

Figure 6-5: Outlet of the reactor, with the outlet pressure manometer (7), the backpressure check valve (8) and the three-way valve (9) with one line for drawing samples and the other line going to the waste bottle. The green arrow indicates the direction of flow.

Figure 6-6: Conversion as function of time on stream for the aldol reaction between acetone and 4-nitrobenzaldehyde using hexane as a solvent, catalyzed by a monofunctional MAP catalyst. (T = 328.15 K, P_{tot} = 180 kPa, site time = 165.1 mol_{site}·s·mol_{4-NB}⁻¹, 0.45 wt% 4-nitrobenzaldehyde, 55.8 wt% acetone, 43.5 wt% hexane, 0.25 wt% IS). Line is a guide for the eye.

- Figure 6-7: Conversion as a function of time on stream for the aldol reaction between acetone and 4-nitrobenzaldehyde using acetone as solvent, catalyzed by a monofunctional MAP catalyst. ($T = 328.15 \text{ K}$, $P = 180 \text{ kPa}$, site time = $165.1 \text{ mol}_{\text{site}} \cdot \text{s} \cdot \text{mol}^{-1}$, 0.45 wt% 4-nitrobenzaldehyde, 99.3 wt% acetone, 0.25 wt% IS.)
- Figure 6-8: Conversion as a function of time on stream for the aldol reaction between acetone and 4-nitrobenzaldehyde using DMSO as a solvent with varying amounts of water. (a): no added water, (b): 1 wt% water added, (c): 2 wt% water added. ($T = 328.15 \text{ K}$, $P = 180 \text{ kPa}$, site time = $165.1 \text{ mol}_{\text{site}} \cdot \text{s} \cdot \text{mol}^{-1}$, 0.45 wt% 4-nitrobenzaldehyde, 44.6 wt% acetone, 52.5 – 55.0 wt% DMSO, 0.25 wt% IS.)
- Figure 6-9. Stability of the cooperative MAP catalyst (◆) and the monofunctional MAP catalyst (●) with time-on-stream for 28 hours. ($T = 328.15 \text{ K}$, $P_{\text{tot}} = 180 \text{ kPa}$, site time = $165.1 \text{ mol}_{\text{site}} \cdot \text{s} \cdot \text{mol}_{4\text{-nitrobenzaldehyde}}^{-1}$, 0.45 wt% 4-nitrobenzaldehyde, 44.6 wt% acetone, 52.5 wt% DMSO, 2.19 wt% water, 0.25 wt% IS). Lines are a guide to the eye.
- Figure 6-10: Conversion as function of site time of a monofunctional MAPS catalyst for the aldol reaction between acetone and 4-nitrobenzaldehyde using hexane as solvent. ($T = 328.15 \text{ K}$, $P_{\text{tot}} = 180 \text{ kPa}$, site time = $81.75 - 330.3 \text{ mol}_{\text{site}} \cdot \text{s} \cdot \text{mol}^{-1}$, 0.45 wt% 4-nitrobenzaldehyde, 55.8 wt% acetone, 43.5 wt% hexane, 0.25 wt% IS. Fixed error of 2.1 %)
- Figure 7-1: Structure of chitosan, consisting of n β -(1-4)-N-acetyl-D-glucosamine units and m D-glucosamine units.
- Figure 7-2: Reaction mechanism for the aldol reaction of acetone with 4-nitrobenzaldehyde on the primary amines of chitosan catalysts, based on reference ²².
- Figure 7-3: Measured total product yield versus reaction time for crude low-molecular weight chitosan as catalyst in the aldol reaction of acetone with 4-nitrobenzaldehyde. ($T = 55 \text{ }^\circ\text{C}$, $m_{\text{acetone}} = 45 \text{ g}$, $m_{4\text{NB}} = 0.45 \text{ g}$, $m_{\text{water}} = 55 \text{ g}$, $m_{\text{chitosan}} = 0.26 \text{ g}$)
- Figure 7-4: FT-IR spectrum of fresh (grey) and spent (black) chitosan for the aldol reaction of acetone with 4-nitrobenzaldehyde employing water as solvent. ($T = 55 \text{ }^\circ\text{C}$, $m_{\text{acetone}} = 45 \text{ g}$, $m_{4\text{NB}} = 0.45 \text{ g}$, $m_{\text{water}} = 55 \text{ g}$, $m_{\text{chitosan}} = 0.26 \text{ g}$)
- Figure 7-5: Measured total product yield versus reaction time for hydrogels of low-molecular weight chitosan as catalyst in the aldol reaction of acetone with 4-nitrobenzaldehyde. First run (●) second run (■). ($T = 55 \text{ }^\circ\text{C}$, $m_{\text{acetone}} = 45 \text{ g}$, $m_{4\text{NB}} = 0.45 \text{ g}$, $m_{\text{water}} = 55 \text{ g}$, $m_{\text{chitosan}} = 0.26 \text{ g}$)
- Figure 7-6: Measured total product yield versus reaction time for aerogels of low-molecular weight chitosan as catalyst in the aldol reaction of acetone with 4-nitrobenzaldehyde. First run (●) second run (■). ($T = 55 \text{ }^\circ\text{C}$, $m_{\text{acetone}} = 45 \text{ g}$, $m_{4\text{NB}} = 0.45 \text{ g}$, $m_{\text{water}} = 55 \text{ g}$, $m_{\text{chitosan}} = 0.26 \text{ g}$)
- Figure 7-7: Total product yield (●, left axis) and 4-nitrobenzaldehyde molar balance (▲, right axis) as a function of time-on-stream in the continuous-flow reactor using crude

- chitosan as catalyst. ($W/F_{4\text{-NB}}^0 = 1510 \text{ kg}_{\text{cat}} \text{ s mol}^{-1}_{4\text{NB}}$, 44.7 m% acetone, 54.6 m% water, 0.45 m% 4-nitrobenzaldehyde, 0.20 m% methyl-4-nitrobenzoate, $T = 55 \text{ }^\circ\text{C}$).
- Figure 7-8: Site-time yield for primary amines in deacetylated chitin from 2.6% to 76.8% deacetylation. Line is a guide for the eye. ($T = 55 \text{ }^\circ\text{C}$, $m_{\text{acetone}} = 45 \text{ g}$, $m_{4\text{NB}} = 0.45 \text{ g}$, $m_{\text{water}} = 55 \text{ g}$, $m_{\text{chitosan}} = 0.26 \text{ g}$, Parr reactor)
- Figure 8-1: Two different PMO materials that will serve as support for the amine catalyst.
- Figure 8-2: Four different amine-PMO catalysts that are synthesized in this work, based on the supports in Figure 8-1.
- Figure 8-3: Cross-linked resin catalysts based on a poly(ethylene glycol) methacrylate (PEGMA-X), functionalized with ethylenediamine (PEGMA-EDA), N,N'-dimethylethylenediamine (PEGMA-DED) or methylamine (PEGMA-MA)
- Figure 8-4: Nitrogen sorption isotherms for the Ethane-bridged PMO material and the catalysts derived from it
- Figure 8-5: Nitrogen sorption isotherms for the Ethylene-bridged PMO material and the catalysts derived from it
- Figure 8-6: DP ^{13}C -NMR at 60°C of PEGMA hydrogel (a) and chlorine functionalized PEGMA (b)
- Figure 8-7: FT-IR spectrum of PEGMA hydrogel (a) and chlorine functionalized PEGMA (b)
- Figure 8-8: $60 \text{ }^\circ\text{C}$ DP ^{13}C -NMR of the PEGMA-EDA catalyst
- Figure 8-9: $60 \text{ }^\circ\text{C}$ DP ^{13}C -NMR of the PEGMA-DED catalyst
- Figure 8-10: Turnover frequency for the PMO catalysts, determined in the Parr[®] batch reactor, for the aldol reaction of acetone with 4-nitrobenzaldehyde. ($T = 55 \text{ }^\circ\text{C}$, $m_{\text{acetone}} = 45 \text{ g}$, $m_{4\text{NB}} = 0.45 \text{ g}$, $m_{\text{water}} = 55 \text{ g}$, 0.1 mmol amine sites)
- Figure 8-11 Leaching of the amine sites in the Amine-Ethane-PMO catalyst through amine catalyzed hydrolysis of the siloxane bonds¹⁴.
- Figure 8-12 Structural degradation of the PMO material through hydrolysis of the siloxane bonds, catalyzed by the amine site can lead to structural degradation.
- Figure 8-13: Turnover frequency for the PEGMA catalysts, determined in the Parr[®] batch reactor, for the aldol reaction of acetone with 4-nitrobenzaldehyde. ($T = 55 \text{ }^\circ\text{C}$, $m_{\text{acetone}} = 45 \text{ g}$, $m_{4\text{NB}} = 0.45 \text{ g}$, $m_{\text{water}} = 55 \text{ g}$, 0.1 mmol amine sites)
- Figure 8-14: Conversion as a function of time on stream for the PEGMA-EDA catalyst in the aldol reaction of acetone with 4-nitrobenzaldehyde. ($T = 328.15 \text{ K}$, $P = 180 \text{ kPa}$, site time = $544 \text{ mol}_{\text{site}} \cdot \text{s} \cdot \text{mol}^{-1}$, 0.45 wt% 4-nitrobenzaldehyde, 44.6 wt% acetone, 54.5 wt% water, 0.25 wt% IS.)
- Figure A-1: Amines with different steric requirements experimentally investigated by Brown et al.¹⁻⁵
- Figure A-2: comparison of the gas-phase experimental trimethylborane basicity (TMBB) by Brown et al.¹⁻⁵ for the amines displayed in Figure A-1, compared to the gas-phase

TMBB values calculated with the CBS-QB3 model chemistry, at 298.15 K and 1 atm.

Figure A-3: comparison of the gas-phase experimental proton basicity (PB) by Hunter and Lias⁶ for the amines displayed in Figure A-1, compared to the gas-phase PB values calculated with the CBS-QB3 model chemistry, at 298.15 K and 1 atm.

Figure A-4: 4R-4-hydroxy-D-proline complexation with trimethylborane (TMB) and protonation (H^+). The hydrogen-bond between the carboxylic acid and the amine is lost upon TMB complexation and a new hydrogen-bond between the hydroxyl group and the carboxylic acid is formed.

Figure A-5: 4S-4-hydroxy-L-proline complexation with trimethylborane (TMB) and protonation (H^+). The hydrogen-bond between the carboxylic acid and the amine is lost upon TMB complexation.

Figure B-1. DRIFT spectrum of the monofunctional base catalyst (a), acid-base cooperative catalyst (b) and the pristine silica gel support material (c).

Figure C-1: Transition state for the addition of acetone with N-methylpropylamine with respectively zero (TS1), one (TS1_{H2O}) or two (TS1_{2H2O}) assisting water molecules.

Figure C-2: Transition state for the carbinolamine dehydration towards the enamine with respectively zero (TS2), one (TS2_{H2O}) or two (TS2_{2H2O}) assisting water molecules.

Figure C-3: carbinolamine dehydration, assisted by three water molecules, passing through the unstable iminium intermediate. Values are ΔG_{liq} in kJ mol^{-1} , relative to the previous stable state. Composite barrier is $131.3 \text{ kJ mol}^{-1}$.

Figure C-4: reaction of 4-nitrobenzaldehyde with the enamine intermediate (c) (TS3) towards the aldol product enamine (d), passing through the iminium intermediate (d').

Figure C-5: Bond scan of 4-nitrobenzaldehyde reaction with enamine (Figure 3S), in vacuum (black) and in DMSO (blue). Vacuum calculations are performed with B3LYP/CBSB7, solvent phase calculations have been performed on the same level of theory and an SMD Polarizable Continuum Model of DMSO ($\epsilon = 46.826$). The electronic energy is calculated relative to the separated reactants.

Figure C-6: Top view of the (111) β -cristobalite surface with isolated silanols 5.26 \AA apart.

Figure C-7: grafted N-methylpropylaminemethoxysilane on the (111) β -cristobalite surface with isolated silanols. Connected with one linker.

Figure C-8: The (100) α -quartz surface with vicinal silanols (2.66 \AA apart from each other)

Figure C-9: N-methylpropylaminemethoxysilane grafted on the (100) α -quartz surface with vicinal silanols, connected with two linkers.

Figure E-1: measured total product yield versus reaction time when no catalyst is used. ($T = 55 \text{ }^\circ\text{C}$, $m_{\text{acetone}} = 45 \text{ g}$, $m_{4\text{NB}} = 0.45 \text{ g}$, $m_{\text{water}} = 55 \text{ g}$)

Figure E-2: 4-nitrobenzaldehyde molar balance versus reaction time for crude low-molecular weight chitosan as catalyst in the aldol reaction of acetone with 4-nitrobenzaldehyde. ($T = 55 \text{ }^\circ\text{C}$, $m_{\text{acetone}} = 45 \text{ g}$, $m_{4\text{NB}} = 0.45 \text{ g}$, $m_{\text{water}} = 55 \text{ g}$, $m_{\text{cat}} = 0.26 \text{ g}$)

- Figure E-3: measured total product yield versus reaction time for low-molecular weight chitosan hydrogel as catalyst in the aldol reaction of acetone with 4-nitrobenzaldehyde in a small scale reaction. ($T = 55\text{ }^{\circ}\text{C}$, $m_{\text{acetone}} = 22.5\text{ g}$, $m_{4\text{NB}} = 0.225\text{ g}$, $m_{\text{water}} = 27.5\text{ g}$, $m_{\text{chitosan}} = 0.05\text{ g}$)
- Figure E-4: DRIFTS spectrum of chitosan reacted with 4-nitrobenzaldehyde in a 45g DMSO, 55g water mixture at $55\text{ }^{\circ}\text{C}$ (black) compared to the catalyst spent in the aldol reaction (grey).
- Figure E-5: 4-nitrobenzaldehyde molar balance as a function of time-on-stream in the continuous-flow reactor using chitosan as catalyst.
- Figure F-1: DRIFTS spectrum of the 100% Ethane-bridged PMO (a), Amine-Ethane-PMO (b) and HMDS-Amine-Ethane-PMO (c).
- Figure F-2: DRIFTS spectrum of the 100% Ethylene-bridged PMO (a), Amine-Ethylene-PMO (b) and HMDS-Amine-Ethylene-PMO (c).
- Figure F-3: DP ^{13}C -NMR at $60\text{ }^{\circ}\text{C}$ for the pristine PEGMA hydrogel (a) and the 100% chlorine functionalized PEGMA material (b) and the corresponding peak assignments.
- Figure F-4: FT-IR spectrum of pristine PEGMA hydrogel (a) and fully chlorine functionalized PEGMA-Cl (b).
- Figure F-5: FT-IR spectrum PEGMA-EDA (a) and PEGMA-DED (b).
- Figure F-6: DP ^{13}C -NMR at $60\text{ }^{\circ}\text{C}$ for high loading PEGMA-EDA ($2.1\text{ mmol}_{\text{diamine}}\text{ g}^{-1}$)
- Figure F-7: FT-IR spectrum of high loading PEGMA-EDA ($2.1\text{ mmol}_{\text{diamine}}\text{ g}^{-1}$).

List of Schemes

- Scheme 1. Reaction mechanism⁸⁻¹⁰ of the aldol reaction of acetone with 4-nitrobenzaldehyde, catalyzed by an N-methylpropylamine catalyst as a model for the methylaminopropyl (MAP) site on mesoporous silica.
- Schema 1. Reactiemechanisme⁸⁻¹⁰ van de aldolreactie van aceton met 4-nitrobenzaldehyde, gekatalyseerd door een N-methylpropylamine-katalysator als een model voor het methylaminopropyl (MAP) actief centrum op mesoporeus silica.
- Scheme 1-1: Generalized example of an aldol reaction between two carbonyl species with the formation of an aldol or ketol product that can dehydrate towards an α,β -unsaturated aldehyde or ketone.
- Scheme 1-2: Industrial production of 2-ethylhexanol from self-aldol condensation of 1-butanol and subsequent hydrogenation.
- Scheme 1-3: Model aldol reaction of acetone with 4-nitrobenzaldehyde, towards the aldol adduct 4-hydroxy-4-(4-nitrophenyl)butan-2-one, and dehydration to the enone product 4-(4-nitrophenyl)-3-buten-2-one.
- Scheme 1-4: Generic mechanism of a Brønsted acid catalyzed aldol reaction
- Scheme 1-5: Generic mechanism of the Brønsted acid catalyzed aldol dehydration
- Scheme 1-6: Generic mechanism of a Brønsted base catalyzed aldol reaction
- Scheme 1-7: Generic mechanism of the Brønsted base catalyzed aldol dehydration
- Scheme 1-8: L-proline-catalyzed enantioselective aldol reaction with $R = C_6H_4-NO_2$. Figure adapted from ref 54.
- Scheme 1-9: Base-induced disproportionation of the non-enolizable benzaldehyde to a primary alcohol and a carboxylic acid (Cannizzaro reaction)⁷⁴
- Scheme 1-10: Ammonia catalyzed reaction of an organosilane with an isolated silanol. Figure adapted from Van Der Voort et al.⁷⁶
- Scheme 1-11: Reaction of HMDS with surface silanols⁸⁰
- Scheme 1-12: Thiol-ene click reaction mechanism, adapted from Lowe et al.¹¹⁷
- Scheme 1-13: Possible imine, and iminium ion, formation of 4-nitrobenzaldehyde on respectively a primary and a secondary amine.
- Scheme 3-1: general pathway to the enamine formation via initial nucleophilic attack on the carbonyl group (a) by an amine catalyst (b), with the formation of a carbinolamine intermediate (c) and dehydration to the enamine (d). Severe steric hindrance around the amine will cause the rate of this first step to decrease and result in a negligible catalytic activity being observed.
- Scheme 4-1. Proposed enamine catalytic reaction cycle of the aldol reaction of acetone with 4-nitrobenzaldehyde, catalyzed by a secondary cooperative aminated silica catalyst^{4, 7, 12}.

- Scheme 4-2. Possible species on the surface of a spent catalyst corresponding with the characterization results and their proposed formation pathways. The iminium intermediate species (5) from the catalytic cycle in Scheme 4-1, or from the aldol product readsorption via (6), can further dehydrate into a conjugated species (5b) via its enamine intermediate (5a). Enone product readsorption via (6') also yields the conjugated species (5b).
- Scheme 5-1: Reaction mechanism of the aldol reaction of acetone with 4-nitrobenzaldehyde, catalyzed by an N-methylpropylamine catalyst (black pathway, no subscripts) or catalyzed by N-methylpropylamine, assisted by one water molecule (green pathway, H₂O subscript). Green water molecules are assisting, black water molecules are from the carbinolamine dehydration (TS2). Species (e) can occur as such without a complexed water molecule, or as (e') with one complexed water molecule.
- Scheme 5-2: Reaction mechanism of the aldol reaction of acetone with 4-nitrobenzaldehyde catalyzed by a monofunctional N-methylpropylamine catalyst, assisted by two water molecules (red subscript 2H₂O).
- Scheme 5-3: Reaction mechanism of the aldol reaction of acetone with 4-nitrobenzaldehyde catalyzed by N-methylpropylamine, assisted by one isolated silanol group (subscript s).
- Scheme 5-4: Amine catalyzed aldol product isomerization to its enol form and subsequent amine catalyzed or uncatalyzed dehydration to the enone product, with the release of water. The N-methylpropylamine catalyst only binds to the transition states and not to the reagents, intermediates, or products.
- Scheme 5-5: Enone product readsorption and dehydration to the conjugated enamine h_s
- Scheme 8-1: Synthesis pathway, involving condensation of ethylene-bridged PMO (1), a thiolene click reaction (2) and an S_N2 nucleophilic substitution reaction (3).
- Scheme 8-2: Synthesis procedure of PEGMA catalysts, in this example functionalized with a primary ethylenediamine (PEGMA-EDA). Other amines or diamines can also be used.
- Scheme C-1: si-faced attack of 4-nitrobenzaldehyde on the enamine of acetone (c) leading to the enamine intermediate (d). Hydration of (d) occurs either si-faced, towards the S,S-diastereomer (e_{SS}) or re-faced towards the R,S-diastereomer (e_{RS})
- Scheme C-2: si-faced attack of 4-nitrobenzaldehyde on the enamine of acetone (c), assisted by two water molecules, leading to iminium ion (d'). Hydration of (d'), with two water molecules, occurs either si-faced, towards the S,S-diastereomer (e_{SS}) or re-faced towards the R,S-diastereomer (e_{RS}) with the release of a water molecule
- Scheme C-3: si-faced attack of 4-nitrobenzaldehyde on the enamine of acetone (c), assisted by one silanol group, leading to iminium ion (d'_s). Hydration of (d'_s), occurs either si-faced, towards the S,S-diastereomer (e_{SS}) or re-faced towards the R,S-diastereomer (e_{RS}).

Scheme C-4: si-faced attack of 4-nitrobenzaldehyde on the enamine of acetone (c), assisted by two silanol groups, leading to iminium ion (d'_{2s}). Hydration of (d'_{2s}), occurs either si-faced, towards the S,S-diastereomer (e_{SS}) or re-faced towards the R,S-diastereomer (e_{RS}).

List of Tables

Table 3-1: Affinity, entropy and basicity calculated at the CBS-QB3 level of theory at 298.15 K and 1 atm for reaction of L-proline derivatives 1 to 12 with the sterically demanding trimethylborane (TMB) or a steric-free proton.

Table 3-2: Affinity, entropy and basicity calculated at the CBS-QB3 level of theory at 298.15 K and 1 atm for reaction of L-proline derivatives 13 to 16 with the sterically demanding trimethylborane (TMB) or a steric-free proton.

Table 3-3: Affinity, entropy and basicity calculated at the CBS-QB3 level of theory at 298.15 K and 1 atm for reaction of groups 17 to 25 with the sterically demanding trimethylborane (TMB) or a steric-free proton. Catalysts 17 to 21 are monofunctional amines, catalysts 22 to 25 are bifunctional amine-hydroxyls.

Table 4-1. Catalyst properties, for both the cooperative acid-base catalyst as well as the monofunctional base catalyst, fresh and spent in the aldol reaction of acetone with 4-nitrobenzaldehyde. BET surface area, pore size and pore volume are determined via nitrogen adsorption–desorption measurements.

Table 5-1: Reaction Gibbs free energy barriers for the aldol reaction of acetone with 4-nitrobenzaldehyde in 50/50 vol% solvent/acetone mixture, catalyzed by N-methylpropylamine. Transition states are assisted by one, two or three water molecules or one isolated silanol group or two vicinal silanol groups. Gibbs free energy diagrams are displayed in Figure 6-1, Figure 6-2, Figure 6-3 and Figure 6-4. Thermodynamics of the considered reaction steps are reported in Table 6-2 and Table 6-3. (* indicates that the composite barrier is reported)

Table 5-2: Thermodynamics of the intermediates in the mechanisms displayed in Figure 6-1 and Figure 6-2.

Table 5-3: Thermodynamics of the intermediates for the aldol reaction of acetone and 4-nitrobenzaldehyde, catalyzed by N-methylpropylamine and assisted by one or two silanol groups (respectively subscript s and 2s). The Gibbs free energy includes a correction term for a 50/50 vol% solvent/acetone liquid phase.

Table 5-4: Gibbs free energy barriers for the reactions displayed in Scheme 6-4 and Scheme 6-5. The Gibbs free energy includes a correction term for a 50/50 vol% solvent/acetone liquid phase.

Table 5-5: Thermodynamics for the intermediates in Scheme 6-4 and Scheme 6-5. The Gibbs free energy includes a correction term for a 50/50 vol% solvent/acetone liquid phase.

Table 6-1: ‘Wetted parts’ in the Eldex 2SMP pump and their chemical compatibility with the solvents used in this work²

Table 6-2: Conversion of 2 different experiments with an identical site time but different flow rate. Hexane was used as solvent.

- Table 6-3: Conversion of 2 different experiments at $149.3 \text{ mol}_{\text{site}} \text{ s mol}^{-1}$ but different pellet sizes. Hexane was used as solvent.
- Table 7-1: Summary of the reaction rate, site-time yield and reusability in a second 4 hour run for the different chitosan catalysts. (*reusability was evaluated in smaller glass batch-type reactor)
- Table 7-2: Summary of reaction rate and site-time yield for chitosan with a different degree-of-deacetylation.
- Table 8-1: Structural properties obtained via nitrogen sorption of the Ethane-bridged and Ethylene-bridged PMO material and catalysts.
- Table 8-2: Diamine loading for the different PEGMA catalysts.
- Table A-1: CBS-QB3 computational results at 298.15 K and 1 atm of the TMB complexation and the protonation with the amines displayed in Figure A-1.
- Table B-1. Properties of the spent cooperative catalysts in the batch reactor
- Table C-1: reaction barriers for the pathway along the (S,S) diastereomer
- Table C-2: Thermodynamic stability of the intermediates in the reaction path along the (S,S) diastereomer
- Table D-1: Association factors of frequently used solvents
- Table D-2: Reactor properties for the Liquid-Solid Lab-Scale (LS)² reactor and catalyst properties for the amine functionalized silica material.
- Table D-3: Properties of the reaction mixture for the aldol reaction between acetone and 4-nitrobenzaldehyde using a 50/50 vol% hexane/acetone liquid mixture.
- Table D-4: Criteria for intrinsic kinetics of the aldol reaction between acetone and 4-nitrobenzaldehyde using a 50/50 vol% hexane/acetone liquid mixture in the (LS)² reactor.
- Table D-5: Properties of the reaction mixture for the aldol reaction between acetone and 4-nitrobenzaldehyde using a 50/50 vol% DMSO/acetone liquid mixture.
- Table D-6: Criteria for intrinsic kinetics of the aldol reaction between acetone and 4-nitrobenzaldehyde using a 50/50 vol% DMSO/acetone liquid mixture in the (LS)² reactor.
- Table D-7: Properties of the reaction mixture for the aldol reaction between acetone and 4-nitrobenzaldehyde using a 100 vol% acetone liquid mixture.
- Table D-8: Criteria for intrinsic kinetics of the aldol reaction between acetone and 4-nitrobenzaldehyde using a 100 vol% acetone liquid mixture in the (LS)² reactor.

List of symbols

Roman symbols

A_i	pre exponential factor of step i	[variable]
a_v	specific external surface area of the catalyst	$[\text{m}^2 \text{m}_{\text{pellet}}^{-3}]$
b_{max}	maximum dilution degree of catalyst bed	$[\text{m}_{\text{inert}}^3 \text{m}_{\text{bed}}^{-3}]$
C_i	concentration of component i	$[\text{mol l}^{-1}]$
C_t	total loading of amine sites	$[\text{mol kg}_{\text{cat}}^{-1}]$
$D_{\text{a,eff}}$	effective diffusivity inside the catalyst particles	$[\text{m}^2 \text{s}^{-1}]$
d_p	pellet diameter	[m]
d_t	reactor diameter	[m]
E	energy	$[\text{kJ mol}^{-1}]$
$\Delta E(0 \text{ K})$	activation barrier at 0 K (including ZPVE)	$[\text{kJ mol}^{-1}]$
E_a	activation energy	$[\text{kJ mol}^{-1}]$
E_{el}	electronic energy	$[\text{kJ mol}^{-1}]$
EE	experimental error in percentage	[-]
f_m	modified friction factor from the Ergun equation	[-]
F_i	molar flowrate of component i	$[\text{mol s}^{-1}]$
g_i	degeneracy of energy level i	[-]
G	Gibbs free energy	$[\text{kJ mol}^{-1}]$
H	enthalpy	$[\text{kJ mol}^{-1}]$
h	Planck's constant: $6.022 \cdot 10^{-34}$	[J s]
\hbar	reduced Planck's constant = $h/(2\pi)$	[J s]
h_{bed}	bed height	[m]
I	moment of inertia	$[\text{kg m}^2]$
J	total angular momentum quantum number	[-]
k	rate coefficient	[variable]
K	equilibrium coefficient	[variable]
k_B	Boltzmann constant = 1.3806×10^{-23}	$[\text{m}^2 \text{kg s}^{-2} \text{K}^{-1}]$
L_B	bed length	[m]
m	mass	[kg]
M	molar	$[\text{mol L}^{-1}]$

MM	molar mass	[kg mol ⁻¹]
n_i	number of moles of component i	[mol]
N	number of experiments	[-]
N_A	Avogadro's number = 6.0225×10^{23}	[molecules mol ⁻¹]
P	pressure	[Pa]
pK_a	the logarithmic acid dissociation constant	[-]
q	molecular partition function	[-]
Q	canonical partition function	[-]
R	universal gas constant 8.315	[J mol ⁻¹ K ⁻¹]
R_i	net rate of formation of component i	[mol s ⁻¹ kg _{cat} ⁻¹]
S	entropy	[J mol ⁻¹ K ⁻¹]
S_{BET}	BET-surface area	[m ² g ⁻¹]
T	temperature	[K]
T	kinetic energy	[-]
t	time	[s]
TOF	turnover frequency	[s ⁻¹]
U	internal energy	[kJ mol ⁻¹]
u_0	linear liquid velocity	[m s ⁻¹]
V	potential energy	[-]
$V_{m,i}$	molar volume of component i	[m ³ mol ⁻¹]
V_P	catalyst pore volume	[m ³ kg _{cat} ⁻¹]
W_{cat}	catalyst mass	[kg]
X	conversion	[mol mol ⁻¹]
x_i	mole fraction of component i	[-]

Greek symbols

α	heat transfer coefficient	[W m ⁻² K ⁻¹]
Δ	deviation on mass balance	[%]
ε	bed porosity	[m ³ m ⁻³]
ε	dielectric constant relative to ε_0	[-]
ε_0	vacuum permittivity	[-]
γ_i	activity coefficient	[-]
λ_p	catalyst pellet heat conductivity	[W m ⁻¹ K]

η	Gaussian function	[-]
ρ	density	[kg m ⁻³]
σ	standard deviation	[variable]
σ	symmetry number	[-]
τ_B	tortuosity of the bed	[m _f ² m _r ⁻²]
τ_{ij}	measure of the binary interaction	[-]
σ	screening charge density	[C m ⁻²]
μ	reduced mass	[kg]
$\mu(\sigma)$	sigma potential	[J mol ⁻¹ m ⁻²]
μ_i	chemical potential of component i	[kJ mol ⁻¹]
μ_{mix}	dynamic viscosity of the liquid mixture	[Pa s]
ν	frequency	[cm ⁻¹]
φ_j	atomic orbital j	[-]
ϕ_i	spatial orbital	[-]
Φ	Weisz modulus	[-]
Ω	nuclear wave function	[-]
χ_i	one-electron wave function	[-]
Ψ	wave function	[-]

Superscripts

‡	transition state
0	initial condition
°	at the standard state
Gas	gas phase
Liq	liquid phase
^	operator

Subscripts

4-NB	4-nitrobenzaldehyde
ace	acetone
ads	adsorption
av	average
el	electronic

HB	Hydrogen-bond
H ₂ O	water
MF	misfit
obs	observed
<i>i</i>	component <i>i</i>
<i>ij</i>	interaction of species <i>i</i> with species <i>j</i>
rot	rotational
R	clockwise stereocenter
S	counter-clockwise stereocenter
solv	solvation
sol	solution
trans	translational
VdW	Van der Waals
vib	vibrational

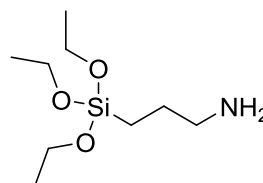
Acronyms

AIBN	azobisisobutyronitrile
B3LYP	Becke, three-parameter, Lee-Yang-Parr
BP86	Becke 1988 exchange functional, Perdew 86 correlation functional
CAP	cyclohexylaminopropyl
CBS-QB3	complete basis set-quadratic Becke3
CC	coupled cluster
COSMO	conductor-like screening model
COSMO-RS	conductor-like screening model for real solvents
CTST	conventional transition state theory
DFT	density functional theory
DMSO	dimethylsulfoxide
EAP	N-ethylaminopropyl
FTIR	Fourier transform infrared
GC	gas chromatography
GGA	generalized gradient approximation
HF	Hartree-Fock
HMDS	1,1,1,3,3,3-hexamethyldisilazane

HO	harmonic oscillator
HT	hydrotalcite
IRC	intrinsic reaction coordinate
KS	Kohn-Sham
LDA	local density approximation
MA	methyl acrylate
MAP	N-methylaminopropyl
MCA	methyl cation affinity
MEDT	methyl ethane dithioate
MI	maleimide
MMA	methyl methacrylate
MP _(n)	<i>n</i> th order Møller-Plesset
NMR	nuclear magnetic resonance
PA	proton affinity
PAP	N-phenylaminopropyl
PB	proton basicity
PEG _x	polyethylene glycol polymer of X monomer units
PES	potential energy surface
PCM	polarizable continuum model
PMO	periodic mesoporous organosilica
SCF	self consistent field
SCRF	self consistent reaction field
SMD	solvation model density
THF	tetrahydrofuran
TMB	trimethylborane
TMBA	trimethylborane affinity
TMBB	trimethylborane basicity
TS	transition state
TZVP	triple zeta valence plus polarization
ZPVE	zero point vibrational energy

List of structures

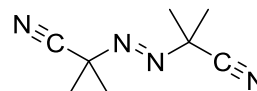
(3-aminopropyl)triethoxysilane (APTES)



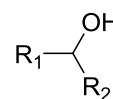
acetone



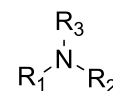
azobisisobutyronitril (AIBN)



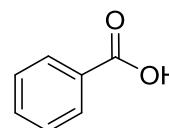
alcohol



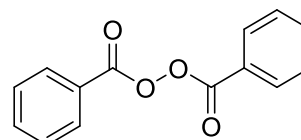
amine



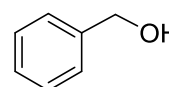
benzoic acid



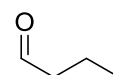
benzoyl peroxide (BPO)



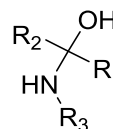
benzylalcohol



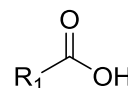
butanal



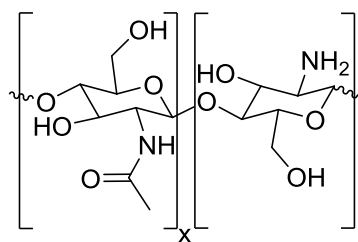
carbinolamine

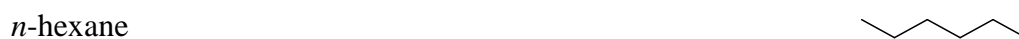
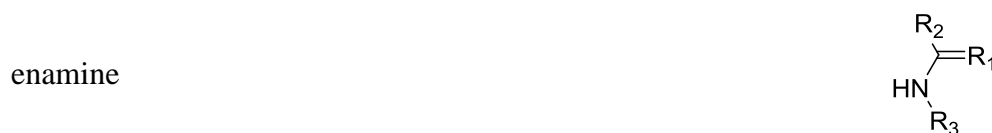


carboxylic acid

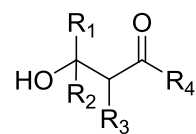


chitosan

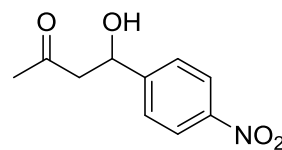




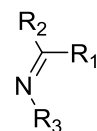
β -hydroxy carbonyl (aldol)



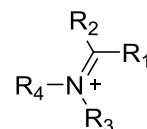
4-hydroxy-4-(4-nitrophenyl)butane-2-one (aldol)



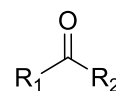
imine



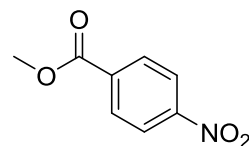
iminium ion



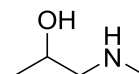
ketone



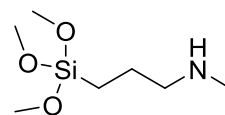
methyl-4-nitrobenzoate



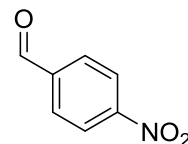
1-(methylamino)propan-2-ol



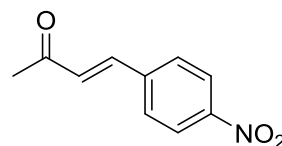
N-methylaminopropyltrimethoxysilane
(MAPTMS)



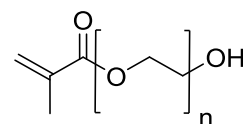
4-nitrobenzaldehyde



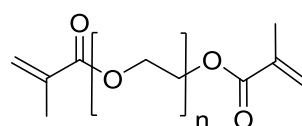
4-(4-nitrophenyl)-3-buten-2-one (ketone)



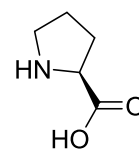
(polyethylene glycol) methacrylate (PEGMA)



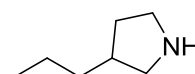
(polyethylene glycol) dimethacrylate (PEGDMA)



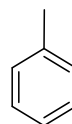
proline



3-propylpyrrolidine group



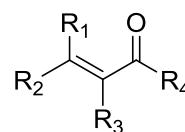
toluene



thiol



α,β -unsaturated carbonyl



Glossary of terms

Ab initio	Latin term for “from first principles”. It refers to the fact that the results are obtained by applying the established laws of nature without assumptions or experimental input. Ab initio methods determine the energy of a system by solving the Schrödinger equation.
Activation energy	For an elementary step, the difference in internal energy between transition state and reactants. A measure for the temperature dependence of the rate coefficient.
Active site	Functional group at the surface of a solid support or on an enzyme which is responsible for the catalytic activity.
Activity coefficient	Coefficient explicitly accounting for the non-ideality of the liquid phase, often denoted as γ .
Aldol condensation	Carbon-carbon coupling reaction between two carbonyl components yielding a β -hydroxy carbonyl component which can, dehydrate to an α,β -unsaturated carbonyl component.
Basis set	Set of (usually Gaussian) functions used to describe the molecular orbitals in ab initio or DFT calculations.
Brønsted acid	A molecule that can lose a proton
Brønsted base	A molecule that can accept a proton
Catalyst	Substance or material, which through repeated cycles of elementary steps, accelerates the conversion of reagents into the desired products. The source of active centers is regenerated at the end of a closed reaction sequence.

CHNS elemental analysis	Method based on the combustion of organic components to determine the weight percentage of carbon, hydrogen, nitrogen and sulfur atoms in a solid or liquid sample.
Conversion	Measure for the amount of a reactant that has been transformed into products as a result of the chemical reaction.
Cooperativity	The interaction process by which interaction of a reactant with one site, <i>i.e.</i> the promoting site, influences the transition states at a second site, <i>i.e.</i> the active site.
Dative bond	A 2-center, 2-electron covalent bond in which the two electrons derive from the same atom.
Deactivation	The irreversible decrease in activity of a catalyst, observed via consecutive batch experiments or with time on stream in a continuous-flow reactor.
Dehydration	A chemical reaction that involves the removal of water.
Density Functional Theory (DFT)	Computational method that derives properties of the molecule based on a determination of the electron density of the molecule. Unlike the wave function, which is not a physical reality but a mathematical construction, electron density is a physical characteristic of all molecules.
Diastereoisomer or diastereomer	One of a pair of stereoisomers which are not related as mirror images. Diastereoisomers are characterized by differences in physical properties, and by some differences in chemical behavior.
Diffuse Reflectance Infrared Fourier Transform (DRIFT) spectroscopy	Infrared spectroscopic technique used to identify chemical functional groups present in porous solid materials.

Elementary step	The irreducible act of reaction in which reactants are transformed into products directly, i.e., without passing through an intermediate that is susceptible to isolation.
Enantiomer	One of a pair of molecular entities which are non-superposable mirror images of each other.
High performance liquid chromatography (HPLC)	The process in which the components of a liquid mixture are separated from one another by injecting the sample into a carrier liquid which is passing through a high-density packed column with different affinities for adsorption of the components to be separated.
Inhibition	The decrease in catalytic reaction rate due to the reversible addition of a non-reactive species to an active site
Lewis acid	A chemical species that contains an empty orbital which is capable of accepting an electron pair from a Lewis base to form a Lewis adduct
Lewis base	Any species that has a filled orbital containing an electron pair which is not involved in bonding but may form a dative bond with a Lewis acid to form a Lewis adduct.
Lignocellulosic biomass	Non-edible biomass composed of carbohydrate polymers (cellulose, hemicellulose), and an aromatic polymer (lignin).
Mesopores	Pores of intermediate size, i.e. between 2 nm and 50 nm.
Nitrogen sorption measurements	Experimental method to determine the specific surface, average pore size and pore size distribution of a porous solid material.
NMR spectroscopy	Technique that exploits the magnetic properties of atomic nuclei in order to determine the

	physical and chemical properties of the atoms or molecules in which they are contained.
Nucleophile	Reactant that forms a bond to its reaction partner, <i>i.e.</i> , the electrophile, by donating an electron pair.
Partition function	A measure for the statistical properties of a system.
Pre-exponential factor	The temperature-independent factor of a rate, also called the frequency factor.
Promoting site	Functional group at the surface of a solid support or on an enzyme which influences the interactions of the reactants and intermediates on the catalytically active site.
Raman spectroscopy	Technique based on inelastic scattering of photons for the identification of chemical function groups.
Reaction mechanism	A sequence of elementary steps in which reactants are converted into products, through the formation of intermediates.
Reaction rate	The number of moles of a component created by a chemical reaction per unit of time and catalyst mass.
Selectivity	Measure for the amount in which a product is formed from the reactants as a result of a chemical reaction.
Stereoselectivity	The preferential formation in a chemical reaction of one stereoisomer over another. When the stereoisomers are enantiomers, the phenomenon is called enantioselectivity and is quantitatively expressed by the enantiomer excess; when they are diastereoisomers, it is called diastereoselectivity and is quantitatively expressed by the diastereoisomer excess.
Silanol	Hydroxy group bonded to a silicon atom.

Support	Also called carrier material, usually of high surface area, on which the active catalytic material, present as the minor component, is dispersed. The support may contribute to the overall catalytic activity.
Transition state	Also called activated complex. The configuration of highest potential energy along the lowest energy path between reactants and products.
Transition state theory	Theory that allows to calculate rate coefficients of chemical reactions assuming quasi-equilibrium between the reactant and transition state.
Turnover frequency	The number of molecules of a component reacting per active site in unit of time.
Zero-point vibrational energy (ZPVE)	The energy of vibration of a molecule at absolute zero (0 K). This is a quantum chemical effect arising from the uncertainty principle.

Summary

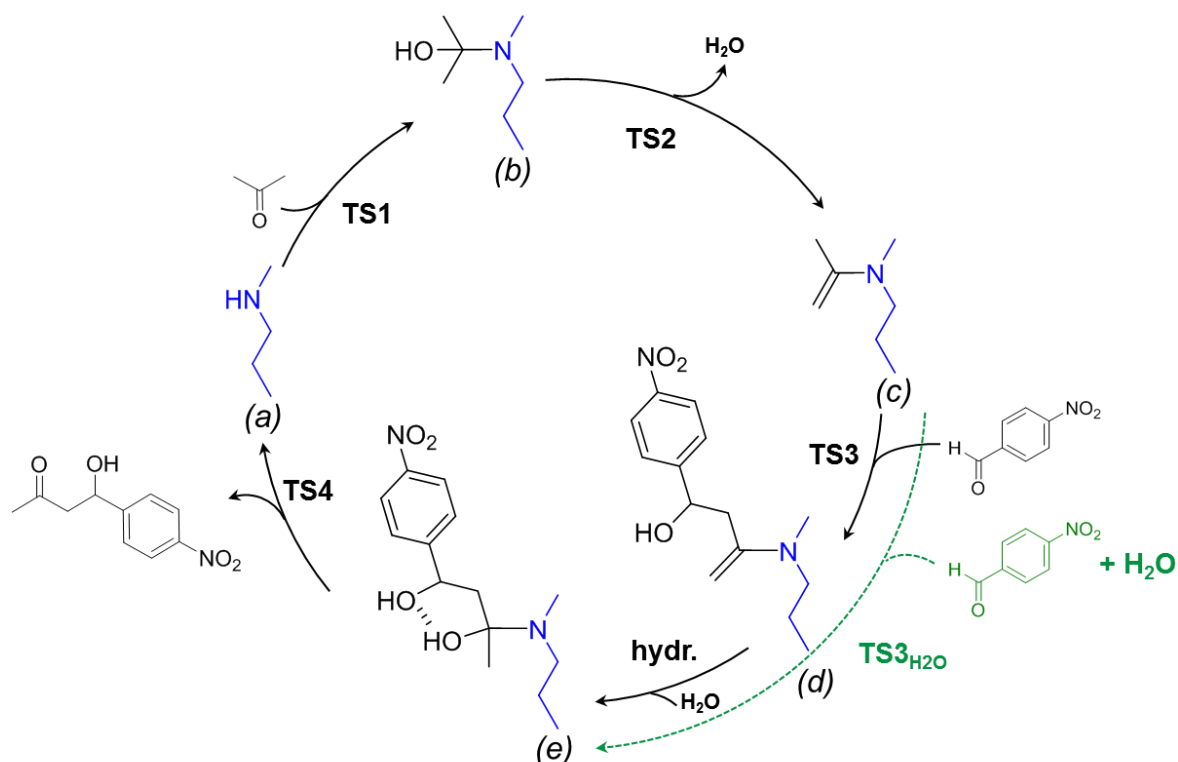
Aldol reactions are carbon coupling reactions between two carbonyl-containing species, which are widely used to synthesize new organic molecules with longer carbon chains. This class of reactions is typically used in the synthesis of fine chemicals¹ and pharmaceuticals². A potential new application is situated in the bio-based industry for the production of liquid fuels from lignocellulosic biomass. The cellulose that can be obtained from this type of feedstock is first converted into aqueous sugars, which can then be reduced and reformed into carbonyl-containing platform molecules with an average carbon chain length between 3 and 6. To upgrade this low carbon chain length to the range desired for application in internal combustion engines, aldol reactions can be performed using the functionality available in these platform molecules³. At present, industrial aldol reactions are typically catalyzed by homogeneous strong bases. Despite their adequate activity, these catalysts are dangerous to handle, pose an environmental risk, and are deactivated upon separation from the product stream¹. Heterogeneous base catalysts, such as amine functionalized mesoporous silica materials, do not have these disadvantages⁴ and are thus more attractive for the use in more industrially relevant continuous-flow reactors.

Catalysts with primary or secondary amine sites, grafted with a linker of three carbon atoms to the mesoporous silica surface, have often been investigated for the model aldol reaction of acetone with 4-nitrobenzaldehyde⁵⁻⁷. It is generally accepted in literature⁸⁻¹⁰ that the secondary amine-catalyzed aldol reaction mechanism starts with the reaction of acetone with the amine site (**a**), as displayed in Scheme 1, resulting in a carbinolamine intermediate (**b**), which subsequently dehydrates to an electron-rich enamine intermediate (**c**). Next, this nucleophilic enamine intermediate (**c**) attacks the carbonyl group of the second reagent, i.e. 4-nitrobenzaldehyde, and a carbon-carbon coupling occurs with the formation of a second enamine species (**d**). Finally, a water assisted desorption step through a carbinolamine intermediate (**e**), releases the aldol product and regenerates the active site (**a**).

Secondary amines are generally preferred as active sites for the aldol reaction, because on primary amines stable imines of both 4-nitrobenzaldehyde and acetone can form which cause active site inhibition^{5,8}. Tertiary amines cannot form the crucial enamine intermediate (**c**)⁵ and have, hence, not been considered in this work. For both the primary and secondary amine functionalized catalysts, it was previously observed that due to a cooperative interplay, hydrogen-bond promoters such as intramolecular hydroxyl groups¹¹ or surface silanol groups¹²,

increase the amine turnover frequency (TOF). These promoted catalysts are denoted as cooperative acid-base catalysts, as opposed to monofunctional base catalysts, which do not have any acidic hydrogen-bond promoters. On mesoporous silica, a monofunctional base catalyst can be obtained by endcapping the cooperative surface silanol groups with an organic group such as the trimethylsilyl group.

Previous experimental work by Lauwaert et al.⁵, and recent work by Xie et al.¹³, has shown that minimizing steric hindrance around the nucleophilic nitrogen atom in secondary amines is crucial for obtaining an adequate catalytic turnover frequency in the aldol reaction. Additionally, Lauwaert et al.¹¹ also showed that a well-placed intramolecular hydroxyl group can promote the amine function to the same extent as a surface silanol group. However, it is crucial that this intramolecular hydroxyl group does not introduce any restrictive steric hindrance around the amine site. Therefore, in this work a computational methodology is developed that provides a quick assessment of potential steric hindrance in novel organic amines and cooperative amine-hydroxyl groups. Specifically the 3-propylpyrrolidine and 1-(methylamino)propan-2-ol groups were proposed as, respectively, the most promising monofunctional amine and intramolecular cooperative amine-hydroxyl pair.



Scheme 1. Reaction mechanism⁸⁻¹⁰ of the aldol reaction of acetone with 4-nitrobenzaldehyde, catalyzed by an N-methylpropylamine catalyst as a model for the methylaminopropyl (MAP) site on mesoporous silica.

In the next part of this work, an experimental investigation was performed on the stability of the current state-of-the-art aminated silica catalysts. The reusability was assessed in an initial and recycle batch aldol reaction at 328.15 K, using dimethylsulfoxide (DMSO) as solvent, and acetone as excess reagent. Only 38% of the TOF was obtained for a second run of the cooperative acid-base catalyst and 77% of the initial TOF was obtained with recycling the monofunctional base catalyst. Characterization of the spent catalysts with nitrogen sorption indicated that the structural properties of the catalyst remained intact. However, CHN analysis indicated a 60% increase in nitrogen content for the spent cooperative acid-base catalyst and a 15% increase for the spent monofunctional base catalyst. Moreover, the originally white catalysts changed to yellow and retained this color even after additional stirring in chloroform and drying. Characterization of the spent catalysts revealed that this was caused by surface species derived from 4-nitrobenzaldehyde that remained attached to the amine site, as displayed in Figure 1.

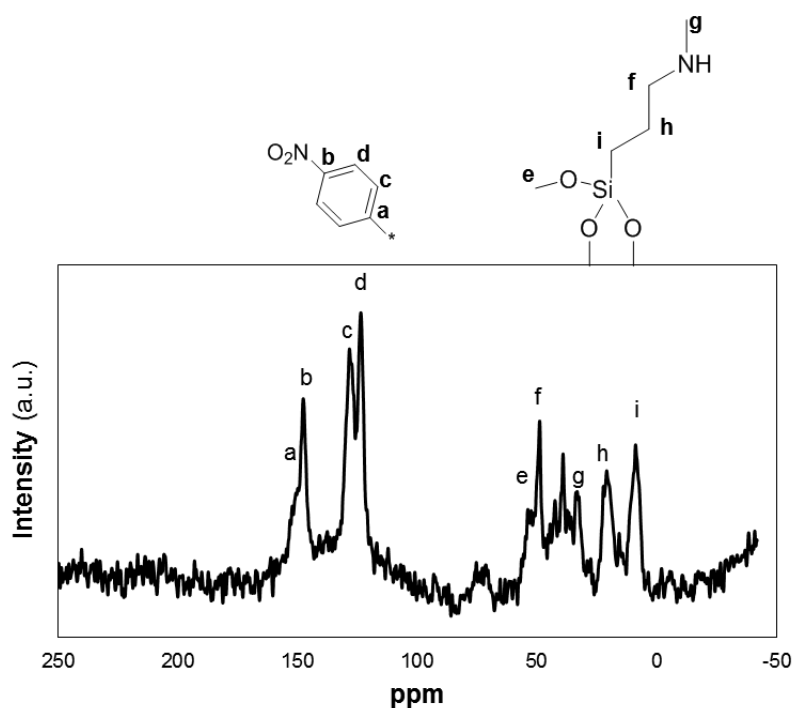


Figure 1. ^{13}C CP/MAS NMR spectrum of the spent cooperative acid-base catalyst. The grafted secondary amine can be identified in the spectrum, as well as the carbon atoms originating from the aromatic ring with a nitro substituent.

The presence of small amounts of water in the reaction was found to reduce the formation of these species, and resulted in a complete reusability for the monofunctional base catalyst, as displayed in Figure 2. Complete reusability was never achieved for the cooperative acid-base catalyst, which is likely due to water molecules deactivating the promoting ability of the silanol groups. To further investigate this hypothesis, a lab scale fixed-bed plug-flow reactor was designed, called the Liquid-Solid Lab-Scale (LS)² reactor. Using this continuous-flow reactor,

it was possible to directly evaluate the stability of a catalyst as a function of time on stream at the same reaction conditions as the batch reactor.

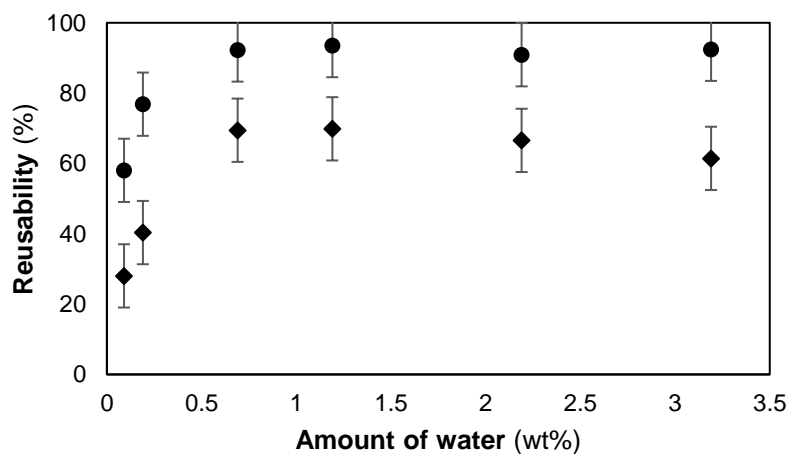


Figure 2: Reusability of the cooperative acid-base MAP catalyst (◆) and monofunctional MAP catalyst (●) in a second batch experiment, using DMSO as solvent and varying water contents.

Figure 3 shows the catalyst activity in the continuous-flow reactor, expressed as 4-nitrobenzaldehyde conversion, as a function of the time on stream for the aldol reaction using DMSO with 2.19 wt% water as solvent. The first, and most rapid, deactivation of the cooperative acid-base catalyst stabilizes after 7 hours at the same activity level as the monofunctional base catalyst. This suggests that, during this period, the promoting ability of the silanol groups is lost and only the activity of the monofunctional base site remained. However, after 7 hours on stream, deactivation continued for both the cooperative acid-base as well as the monofunctional base catalyst. This deactivation region is suggested to be related to hydrolysis of Si-O-Si bonds which causes leaching of active sites and silica dissolution. Surface hydrophobization by trimethylsilation of the silanol groups on the monofunctional base catalyst appears to somewhat slow down this deactivation, but cannot completely prevent it.

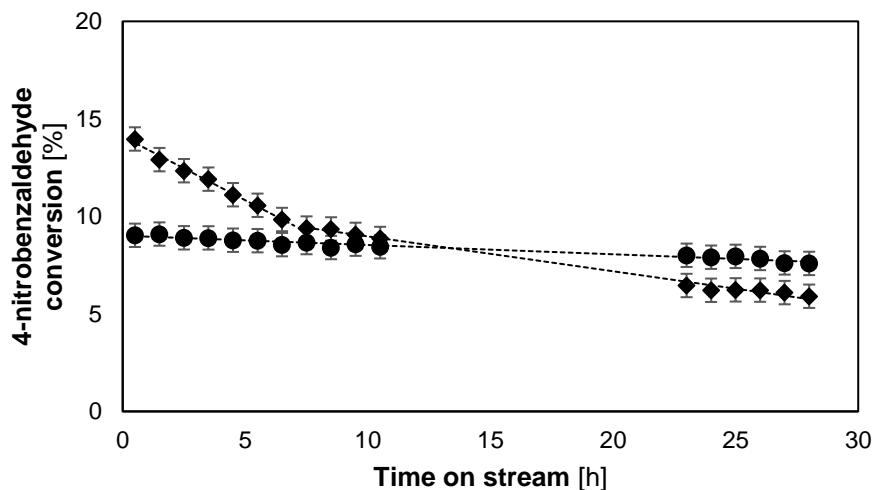


Figure 3. Stability of the cooperative acid-base MAP catalyst (◆) and monofunctional MAP catalyst (●) as a function of time on stream in the aldol reaction using DMSO + 2.19 wt% water as solvent.

To gain a more fundamental insight into the effects occurring on a molecular level, and to understand the reason why co-feeding water increased the reusability of the amine sites, computational quantum chemical calculations were performed. Gibbs free energies and reaction barriers were calculated at the CBS-QB3 level of theory and were corrected for solvent effects according to COSMO-RS theory. The reaction barriers, as shown in Figure 4, indicate that in the carbon-carbon formation step (**TS3**), a concerted addition-hydration (**TS3_{H2O}**), under sufficiently “wet” reaction conditions, yields the carbinolamine of the aldol product (**e**), which can relatively easily desorb from the active site as the aldol product. However, the unassisted addition of 4-nitrobenzaldehyde (**TS3**), which is expected to dominate under “dry” reaction conditions, yields an enamine (**d**). Hydrating this enamine (**d**) towards the product carbinolamine (**e**) has a high barrier, and can thus be the cause of active-site blocking under “dry” reaction conditions.

Moreover, it was concluded from calculations with different solvent models that mainly the value of the solvation Gibbs free energy (ΔG_{solv}) of water in the different solvent mixtures is important to reduce the amine site deactivation. For example, using hexane as a solvent, instead of DMSO, leads to a less negative ΔG_{solv} for water and, hence, a lower barrier for **TS3_{H2O}**.

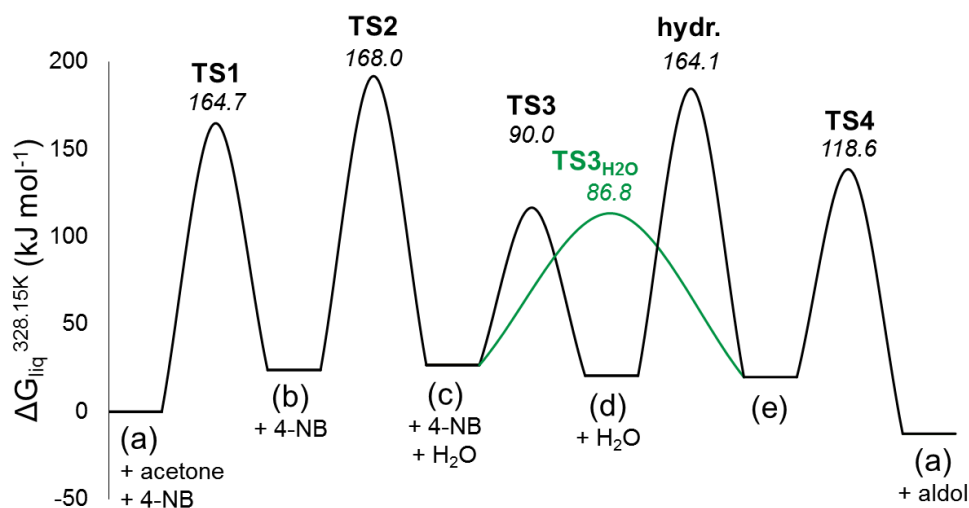


Figure 4: Gibbs free energy diagram calculated with CBS-QB3 for the aldol reaction of acetone with 4-nitrobenzaldehyde, according to the mechanism displayed in Scheme 1, with 50 vol% DMSO as solvent and 50% acetone as excess reagent at 328.15 K.

As water prevents deactivation of the amine active site, it appeared as an attractive solvent for the amine catalyzed aldol reaction. Moreover, it is cheap, readily available and not toxic¹⁴, making it even more attractive. However, the current state-of-the-art aminated silica catalysts are not stable under these conditions due to hydrolysis of Si-O-Si bonds¹⁵. Hence, a naturally occurring biopolymer which contains primary amines and cannot undergo hydrolysis reactions, called chitosan, was investigated as an alternative heterogeneous catalyst for the aqueous aldol reaction.

Chitosan was found to catalyze the aldol reaction, but the primary amine sites suffered from inhibition by the formation of stable imines derived from 4-nitrobenzaldehyde. When this active site inhibition was equilibrated, the catalytic activity of chitosan was found to be stable in repeat batch experiments and during continuous-flow experiments. However, the resulting catalytic activity of the amines was a factor 10 lower as compared to the state-of-the-art aminated silica catalysts. Yet, organic polymers with amine sites appear very attractive as catalysts for the aldol reaction due to their remarkable catalytic stability under aqueous conditions, and their possibility for a high active site loading on a mass basis.

Because it is clear that catalyst support stability is limiting the application of aminated silica catalysts in the aqueous aldol reaction, its hydrothermal stability was attempted to be improved by incorporating ethane or ethylene groups in the walls of the support material. This yielded a so-called periodic mesoporous organosilica (PMO) materials. However, despite the hydrophobic organic groups in the PMO material, the aminated PMO catalysts were not stable in the aqueous aldol reaction. Most likely, amine catalyzed hydrolysis reactions at Si-O-Si

interfaces were still possible, leading to leaching of active sites and PMO dissolution. Hence, taking inspiration from chitosan, a resin catalyst was developed based on (polyethylene glycol)methacrylate (PEGMA) as organic backbone. Because these catalysts do not contain any such Si-O-Si bonds, a much better catalytic stability was obtained, as displayed for ethylenediamine functionalized PEGMA catalyst in Figure 5. After 1.5 hour on stream, when the hydrodynamic effects of the reactor operation have completely dissipated, a stable conversion was obtained up to at least 8 hours on stream. Moreover, the TOF obtained for this catalyst in the aqueous aldol reaction in the same order of magnitude as the state-of-the-art amine functionalized silica catalysts which were evaluated using hexane as solvent.

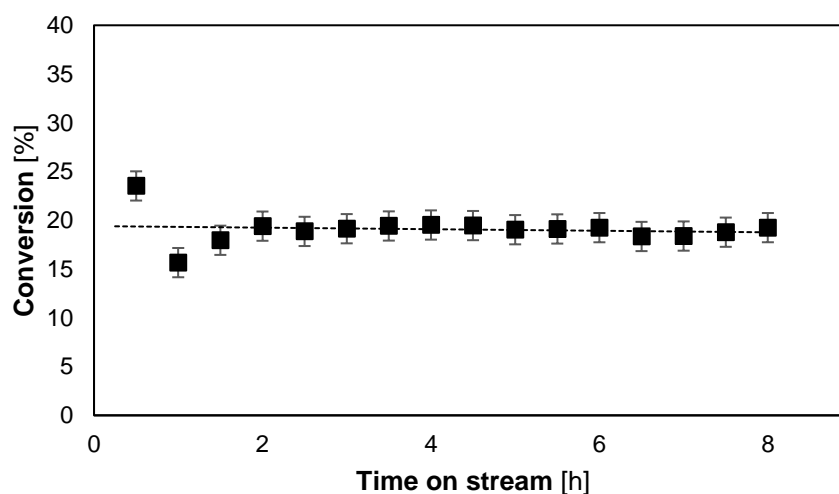


Figure 5: Conversion as a function of time on stream for the PEGMA-EDA catalyst (■) in the aqueous aldol reaction of acetone with 4-nitrobenzaldehyde.

Concluding, this work has focused on improving the activity and stability of heterogeneous amine catalysts for the aldol reaction by combining insights from theoretical chemistry and experiments. The design of new monofunctional base sites and cooperative amine-hydroxyl sites was facilitated by providing a computational methodology which can, before their respective laboratory synthesis, determine whether a restrictive steric hindrance will occur around the amine site which will limit its activity in the aldol reaction. Next, this work has also focused on improving the stability of the current state-of-the-art heterogeneous amine catalysts in the aldol reaction by tuning both the reaction environment and the support properties. It was found from recycle experiments in a batch reactor that water plays a key role in preventing the formation of site-blocking species during the catalytic cycle, which results in an increased reusability of the amine site when water is co-fed. To evaluate the stability of the catalyst during a prolonged exposure to the reaction environment, without filtering and recycling the catalyst in consecutive batch experiments, a packed-bed plug-flow reactor was

designed and built. Using this reactor, insight was gained into the stability of the support material in the amine functionalized silica catalysts, which was found to be unstable as a function of time on stream. Specifically, this instability was related to the degradation of the silica material by amine catalyzed hydrolysis reactions. Hence, new types of catalysts were designed based on support materials with an increased hydrothermal stability. In that sense, both periodic mesoporous organosilica (PMO) materials as well as polymer resins, based on (polyethylene glycol)methacrylate (PEGMA), have been evaluated. The amine catalysts with a PMO support were still found to degrade due to silica hydrolysis reactions at the interface between organic groups. On the contrary, the primary amine functionalized PEGMA catalyst, which does not contain bonds that are prone to hydrolysis, was found to be stable in the aqueous aldol reaction. While an adequate turnover frequency was obtained with the PEGMA catalysts, future work should focus on improving them for increased activity. This can, for example, be realized by tuning both the PEG amount in the resin to ensure optimal absorption of reagents and water in the catalyst, and by tuning the solvent and reagent ratios.

References

1. Kelly, G.; King, F.; Kett, M., Waste elimination in condensation reactions of industrial importance. *Green Chemistry* **2002**, *4* (4), 392-399.
2. Nasir Abbas Bukhari, S.; Jasamai, M.; Jantan, I.; Ahmad, W., Review of methods and various catalysts used for chalcone synthesis. *Mini-Reviews in Organic Chemistry* **2013**, *10* (1), 73-83.
3. Barrett, C.; Chheda, J.; Huber, G.; Dumesic, J., Single-reactor process for sequential aldol-condensation and hydrogenation of biomass-derived compounds in water. *Applied Catalysis B: Environmental* **2006**, *66* (1-2), 111-118.
4. Price, P. M.; Clark, J. H.; Macquarrie, D. J., Modified silicas for clean technology. *Journal of the Chemical Society, Dalton Transactions* **2000**, (2), 101-110.
5. Lauwaert, J.; De Canck, E.; Esquivel, D.; Van Der Voort, P.; Thybaut, J. W.; Marin, G. B., Effects of amine structure and base strength on acid–base cooperative aldol condensation. *Catalysis Today* **2015**, *246*, 35-45.
6. Brunelli, N. A.; Jones, C. W., Tuning acid–base cooperativity to create next generation silica-supported organocatalysts. *Journal of Catalysis* **2013**, *308*, 60-72.
7. Kubota, Y.; Goto, K.; Miyata, S.; Goto, Y.; Fukushima, Y.; Sugi, Y., Enhanced Effect of Mesoporous Silica on Base-Catalyzed Aldol Reaction. *Chemistry Letters* **2003**, *32* (3), 234-235.
8. Kandel, K.; Althaus, S. M.; Peeraphatdit, C.; Kobayashi, T.; Trewyn, B. G.; Pruski, M.; Slowing, I. I., Substrate inhibition in the heterogeneous catalyzed aldol condensation: A mechanistic study of supported organocatalysts. *Journal of Catalysis* **2012**, *291*, 63-68.
9. Shylesh, S.; Hanna, D.; Gomes, J.; Krishna, S.; Canlas, C. G.; Head-Gordon, M.; Bell, A. T., Tailoring the Cooperative Acid–Base Effects in Silica-Supported Amine Catalysts: Applications in the Continuous Gas-Phase Self-Condensation of n-Butanal. *ChemCatChem* **2014**, *6* (5), 1283-1290.
10. Lauwaert, J.; De Canck, E.; Esquivel, D.; Thybaut, J. W.; Van Der Voort, P.; Marin, G. B., Silanol-Assisted Aldol Condensation on Aminated Silica: Understanding the Arrangement of Functional Groups. *ChemCatChem* **2014**, *6* (1), 255-264.

11. Lauwaert, J.; Moschetta, E. G.; Van Der Voort, P.; Thybaut, J. W.; Jones, C. W.; Marin, G. B., Spatial arrangement and acid strength effects on acid–base cooperatively catalyzed aldol condensation on aminosilica materials. *Journal of Catalysis* **2015**, *325*, 19-25.
12. Kubota, Y.; Yamaguchi, H.; Yamada, T.; Inagaki, S.; Sugi, Y.; Tatsumi, T., Further Investigations on the Promoting Effect of Mesoporous Silica on Base-Catalyzed Aldol Reaction. *Topics in Catalysis* **2010**, *53* (7-10), 492-499.
13. Xie, J.; Ellebracht, N. C.; Jones, C. W., Inter- and Intramolecular Cooperativity Effects in Alkanolamine-Based Acid–Base Heterogeneous Organocatalysts. *ACS Omega* **2019**, *4* (1), 1110-1117.
14. Simon, M.-O.; Li, C.-J., Green chemistry oriented organic synthesis in water. *Chemical Society Reviews* **2012**, *41* (4), 1415-1427.
15. Etienne, M.; Walcarius, A., Analytical investigation of the chemical reactivity and stability of aminopropyl-grafted silica in aqueous medium. *Talanta* **2003**, *59* (6), 1173-1188.

Samenvatting

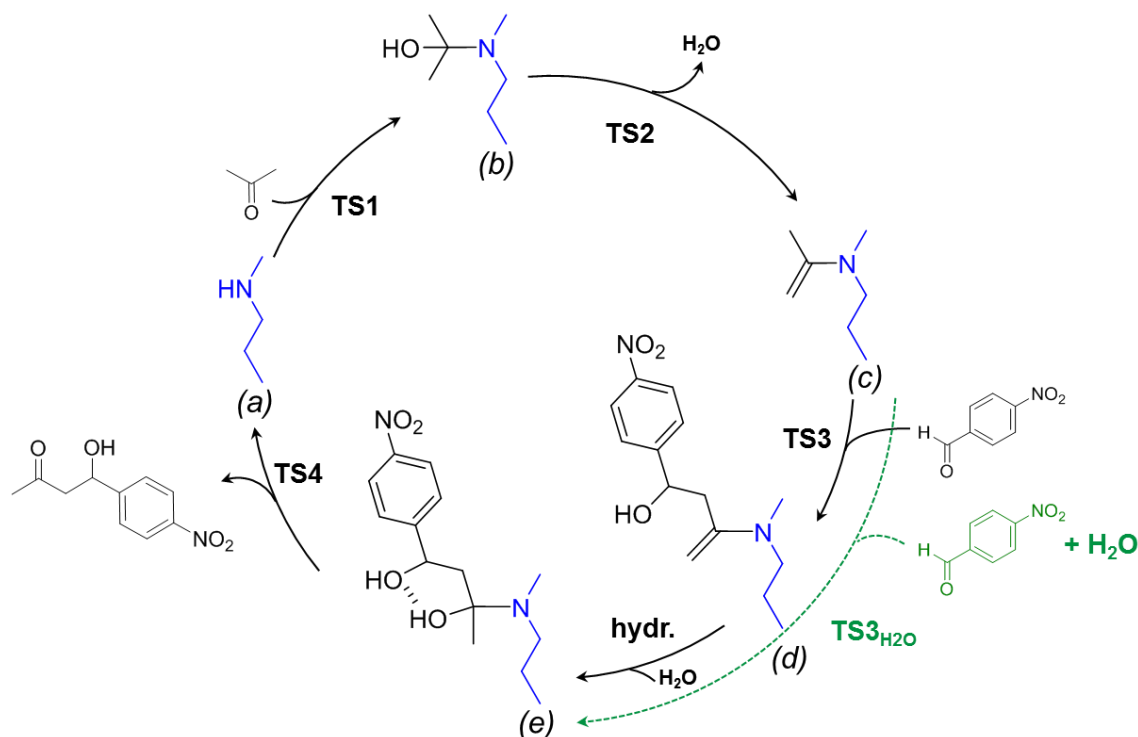
Aldol reacties zijn koolstofkoppelingsreacties tussen twee carbonylverbindingen, die op grote schaal worden gebruikt voor het synthetiseren van nieuwe organische moleculen met langere koolstofketens. Deze soort reacties worden vaak gebruikt in de synthese van fijn chemicaliën¹ en medicijnen². Een potentiële nieuwe toepassing bevindt zich in de groene industrie voor de productie van vloeibare brandstoffen uit lignocellulosehoudende biomassa. De cellulose die uit dit type materiaal kan worden verkregen, wordt eerst omgezet in suikers, die vervolgens kunnen worden omgezet in carbonylbevattende platformmoleculen³ met een gemiddelde koolstofketenlengte tussen 3 en 6. Om dit lage koolstofgehalte te verhogen naar het gewenste bereik voor toepassing in verbrandingsmotoren kunnen aldolreacties worden uitgevoerd met behulp van de functionaliteit die beschikbaar is in deze platformmoleculen. Op dit moment worden industriële aldolreacties typisch gekatalyseerd door homogene sterke basen. Ondanks hun adequate activiteit zijn deze katalysatoren gevaarlijk om te hanteren, vormen ze een milieurisico, en worden ze gedeactiveerd bij scheiding van de productstroom¹. Heterogene basische katalysatoren, zoals amine gefunctionaliseerde mesoporeuze silica-materialen, hebben deze nadelen niet⁴ en zijn dus aantrekkelijker voor het gebruik in meer industrieel relevante continue stroomreactoren.

Katalysatoren met primaire of secundaire amines, geënt met een linker van drie koolstofatomen aan het mesoporeuze silica oppervlak, zijn al vaak gebruikt voor de aldolreactie van aceton met 4-nitrobenzaldehyde⁵⁻⁷. In de literatuur wordt algemeen aangenomen⁸⁻¹⁰ dat, in het geval van een secundair amine, het katalytische mechanisme begint met de reactie van aceton met het amine (**a**), zoals weergegeven in Schema 1, resulterend in een carbinolamine (**b**), dat vervolgens dehydrateert tot een elektronenrijk enamine (**c**). Vervolgens reageert dit nucleofiele enamine (**c**) met de carbonylgroep van het tweede reagens, 4-nitrobenzaldehyde, en vindt de koolstofkoppeling plaats met de vorming van een tweede enamine (**d**). Ten slotte geeft een desorptiestap met water, via een carbinolaminetussenproduct (**e**), het uiteindelijke aldolproduct met herwinning van het actieve centrum (**a**).

Secundaire amines hebben in het algemeen de voorkeur als actieve centra voor de aldolreactie, omdat op primaire amines stabiele imines van zowel 4-nitrobenzaldehyde als aceton kunnen worden gevormd die inhibitie van het actieve centrum veroorzaken^{5, 8}. Tertiaire amines kunnen het cruciale enamine (**c**) niet vormen⁵ en werden daarom niet beschouwd in dit werk. Voor zowel de primaire als secundaire amine gefunctionaliseerde katalysatoren werd

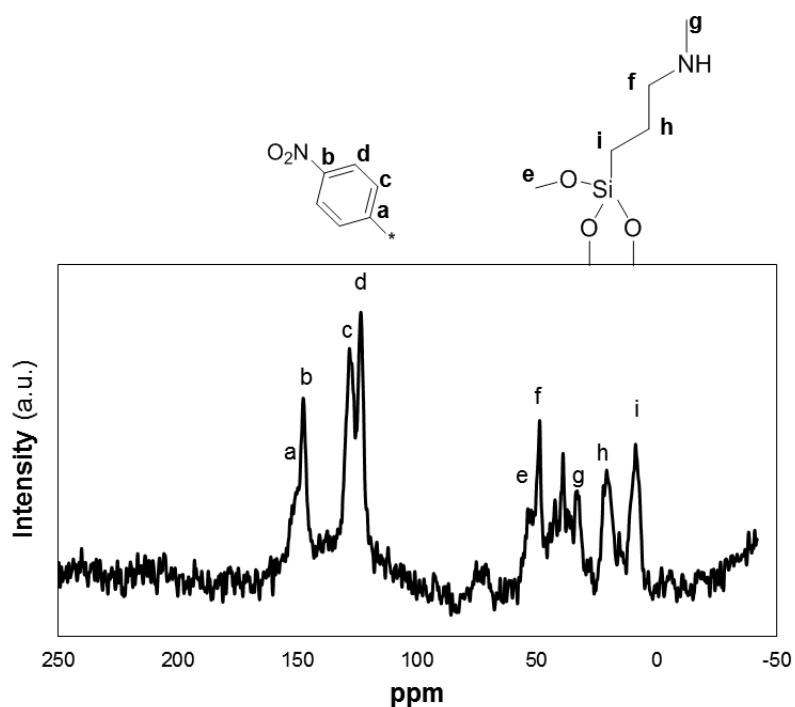
eerder waargenomen dat, als gevolg van een coöperatief samenspel, waterstofbrug-promotors zoals intramoleculaire hydroxylgroepen¹¹ en silanolgroepen¹², de omzetsfrequentie van het amine verhogen. Deze gepromote katalysatoren worden coöperatieve zuur-base-katalysatoren genoemd, in tegenstelling tot de katalysatoren zonder waterstofbrug-promotors, welke monofunctionele basekatalysatoren worden genoemd. Op mesoporeuze silica kan een monofunctionele basekatalysator worden verkregen door de coöperatieve silanolgroepen met een organische groep, zoals de trimethylsilylgroep, af te sluiten.

Eerder experimenteel werk van Lauwaert et al.⁵, en meer recent werk van Xie et al.¹³, hebben aangetoond dat het minimaliseren van de sterische hinder rond het nucleofiele stikstofatoom in secundaire amines cruciaal is voor het verkrijgen van een adequate katalytische omzetsfrequentie. Bovendien toonden Lauwaert et al.¹¹ ook aan dat een goedgeplaatste intramoleculaire hydroxylgroep de aminefunctie in dezelfde mate kan promoten als een silanolgroep. Het is echter cruciaal dat deze intramoleculaire hydroxylgroep geen restrictieve sterische hindering rond het amine introduceert. Daarom werd in dit werk een computationele methodologie ontwikkeld die een snelle beoordeling geeft van potentiële sterische hindering in nieuwe organische amines en coöperatieve amine-hydroxylgroepen. Specifiek werden de 3-propylpyrrolidine en de 1-(methylamino)-propan-2-ol-groepen voorgesteld als respectievelijk het meest veelbelovende monofunctionele amine en intramoleculaire coöperatieve amine-hydroxyl-paar.



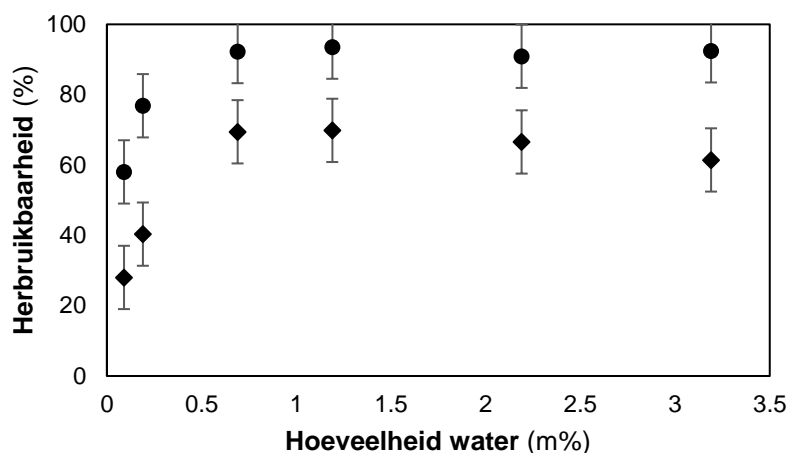
Schema 1. Reactiemechanisme⁸⁻¹⁰ van de aldolreactie van aceton met 4-nitrobenzaldehyde, gekatalyseerd door een N-methylpropylamine-katalysator als een model voor het methylaminopropyl (MAP) actief centrum op mesoporeus silica.

In het volgende deel van dit werk werd een experimenteel onderzoek uitgevoerd naar de stabiliteit van de huidige *state-of-the-art* amine gefunctionaliseerde silicakatalysatoren. De herbruikbaarheid werd bepaald in twee opeenvolgende batch aldolreacties bij 328.15 K, met dimethylsulfoxide (DMSO) als solvent en aceton als overmaat reagens. Slechts 38% van de initiële omzetsfrequentie werd verkregen bij een tweede gebruik van de coöperatieve zuur-base katalysator en slechts 77% van de initiële omzetsfrequentie werd verkregen bij het hergebruiken van de monofunctionele basekatalysator. Karakterisering van de gebruikte katalysatoren met stikstofsorptie gaf aan dat de structurele eigenschappen van de katalysator intact bleven. CHN-analyse gaf echter een 60% toename van het stikstofgehalte aan voor de gebruikte coöperatieve zuur-base-katalysator en een toename van 15% voor de gebruikte monofunctionele basekatalysator. Bovendien veranderde de kleur van de oorspronkelijk witte katalysatoren naar geel en behielden ze deze kleur zelfs na extra wassen in chloroform. Karakterisering van de gebruikte katalysatoren toonde aan dat dit werd veroorzaakt door 4-nitrobenzaldehyde afgeleide componenten die aan het actief centrum vast bleven zitten, zoals weergegeven in figuur 1.



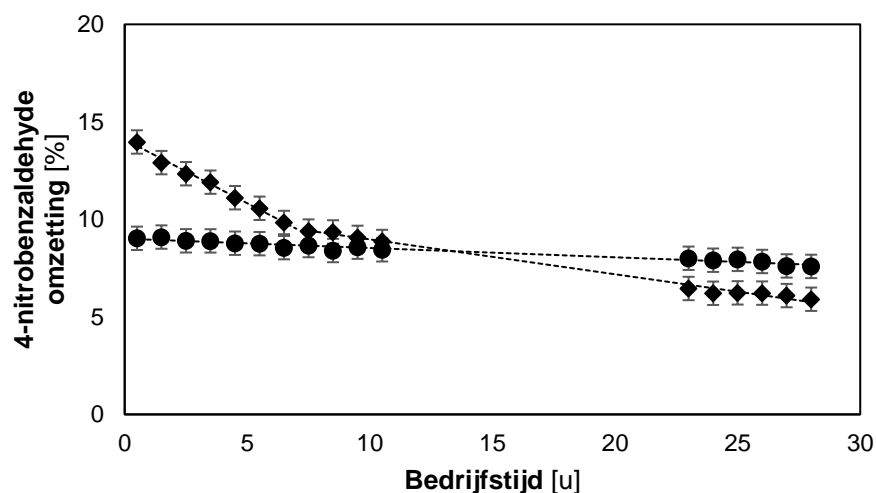
Figuur 1. ^{13}C CP/MAS NMR van de gebruikte coöperatieve zuur-base katalysator. Het geënte secundaire amine kan in het spectrum worden geïdentificeerd, evenals de koolstofatomen die afkomstig zijn van de aromatische ring met een nitrogroep.

De aanwezigheid van kleine hoeveelheden water in de reactie bleek de vorming van deze 4-nitrobenzaldehyde afgeleide componenten te verminderen en resulteerde in een volledige herbruikbaarheid voor de monofunctionele basekatalysator, zoals weergegeven in figuur 2. Echter, volledige herbruikbaarheid werd niet bereikt voor de coöperatieve zuur-base katalysator, wat waarschijnlijk te wijten is aan watermoleculen die het vermogen van de silanolgroepen om een amine centrum te promoten deactiveren. Om deze hypothese verder te onderzoeken, werd een laboschaal propstroomreactor met een vast bed ontworpen, de *Liquid-Solid Lab-Scale (LS)²* reactor. Met behulp van deze continue reactor was het mogelijk om rechtstreeks de stabiliteit van een katalysator te evalueren als een functie van de bedrijfstijd.



Figuur 2. Herbruikbaarheid van de coöperatieve zuur-base MAP-katalysator (◆) en monofunctionele MAP-katalysator (●) in een tweede batch-experiment, met DMSO als solvent en een variërend watergehalte.

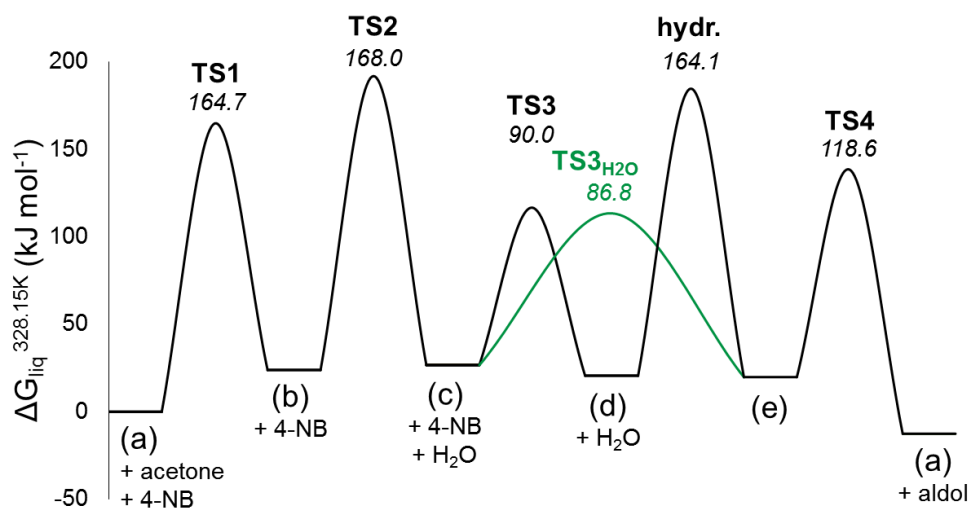
Figuur 3 toont de katalysatoractiviteit in de propstroomreactor, uitgedrukt als 4-nitrobenzaldehydomzetting, als een functie van de bedrijfstijd voor de aldolreactie met DMSO en 2.19 m% water als solvent. De eerste, en meest snelle, deactivering van de coöperatieve zuur-base-katalysator stabiliseert na 7 uur bij hetzelfde activiteitsniveau als de monofunctionele basekatalysator. Dit suggereert dat gedurende deze periode het promotievermogen van de silanolgroepen verloren is gegaan en dat alleen de activiteit van de monofunctionele base werd gemeten. Na 7 uur in bedrijf bleef de deactivering zich echter voortzetten, voor zowel de coöperatieve zuur-base als de monofunctionele basekatalysator. Dit deactiveringsgebied zou gerelateerd zijn aan de hydrolyse van Si-O-Si-bindingen die uitloging van actieve centra en het afbreken van silica veroorzaakten. De hydrofobe trimethylsilyl groepen die aangebracht werden op de silanolgroepen in de monofunctionele basekatalysator lijken deze deactivering enigszins te vertragen, maar kunnen het niet volledig voorkomen.



Figuur 3. Stabiliteit van de coöperatieve zuur-base MAP-katalysator (◆) en de monofunctionele MAP-katalysator (●) als functie van de bedrijfstijd in de aldolreactie met DMSO + 2.19 m% water als solvent.

Om een meer fundamenteel inzicht te krijgen in de effecten die op moleculair niveau optreden, en om de reden te begrijpen waarom het toevoegen van water de herbruikbaarheid van de amine centra verhoogt, werden computationele kwantumchemische berekeningen gedaan. Gibbs vrije energieën en reactiebarrières werden berekend op het CBS-QB3-niveau en werden gecorrigeerd voor solventeffecten volgens de COSMO-RS-theorie. De reactiebarrières, zoals getoond in Figuur 4, geven aan dat in de koolstof-koolstofvormingsstap (**TS3**) een gecoördineerde additiehhydratatie (**TS3_{H2O}**), onder voldoende "natte" reactieomstandigheden, het carbinolamine van het aldolproduct oplevert (**e**), dat relatief gemakkelijk kan desorberen van het actief centrum als het aldolproduct. De ongeassisteerde additie van 4-nitrobenzaldehyde (**TS3**), welke domineert onder "droge" reactieomstandigheden, levert echter een enamine (**d**) op. Hydrateren van dit enamine (**d**) naar het product carbinolamine (**e**) heeft een hoge barrière en kan dus de oorzaak zijn van actief centrum deactivering onder "droge" reactieomstandigheden.

Bovendien werd geconcludeerd uit berekeningen met verschillende solvent modellen dat voornamelijk de waarde van de solvatatie Gibbs-vrije energie (ΔG_{solv}) van water in de verschillende solventmengsels belangrijk is om de deactivering van het amine te verminderen. Het gebruik van, bijvoorbeeld, hexaan als solvent in de plaats van DMSO leidt tot een minder negatieve ΔG_{solv} voor water en dus een lagere barrière voor **TS3_{H2O}**.



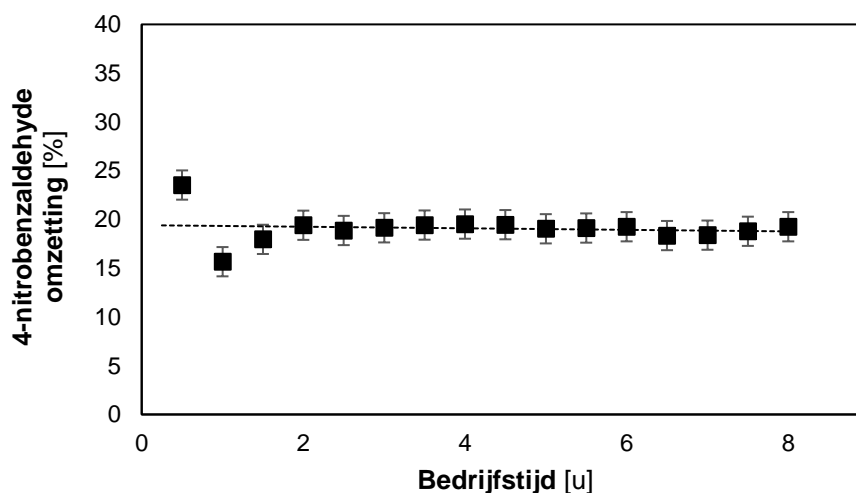
Figuur 4. Gibbs-vrije energiediagram berekend met CBS-QB3 voor de aldolreactie van acetone met 4-nitrobenzaldehyde, volgens het mechanisme weergegeven in Schema 1, met 50 vol% DMSO als solvent en 50% acetone als overmaat reagens bij 328.15 K.

Omdat water de deactivering van het amine actief centrum voorkomt, leek het als een aantrekkelijk solvent voor de amine gekatalyseerde aldolreactie. Bovendien is het goedkoop, gemakkelijk verkrijgbaar, en niet giftig¹⁴, waardoor het nog aantrekkelijker wordt. De huidige amine gefunctionaliseerde silicakatalysatoren zijn echter niet stabiel onder deze reactiecondities door amine gekatalyseerde hydrolyse van Si-O-Si-bindingen¹⁵. Derhalve werd een natuurlijk voorkomend biopolymeer genaamd chitosan, met primaire amines en niet onderhevig aan deze hydrolyse reacties, onderzocht als een alternatieve heterogene katalysator voor de aldolreactie met water als solvent.

Er werd gevonden dat chitosan de aldol reactie katalyseerde, maar ook dat de primaire amines leden aan inhibitie door de vorming van stabiele imines afgeleid van 4-nitrobenzaldehyde. Wanneer deze inhibitie geëquilibreerd was, bleek de katalytische activiteit van chitosan stabiel te zijn in herhaalde batch-experimenten en tijdens continueestroom-experimenten. De katalytische activiteit van de amines was echter een factor 10 lager dan de amine gefunctionaliseerde silicakatalysatoren. Toch lijken organische polymeren met amines zeer aantrekkelijk als katalysatoren voor de aldol reactie vanwege hun opmerkelijke katalytische stabiliteit met water als solvent, en hun mogelijkheid voor een hoge actieve centra belading op massabasis.

Omdat het duidelijk is dat de toepassing van geamineerde silicakatalysatoren in de aldolreactie met water als solvent beperkt is door de instabiliteit van het dragermateriaal, werd geprobeerd de hydrothermische stabiliteit van deze katalysatoren te verbeteren door het inbrengen van ethaan- of ethyleengroepen in de wanden van het silica materiaal. Dit leverde

een zogenaamde periodieke mesoporeuze organosilica (PMO) materiaal op. Echter, ondanks de hydrofobe organische groepen in het PMO-materiaal waren de geamioneerde PMO-katalysatoren niet stabiel in de aldolreactie met water als solvent. Hoogstwaarschijnlijk waren de amine gekatalyseerde hydrolyse reacties op de Si-O-Si-grensvlakken nog steeds mogelijk, wat leidde tot uitloging van actieve sites en degradatie van het dragermateriaal. Daarom werd, geïnspireerd door de resultaten met het biopolymeer chitosan, een harskatalysator ontwikkeld op basis van poly(ethyleen glycol) methacrylaat (PEGMA). Omdat deze katalysatoren geen Si-O-Si-bindingen bevatten, werd een veel betere katalytische stabiliteit verkregen, zoals weergegeven in Figuur 5 voor een primaire diamine gefunctionaliseerde PEGMA-katalysator. Na 1.5 uur in bedrijf, wanneer de hydrodynamische effecten van de reactorwerking volledig zijn verdwenen, werd een stabiele conversie verkregen gedurende nog minstens 6.5 uur. Bovendien was de omzetsfrequentie voor deze katalysator in de aldolreactie met water als solvent in dezelfde grootte orde als de amine gefunctionaliseerde silicakatalysatoren met hexaan als solvent.



Figuur 5. Conversie als een functie van de bedrijfstijd voor de PEGMA-EDA-katalysator (■) in de aldolreactie van aceton met 4-nitrobenzaldehyde met water als solvent.

Afsluitend, in dit werk werd gefocust op het verbeteren van de activiteit en stabiliteit van heterogene aminekatalysatoren voor de aldolreactie door inzichten uit de theoretische chemie en experimenten te combineren. Het ontwerp van nieuwe monofunctionele amines en coöperatieve amine-hydroxyl paren werd vergemakkelijkt door een computationele methodologie die kan bepalen of een beperkende sterische hindering zal optreden rond het amine actief centrum. Daarnaast heeft dit werk zich ook gericht op het verbeteren van de stabiliteit van de huidige amine gefunctionaliseerde silicakatalysatoren in de aldolreactie door zowel de reactieomgeving als de eigenschappen van het dragersmateriaal op elkaar af te

stemmen. Uit hergebruik-experimenten in een batchreactor werd gevonden dat water een sleutelrol speelt bij het voorkomen van actief centrum deactivering tijdens de katalytische cyclus, wat resulteert in een verhoogde herbruikbaarheid van het amine wanneer water wordt toegevoegd. Om de stabiliteit van de katalysator tijdens een langdurige blootstelling aan de reactieomgeving te evalueren, zonder de katalysator te filteren en te hergebruiken in een volgend batchexperiment, werd een gepakte propstroomreactor ontworpen en gebouwd. Met behulp van deze reactor werd inzicht verkregen in de stabiliteit van het dragermateriaal van de amine gefunctionaliseerde silicakatalysatoren. Deze bleek onstabiel te zijn als een functie van de bedrijfstijd. Deze instabiliteit werd gerelateerd aan de afbraak van het siliciumdioxidemateriaal door amine gekatalyseerde hydrolysereacties. Daarom werden nieuwe katalysatoren ontworpen op basis van dragermaterialen met een verhoogde hydrothermische stabiliteit. Zowel periodieke mesoporeuze organosilica (PMO) materialen als polymeerharsen op basis van poly(ethyleen glycol) methacrylaat (PEGMA) werden hiervoor geëvalueerd. De aminekatalysatoren met een PMO-drager bleken nog steeds te degraderen als gevolg van silica-hydrolysereacties op het grensvlak tussen organische groepen. De amine gefunctionaliseerde PEGMA-katalysator, die geen bindingen bevat die gevoelig zijn voor hydrolyse, bleek daarentegen stabiel te zijn in de aldolreactie met water als solvent. Hoewel een adequate omzetsfrequentie werd verkregen met de PEGMA-katalysatoren, moeten toekomstig onderzoek zich richten op het verbeteren van de activiteit. Dit kan bijvoorbeeld worden gerealiseerd door de PEG-hoeveelheid in de hars af te stemmen om optimale absorptie van reagentia en water in de katalysator te verzekeren, en door de verhoudingen van oplosmiddel en reagens te optimaliseren.

Referenties

1. Kelly, G.; King, F.; Kett, M., Waste elimination in condensation reactions of industrial importance. *Green Chemistry* **2002**, *4* (4), 392-399.
2. Nasir Abbas Bukhari, S.; Jasamai, M.; Jantan, I.; Ahmad, W., Review of methods and various catalysts used for chalcone synthesis. *Mini-Reviews in Organic Chemistry* **2013**, *10* (1), 73-83.
3. Barrett, C.; Chheda, J.; Huber, G.; Dumesic, J., Single-reactor process for sequential aldol-condensation and hydrogenation of biomass-derived compounds in water. *Applied Catalysis B: Environmental* **2006**, *66* (1-2), 111-118.
4. Price, P. M.; Clark, J. H.; Macquarrie, D. J., Modified silicas for clean technology. *Journal of the Chemical Society, Dalton Transactions* **2000**, (2), 101-110.
5. Lauwaert, J.; De Canck, E.; Esquivel, D.; Van Der Voort, P.; Thybaut, J. W.; Marin, G. B., Effects of amine structure and base strength on acid-base cooperative aldol condensation. *Catalysis Today* **2015**, *246*, 35-45.
6. Brunelli, N. A.; Jones, C. W., Tuning acid-base cooperativity to create next generation silica-supported organocatalysts. *Journal of Catalysis* **2013**, *308*, 60-72.

7. Kubota, Y.; Goto, K.; Miyata, S.; Goto, Y.; Fukushima, Y.; Sugi, Y., Enhanced Effect of Mesoporous Silica on Base-Catalyzed Aldol Reaction. *Chemistry Letters* **2003**, 32 (3), 234-235.
8. Kandel, K.; Althaus, S. M.; Peeraphatdit, C.; Kobayashi, T.; Trewyn, B. G.; Pruski, M.; Slowing, I. I., Substrate inhibition in the heterogeneous catalyzed aldol condensation: A mechanistic study of supported organocatalysts. *Journal of Catalysis* **2012**, 291, 63-68.
9. Shylesh, S.; Hanna, D.; Gomes, J.; Krishna, S.; Canlas, C. G.; Head-Gordon, M.; Bell, A. T., Tailoring the Cooperative Acid–Base Effects in Silica-Supported Amine Catalysts: Applications in the Continuous Gas-Phase Self-Condensation of n-Butanal. *ChemCatChem* **2014**, 6 (5), 1283-1290.
10. Lauwaert, J.; De Canck, E.; Esquivel, D.; Thybaut, J. W.; Van Der Voort, P.; Marin, G. B., Silanol-Assisted Aldol Condensation on Aminated Silica: Understanding the Arrangement of Functional Groups. *ChemCatChem* **2014**, 6 (1), 255-264.
11. Lauwaert, J.; Moschetta, E. G.; Van Der Voort, P.; Thybaut, J. W.; Jones, C. W.; Marin, G. B., Spatial arrangement and acid strength effects on acid–base cooperatively catalyzed aldol condensation on aminosilica materials. *Journal of Catalysis* **2015**, 325, 19-25.
12. Kubota, Y.; Yamaguchi, H.; Yamada, T.; Inagaki, S.; Sugi, Y.; Tatsumi, T., Further Investigations on the Promoting Effect of Mesoporous Silica on Base-Catalyzed Aldol Reaction. *Topics in Catalysis* **2010**, 53 (7-10), 492-499.
13. Xie, J.; Ellebracht, N. C.; Jones, C. W., Inter- and Intramolecular Cooperativity Effects in Alkanolamine-Based Acid–Base Heterogeneous Organocatalysts. *ACS Omega* **2019**, 4 (1), 1110-1117.
14. Simon, M.-O.; Li, C.-J., Green chemistry oriented organic synthesis in water. *Chemical Society Reviews* **2012**, 41 (4), 1415-1427.
15. Etienne, M.; Walcarius, A., Analytical investigation of the chemical reactivity and stability of aminopropyl-grafted silica in aqueous medium. *Talanta* **2003**, 59 (6), 1173-1188.

Chapter 1

Introduction

In the 1950s and 1960s, the booming chemical industry was seen as the solution to many of society's needs. For example, by enhancing the quality of life for millions of people by creating new chemicals for drugs, plastics and synthetic fertilizers. Moreover, there was an unbridled optimism about what scientists and engineers could achieve with chemistry¹. Unfortunately, amid the numerous successes were also some unforeseen outcomes. For example, the insecticide known as dichlorodiphenyltrichloroethane (DDT) was found to bioaccumulate in birds². This caused dramatic declines in the population of species such as the bald eagle. Chlorofluorocarbons, developed as a safer alternative to ammonia as refrigerant, played an important role in the destruction of the ozone layer². Soon, the initial optimism around, and expectations from, the chemical industry were replaced by concerns over its potentially negative impact on the environment and its possible risk to human well-being.

1.1 Sustainable development and green chemistry

One of the first responses to the escalating environmental and health concerns related to the chemical industry was the concept of green chemistry^{3, 4}, starting in the 1980s⁵ and defined in the 1990s by Paul Anastas and John Warner as *the design of chemical products and processes that reduce or eliminate the use and generation of hazardous substances*⁶. This definition was concretized in the 'Twelve Principles of Green Chemistry', of which at least three are applicable to this work and are discussed more elaborately below.

1.1.1 Catalysis

Organic reactions performed in the fine chemical industry and the pharmaceutical industry typically produce copious amounts of inorganic salts generated from the mineral acids such as H₂SO₄, and bases such as NaOH and KOH that are used as homogeneous catalysts⁷. Replacement of these homogeneous catalysts by a heterogeneous alternative, which can easily be recovered from the reaction mixture and recycled, is a key step in the reduction of waste^{8, 9}.

These catalysts should also be designed to exhibit a performance as selective as possible to reduce the amount of by-products formed and maximize the desired product yield.

Zeolite catalysts are an example of heterogeneous catalysts that are widely applied on an industrial scale for a variety of acid-catalyzed reactions in the petrochemical industry^{10, 11}. However, they have not yet found widespread application in the fine chemical and pharmaceutical industry yet¹². One of the reasons for this is that the typical organic molecules that are synthesized are too bulky for the microporous zeolite¹³. Recently, so-called hierarchical zeolite materials containing larger mesopores have been developed to overcome this disadvantage^{14, 15}. A variety of ‘solid base’ catalysts also exists, such as hydrotalcites and mixed oxides, but their application in liquid-phase organic reactions remains limited due to their micropore size and their tendency to deactivate by adsorbing CO₂ and H₂O when exposed to atmospheric environments^{16, 17}. Functionalized mesoporous silica catalysts or macroporous ion-exchange polymer resins are another class of promising heterogeneous catalysts for the fine chemical and pharmaceutical industry^{18, 19}, and are investigated in this work.

1.1.2 Safer solvents

Solvents account for 80% to 90% of the mass in a typical pharmaceutical or fine chemicals batch chemical operation and are a determining factor in the toxicity and environmental impact of the whole process²⁰. Many of the solvents used are known to cause harm to ecosystems, have a neurotoxic character, or may cause cancer to individuals as a result of frequent exposure²¹. While contained use is strived for, traces of solvent still end up in aqueous waste streams and the air. Where possible, the use of potentially harmful solvents should thus be eliminated. Because solvents are often indispensable in synthetic organic reactions, safer and more sustainable ones should be sought for these processes.

Water as solvent appears as a very attractive alternative from both an economical and an environmental point of view, because it is inherently safe, nontoxic, readily available, and nonflammable²²⁻²⁴. However, water appears at first sight as a poor solvent for organic reactions due to the low solubility of many nonpolar organic compounds²⁴. Even traces of water in organic synthesis reactions are often regarded as undesired contaminants²⁵. During the last decades, however, it has become clear that the unique structure and physicochemical properties of water lead to complex new interactions induced by polarity, hydrogen bonding or hydrophobic effects that can positively influence the reaction rate and product yield in an organic reaction²⁶⁻²⁹.

1.1.3 Renewable feedstocks

Mankind currently extracts fossil fuels in the form of coal, oil and natural gas originating from carbon deposition of eons ago^{30,31}. Burning these fossil fuels, or burning materials derived from crude oil at the end of their lifetime, results in a net increase in atmospheric CO₂ that contributes to global warming and climate change³², see Figure 1-1. Manufacturing fuels, chemicals and materials from feedstocks that have captured CO₂ during a limited number of years, and never deplete, such as biomass, is thus of utmost importance to establish a sustainable future³³. This results in a closed CO₂ loop, as presented in Figure 1-1.

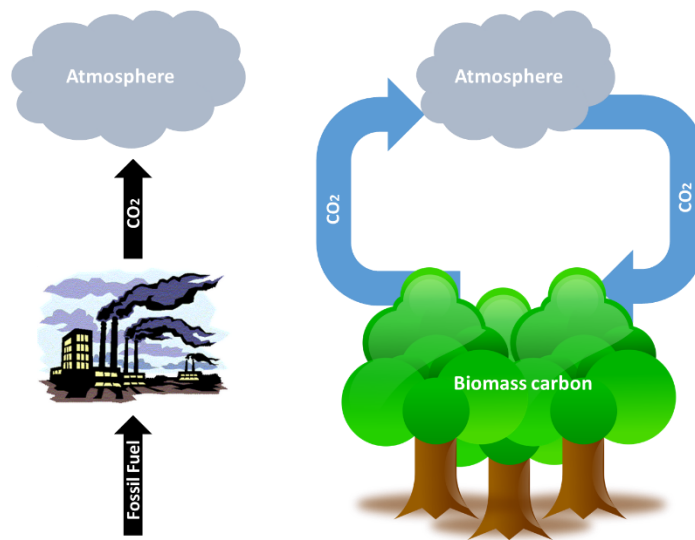


Figure 1-1: Burning fuels from eons old fossil resources produces a net increase in CO₂ (left), while the CO₂ emitted by burning biomass is again taken up by the biomass in the course of a few years (right).

Both bio-ethanol and biodiesel are examples of biomass derived fuels that are already produced on an industrial scale. They are, however, controversial because edible crops are used for their production, which directly competes with the agricultural supply of food. In that regard, lignocellulosic biomass is one of the most promising renewable carbon sources, because it is abundantly available and, at most, indirectly competes with the production of food³⁴. Several different pathways for the production of biofuels, or chemicals, from lignocellulosic biomass are currently being investigated: fast pyrolysis³⁵, gasification³⁵, liquefaction³⁶, and hydrolysis³⁷⁻³⁹.

The hydrolysis route is displayed in Figure 1-2. In this route, first the rigid lignocellulose polymer is broken down into lignin and (hemi)cellulose⁴⁰. The lignin fraction is typically removed and burned for energy, while hydrolysis of the cellulose yields smaller aqueous sugars.

Further processing of these sugars via dehydration yields chemical platform molecules, of which a selection is displayed in Figure 1-2.

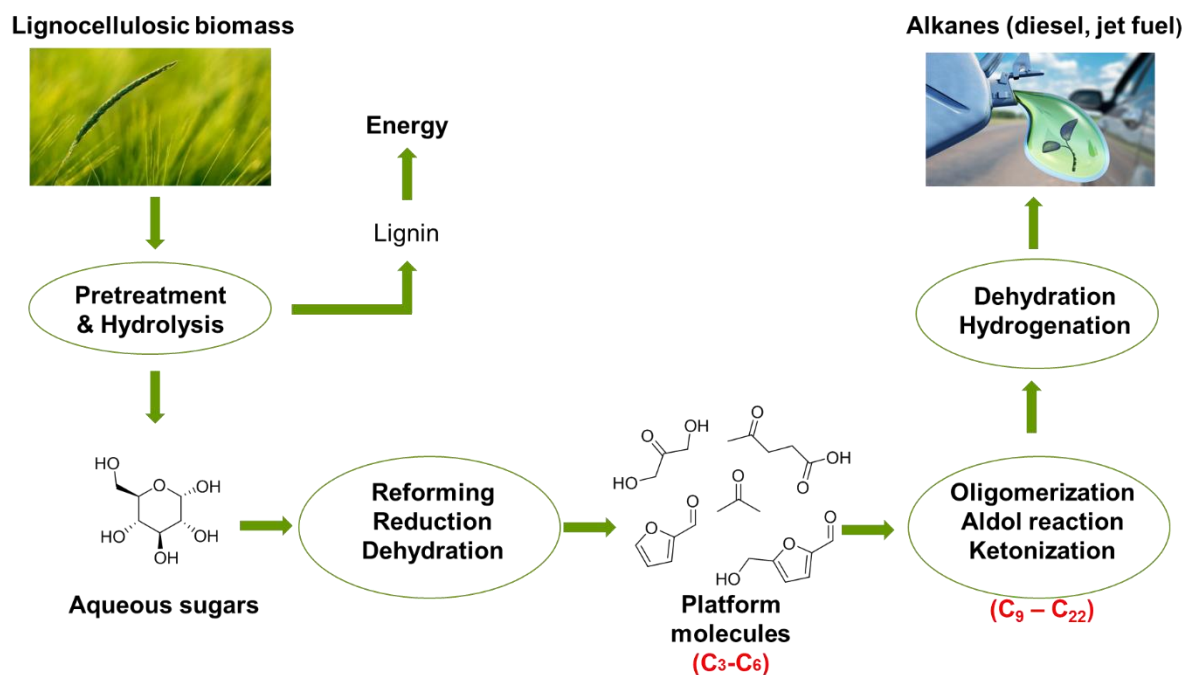


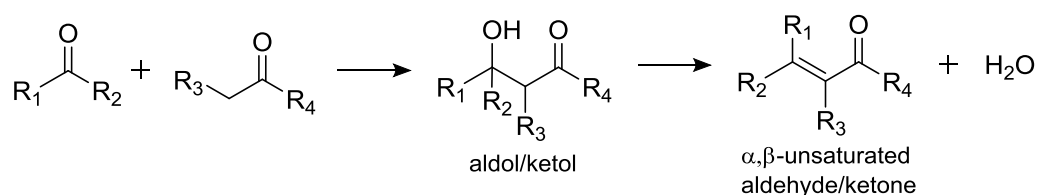
Figure 1-2: Conversion of lignocellulose into liquid hydrocarbon fuels. Scheme based on ref 37.

These platform molecules typically comprise of 3 to 6 carbon atoms, which is too low as compared to hydrocarbon fuels that have a carbon chain length in the range of 9 to 22³⁹. The carbon number thus has to be increased substantially, which can be achieved through a carbon-carbon coupling reaction, such as an aldol reaction, exploiting the functionality of the available carbonyl groups. Finally, the resulting molecules are dehydrated and hydrogenated to remove unsaturated bonds, yielding the desired liquid hydrocarbon fuels^{41, 42}.

1.2 Aldol reactions

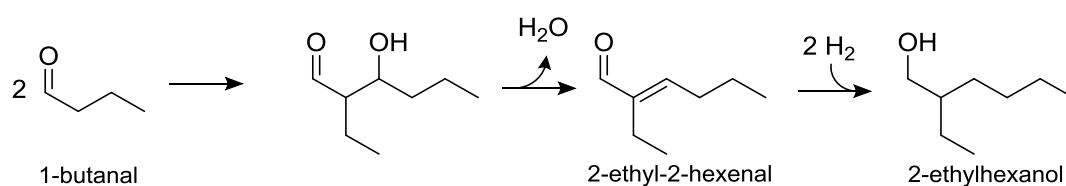
As demonstrated above, aldol reactions are important organic reactions yielding new carbon-carbon bonds and thus creating larger and more complex molecules. The reaction can occur between two molecules with a carbonyl group, i.e., two aldehydes, two ketones or an aldehyde and a ketone. In case the two reacting species are identical, the reaction and subsequent dehydration is referred to as a ‘self-condensation’, while the aldol reaction and dehydration of two different species is referred to as a ‘cross-condensation’⁴³. The presence of at least one α -hydrogen in one of these carbonyl species is essential for the reaction to take place, because it allows this carbonyl group, which is essentially electrophilic, to be converted

into a nucleophilic group and attack the other carbonyl species. This nucleophilic group can be in the form of either an enol, enolate, or enamine, depending on the catalyst employed. A generic example of an aldol reaction is given in Scheme 1-1. The product of this reaction is either a β -hydroxyaldehyde (aldol) or a β -hydroxyketone (ketol). Throughout this work, this reaction product will be referred to as the ‘aldol product’. Dehydration of this product then yields either an α,β -unsaturated aldehyde or ketone. This reaction product will be referred to as the ‘enone product’. The overall reaction, including dehydration of the aldol product, is referred to as the ‘aldol condensation’⁴³.



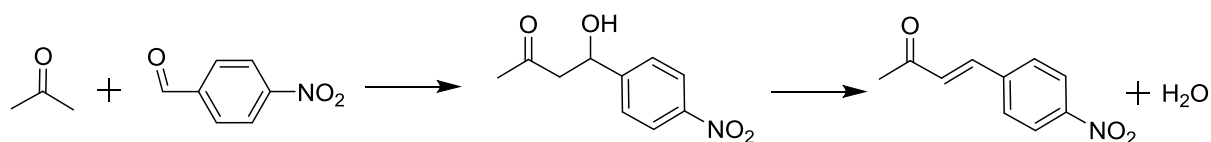
Scheme 1-1: Generalized example of an aldol reaction between two carbonyl species with the formation of an aldol or ketol product that can dehydrate towards an α,β -unsaturated aldehyde or ketone.

One of largest applications of aldol reactions in terms of volume, can be found in the production of 2-ethylhexanol, which is an important starting material in the production of PVC plasticizers, hydraulic oils, synthetic lubricants and perfumes⁸. It is currently produced by Oxochimie, a joint venture in France between INEOS and Arkema, as well as by Dow and Eastman, totaling a yearly production capacity of 2.8 million tonnes in 2009⁴⁴. The process starts with the self-aldol condensation of butanal to the enone product 2-ethyl-2-hexenal, as displayed in Scheme 1-2. Subsequent hydrogenation yields 2-ethylhexanol⁴⁵. This process is called the ‘Aldox process’ and is catalyzed by a strong homogeneous base catalyst.



Scheme 1-2: Industrial production of 2-ethylhexanol from self-aldol condensation of 1-butanal and subsequent hydrogenation.

In academic research, a model aldol reaction is frequently used to assess the performance of the developed catalysts⁴⁶⁻⁴⁸. Typically, the reaction between 4-nitrobenzaldehyde and a symmetrical ketone bearing an α -hydrogen, such as acetone, is chosen, as displayed in Scheme 1-3.



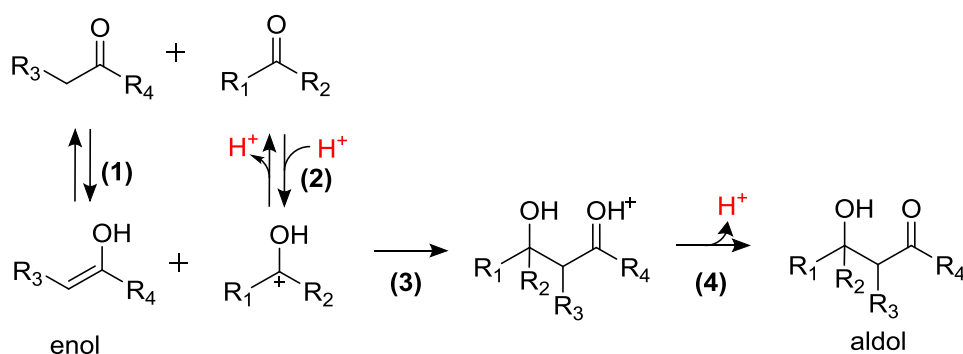
Scheme 1-3: Model aldol reaction of acetone with 4-nitrobenzaldehyde, towards the aldol adduct 4-hydroxy-4-(4-nitrophenyl)butan-2-one, and dehydration to the enone product 4-(4-nitrophenyl)-3-buten-2-one.

This reaction has several advantages as model reaction. First, due to the absence of an α -hydrogen in 4-nitrobenzaldehyde, its self-condensation is avoided. Second, the electron-withdrawing nitro group on 4-nitrobenzaldehyde typically allows for appreciable conversion at mild reaction conditions for the catalysts employed in this work⁴⁹. Specifically, this reaction can be performed at temperatures below the boiling point of acetone, avoiding the use of pressurized equipment. Third, because acetone is a symmetrical ketone, and self-condensation of 4-nitrobenzaldehyde is avoided, the product spectrum will remain limited and allow for accurate lab-scale measurements of the products and mass balance verification.

As discussed previously, a catalyst converts the electrophilic carbonyl group into a nucleophilic group, which allows the aldol reaction to proceed. For this, acids and bases can be used, both either of the Brønsted⁴³ or Lewis⁵⁰ type. In this work, only the Brønsted acid, Brønsted base, and Lewis base reaction mechanisms are discussed.

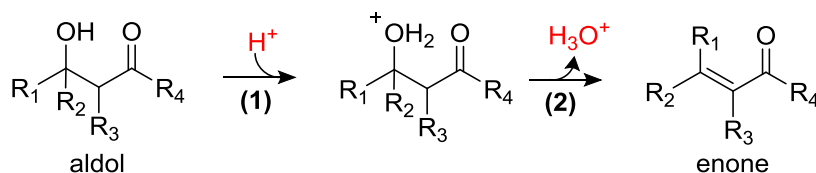
1.2.1 Brønsted acid catalyzed reaction mechanism

The reaction mechanism for the Brønsted acid catalyzed aldol reaction is presented in Scheme 1-4. The first step in this mechanism is the acid catalyzed reversible shift of a proton from an α -carbon to the carbonyl oxygen atom (**1**), with formation of an electron rich enol. This chemical equilibrium reaction is known as the keto-enol tautomerism. Next, the acid protonates a second carbonyl compound (**2**), which is now more susceptible for a nucleophilic attack by the enol. This nucleophilic attack (**3**) forms the new carbon-carbon bond, after which deprotonation (**4**) leads to the aldol product.



Scheme 1-4: Generic mechanism of a Brønsted acid catalyzed aldol reaction

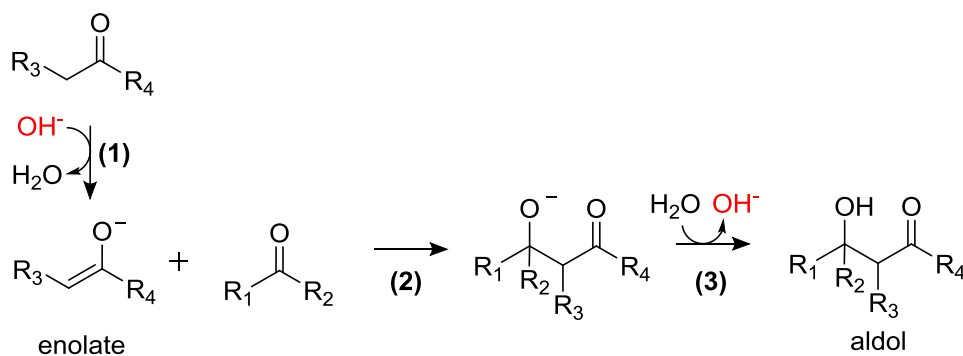
The acid-catalyzed dehydration of the aldol product is displayed in Scheme 1-5 and starts with the protonation of the hydroxyl group (1). This converts it into a better leaving group, i.e., as an H₂O molecule. A deprotonation (2) then yields the enone product.



Scheme 1-5: Generic mechanism of the Brønsted acid catalyzed aldol dehydration

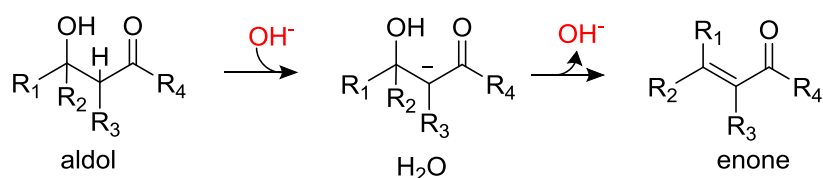
1.2.2 Brønsted base catalyzed reaction mechanism

The reaction mechanism for the base catalyzed aldol reaction is presented in Scheme 1-6. In the first step (1), an enolate ion is formed by abstraction of an α -hydrogen from the aldehyde or ketone. The resonance-stabilized enolate-anion is nucleophilic, and will attack the carbonyl group of a second aldehyde or ketone (2) to form the new carbon-carbon bond. The aldol product is formed by protonation of the alkoxide ion, regenerating the base catalyst (3).



Scheme 1-6: Generic mechanism of a Brønsted base catalyzed aldol reaction

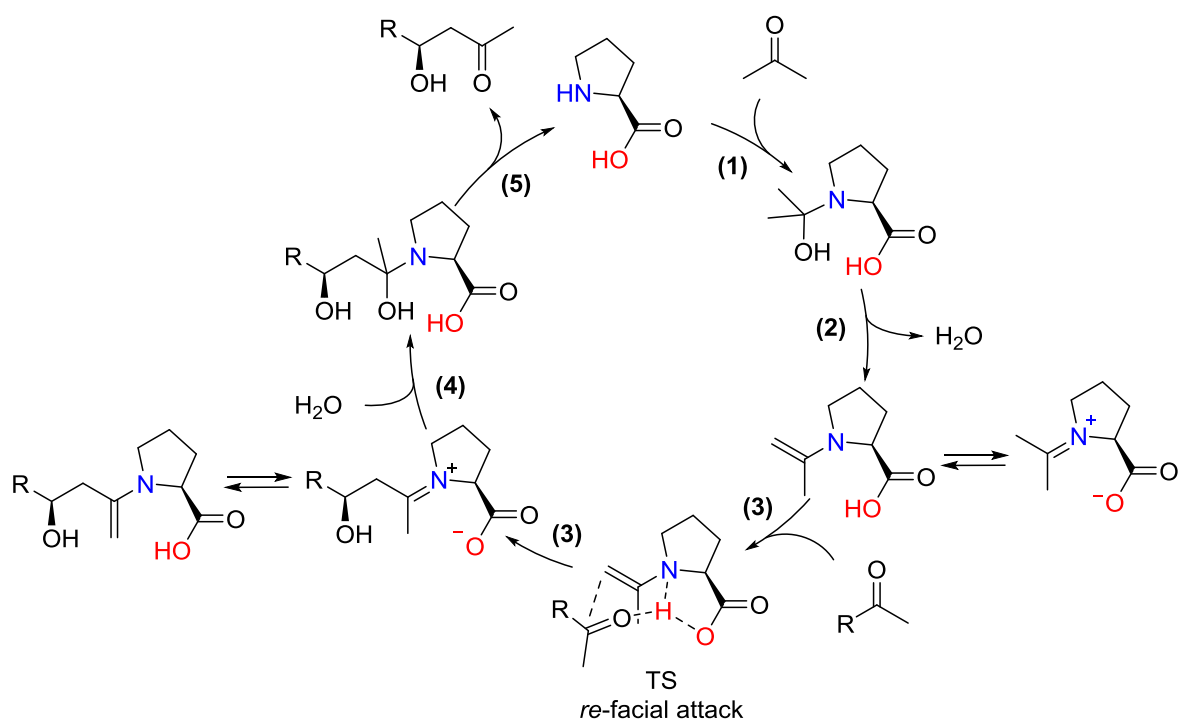
The base catalyzed dehydration of the aldol product proceeds through an E1cB elimination⁴³, as displayed in Scheme 1-7. The strong base abstracts a proton from the aldol product (**1**), resulting in an enolate, followed by the elimination of the hydroxide ion (**2**), restoring the catalytically active species and yielding the enone product.



Scheme 1-7: Generic mechanism of the Brønsted base catalyzed aldol dehydration

1.2.3 Lewis basic amine catalyzed reaction mechanism

In 1971, the first amine-catalyzed aldol reaction, promoted by an intramolecular acid group, was reported independently by Eder, Sauer, and Wiechert at Schering⁵¹, and Hajos and Parrish at Hoffmann-La Roche^{52,53}. An excellent yield and enantioselectivity was obtained with 3 mol% of L-proline as catalyst at room temperature. The reaction was described⁵³ as “a simplified model of a biological system in which L-proline plays the role of an enzyme”. This method was not developed further, until 30 years later when List et al.⁵⁴ published their breakthrough work on the L-proline-catalyzed aldol reaction between acetone and 4-nitrobenzaldehyde. The mechanism that was proposed in this work⁵⁴ is shown in Scheme 1-8.



Scheme 1-8: L-proline-catalyzed enantioselective aldol reaction with R = C₆H₄-NO₂. Figure adapted from ref 54.

The L-proline-catalyzed aldol reaction mechanism starts with a nucleophilic addition of acetone to the secondary amine in L-proline (**1**) with formation of a carbinolamine intermediate. This step is facilitated by the formation of a hydrogen bond between acetone and the carboxylic acid group. Dehydration of the carbinolamine then leads to formation of an enamine (**2**), a key electron-rich intermediate^{55, 56} that plays the same role as the enol or enolate in, respectively, the Brønsted acid or Brønsted base catalyzed aldol reaction. This enamine is in equilibrium with its corresponding iminium ion, which is electrophilic in nature and cannot react with a carbonyl group. In a next step, the enamine intermediate reacts (**3**) with the carbonyl group of 4-nitrobenzaldehyde and forms an iminium ion. In this step, enantioselectivity is achieved by the carboxylic acid group that promotes the *re*-facial attack. Hydration (**4**) of the resulting iminium ion leads to the formation of a carbinolamine which can detach as the aldol product and thereby liberate (**5**) the amine site.

As described above, the carboxylic acid group in L-proline is important to establish a high enantioselectivity. It also increases the reaction rate by assisting in proton transfers, but is not required for the reaction to take place⁵⁷. This carboxylic acid group is therefore regarded as a ‘promoting’ group that is acting ‘cooperatively’ with the amine.

Cordova et al.⁵⁸ have demonstrated that primary amines are also active catalysts for aldol reactions. Indeed, the enamine intermediate can form on both a secondary and a primary amine. However, on a primary amine, the reactive enamine intermediate is in equilibrium with an imine. Similar to the iminium ion on a secondary amine, an imine is electrophilic in nature and can thus not directly react with a carbonyl group. When its formation during the aldol reaction is stabilized, it can be regarded as inhibiting.

1.3 Heterogeneous catalysts for the aldol reaction

Different types of heterogeneous catalysts, with either acid, base or amine sites, have been explored for the aldol reaction. A brief literature survey is presented below, highlighting the most important features induced by each type of catalyst.

1.3.1 Zeolites

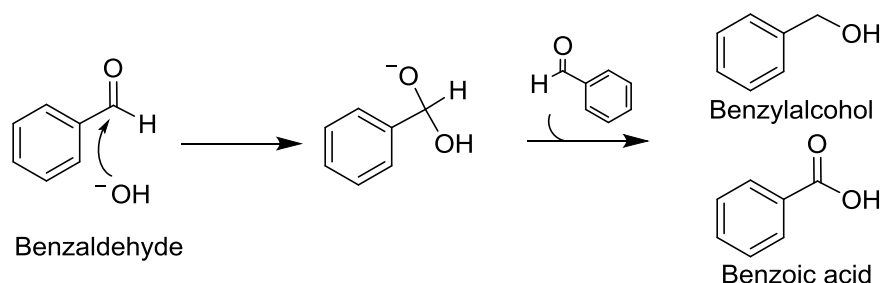
The industrially widely employed zeolite-type materials have often been investigated for liquid-phase aldol reactions⁵⁹⁻⁶². Different structural morphologies have been investigated, such as MFI^{59, 60}, FAU⁶² and BEA⁶². Alkali metal Y zeolites with basic sites were evaluated by Rode et al⁶³. However, it was reported that the formation of large condensation products inside the

micropores causes rapid pore-blocking and subsequent deactivation⁶². Development of zeolites with larger mesopores slightly reduces the catalyst's susceptibility to coking, but also decreases its acid strength and thus its catalytic activity⁶⁰. Hence, zeolites appear not to be ideal as reusable, sustainable heterogeneous catalysts for liquid-phase aldol reactions.

1.3.2 Layered double hydroxides

Catalysts derived from layered double hydroxides of which hydrotalcite is the most well-known, have already been frequently investigated for the aldol reaction⁶⁴⁻⁷⁰. As-prepared hydrotalcite materials are solids with a structure of general formula $Mg_6Al_2(OH)_{16}CO_3 \cdot 4 H_2O$ ⁷¹. The hydrotalcites can be used as catalysts either in the form of mixed oxides $Mg(Al)O$ with Lewis basicity obtained by calcination of the as-prepared precursor, or in the form of reconstructed hydrotalcite with OH^- counter ions as Brønsted basicity in its rehydrated form⁷².

These catalysts, however, typically suffer from fast deactivation in the liquid-phase aldol reaction by strong adsorption of reagents and products. Additionally, ambient CO_2 adsorbs on the basic sites when the material is exposed to atmospheric conditions⁶⁸. Regeneration of its basic character is possible, but is never complete⁷³. Side-reactions such as the Cannizzaro reaction, shown in Scheme 1-9, also typically occur to a significant extent with Brønsted base catalysts⁷⁴.



Scheme 1-9: Base-induced disproportionation of the non-enolizable benzaldehyde to a primary alcohol and a carboxylic acid (Cannizzaro reaction)⁷⁴

1.3.3 Functionalized silica

Mesoporous silica materials are extensively studied in heterogeneous catalysis due to favorable properties such as large pore size, large surface area and the easy incorporation of different functionalities via reaction with the surface silanol groups¹⁹. Mesoporous silicas are synthesized by condensation of tetraethyl orthosilicate (TEOS) around a surfactant. An ordered regular porous structure can be obtained, such as is the case with the widely known SBA-15

and MCM-41 materials, or an unordered mesoporous structure can be obtained, which is the case for silica gel.

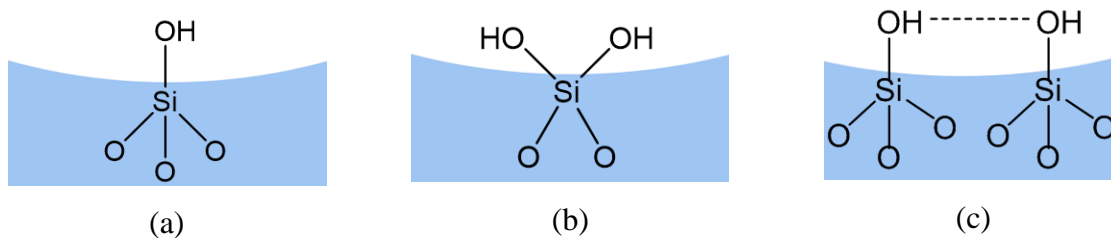


Figure 1-3: Surface silanol types: isolated (a), geminal (b) and vicinal (c), adapted from Van Der Voort et al.⁷⁶

The surface of both the ordered and unordered silica materials is random in nature and consists of siloxane links ($\equiv\text{Si-O-Si}\equiv$) and silanol groups ($\equiv\text{Si-OH}$). The mildly acidic silanols do not allow to directly catalyze the aldol reaction, but can easily be reacted with a wide variety of silanes⁷⁶, resulting in the functionalization of the silica. Depending on the calcination procedure, several types of silanols can be obtained on the silica surface. A distinction is made between isolated, vicinal and geminal silanol groups, as illustrated in Figure 1-3. Isolated silanol groups consist of a single hydroxyl group on the silica surface, whereas geminal silanol groups consist of two hydroxyl groups attached to the same silicon atom. In the case of vicinal silanol groups, two single hydroxyl groups attached to different silicon atoms are close enough to form a hydrogen bond. Calcination of the silica material will induce condensation of the silanol groups and thus a change in their distribution⁷⁶, according to the graph displayed in Figure 1-4.

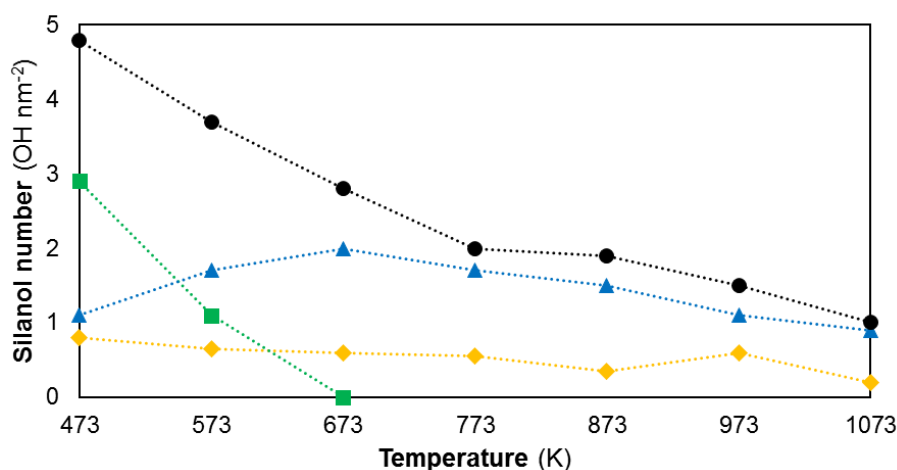
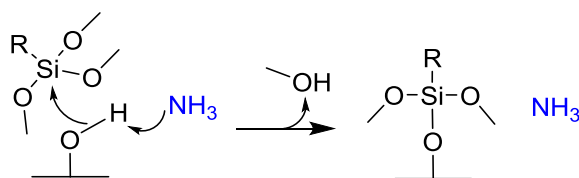


Figure 1-4: Silanol type distribution as a function of calcination temperature (■, green, vicinal silanols, ▲, blue, isolated silanols, ◆, yellow, geminal silanols, ●, black, total silanols). Figure adapted from Van Der Voort et al.⁷⁶

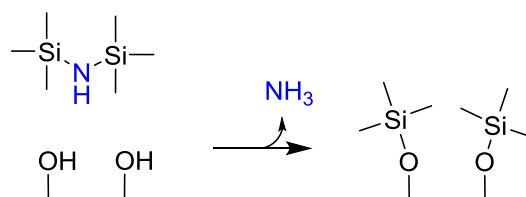
Functionalization of the silica surface with organosilanes, catalyzed by ammonia in an organic solvent, occurs via the mechanism displayed in Scheme 1-10. Ammonia will

deprotonate the silanol group, which makes it a better nucleophile for attack on the silane^{77,78}, thereby increasing the reaction rate. Aminosilanes, which are further discussed in section 1.3.3.1, have the catalyzing amine function already embedded in their structure and, hence, do not require the addition of ammonia⁷⁶.



Scheme 1-10: Ammonia catalyzed reaction of an organosilane with an isolated silanol. Figure adapted from Van Der Voort et al.⁷⁶

Similar to the above described grafting of organosilanes, trimethylsilyl groups can be placed on the silanol groups by reacting the silica material with 1,1,1,3,3,3-hexamethyldisilazane (HMDS), as displayed in Scheme 1-11. Stoichiometrically, it can be used to determine the number of silanol groups on the surface via, for example, elemental CHN analysis. However, due to steric hindrance of nearby silanols, the upper limit^{79,80} of determining the silanol number with this method is in the range of 2.2 to 2.7 per nm².



Scheme 1-11: Reaction of HMDS with surface silanols⁸⁰

Additionally, by treating the silica surface with HMDS, the hydrophilic silanol groups are replaced by hydrophobic trimethylsilyl groups^{81,82}. This will, among others, have a pronounced effect on the water adsorption behavior of the material⁸².

1.3.3.1 Monofunctional base catalysts

A heterogeneous amine catalyst for the aldol reaction can be synthesized by functionalizing aminosilanes on mesoporous silica^{46-48, 76, 83-96}. Secondary amines were found to perform best as catalysts for the aldol reaction in organic solvents, because primary amines cannot avoid the formation of a stable inhibiting imine species and tertiary amines do not allow the formation of the crucial enamine intermediate for the aldol reaction^{85, 86, 97}. However, care should be taken that the substituent on the secondary amine is not too large, in order to minimize

steric hindrance when approaching the nitrogen lone electron pair^{87, 98}. Lauwaert et al.⁸⁷ concluded from a range of secondary amines attached with a propyl linker to silica that a methyl group, i.e., N-methylaminopropane as displayed in Figure 1-5, exhibits the lowest steric hindrance and thus yields the highest activity for the aldol reaction using hexane as solvent.

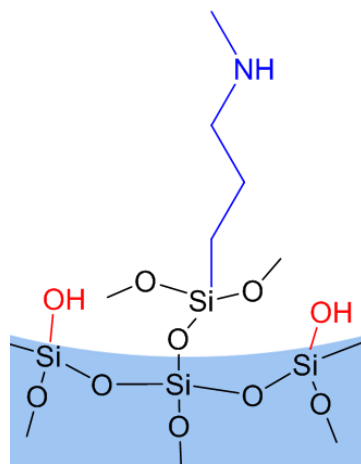


Figure 1-5: Currently the most active secondary amine site for the aldol reaction using hexane as solvent, as determined by Lauwaert et al⁸⁷.

1.3.3.2 Intermolecular cooperative acid-base catalysts

The weakly acidic silanol groups, which are intrinsically present at the silica surface as displayed in Figure 1-5, were found to act as a cooperative partner in the reaction mechanism, equivalent to the cooperative effect of the carboxylic acid in L-proline^{91,96}. However, increasing the acid strength of the promoting acid function on mesoporous silica, by grafting of carboxylic acid groups near the amines, was found to decrease the catalytic activity^{47, 92-94}. This has been related to a shift from the free acid and free base pair towards the resulting neutralized ion pair^{47, 88, 93, 94}, as displayed in Figure 1-6. In its protonated form, the electron pair of the amine is no longer available for interaction with the carbonyl species. Hence, optimal promoting sites are H-bond donors, like silanol groups, and not strong acids⁴⁷.

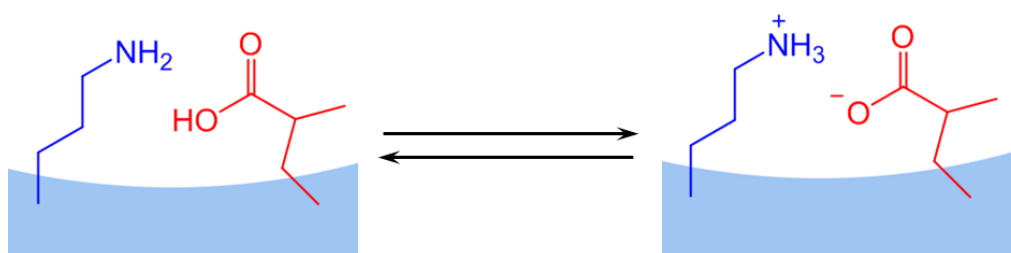


Figure 1-6: Unfavorable protonation/deprotonation equilibrium when a strong carboxylic acid is employed as promoting group, figure adapted from Brunelli et al.⁴⁷

It has also been reported that the amine and acid functions of the cooperative catalyst should be situated sufficiently close to interact with each other^{47, 99}. One way to tune this distance is by altering the silica pore diameter and as such the surface curvature. This was found to be especially important for amines with an ethane linker, but showed no improvements for propyl chains⁴⁷. Generally, for randomly grafted amines on SBA-15 with a pore diameter of 6.5 nm, an increase in cooperativity was observed with increasing length of the alkyl chain, up to a propyl chain, after which it levelled off for longer alkyl chains⁹¹. On silica gel with a pore diameter of 6 nm, it was found that, when the amines are grafted randomly on the surface, at least 1.7 of these silanol groups are required per amine function to assure full promotion⁴⁶, as shown in Figure 1-7.

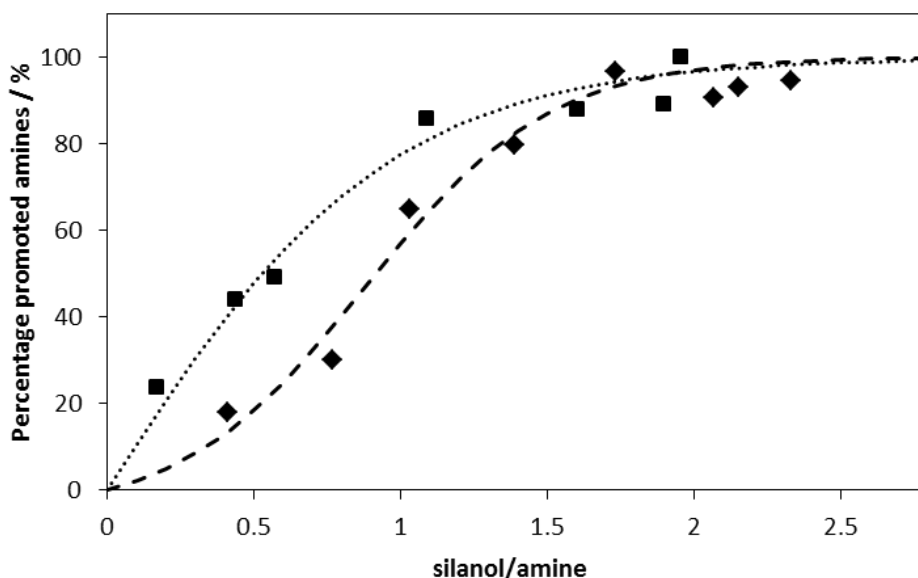


Figure 1-7: Promotion of silanol groups on primary amines (◆) and secondary amines (■) for the aldol reaction. Figure from Lauwaert et al.⁴⁶

In Figure 1-7 it appears that both a grafted primary amine as well as a grafted secondary amine require the same excess silanol-to-amine ratio for full promotion. However, in the region of a low silanol-to-amine ratio, a noticeable difference is seen for both catalysts. This difference has been related to the grafting process, where it was found that primary amine precursors are more likely to cluster because of hydrogen bond formation around the amines⁸⁷. Secondary, and tertiary, amine sites are more randomly distributed over the silica surface, rendering them eventually more susceptible for promotion by silanols.

In summary, a methyl substituted secondary amine with a propane linker, grafted on mesoporous silica as displayed in Figure 1-5, and promoted by an excess of silanol groups, is currently the most performant heterogeneous amine catalyst for the aldol condensation⁸⁸⁻⁹⁰.

1.3.3.3 Intramolecular cooperative acid-base catalysts

In order to ensure promotion of all amine groups on the silica surface, an excess of silanol groups was maintained, which resulted in a low active site loading^{46, 87}. To improve the activity on a mass basis, a higher active site density should be pursued without compromising on the intrinsic activity of the amine site. This could be achieved by incorporating the promoting group intramolecularly with the amine function. To investigate this, Lauwaert et al.⁹⁴ evaluated a range of promoted amine functions, as displayed in Figure 1-8.

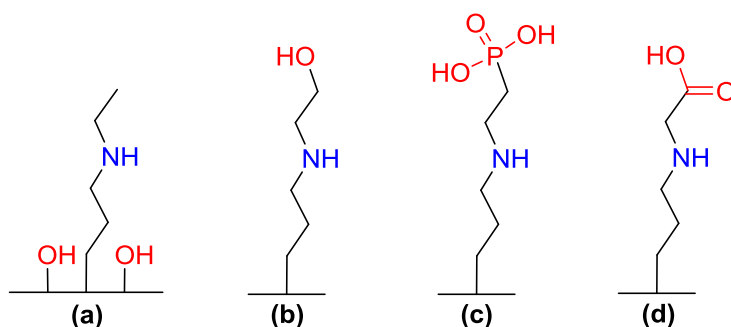


Figure 1-8: Inter- and intramolecularly promoted amine catalysts evaluated by Lauwaert et al.⁹⁴

From this work, it was concluded that the weakly acidic hydroxyl group (**b** in Figure 1-8) is a better promoting group than the more acidic promoting groups such as a phosphorus acid (**c**) and a carboxylic acid group (**d**)⁹⁴. This is consistent with previous work on intermolecular promotion⁴⁷. Moreover, it was found that the intramolecular placed hydroxyl group in (**b**) can promote the secondary amine to the same extent as a silanol group on the silica surface (**a**).

More recently, Xie et al.¹⁰⁰ investigated a range of intramolecularly promoted amine-hydroxyl functions with a varying amount of carbon atoms in-between. It was found that for catalysts where inter- and intramolecular cooperativity is possible, alkyl linkers separating the amine from the hydroxyl function by at least three carbons are more active than a short two-carbon linker¹⁰⁰. Further increasing the flexibility of the linker by changing the length with more than three carbon atoms did not change the activity¹⁰⁰. Catalysts with alkyl-substituted amines lacking a terminal hydroxyl demonstrated an adverse effect of chain length, where the larger alkyl substituent on the amine provides additional steric hindrance, lowering the catalytic activity. However, with HMDS treated catalysts, where cooperativity with surface silanol groups is eliminated, the catalyst with a hydroxyl function separated from the amine by a five carbon alkyl linker exhibited a significantly higher activity than all the shorter alkyl linker catalysts. This was attributed to the increased flexibility of the five-carbon alkyl linker, and hydrophobized surface which inhibits negative silanol-hydroxyl hydrogen bond interactions¹⁰⁰.

The above studies confirm the feasibility of intramolecular promotion by hydroxyl groups, but also show that the incorporation of a hydroxyl as a terminal group on the amine always increases the steric hindrance relative to the most optimal intermolecularly promoted secondary amine, and thus leads to lower activities than expected^{94, 100}. Theoretical probing of the added steric hindrance upon inclusion of an intramolecular promoting hydroxyl group could thus help in the search of a more optimal intramolecular promoted amine-hydroxyl function.

1.3.4 Functionalized organosilicas

Mesoporous organosilicas are a recently developed group of organic/inorganic hybrid materials composed of siloxane units that are bridged by organic groups¹⁰¹⁻¹⁰⁴. They typically exhibit a periodic mesoporous structure, have a high surface area, and display an improved hydrothermal, chemical and mechanical stability as compared to purely inorganic mesoporous silica¹⁰⁵⁻¹⁰⁷. Applications of periodic mesoporous organosilicas (PMO) can be found in different fields, such as chromatography and selective (gas) adsorption^{108, 109}, in low- κ dielectric films¹¹⁰ and in heterogeneous catalysis¹¹¹⁻¹¹⁵. The synthesis of these materials is comparable to the synthesis of ordered, or unordered, mesoporous silica, the main distinction being that, instead of tetraethylorthosilicate (TEOS), hydrolysable bis-silanes are employed for organosilicasⁱ. These hydrolysable bis-silanes are generally in the form of $(R'O)_3Si-R-Si(OR')_3$ with R the organic linker, anchored between two silicon atoms, and R'O a hydrolysable group, typically a methoxy or ethoxy group. Typical synthesis conditions produce a periodic structure because of hydrophobic and hydrophilic interactions between hydrolyzed precursors that self-assemble. Some examples are shown in Figure 1-9.

ⁱ An additional difference in the synthesis of inorganic silica and organosilica is that in the latter case calcination cannot be used to remove the surfactant material, as this would also destroy the organic groups in the pore walls. The surfactant is thus generally removed from organosilica materials by washing it extensively in a solvent.

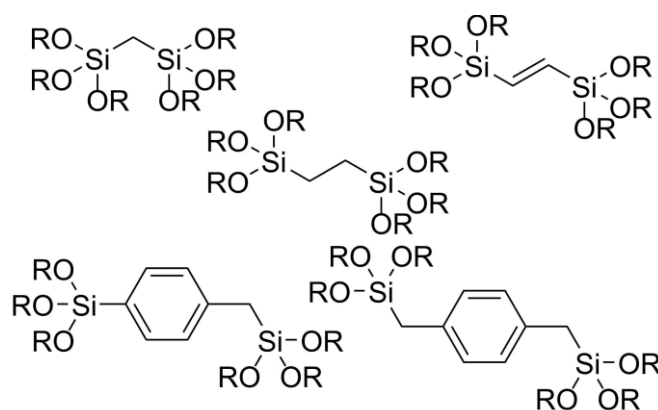


Figure 1-9: Non-exhaustive list of example organosilica precursors that have been successfully condensed into a PMO material. Terminal Si(OR) with R = CH₃ or C₂H₅. Figure adapted from Hoffmann et al.¹⁰⁷

The use of specific precursors in the PMO synthesis allows to create materials with well-defined functions and specific properties. An example PMO is shown in Figure 1-10, where ethylene linkers are incorporated in the pore-walls. The double bond that is now incorporated in the surface of the material can act as a potentially hydrothermally stable anchoring point for catalytic sites¹¹⁴. It should also be noted that, similar to silica materials, silanol groups are still present on an organosilica surface¹¹⁶. These can also be employed as potential grafting sites, and can act as a cooperative partner to an amine in the aldol reaction.

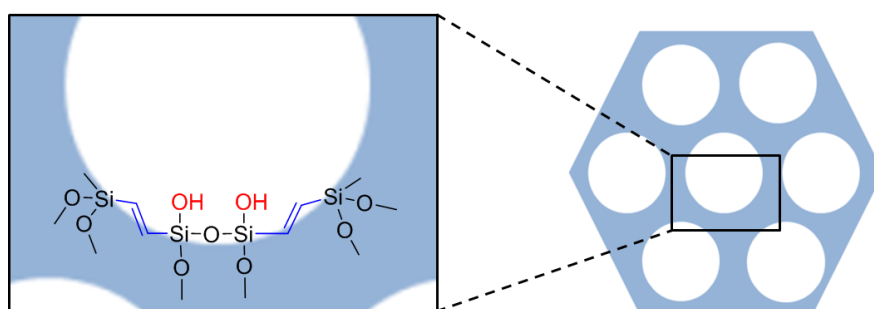
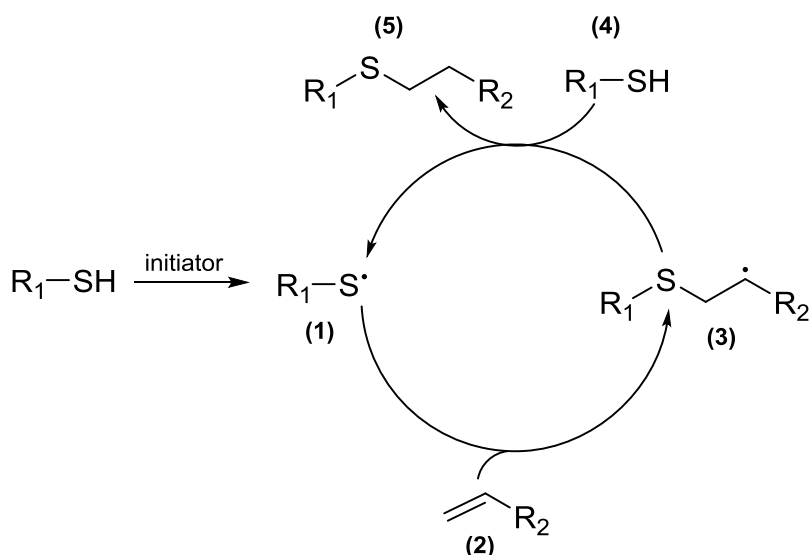


Figure 1-10: Example organosilica material with an ethylene bridge

Ouwehand et al.¹¹⁴ synthesized an ethylene-bridged PMO, such as the one displayed in Figure 1-10, and used the double bonds in this material as anchoring points for incorporation of amine sites. Anchoring was accomplished via a thiol-ene click reaction, the mechanism of which is displayed in Scheme 1-12, using the amino-acids cysteine and cysteamine which naturally contain a terminal thiol group.



Scheme 1-12: Thiol-ene click reaction mechanism, adapted from Lowe et al.¹¹⁷

The thiol-ene click reaction is a fast, facile and selective single-step reaction for functionalizing the double bond in an ethylene-PMO material¹¹⁷. The mechanism starts with reaction of a thiol with an initiator, either UV or thermally activated, with formation of a thiyl radical (1). In the propagation, the thiyl radical reacts with the ethylene moiety (2), with formation of an intermediate radical (3). This is followed by chain transfer to a new thiol molecule (4) and the formation of the thiol-ene product (5).

The catalysts obtained by Ouwehand et al.¹¹⁴ have primary amine sites, with, in the case of cysteine, also an adjacent cooperative carboxyl group. The catalytic activity of these catalysts was investigated for the aldol reaction of 4-nitrobenzaldehyde with acetone, using hexane as solvent. Results indicate that the intrinsic catalytic activity of the amine site is in the same order of magnitude as those of the corresponding silica materials^{87, 114}. Also, in agreement with the literature on functionalized silica catalysts⁴⁷, the silanol groups on the periodic organosilica surface were observed to be more efficient promoting sites than the intramolecular carboxylic acid group¹¹⁴.

The large variety of mesoporous organosilica materials that can be synthesized, intrinsically guarantees a large potential for creating next generations of supported amines for the aldol reaction. The possibility to tailor the support properties will allow to tune for selective adsorption of reagents in the pores of the catalyst and could thereby enhance the measured reaction rates¹¹³. Effects related to these solvent-support interactions will be further discussed in paragraph 1.4.

1.3.5 Functionalized polymer resins

Polymer resins are soft or highly viscous support materials, made entirely of organic groups, which contain reactive end groups potentially useful for catalysis¹¹⁸⁻¹²⁰ or as sorbents¹²¹. Resins are susceptible to dissolution in solvents, depending on both the resin and the solvent properties. Such dissolution renders the active sites more accessible. Of course, complete dissolution is not desired for heterogeneous catalysts. Hence, when the polymer chains are lightly cross-linked, the resin will swell in that solvent instead of dissolving¹²², as displayed in Figure 1-11. This increases the porosity of the material and renders the active sites more accessible, while still remaining a heterogeneous solid in the liquid. Resins with a high degree of crosslinking also exhibit porosity under dry conditions, and will not, or only to a limited degree, swell in the presence of a solvent.

In the case of a liquid mixture, selective absorption of one component in the pores of the resin can occur¹²³. This is one of the most interesting properties of these materials for catalytic applications, because it allows tuning the local component enrichment in areas around the catalytically active sites¹²⁰.

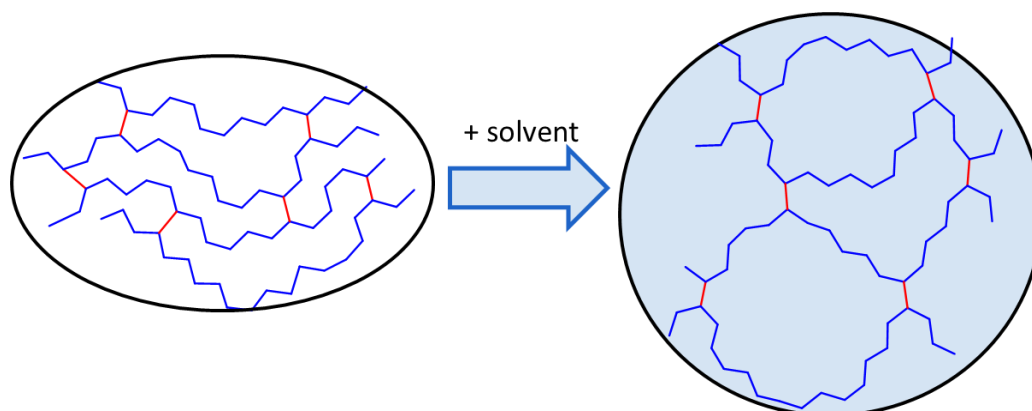


Figure 1-11: Swelling of a cross-linked polymer resin in a compatible solvent.

The most frequently commercially employed resins are ion-exchange resins based on crosslinked polystyrene, where the actual ion-exchanging sites are introduced after polymerization. Crosslinking can be easily established by copolymerizing a few percent of divinylbenzene (DVB) with styrene. Four main types of ion-exchange resins can be made:

- strongly acidic, typically featuring sulfonic acid groups.
- strongly basic, typically featuring quaternary amino groups with OH^- counterions.
- weakly acidic, typically featuring carboxylic acid groups.
- weakly basic, typically featuring primary, secondary, and/or tertiary amino groups.

1.3.5.1 Strong acidic resins

Amberlyst, produced by Dow Inc., and Amberlite, produced by DuPont, are sulfonic acid type resins that are most often commercially used as strong acidic resins^{124, 125}. They have been evaluated in an aldol reaction by Lahyani et al.¹²⁶ for the synthesis of trans-chalcones. Despite obtaining good yields, the catalyst showed deactivation in consecutive batch experiments due to neutralization of the acid sites. While improvements the stability of sulfonic acids on polymer resins have been made for the aldol reaction¹²⁷, no long-term stability has yet been obtained.

1.3.5.2 Strong basic resins

The strongly basic ion-exchange resins are composed of quaternary ammonium ions that interact with OH⁻ ions, which are the actual active sites. These catalysts are also subject to deactivation, caused by neutralization of the OH⁻ ions and pore-blocking^{128, 129} and are thus not ideal stable heterogeneous catalysts for the aldol reaction.

1.3.5.3 Weak acidic resins

No reports have been found of the use of weakly acidic resins for catalyzing the aldol reaction. This is most likely due to the low acidity of the carboxylic acid on these materials¹³⁰, which is unable to catalyze the reaction.

1.3.5.4 Weak basic resins

For weakly basic resins, it was found that the tertiary amine resins exhibit a lower activity^{131, 132} than the quaternary ion-exchange resins in the aldol reaction, but this also allowed avoiding side-reactions such as the Cannizzaro reaction^{133, 134}. Primary or secondary amine functionalized resins have not often been investigated for the aldol reaction. However, pioneering work by Hoyt et al.¹³⁵ investigated bifunctional block-copolymer resins for the aldol reaction. One major disadvantage of these first-generation bifunctional resin catalysts was their inability to dissolve, or swell, in the solvents of choice¹³⁵. This again emphasizes the absorption behavior of the resin material is an important parameter to tune in order to obtain an active catalyst.

1.4 Solvent effects in the amine catalyzed aldol reaction

The solvent selection has an effect on the reaction catalyzed by heterogeneous catalysts due to its interaction with the reagents, and intermediate species on the active site¹³⁶⁻¹³⁹. Moreover, as described above, the solvent in the liquid-phase reaction significantly impacts on the swelling of a polymer resin to such an extent that it will determine the accessibility of the active sites and thus the catalytic activity^{140, 141}. All these effects are caused by the contribution of solvation energy to the total free energy of the systems, and by stabilization or destabilization of the transition states, which could even lead to different reaction pathways being preferred¹³⁶.

Several solvent effects in the amine catalyzed aldol reaction are discussed next, examples from both homogeneous as well as heterogeneous catalysis are discussed. Care should be taken when these results are compared to each other, as the nature of the heterogeneous support also affects the local solvent environment around the amine site, having a potential impact on the occurring phenomena.

1.4.1 The homogeneous aldol reaction catalyzed by L-proline

The initial work on the L-proline catalyzed aldol reaction by List et al.⁵⁴ already highlighted that solvent polarity has a pronounced influence on the catalytic activity and the obtained enantioselectivity. DMSO was found to be the most optimal solvent for their application, but phenomena at the origin of this behavior were not discussed in detail. Further work highlighted the inability to catalyze the aldol reaction with L-proline in water^{142, 143}, most likely due to mutual neutralization of the acid-base pair. However, it was later noted that small amounts of water can regenerate deactivated L-proline molecules and thereby increase the catalytic activity¹⁴⁴. These examples indicate the complex role that the solvent, such as water, can play in a reaction. Especially the effects of performing an organic reaction ‘in-water’, ‘on-water’ or ‘in the presence of water’ are currently widely discussed in literature^{28, 145-148}.

1.4.2 The heterogeneous aldol reaction catalyzed by aminated silica

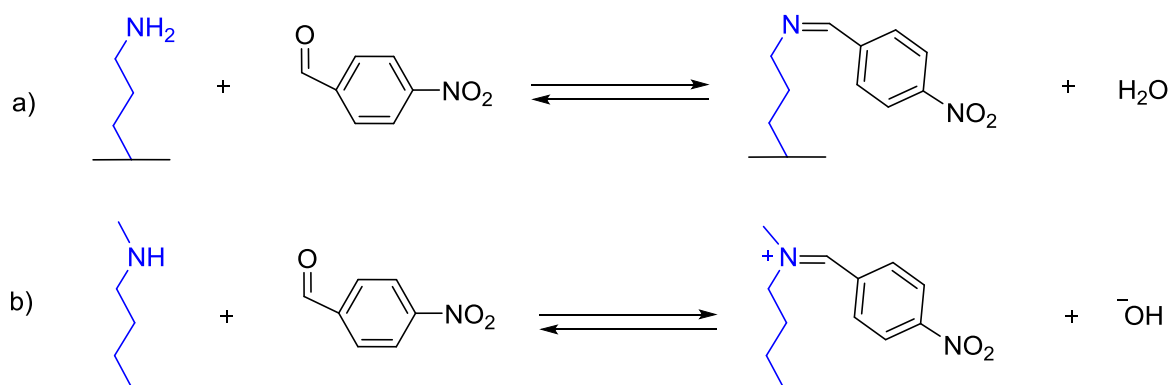
1.4.2.1 Acid-base pair neutralization

In the aldol reaction catalyzed by a heterogeneous cooperative acid-base catalyst, the solvent affects the equilibrium between the free acid and base and the neutralized ion pair. In some solvents, the acid and base sites are subject to neutralization, accompanied by loss of the

catalytic activity. This is, however, most relevant for acid-base catalysts with acidic groups such as a carboxylic acid or a sulfonic acid, which are considerably stronger acids than silanol groups. Zeidan et al.⁹³ investigated different protic and aprotic solvents that could stabilize the neutralized ion pair on a silica catalyst with primary amine sites and promoting sulfonic acid groups. In polar, protic solvents (e.g. water, methanol), the equilibrium lies strongly towards the neutralized ion pair, exhibiting a negative effect on the catalyst activity. Improvements are observed for moderately polar, aprotic solvents (e.g. diethyl ether, chloroform). Further improvements are obtained for nonpolar, aprotic solvents (e.g. hexane, benzene), which cause a reduced stabilization of the neutralized ion pair⁹³.

1.4.2.2 Imine inhibition of primary amine sites

Kandel et al.⁸⁵ reported that mesoporous silica materials functionalized with primary amines are poor catalysts for the aldol reaction in hexane because of the formation of a stable imine of 4-nitrobenzaldehyde (pathway a in Scheme 1-13).



Scheme 1-13: Possible imine, and iminium ion, formation of 4-nitrobenzaldehyde on respectively a primary and a secondary amine.

The extent of imine inhibition could be reduced by replacing the primary amine with a secondary one, bearing a small substituent such as a methyl group. As displayed in Scheme 1-13, pathway **b**, no imine can be formed on this secondary amine. Instead, an iminium ion can be formed which is not stable in an apolar medium and, hence, does not exert any effect in hexane. However, switching the reaction solvent from hexane to water has been observed to lead to a reversal in the activity between the primary and secondary amine¹⁴⁹. The primary amine was found to be more active, possibly due to the equilibrium of pathway **a** in Scheme 1-13 shifting to the reactant side, and thereby generating more free sites. The secondary amine,

however, was found to be less active, which can be explained by the stabilization of the iminium ion and hydroxide counter-ion by water molecules (pathway **b** in Scheme 1-13).

1.4.2.3 Tuning the dielectric environment around the active site

Recent work by Singappuli-Arachchige et al.¹⁵⁰ suggest that a combination of a low dielectric constant around the active site, coupled with water as a solvent, leads to an increased activity and decreased active site deactivation on aminated silica catalysts for the aldol reaction. Controlling the dielectric properties around a supported primary amine site was achieved by immobilizing hexyltrimethoxysilane next to it. These hexyl groups interfere with solvation at the support-water interface, leading to a local dielectric property that is different from the bulk. This has led to a 5 times higher activity being measured with a hexyl-modified aminated silica catalyst as compared to the benchmark aminated silica catalyst. While it was shown that deactivation of the hexyl-modified aminated silica catalyst was lower, complete reusability was not achieved.

1.4.3 Tuning hydrophobicity in the support material

The properties of the heterogeneous support material can also significantly impact the measured reaction rates, as shown by Lauwaert et al.¹¹³ They synthesized PMO materials with either ethane or aromatic linkers, combined with a small amount of vinyltriethoxysilane (VTES) for thiol-ene click functionalization with the primary amino-acid cysteine. As a benchmark material, the hydrophilic tetraethyl orthosilicate (TEOS) was also used as a precursor, in combination with a small amount of VTES for functionalization. Due to the predominance of TEOS, this catalyst will be referred to as the silica catalyst. The activity of these three catalysts was evaluated in the aldol reaction of acetone with 4-nitrobenzaldehyde in a 50:50 vol% acetone/n-hexane solvent mixture, and subsequently repeated with 1 vol% of water added. The aromatic PMO catalyst exhibited a low catalytic activity in both solvent mixtures, which was attributed to a too pronounced 4-nitrobenzaldehyde enrichment caused by pi-stacking interactions with the support, enhancing the formation of inhibiting species with 4-nitrobenzaldehyde. However, when the silica catalyst is compared to the ethane PMO catalyst, the latter exhibited a superior activity in both solvent mixtures. This was attributed to the hydrophobicity of the support, without the possibility of pi-stacking interactions, which might lead to a better acetone to 4-nitrobenzaldehyde ratio inside its pores. Moreover, while the

ethane PMO catalyst retained its activity with 1 vol% water, it was found that the hydrophilic silica catalyst loses about 40% of its activity¹¹³.

An et al.¹⁵¹ investigated the effect of the hydrophobicity of the support material on the catalytic activity for the aldol reaction by incorporating different quantities of hydrophobic organic blocks in a mesoporous silica material via co-condensation. The materials were functionalized with L-proline via a thiol-ene click reaction, which served as active site for the aldol reaction of cyclohexanone with different aldehydes. The catalysts were tested using either cyclohexanone or water as a solvent. For all materials, the catalytic activity was higher with water as solvent in comparison to cyclohexanone. Moreover, in each case, an increase in activity was observed for the catalyst with a higher fraction of hydrophobic groups. The latter is ascribed to the synergistic effects of the hydrophobic blocks in the pores, attracting the organic reactions from bulk towards the active sites inside the pores. Especially in aqueous medium, the organic molecules were attracted from the water and concentrated around the active sites¹⁵¹.

1.5 Scope and outline of this work

The aim of this work is to develop a new type of catalyst for aldol reactions which show an appreciable activity level over a prolonged time under reactive conditions. As zeolite catalysts are prone to very rapid deactivation by coking, and the less acidic functionalized resin catalysts show a low activity for the aldol reaction, it is chosen to optimize the stability and activity of amine functionalized mesoporous silica catalysts. The computational procedures used in this work are thoroughly discussed in Chapter 2, while the experimental procedures are always discussed in the respective chapters. Optimization of the amine functionalized catalysts is first performed by a computational assessment of steric and electronic effects around amine sites in Chapter 3. Next, in Chapter 4, the deactivation mechanisms responsible for the limited reusability in subsequent batch reactions with the current state-of-the-art aminated mesoporous silica catalysts is thoroughly investigated. This is done by combining experimental activity measurements with characterization of the spent catalyst and, in Chapter 5, theoretical modeling of possible deactivation pathways. Via a molecular level understanding of the effects responsible for deactivation, synthesis parameters and reaction conditions are adapted to reduce this deactivation. Evaluation of the catalytic activity for a prolonged time under reactive conditions is done making use of a liquid-phase continuous-flow fixed bed reactor, which has been developed in-house, as discussed in Chapter 6. As possible sustainable heterogeneous

alternative catalyst for the aqueous aldol reaction, chitosan is evaluated in Chapter 7. The insights gained from chitosan as catalyst, using the continuous-flow reactor setup, are then used in Chapter 8 to develop a stable catalyst for the aldol reaction.

1.6 References

1. Ilgen, T. L., “Better living through chemistry”: the chemical industry in the world economy. *International Organization* **1983**, *37* (4), 647-680.
2. Matlack, A., *Introduction to green chemistry*. CRC Press: 2010.
3. Horváth, I. T., *Introduction: Sustainable Chemistry*. ACS Publications: 2018.
4. Linthorst, J., An overview: origins and development of green chemistry. *Foundations of chemistry* **2010**, *12* (1), 55-68.
5. Brundland, G., *World Commission on Environment and Development: Our Common Future*. Oxford University Press: 1987.
6. Anastas, P. T.; Warner, J. C., *Principles of green chemistry. Green chemistry: Theory and practice* **1998**, 29-56.
7. Sheldon, R. A.; Arends, I.; Hanefeld, U., *Green chemistry and catalysis*. John Wiley & Sons: 2007.
8. Kelly, G.; King, F.; Kett, M., Waste elimination in condensation reactions of industrial importance. *Green Chemistry* **2002**, *4* (4), 392-399.
9. Sheldon, R. A., Engineering a more sustainable world through catalysis and green chemistry. *Journal of The Royal Society Interface* **2016**, *13* (116), 20160087.
10. Kulprathipanja, S., *Zeolites in industrial separation and catalysis*. John Wiley & Sons: 2010.
11. Fecheté, I.; Wang, Y.; Védrine, J. C., The past, present and future of heterogeneous catalysis. *Catalysis Today* **2012**, *189* (1), 2-27.
12. Seghers, S.; Lefevère, J.; Mullens, S.; De Vylder, A.; Thybaut, J. W.; Stevens, C. V., Enhancing Zeolite Performance by Catalyst Shaping in a Mesoscale Continuous-Flow Diels–Alder Process. *ChemSusChem* **2018**, *11* (10), 1686-1693.
13. Van Bekkum, H.; Kouwenhoven, H., The use of zeolites in organic reactions. *Recueil des Travaux Chimiques des Pays-Bas* **1989**, *108* (9), 283-294.
14. Schwieger, W.; Machoke, A. G.; Weissenberger, T.; Inayat, A.; Selvam, T.; Klumpp, M.; Inayat, A., Hierarchy concepts: classification and preparation strategies for zeolite containing materials with hierarchical porosity. *Chemical society reviews* **2016**, *45* (12), 3353-3376.
15. Li, K.; Valla, J.; Garcia-Martinez, J., Realizing the commercial potential of hierarchical zeolites: new opportunities in catalytic cracking. *ChemCatChem* **2014**, *6* (1), 46-66.
16. Hattori, H., Solid base catalysts: fundamentals and their applications in organic reactions. *Applied Catalysis A: General* **2015**, *504*, 103-109.
17. Xu, C.; Gao, Y.; Liu, X.; Xin, R.; Wang, Z., Hydrotalcite reconstructed by in situ rehydration as a highly active solid base catalyst and its application in aldol condensations. *RSC Advances* **2013**, *3* (3), 793-801.
18. Bhandari, V. M.; Sorokhaibam, L. G.; Ranade, V. V., Chapter 9 - Ion Exchange Resin Catalyzed Reactions—An Overview. In *Industrial Catalytic Processes for Fine and Specialty Chemicals*, Joshi, S. S.; Ranade, V. V., Eds. Elsevier: Amsterdam, 2016; pp 393-426.
19. Price, P. M.; Clark, J. H.; Macquarrie, D. J., Modified silicas for clean technology. *Journal of the Chemical Society, Dalton Transactions* **2000**, (2), 101-110.
20. Constable, D. J.; Jimenez-Gonzalez, C.; Henderson, R. K., Perspective on solvent use in the pharmaceutical industry. *Organic process research & development* **2007**, *11* (1), 133-137.
21. Sherman, J.; Chin, B.; Huibers, P.; Garcia-Valls, R.; Hatton, T. A., Solvent replacement for green processing. *Environmental Health Perspectives* **1998**, *106* (suppl 1), 253-271.
22. Li, C.-J.; Chen, L., Organic chemistry in water. *Chemical Society Reviews* **2006**, *35* (1), 68-82.
23. Lindström, U. M., Stereoselective Organic Reactions in Water. *Chemical Reviews* **2002**, *102* (8), 2751-2772.

24. Simon, M.-O.; Li, C.-J., Green chemistry oriented organic synthesis in water. *Chemical Society Reviews* **2012**, *41* (4), 1415-1427.
25. Butler, R. N.; Coyne, A. G., Water: Nature's Reaction Enforcer □ Comparative Effects for Organic Synthesis "In-Water" and "On-Water". *Chemical reviews* **2010**, *110* (10), 6302-6337.
26. Lindstrom, U. M., *Organic reactions in water: principles, strategies and applications*. John Wiley & Sons: 2008.
27. Klijn, J. E.; Engberts, J. B., Organic chemistry: Fast reactions 'on water'. *Nature* **2005**, *435* (7043), 746.
28. Hayashi, Y., In water or in the presence of water? *Angewandte Chemie International Edition* **2006**, *45* (48), 8103-8104.
29. Narayan, S.; Muldoon, J.; Finn, M.; Fokin, V. V.; Kolb, H. C.; Sharpless, K. B., "On water": Unique reactivity of organic compounds in aqueous suspension. *Angewandte Chemie International Edition* **2005**, *44* (21), 3275-3279.
30. Pachauri, R. K.; Meyer, L. A. *Climate Change 2014: Synthesis Report. Contribution of Working Groups I, II and III to the Fifth Assessment Report of the Intergovernmental Panel on Climate Change*; Geneva, Switzerland, 2014.
31. Martens, J. A.; Bogaerts, A.; De Kimpe, N.; Jacobs, P. A.; Marin, G. B.; Rabaey, K.; Saeys, M.; Verhelst, S., The chemical route to a carbon dioxide neutral world. *ChemSusChem* **2017**, *10* (6), 1039-1055.
32. Zou, C.; Zhao, Q.; Zhang, G.; Xiong, B., Energy revolution: From a fossil energy era to a new energy era. *Natural Gas Industry B* **2016**, *3* (1), 1-11.
33. Corma, A.; Iborra, S.; Velty, A., Chemical routes for the transformation of biomass into chemicals. *Chemical reviews* **2007**, *107* (6), 2411-2502.
34. Chheda, J. N.; Huber, G. W.; Dumesic, J. A., Liquid-phase catalytic processing of biomass-derived oxygenated hydrocarbons to fuels and chemicals. *Angewandte Chemie International Edition* **2007**, *46* (38), 7164-7183.
35. Dickerson, T.; Soria, J., Catalytic fast pyrolysis: a review. *Energies* **2013**, *6* (1), 514-538.
36. Lange, J. P., Lignocellulose Liquefaction to Biocrude: A Tutorial Review. *ChemSusChem* **2018**, *11* (6), 997-1014.
37. Serrano-Ruiz, J. C.; Dumesic, J. A., Catalytic routes for the conversion of biomass into liquid hydrocarbon transportation fuels. *Energy & Environmental Science* **2011**, *4* (1), 83-99.
38. Kunkes, E. L.; Simonetti, D. A.; West, R. M.; Serrano-Ruiz, J. C.; Gärtner, C. A.; Dumesic, J. A., Catalytic conversion of biomass to monofunctional hydrocarbons and targeted liquid-fuel classes. *Science* **2008**, *322* (5900), 417-421.
39. Simonetti, D. A.; Dumesic, J. A., Catalytic production of liquid fuels from biomass-derived oxygenated hydrocarbons: Catalytic coupling at multiple length scales. *Catalysis Reviews* **2009**, *51* (3), 441-484.
40. Bond, J. Q.; Upadhye, A. A.; Olcay, H.; Tompsett, G. A.; Jae, J.; Xing, R.; Alonso, D. M.; Wang, D.; Zhang, T.; Kumar, R.; Foster, A.; Sen, S. M.; Maravelias, C. T.; Malina, R.; Barrett, S. R. H.; Lobo, R.; Wyman, C. E.; Dumesic, J. A.; Huber, G. W., Production of renewable jet fuel range alkanes and commodity chemicals from integrated catalytic processing of biomass. *Energy & Environmental Science* **2014**, *7* (4), 1500-1523.
41. Chheda, J. N.; Dumesic, J. A., An overview of dehydration, aldol-condensation and hydrogenation processes for production of liquid alkanes from biomass-derived carbohydrates. *Catalysis Today* **2007**, *123* (1), 59-70.
42. West, R. M.; Liu, Z. Y.; Peter, M.; Dumesic, J. A., Liquid alkanes with targeted molecular weights from biomass-derived carbohydrates. *ChemSusChem: Chemistry & Sustainability Energy & Materials* **2008**, *1* (5), 417-424.
43. Bruice, Y. P., *Organic Chemistry*. Prentice Hall: 2003; Vol. 4th edition.
44. ICIS Chemical profile: 2-ethylhexanol. <http://www.icis.com> (accessed 24 August).
45. Raff, D. K., Butanals. *Ullmann's Encyclopedia of Industrial Chemistry* **2013**.
46. Lauwaert, J.; De Canck, E.; Esquivel, D.; Thybaut, J. W.; Van Der Voort, P.; Marin, G. B., Silanol-Assisted Aldol Condensation on Aminated Silica: Understanding the Arrangement of Functional Groups. *ChemCatChem* **2014**, *6* (1), 255-264.

47. Brunelli, N. A.; Jones, C. W., Tuning acid–base cooperativity to create next generation silica-supported organocatalysts. *Journal of Catalysis* **2013**, *308*, 60-72.
48. Kubota, Y.; Goto, K.; Miyata, S.; Goto, Y.; Fukushima, Y.; Sugi, Y., Enhanced Effect of Mesoporous Silica on Base-Catalyzed Aldol Reaction. *Chemistry Letters* **2003**, *32* (3), 234-235.
49. Collier, V. E.; Ellebracht, N. C.; Lindy, G. I.; Moschetta, E. G.; Jones, C. W., Kinetic and Mechanistic Examination of Acid–Base Bifunctional Aminosilica Catalysts in Aldol and Nitroaldol Condensations. *ACS Catalysis* **2016**, *6* (1), 460-468.
50. Mahrwald, R., *Aldol Reactions*. Springer Science & Business Media: 2009.
51. Eder, U.; Sauer, G.; Wiechert, R., New type of asymmetric cyclization to optically active steroid CD partial structures. *Angewandte Chemie International Edition in English* **1971**, *10* (7), 496-497.
52. Hajos, Z. G.; Parrish, D. R., Asymmetric synthesis of optically active polycyclic organic compounds. *German patent DE* **1971**, *2102623*.
53. Hajos, Z. G.; Parrish, D. R., Asymmetric synthesis of bicyclic intermediates of natural product chemistry. *The Journal of Organic Chemistry* **1974**, *39* (12), 1615-1621.
54. List, B.; Lerner, R. A.; Barbas, C. F., Proline-catalyzed direct asymmetric aldol reactions. *Journal of the American Chemical Society* **2000**, *122* (10), 2395-2396.
55. Schmid, M. B.; Zeitler, K.; Gschwind, R. M., The elusive enamine intermediate in proline-catalyzed aldol reactions: NMR detection, formation pathway, and stabilization trends. *Angewandte Chemie International Edition* **2010**, *49* (29), 4997-5003.
56. Allemann, C.; Gordillo, R.; Clemente, F. R.; Cheong, P. H.-Y.; Houk, K., Theory of asymmetric organocatalysis of aldol and related reactions: Rationalizations and predictions. *Accounts of chemical research* **2004**, *37* (8), 558-569.
57. Sakthivel, K.; Notz, W.; Bui, T.; Barbas, C. F., Amino acid catalyzed direct asymmetric aldol reactions: a bioorganic approach to catalytic asymmetric carbon-carbon bond-forming reactions. *Journal of the American Chemical Society* **2001**, *123* (22), 5260-5267.
58. Córdova, A.; Zou, W.; Ibrahim, I.; Reyes, E.; Engqvist, M.; Liao, W.-W., Acyclic amino acid-catalyzed direct asymmetric aldol reactions: alanine, the simplest stereoselective organocatalyst. *Chemical Communications* **2005**, (28), 3586-3588.
59. Dumitriu, E.; Hulea, V.; Fechet, I.; Auroux, A.; Lacaze, J.-F.; Guimon, C., The aldol condensation of lower aldehydes over MFI zeolites with different acidic properties. *Microporous and Mesoporous Materials* **2001**, *43* (3), 341-359.
60. Ungureanu, A.; Royer, S.; Hoang, T. V.; Trong On, D.; Dumitriu, E.; Kaliaguine, S., Aldol condensation of aldehydes over semicrystalline zeolitic-mesoporous UL-ZSM-5. *Microporous and Mesoporous Materials* **2005**, *84* (1-3), 283-296.
61. Chang, Y.-C.; Ko, A.-N., Vapor phase reactions of acetaldehyde over type X zeolites. *Applied Catalysis A: General* **2000**, *190* (1-2), 149-155.
62. Kikhtyanin, O.; Kelbichová, V.; Vitvarová, D.; Kubů, M.; Kubička, D., Aldol condensation of furfural and acetone on zeolites. *Catalysis Today* **2014**, *227*, 154-162.
63. Rode, E. J.; Gee, P. E.; Marquez, L. N.; Uemura, T.; Bazargani, M., Aldol condensation of butanal over alkali metal zeolites. *Catalysis letters* **1991**, *9* (1-2), 103-113.
64. Hora, L.; Kikhtyanin, O.; Čapek, L.; Bortnovskiy, O.; Kubička, D., Comparative study of physico-chemical properties of laboratory and industrially prepared layered double hydroxides and their behavior in aldol condensation of furfural and acetone. *Catalysis Today* **2015**, *241*, 221-230.
65. Hora, L.; Kelbichová, V.; Kikhtyanin, O.; Bortnovskiy, O.; Kubička, D., Aldol condensation of furfural and acetone over Mg Al layered double hydroxides and mixed oxides. *Catalysis Today* **2014**, *223*, 138-147.
66. Kikhtyanin, O.; Tišler, Z.; Velvarská, R.; Kubička, D., Reconstructed Mg-Al hydrotalcites prepared by using different rehydration and drying time: Physico-chemical properties and catalytic performance in aldol condensation. *Applied Catalysis A: General* **2017**, *536*, 85-96.
67. Tichit, D.; Bennani, M. N.; Figueras, F.; Tessier, R.; Kervennal, J., Aldol condensation of acetone over layered double hydroxides of the meixnerite type. *Applied Clay Science* **1998**, *13* (5-6), 401-415.

68. Cueto, J.; Faba, L.; Díaz, E.; Ordóñez, S., Performance of basic mixed oxides for aqueous-phase 5-hydroxymethylfurfural-acetone aldol condensation. *Applied Catalysis B: Environmental* **2017**, *201*, 221-231.
69. Faba, L.; Díaz, E.; Ordóñez, S., Aqueous-phase furfural-acetone aldol condensation over basic mixed oxides. *Applied Catalysis B: Environmental* **2012**, *113–114*, 201-211.
70. Tichit, D.; Lutić, D.; Coq, B.; Durand, R.; Teissier, R., The aldol condensation of acetaldehyde and heptanal on hydrotalcite-type catalysts. *Journal of Catalysis* **2003**, *219* (1), 167-175.
71. Rives, V., *Layered double hydroxides: present and future*. Nova Publishers: 2001.
72. Debecker, D. P.; Gaigneaux, E. M.; Busca, G., Exploring, tuning, and exploiting the basicity of hydrotalcites for applications in heterogeneous catalysis. *Chemistry—A European Journal* **2009**, *15* (16), 3920-3935.
73. Abelló, S.; Vijaya-Shankar, D.; Pérez-Ramírez, J., Stability, reutilization, and scalability of activated hydrotalcites in aldol condensation. *Applied Catalysis A: General* **2008**, *342* (1), 119-125.
74. Kikhtyanin, O.; Lesnik, E.; Kubička, D., The occurrence of Cannizzaro reaction over Mg-Al hydrotalcites. *Applied Catalysis A: General* **2016**, *525*, 215-225.
75. Vansant, E. F.; Van Der Voort, P.; Vrancken, K. C., *Characterization and chemical modification of the silica surface*. Elsevier: 1995; Vol. 93.
76. Der Voort, P. V.; Vansant, E., Silylation of the silica surface a review. *Journal of liquid chromatography & related technologies* **1996**, *19* (17-18), 2723-2752.
77. Blitz, J.; Murthy, R. S.; Leyden, D., Ammonia-catalyzed silylation reactions of Cab-O-Sil with methoxymethylsilanes. *Journal of the American Chemical Society* **1987**, *109* (23), 7141-7145.
78. Blitz, J. P.; Murthy, R. S.; Leyden, D. E., Studies of silylation of Cab-O-Sil with methoxymethylsilanes by diffuse reflectance FTIR spectroscopy. *Journal of colloid and interface science* **1988**, *121* (1), 63-69.
79. Van Der Voort, P.; Vercauteren, S.; Peeters, K.; Vansant, E. F., Some precautions when determining the silanol number, using chemical modification with methylchlorosilanes. *Journal of colloid and interface science* **1993**, *157* (2), 518-519.
80. Anwander, R.; Nagl, I.; Widenmeyer, M.; Engelhardt, G.; Groeger, O.; Palm, C.; Röser, T., Surface characterization and functionalization of MCM-41 silicas via silazane silylation. *The Journal of Physical Chemistry B* **2000**, *104* (15), 3532-3544.
81. Takei, T.; Yamazaki, A.; Watanabe, T.; Chikazawa, M., Water adsorption properties on porous silica glass surface modified by trimethylsilyl groups. *Journal of colloid and interface science* **1997**, *188* (2), 409-414.
82. Tatsumi, T.; Koyano, K.; Tanaka, Y.; Nakata, S., Stabilization of M41S materials by trimethylsilylation. In *Studies in Surface Science and Catalysis*, Elsevier: 1998; Vol. 117, pp 143-150.
83. Cheng, S.; Wang, X.; Chen, S.-Y., Applications of amine-functionalized mesoporous silica in fine chemical synthesis. *Topics in Catalysis* **2009**, *52* (6-7), 681-687.
84. Chong, A. M.; Zhao, X.; Kustedjo, A. T.; Qiao, S., Functionalization of large-pore mesoporous silicas with organosilanes by direct synthesis. *Microporous and Mesoporous Materials* **2004**, *72* (1), 33-42.
85. Kandel, K.; Althaus, S. M.; Peeraphatdit, C.; Kobayashi, T.; Trewyn, B. G.; Pruski, M.; Slowing, I. I., Substrate inhibition in the heterogeneous catalyzed aldol condensation: A mechanistic study of supported organocatalysts. *Journal of Catalysis* **2012**, *291*, 63-68.
86. Shylesh, S.; Hanna, D.; Gomes, J.; Krishna, S.; Canlas, C. G.; Head-Gordon, M.; Bell, A. T., Tailoring the Cooperative Acid–Base Effects in Silica-Supported Amine Catalysts: Applications in the Continuous Gas-Phase Self-Condensation of n-Butanal. *ChemCatChem* **2014**, *6* (5), 1283-1290.
87. Lauwaert, J.; De Canck, E.; Esquivel, D.; Van Der Voort, P.; Thybaut, J. W.; Marin, G. B., Effects of amine structure and base strength on acid–base cooperative aldol condensation. *Catalysis Today* **2015**, *246*, 35-45.
88. Zeidan, R. K.; Davis, M. E., The effect of acid–base pairing on catalysis: An efficient acid–base functionalized catalyst for aldol condensation. *Journal of Catalysis* **2007**, *247* (2), 379-382.

89. Hruby, S. L.; Shanks, B. H., Acid–base cooperativity in condensation reactions with functionalized mesoporous silica catalysts. *Journal of Catalysis* **2009**, *263* (1), 181-188.
90. Kim, K. C.; Moschetta, E. G.; Jones, C. W.; Jang, S. S., Molecular Dynamics Simulations of Aldol Condensation Catalyzed by Alkylamine-Functionalized Crystalline Silica Surfaces. *Journal of the American Chemical Society* **2016**, *138* (24), 7664-7672.
91. Brunelli, N. A.; Didas, S. A.; Venkatasubbaiah, K.; Jones, C. W., Tuning cooperativity by controlling the linker length of silica-supported amines in catalysis and CO₂ capture. *Journal of the American Chemical Society* **2012**, *134* (34), 13950-13953.
92. Brunelli, N. A.; Venkatasubbaiah, K.; Jones, C. W., Cooperative catalysis with acid–base bifunctional mesoporous silica: impact of grafting and co-condensation synthesis methods on material structure and catalytic properties. *Chemistry of Materials* **2012**, *24* (13), 2433-2442.
93. Zeidan, R. K.; Hwang, S. J.; Davis, M. E., Multifunctional Heterogeneous Catalysts: SBA-15-Containing Primary Amines and Sulfonic Acids. *Angewandte Chemie International Edition* **2006**, *45* (38), 6332-6335.
94. Lauwaert, J.; Moschetta, E. G.; Van Der Voort, P.; Thybaut, J. W.; Jones, C. W.; Marin, G. B., Spatial arrangement and acid strength effects on acid–base cooperatively catalyzed aldol condensation on aminosilica materials. *Journal of Catalysis* **2015**, *325*, 19-25.
95. Massi, A.; Cavazzini, A.; Del Zoppo, L.; Pandoli, O.; Costa, V.; Pasti, L.; Giovannini, P. P., Toward the optimization of continuous-flow aldol and α -amination reactions by means of proline-functionalized silicon packed-bed microreactors. *Tetrahedron Letters* **2011**, *52* (5), 619-622.
96. Kubota, Y.; Yamaguchi, H.; Yamada, T.; Inagaki, S.; Sugi, Y.; Tatsumi, T., Further Investigations on the Promoting Effect of Mesoporous Silica on Base-Catalyzed Aldol Reaction. *Topics in Catalysis* **2010**, *53* (7-10), 492-499.
97. Xie, Y.; Sharma, K. K.; Anan, A.; Wang, G.; Biradar, A. V.; Asefa, T., Efficient solid-base catalysts for aldol reaction by optimizing the density and type of organoamine groups on nanoporous silica. *Journal of Catalysis* **2009**, *265* (2), 131-140.
98. De Vylder, A.; Lauwaert, J.; Sabbe, M. K.; Reyniers, M.-F.; De Clercq, J.; Van Der Voort, P.; Thybaut, J. W., Rational Design of Nucleophilic Amine Sites via Computational Probing of Steric and Electronic Effects. *Catalysis Today* **2019**.
99. Yu, X.; Yu, X.; Wu, S.; Liu, B.; Liu, H.; Guan, J.; Kan, Q., The effect of the distance between acidic site and basic site immobilized on mesoporous solid on the activity in catalyzing aldol condensation. *Journal of Solid State Chemistry* **2011**, *184* (2), 289-295.
100. Xie, J.; Ellebracht, N. C.; Jones, C. W., Inter- and Intramolecular Cooperativity Effects in Alkanolamine-Based Acid–Base Heterogeneous Organocatalysts. *ACS Omega* **2019**, *4* (1), 1110-1117.
101. Asefa, T.; MacLachlan, M. J.; Coombs, N.; Ozin, G. A., Periodic mesoporous organosilicas with organic groups inside the channel walls. *Nature* **1999**, *402* (6764), 867.
102. Inagaki, S.; Guan, S.; Fukushima, Y.; Ohsuna, T.; Terasaki, O., Novel mesoporous materials with a uniform distribution of organic groups and inorganic oxide in their frameworks. *Journal of the American Chemical Society* **1999**, *121* (41), 9611-9614.
103. Melde, B. J.; Holland, B. T.; Blanford, C. F.; Stein, A., Mesoporous sieves with unified hybrid inorganic/organic frameworks. *Chemistry of Materials* **1999**, *11* (11), 3302-3308.
104. Van Der Voort, P.; Esquivel, D.; De Canck, E.; Goethals, F.; Van Driessche, I.; Romero-Salguero, F. J., Periodic mesoporous organosilicas: from simple to complex bridges; a comprehensive overview of functions, morphologies and applications. *Chemical Society Reviews* **2013**, *42* (9), 3913-3955.
105. Goethals, F.; Meeus, B.; Verberckmoes, A.; Van Der Voort, P.; Van Driessche, I., Hydrophobic high quality ring PMOs with an extremely high stability. *Journal of Materials Chemistry* **2010**, *20* (9), 1709-1716.
106. Smeulders, G.; Meynen, V.; Silvestre-Albero, A.; Houthoofd, K.; Mertens, M.; Silvestre-Albero, J.; Martens, J. A.; Cool, P., The impact of framework organic functional groups on the hydrophobicity and overall stability of mesoporous silica materials. *Materials Chemistry and Physics* **2012**, *132* (2-3), 1077-1088.

107. Hoffmann, F.; Cornelius, M.; Morell, J.; Fröba, M., Silica-based mesoporous organic–inorganic hybrid materials. *Angewandte Chemie International Edition* **2006**, *45* (20), 3216-3251.
108. Rebbin, V.; Schmidt, R.; Fröba, M., Spherical particles of phenylene-bridged periodic mesoporous organosilica for high-performance liquid chromatography. *Angewandte Chemie International Edition* **2006**, *45* (31), 5210-5214.
109. Carpio, A.; Esquivel, D.; Arce, L.; Romero-Salguero, F. J.; Van Der Voort, P.; Jiménez-Sanchidrián, C.; Válcárcel, M., Evaluation of phenylene-bridged periodic mesoporous organosilica as a stationary phase for solid phase extraction. *Journal of Chromatography A* **2014**, *1370*, 25-32.
110. Goethals, F.; Ciofi, I.; Madia, O.; Vanstreels, K.; Baklanov, M. R.; Detavernier, C.; Van Der Voort, P.; Van Driessche, I., Ultra-low-k cyclic carbon-bridged PMO films with a high chemical resistance. *Journal of Materials Chemistry* **2012**, *22* (17), 8281-8286.
111. Van Der Voort, P.; Vercaemst, C.; Schaubroeck, D.; Verpoort, F., Ordered mesoporous materials at the beginning of the third millennium: new strategies to create hybrid and non-siliceous variants. *Physical Chemistry Chemical Physics* **2008**, *10* (3), 347-360.
112. Kuschel, A.; Polarz, S., Effects of primary and secondary surface groups in enantioselective catalysis using nanoporous materials with chiral walls. *Journal of the American Chemical Society* **2010**, *132* (18), 6558-6565.
113. Lauwaert, J.; Ouwehand, J.; De Clercq, J.; Cool, P.; Van Der Voort, P.; Thybaut, J. W., Tuning component enrichment in amino acid functionalized (organo)silicas. *Catalysis Communications* **2017**, *88*, 85-89.
114. Ouwehand, J.; Lauwaert, J.; Esquivel, D.; Hendrickx, K.; Van Speybroeck, V.; Thybaut, J. W.; Van Der Voort, P., Facile Synthesis of Cooperative Acid–Base Catalysts by Clicking Cysteine and Cysteamine on an Ethylene-Bridged Periodic Mesoporous Organosilica. *European Journal of Inorganic Chemistry* **2016**.
115. Huybrechts, W.; Lauwaert, J.; De Vylder, A.; Mertens, M.; Mali, G.; Thybaut, J. W.; Van Der Voort, P.; Cool, P., Synthesis of L-serine modified benzene bridged periodic mesoporous organosilica and its catalytic performance towards aldol condensations. *Microporous and Mesoporous Materials* **2017**, *251*, 1-8.
116. Ide, M.; El-Roz, M.; De Canck, E.; Vicente, A.; Planckaert, T.; Bogaerts, T.; Van Driessche, I.; Lynen, F.; Van Speybroeck, V.; Thybaut-Starzyk, F.; Van Der Voort, P., Quantification of silanol sites for the most common mesoporous ordered silicas and organosilicas: total versus accessible silanols. *Physical Chemistry Chemical Physics* **2013**, *15* (2), 642-650.
117. Lowe, A. B., Thiol-ene “click” reactions and recent applications in polymer and materials synthesis. *Polymer Chemistry* **2010**, *1* (1), 17-36.
118. Benaglia, M.; Puglisi, A.; Cozzi, F., Polymer-supported organic catalysts. *Chemical reviews* **2003**, *103* (9), 3401-3430.
119. Harmer, M. A.; Sun, Q., Solid acid catalysis using ion-exchange resins. *Applied Catalysis A: General* **2001**, *221* (1-2), 45-62.
120. Van Vaerenbergh, B.; Lauwaert, J.; Bert, W.; Thybaut, J. W.; De Clercq, J.; Vermeir, P., Effect of Ion Exchange Resin Functionality on Catalytic Activity and Leaching of Palladium Nanoparticles in Suzuki Cross-Coupling Reactions. *ChemCatChem* **2017**, *9* (3), 451-457.
121. Meenakshi, S.; Viswanathan, N., Identification of selective ion-exchange resin for fluoride sorption. *Journal of colloid and interface science* **2007**, *308* (2), 438-450.
122. Ishihara, K.; Hasegawa, A.; Yamamoto, H., Polystyrene-Bound Tetrafluorophenylbis (triflyl) methane as an Organic-Solvent-Swellable and Strong Brønsted Acid Catalyst. *Angewandte Chemie* **2001**, *113* (21), 4201-4203.
123. Mazzotti, M.; Neri, B.; Gelosa, D.; Kruglov, A.; Morbidelli, M., Kinetics of liquid-phase esterification catalyzed by acidic resins. *Industrial & engineering chemistry research* **1997**, *36* (1), 3-10.
124. Pal, R.; Sarkar, T.; Khasnobis, S., Amberlyst-15 in organic synthesis. *Arkivoc* **2012**, *1*, 570-609.
125. Harmer, M. A.; Sun, Q., Solid acid catalysis using ion-exchange resins. *Applied Catalysis A: General* **2001**, *221* (1), 45-62.

126. Lahyani, A.; Chtourou, M.; Frikha, M. H.; Trabelsi, M., Amberlyst-15 and Amberlite-200C: Efficient catalysts for aldol and cross-aldol condensation under ultrasound irradiation. *Ultrasonics Sonochemistry* **2013**, *20* (5), 1296-1301.
127. Muylaert, I.; Verberckmoes, A.; Spileers, J.; Demuynck, A.; Peng, L.; De Clippel, F.; Sels, B.; Van Der Voort, P., Synthesis of sulphonated mesoporous phenolic resins and their application in esterification and asymmetric aldol reactions. *Materials Chemistry and Physics* **2013**, *138* (1), 131-139.
128. Schütz, J.; Bonrath, W.; Pressel, Y.; Ferfecki, E.; Topp, K.-D., Aldol Condensations Catalysed by Basic Anion Exchange Resins. *ChemCatChem* **2016**, *8* (23), 3584-3591.
129. Podrebarac, G. G.; Ng, F. T. T.; Rempel, G. L., A kinetic study of the aldol condensation of acetone using an anion exchange resin catalyst. *Chemical Engineering Science* **1997**, *52* (17), 2991-3002.
130. Kunin, R.; Barry, R. E., Carboxylic, Weak Acid Type, Cation Exchange Resin. *Industrial & Engineering Chemistry* **1949**, *41* (6), 1269-1272.
131. Pyo, S.-H.; Hedström, M.; Lundmark, S.; Rehnberg, N.; Hatti-Kaul, R., Self- and Cross-Aldol Condensation of Propanal Catalyzed by Anion-Exchange Resins in Aqueous Media. *Organic Process Research & Development* **2011**, *15* (3), 631-637.
132. Serra-Holm, V.; Salmi, T.; Mäki-Arvela, P.; Paatero, E.; Lindfors, L. P., Comparison of Activity and Selectivity of Weakly Basic Anion-Exchange Catalysts for the Aldolization of Butyraldehyde with Formaldehyde. *Organic Process Research & Development* **2001**, *5* (4), 368-375.
133. Mestres, R., A green look at the aldol reaction. *Green Chemistry* **2004**, *6* (12), 583-603.
134. Serra-Holm, V.; Salmi, T.; Multamäki, J.; Reinik, J.; Mäki-Arvela, P.; Sjöholm, R.; Lindfors, L. P., Aldolization of butyraldehyde with formaldehyde over a commercial anion-exchange resin — kinetics and selectivity aspects. *Applied Catalysis A: General* **2000**, *198* (1), 207-221.
135. Hoyt, C. B.; Lee, L. C.; Cohen, A. E.; Weck, M.; Jones, C. W., Bifunctional Polymer Architectures for Cooperative Catalysis: Tunable Acid–Base Polymers for Aldol Condensation. *ChemCatChem* **2017**, *9* (1), 137-143.
136. Reichardt, C.; Welton, T., *Solvents and solvent effects in organic chemistry*. John Wiley & Sons: 2011.
137. Reichardt, C., Solvents and solvent effects: an introduction. *Organic process research & development* **2007**, *11* (1), 105-113.
138. Bass, J. D.; Solovoyov, A.; Pascall, A. J.; Katz, A., Acid-base bifunctional and dielectric outer-sphere effects in heterogeneous catalysis: A comparative investigation of model primary amine catalysts. *Journal of the American Chemical Society* **2006**, *128* (11), 3737-3747.
139. Sievers, C.; Noda, Y.; Qi, L.; Albuquerque, E. M.; Rioux, R. M.; Scott, S. L., Phenomena affecting catalytic reactions at solid–liquid interfaces. *ACS Catalysis* **2016**, *6* (12), 8286-8307.
140. Alam, T. M.; Hibbs, M. R., Characterization of heterogeneous solvent diffusion environments in anion exchange membranes. *Macromolecules* **2014**, *47* (3), 1073-1084.
141. Sainio, T.; Laatikainen, M.; Paatero, E., Phase equilibria in solvent mixture–ion exchange resin catalyst systems. *Fluid Phase Equilibria* **2004**, *218* (2), 269-283.
142. Mase, N.; Nakai, Y.; Ohara, N.; Yoda, H.; Takabe, K.; Tanaka, F.; Barbas, C. F., Organocatalytic direct asymmetric aldol reactions in water. *Journal of the American Chemical Society* **2006**, *128* (3), 734-735.
143. Córdova, A.; Notz, W.; Barbas III, C. F., Direct organocatalytic aldol reactions in buffered aqueous media. *Chemical Communications* **2002**, (24), 3024-3025.
144. Zotova, N.; Franzke, A.; Armstrong, A.; Blackmond, D. G., Clarification of the role of water in proline-mediated aldol reactions. *Journal of the American Chemical Society* **2007**, *129* (49), 15100-15101.
145. Chanda, A.; Fokin, V. V., Organic Synthesis “On Water”. *Chemical Reviews* **2009**, *109* (2), 725-748.
146. Butler, R. N.; Coyne, A. G., Water: Nature’s Reaction Enforcer—Comparative Effects for Organic Synthesis “In-Water” and “On-Water”. *Chemical Reviews* **2010**, *110* (10), 6302-6337.

147. Torii, H.; Nakadai, M.; Ishihara, K.; Saito, S.; Yamamoto, H., Asymmetric Direct Aldol Reaction Assisted by Water and a Proline-Derived Tetrazole Catalyst. *Angewandte Chemie International Edition* **2004**, *43* (15), 1983-1986.
148. Pirrung, M. C., Acceleration of organic reactions through aqueous solvent effects. *Chemistry—A European Journal* **2006**, *12* (5), 1312-1317.
149. Kandel, K.; Althaus, S. M.; Peeraphatdit, C.; Kobayashi, T.; Trewyn, B. G.; Pruski, M.; Slowing, I. I., Solvent-Induced Reversal of Activities between Two Closely Related Heterogeneous Catalysts in the Aldol Reaction. *ACS Catalysis* **2013**, *3* (2), 265-271.
150. Singappuli-Arachchige, D.; Kobayashi, T.; Wang, Z.; Burkhov, S. J.; Smith, E. A.; Pruski, M.; Slowing, I. I., Interfacial Control of Catalytic Activity in the Aldol Condensation: Combining the Effects of Hydrophobic Environments and Water. *ACS Catalysis* **2019**.
151. An, Z.; Guo, Y.; Zhao, L.; Li, Z.; He, J., 1-Proline-Grafted Mesoporous Silica with Alternating Hydrophobic and Hydrophilic Blocks to Promote Direct Asymmetric Aldol and Knoevenagel–Michael Cascade Reactions. *ACS Catalysis* **2014**, *4* (8), 2566-2576.

Chapter 2

Computational procedures

To gain a more fundamental insight into the chemical problems encountered in this work, molecular modeling is performed using computational chemistry. This branch of chemistry uses mathematical models from theoretical chemistry, implemented in computer software, to describe and predict the properties of molecules. Depending on the size of the chemical system, a wide variety of such kind of theoretical models can be applied, ranging from (semi-)empirical parameterized models to models based on the fundamentals of quantum mechanics, i.e. the Schrödinger equation. In this work, the focus is on the last type, and a brief introduction into the theoretical background is given in this chapter. The main purpose, however, is to provide an application oriented understanding rather than a purist theoretical derivation. Readers who have also an affinity towards the latter are referred to work by Szabo and Ostlund¹ on wave function methods and Parr and Yang² on density functional theory.

2.1 Fundamentals of quantum chemistry

Quantum mechanics states that the energy, and other related properties of a molecule, may be obtained by solving the time-independent, non-relativistic^a Schrödinger equation³:

$$\left(-\frac{\hbar^2}{2m} \nabla^2 + V(\mathbf{r}) \right) \Psi(\mathbf{r}) = E\Psi(\mathbf{r}) \quad (2.1)$$

In this equation, $\Psi(\mathbf{r})$ is the wave function, $V(\mathbf{r})$ the potential, and E the energy of the system that is described by this wave function. While the term $\Psi(\mathbf{r})$ itself does not have any direct physical meaning, the product with its complex conjugate $\Psi^H\Psi$ has units of probability density. The term between brackets is called the Hamiltonian operator \hat{H} and E is a scalar value of the system energy. It should be noted that, while there are many wave functions $\Psi(\mathbf{r})$ which satisfy equation (2.1), there is only one wave function for which E is minimal⁴: this is the ground state.

^a Relativistic effects are neglected in this work, which is justifiable for the first three rows in the periodic table (i.e. $Z < 36$).

Other wave functions will always lead to a higher energy, which is known as the variational principle.

Only for non-interacting one-electron systems, such as the hydrogen atom, an algebraic solution to equation (2.1) is possible. For a chemical system consisting of multiple atoms, the Hamiltonian readily becomes much more complex:

$$\hat{H} = \hat{T}_e + \hat{T}_n + \hat{V}_{ne} + \hat{V}_{ee} + \hat{V}_{nn} \quad (2.2)$$

The Hamiltonian operator now consists of terms for the kinetic energy of the electrons (T_e) and nuclei (\hat{T}_n), the potential energy between nuclei and electrons (\hat{V}_{ne}), between electrons and electrons (\hat{V}_{ee}), and between nuclei and nuclei (\hat{V}_{nn}). Due to these mutual interactions, an exact solution is all but trivial. Hence, one of the first approximations made to solve this equation is the Born-Oppenheimer approximation^{5,6}, in which it is assumed that the motion of nuclei and electrons in a molecule can be decoupled, with the nuclei stationary at certain positions in space. This allows the wave function to be separated into an electronic and nuclear part:

$$\Psi_{\text{total}} = \psi_{\text{electronic}} \psi_{\text{nuclear}} \quad (2.3)$$

For a given set of nuclear coordinates, this results in a zero nuclear kinetic energy ($\hat{T}_n = 0$) and a constant nuclear-nuclear repulsion term ($\hat{V}_{nn} = \text{constant}$). Thus, the complete Hamiltonian can be reduced to the so-called electronic Hamiltonian \hat{H}_{elec} :

$$\hat{H}_{\text{elec}} = \hat{T}_e + \hat{V}_{ne} + \hat{V}_{ee} \quad (2.4)$$

The solution of the Schrödinger equation (2.1) with \hat{H}_{elec} is the electronic wave function Ψ_{elec} and the electronic energy E_{elec} , which both parametrically depend on the nuclear positions. The total energy E_{tot} is then the sum of E_{elec} and the constant nuclear-nuclear repulsion term E_{nn} . Each different set of nuclear coordinates thus leads to a different total energy, which defines an n-dimensional Potential Energy Surface (PES)⁴. The minimum of this PES is called the minimum energy conformation, a saddle-point is referred to as a transition state.

2.2 Molecular Orbital Theory

The simplest approximation to the complicated many-electron wave function consists of approximating the wave function Ψ_{elec} by a product of N one-electron wave functions⁷ χ_i :

$$\Psi_{\text{elec}}(r_1, r_2, \dots, r_N) \approx \chi_1(r_1) \chi_2(r_2) \dots \chi_N(r_N) \quad (2.5)$$

In this equation, N is the number of electrons and χ_i are molecular orbitals, consisting of a spatial part and a spin part. These molecular orbitals χ_i are linear combination of atomic orbitals φ_j :

$$\chi_i(\mathbf{r}_i) = \sum_{j=1}^N a_{ij} \varphi_j(\mathbf{r}_i) \quad (2.6)$$

The atomic orbitals φ_j are, in turn, constructed using basis functions which are often formed by a linear combination of Gaussian functions. A group of these basis functions is referred to as a basis set, and is discussed in more detail in paragraph 2.2.3.

Expressing the wave function as equation (2.5), however, fails to satisfy the antisymmetry principle⁸. This principle is one of the postulates of quantum mechanics, which mathematically states that the total wave function must change sign upon interchanging any two electrons. The problem can be overcome by arranging the molecular orbitals in a so-called Slater determinant⁹:

$$\Psi_{\text{elec}}(r_1, r_2, \dots, r_N) \approx \frac{1}{\sqrt{N!}} \begin{vmatrix} \chi_1(r_1) & \cdots & \chi_N(r_1) \\ \vdots & \ddots & \vdots \\ \chi_1(r_N) & \cdots & \chi_N(r_N) \end{vmatrix} \quad (2.7)$$

The use of Slater determinants naturally incorporates antisymmetry and, correspondingly, also agrees with the concept of Pauli's Exclusion Principle. Indeed, the Slater determinant changes sign when two electrons are interchanged and vanishes if one of the sets $\{\chi_i\}$ is linearly dependent. In chemical terms, this latter feature is expressed by the fact that no two electrons with the same spin can occupy the same spatial orbital.

2.2.1 Hartree-Fock theory

In the Hartree-Fock theory¹⁰, the N -electron wave function Ψ_{elec} is approximated by a single Slater determinant of N 1-electron molecular orbitals χ_i . In the case of a restricted Hartree-Fock approach, which is applicable in cases with only paired electrons, the problem is redefined into solving the set of $N/2$ Hartree-Fock equations for the spatial orbitals ϕ_i :

$$\hat{F} \phi_i(\mathbf{r}) = \varepsilon_i \phi_i(\mathbf{r}) \quad (2.8)$$

Where ε_i has the physical interpretation of orbital energy and \hat{F} is the one-electron Fock-operator, defined as:

$$\hat{F} = \hat{H} + \hat{V}_{\text{HF}}(i) = \hat{H} + \sum_{j=1}^{N/2} (2\hat{J}_j(i) - \hat{K}_j(i)) \quad (2.9)$$

In this equation, \hat{H} is the one-electron core Hamiltonian which describes the kinetic and potential energy of electron i in the field of the nuclei. $\hat{V}_{\text{HF}}(i)$ is the average repulsive potential experienced by the i^{th} electron due to the remaining $N-1$ electrons and is called the Hartree-Fock potential. In this Fock potential, \hat{J}_j is the Coulomb operator, which defines the potential that an electron i experiences due to the average charge distribution of another electron in spin orbital χ_j . \hat{K}_j is the electron exchange term describing the correlation between electrons with parallel spin, preventing them from being found at the same point in space.

Solving these equations involves evaluating the repulsion that each electron experiences due to the presence of the other electrons¹¹. This means that the HF equations depend on their own solution. Therefore, an iterative ‘self-consistent field’ (SCF) procedure is applied that starts with a ‘guessed’ set of orbitals to eventually determine the best set of orbitals^{12, 13}. The molecular orbitals obtained in this way are then said to be self-consistent with the mean field generated by all the electrons.

The most important shortcoming in the HF theory is that electron-electron repulsion is only included as an average effect, thus ignoring direct electron correlation. Methods that correct for this are known as post-Hartree-Fock methods.

2.2.1.1 Electron correlation

Representing the wave function by a single Slater determinant in the Hartree-Fock theory leads to E_{HF} always being higher than the exact ground state energy E_0 , according to the variational principle⁴. The difference between these two energies is called the correlation energy¹⁴ E_{C} .

$$E_{\text{C}} = E_0 - E_{\text{HF}} \quad (2.10)$$

Electron correlation is mainly caused by the instantaneous repulsion of the electrons, something which is not covered by the mean field Hartree-Fock potential. This has as implication that in the HF theory, electrons often get ‘too close’ to each other because the electrostatic interaction is treated only in an average manner. Consequently, the electron-electron repulsion term is too large, resulting in $E_{\text{HF}} > E_0$. This kind of electron correlation is usually called dynamical electron correlation¹⁵, because it is related to the actual movements of the individual electrons and is known to be a short range effect. On the contrary, static electron correlation is related to the fact that in certain specific circumstances the ground state Slater determinant is not a good approximation to the true ground state. This is, for example, the case in bond breaking situations, where this kind of correlation is often referred to as ‘left-right correlation’¹⁶ because

it describes the effect that if one electron is at the left nucleus, the other will most likely be at the right one. Another cause of static electron correlation is when the molecular ground state is quasi-degenerate with low-lying excited states.

Several advanced methods exist to determine the correlation contributions accurately, and efficiently. These methods are, for example, configuration interaction¹⁷, Møller-Plesset perturbation theory¹⁸ and coupled cluster theory¹⁹ for the dynamic correlation, and multi-configurational SCF methods²⁰ to describe static correlation. All these methods have in common that, instead of considering merely one Slater determinant for the wave function, multiple excited Slater determinants are considered. In theory, it would be possible to express the exact many-electron wave function by taking into account all possible Slater determinants obtained by exciting all possible electrons to all possible virtual orbitals in an infinite basis set. This means that this method of considering more excited Slater determinants will systematically lead to a better description of the real wave function. The mathematical details of these post-Hartree-Fock methods are not discussed here, but it is clear that the choice of electron correlation method will primarily depend on the size of the chemical system and the available computational resources.

2.2.2 Density functional theory

Density Functional Theory (DFT) is based on the theory that the ground state of a system is uniquely determined by the electron density ρ , which only depends on 3 spatial coordinates instead of the $3N$ coordinates of the electronic wave function^{21,22}. This allows DFT to be applied to much larger chemical systems than the (post-Hartree-Fock) wave function based methods. The energy of a system is obtained making use of a functional $E[\rho]^b$, expressed as:

$$E[\rho] = T[\rho] + V_{ne}[\rho] + V_{ee}[\rho] = T[\rho] + V_{ne}[\rho] + J[\rho] + E_{ncl}[\rho] \quad (2.11)$$

Equation (2.11) contains T , the functional for the kinetic energy, V_{ne} the potential energy due to the nuclei-electron attraction, and V_{ee} the electron-electron interaction. This latter functional V_{ee} can further be split into J the classical Coulomb interaction and E_{ncl} the non-classical contribution to the electron-electron interaction. Only J and V_{ne} are known functionals, both T and E_{ncl} are unknown functionals.

^b Since ρ is a function, $E[\rho]$ is a function of a function: this is known as a functional.

Kohn and Sham²³ developed a scheme for solving equation (2.11) by first considering the kinetic energy functional T_s in a non-interacting reference system, with a Hamiltonian in which an effective local potential $V_s(\mathbf{r})$ appears.

$$\hat{H}_s = -\frac{1}{2} \sum_i^N \nabla_i^2 + \sum_i^N V_s(\mathbf{r}) \quad (2.12)$$

Since this Hamilton operator does not contain any electron-electron interactions, its ground state wave function is represented by a single Slater determinant containing so-called Kohn-Sham orbitals Φ_i . Relating this non-interacting artificial system to the one we are interested in is now done by choosing the effective potential V_s such that the total density of the KS orbitals equals the ground state density ρ_0 of our real target system of interacting electrons²¹. This, of course, requires an iterative procedure similar to the SCF procedure in the HF method.

$$\rho_s(\mathbf{r}) = \sum_i^N |\Phi_i(\mathbf{r})|^2 = \rho_0(\mathbf{r}) \quad (2.13)$$

Doing this allows to define a non-interacting kinetic energy T_s , resulting in

$$E[\rho] = T_s[\rho] + V_{ne}[\rho] + J[\rho] + E_{XC}[\rho] \quad (2.14)$$

With

$$E_{XC}[\rho] = (T[\rho] - T_s[\rho]) + E_{ncl}[\rho] \quad (2.15)$$

In other words, the exchange-correlation energy E_{XC} is the functional which contains everything that is unknown, i.e., the non-classical quantum-mechanical contributions such as self-interaction correction, exchange and correlation, and the part of the true kinetic energy that is not covered by T_s .

It can be shown^{4, 21} that the effective potential V_s , which is needed to get the correct orbitals of the non-interacting reference system, exactly equals the sum of the potential due to the nuclei, V_{ne} , the classical Coulomb potential, J , and the potential generated by E_{XC} , i.e., V_{XC} . If the explicit forms of all these potentials would be known, V_s would be known and it would be possible to iteratively derive the exact ground state density and the exact ground state energy. Unfortunately, in all real applications, approximations for the unknown functional E_{XC} have to be used.

There exists an abundance of approaches in which the unknown functional E_{XC} is approximated, leading to a plethora of different DFT methods²⁴, each developed for specific fields of application. Specifically, in the local density approximation (LDA), it is assumed that locally the electrons in the system constitute a homogeneous, uniform electron gas². However,

the LDA fails in situations where the density undergoes rapid changes such as in molecules. Thus, an improvement can be made by considering the gradient of the electron density, the so-called generalized gradient approximation (GGA)²⁵. Also hybrid functionals exist, which make use of the Hartree-Fock exact exchange functional combined with correlation terms calculated either with the LDA or the GGA approach. It should be emphasized that due to the approximate nature of the E_{XC} term, DFT methods do not have a systematic way to improve their accuracy.

2.2.3 Basis sets

As mentioned previously, the atomic orbitals that constitute a molecular orbital (equation 2.6) are based on a collection of mathematical functions called a basis set²⁶. For practical application, these mathematical functions, called basis functions, are typically a linear combination of Gaussian functions²⁷ of the general form:

$$\eta = N x^l y^m z^n \exp(-\alpha r^2) \quad (2.16)$$

In this equation, α is an exponent controlling the width of the Gaussian Type Orbital (GTO), i.e., how compact (large α) or diffuse (small α) the resulting orbital is. The integers l , j and k are non-negative values that represent the nature of the orbital and N is a normalization constant. Very large basis sets are especially required when high quality wave functions including electron correlation are the target²¹. In particular, basis functions with added polarization functions (see below) are a necessity. A complete description of the real wave function would require an infinite amount of basis functions, which can be approximated by extrapolation, and is referred to as the complete basis set limit^{28, 29}.

In so-called split-valence basis sets, the valence orbitals are represented by more basis functions than the inner shell orbitals. This is rationalized by the fact that, in chemical reactions, it is the valence electrons that principally affect the bonding. For example in the 6-31+G* basis set, developed by the group of John Pople³⁰, each core atomic orbital is represented by one basis function constructed out of six primitive Gaussians, and a valence orbital by two basis functions, one constructed out of three primitive Gaussians and one constructed out of one. Additionally, the * and the + indicate that, respectively, polarization and diffusion functions have been added. Polarization functions add some flexibility to the basis set so that, for example, molecular orbitals involving the hydrogen atoms can be asymmetric around the hydrogen nucleus. Diffusive functions are very shallow Gaussian basis functions (equation 2.15

with a small value of α), which more accurately represent the ‘tail’ portion of the orbital further away from the nucleus.

While the Pople basis sets are somewhat outdated compared to the newer correlation-consistent basis sets³¹, they remain immensely popular in computational chemistry³², and are used in this work as part of the CBS-QB3 composite method³³.

2.2.4 Quantum chemical composite methods

Composite methods are computational chemistry methods that aim for high thermochemical accuracy, which is typically within 4.18 kJ mol⁻¹ (= 1 kcal mol⁻¹) of the experimental value, by combining the results of several calculations³⁴. The composite method used in this work is the CBS-QB3 method, based on the Complete-Basis-Set (CBS) methods of Petersson and co-workers³³. A key property that distinguishes these systems from other composite methods is the basis set extrapolation to the complete-basis-set limit, thus avoiding basis set incompleteness effects. The CBS-QB3 method for closed-shell systems is composed of the following five steps:

1. A geometry optimization is performed at the B3LYP/6-311G(2d,d,p) level of theory, which then yields the reference geometry
2. A frequency calculation is performed at the B3LYP/6-311G(2d,d,p) level of theory and scaled by 0.9854 to produce the zero-point vibrational energy
3. An MP2/6-311+G(3d2f,2df,2p) calculation is performed and extrapolated to the basis set limit.
4. Calculations at the CCSD(T)/6-31+G(d’) and MP4SDQ/6-31+G(d,p) levels of theory are performed to estimate the effect from higher-order electron correlation.
5. Remaining electron correlation is accounted for by an empirical expression.

The computational efficiency and the high overall accuracy makes CBS-QB3 method of particular interesting for determining very accurate energies for closed-shell systems containing first and second row atoms^{35, 36}.

2.3 Reintroducing nuclear motion in the Hamiltonian

In order to solve the full molecular Schrödinger equation (equation 2.1), it is assumed that that the molecule is semi-rigid, and its nuclear kinetic energy operator \widehat{T}_n is reintroduced²¹.

With a defined potential energy surface (PES), it is possible to formulate and solve the Schrödinger equations for nuclear motion:

$$\left(\widehat{T}_n + \widehat{V}(\mathbf{q})\right)\Omega(\mathbf{q}) = E\Omega(\mathbf{q}) \quad (2.17)$$

With N the number of atoms, m the atomic mass, V the potential energy from the PES as a function of the $3N$ nuclear coordinates \mathbf{q} , and Ω the nuclear wave function. Nuclear motion is classified in three types: translation, rotation, and vibration. This is, respectively, the motion of the center of mass, the motion around the center of mass and the motion of different (sub)parts of the system relative to each other.

2.3.1 Translation

Assuming that no collisions take place, molecular translation can be treated independently from vibration and rotation³⁷. To derive an expression for the translational energy, the Schrödinger equation is solved for a particle of mass m in a 1-dimensional box with sides a , b , and c (equation 2.18). This system describes the translational motion of a single particle confined inside an infinitely deep well from which it cannot escape.

$$\varepsilon_{\text{trans}} = \frac{h^2}{32\pi^2m} \left(\frac{n_x^2}{a^2} + \frac{n_y^2}{b^2} + \frac{n_z^2}{c^2} \right) \quad (2.18)$$

With n_x^2 , n_y^2 and n_z^2 three independent quantum numbers that take integer values from 1 to infinity.

2.3.2 Rotation

To obtain an expression for the rotational energy, it is assumed that the molecular geometry stays fixed during rotation. This approximation is called the rigid rotor approximation. Furthermore, it is assumed that the vibrations are small enough not to significantly influence the mass distribution of the system, allowing to treat external rotation independently from vibrations.

The expression for the allowed rotational energies in the simplest case of a diatomic rigid-rotor³⁷ is:

$$\varepsilon_{\text{rot}} = \frac{\hbar^2}{2I} J(J + 1) \quad (2.19)$$

With J is the total angular momentum quantum number and I the moment of inertia, obtained using classical mechanics. In the case of a general shaped nonlinear molecule, with three

different principal moments of inertia, an exact solution for the rotational energy levels is not possible and approximate solutions are used.

2.3.3 Vibration

The vibrational energy is determined by Hooke's law, under the harmonic oscillator approximation³⁷. The vibrational energy levels are defined as:

$$\varepsilon_{\text{vib}} = \nu \left(i + \frac{1}{2} \right) \quad (2.20)$$

With i starting at zero and running over the different vibrational energy levels, and ν the vibrational frequency calculated by:

$$\nu = \frac{1}{2\pi} \sqrt{\frac{k}{\mu}} \quad (2.21)$$

With k the force constant and μ the reduced mass of the system. The force constant k is determined via the second derivative of the potential energy surface (PES) at the equilibrium bond length. When the system is in a minimum of the PES, all values of k are positive. When it is not in a minimum, one or multiple values of k are negative. A special case is the transition state where exactly one of the force constants is negative, resulting in an imaginary frequency that describes the motion of a col in the PES, as will be further discussed in paragraph 2.5.

In the special case of a simple diatomic molecule, the reduced mass μ is equal to:

$$\mu = \frac{m_1 m_2}{m_1 + m_2} \quad (2.22)$$

When adding a third particle to the system, the problem becomes very complicated and more approximate expressions are used.

2.4 Statistical mechanics

Statistical mechanics relates microscopic properties of particles, obtained from quantum mechanics, to macroscopic thermodynamic properties³⁸. To accomplish this, the concept 'ensemble' is introduced^{37, 39}. This can be seen as a large number of copies of a system, each representing a possible state. The so-called canonical partition function can be directly used to obtain the internal energy U , the enthalpy H , the entropy S , and the Gibbs free energy G , according to the following formulas:

$$U = k_B T^2 \left(\frac{\partial \ln Q}{\partial T} \right)_{N,V} \quad (2.23)$$

$$H = U + PV \quad (2.24)$$

$$S = k_B \ln Q + k_B T \left(\frac{\partial \ln Q}{\partial T} \right)_{N,V} \quad (2.25)$$

$$G = H - TS \quad (2.26)$$

The subscripts associated with the partial derivatives in equations (2.23) and (2.25) implies N and V are held constant during differentiation with respect to T . By assuming an ideal gas, i.e., non-interacting molecules in the ensemble, the partition function Q can be rewritten as a function of the molecular partition functions q :

$$Q(N, V, T) = \frac{[q(V, T)]^N}{N!} \quad (2.27)$$

The molecular partition functions can now be constructed based on their molecular energies in a Boltzmann distribution:

$$q(V, T) = \sum_i g_i e^{\frac{-\varepsilon_i(V)}{k_B T}} \quad (2.28)$$

Where i runs over all energy levels and g_i is the degeneracy of the energy level. For further simplification, the molecular energy is separated into an independent electronic, translational, rotational and vibrational part:

$$\begin{aligned} q(V, T) &= \sum_k g_k e^{\frac{-\varepsilon_{e,k}}{k_B T}} \sum_l g_l e^{\frac{-\varepsilon_{\text{trans},l}(V)}{k_B T}} \sum_m g_m e^{\frac{-\varepsilon_{\text{rot},m}}{k_B T}} \sum_n g_n e^{\frac{-\varepsilon_{\text{vib},n}}{k_B T}} \\ &= q_e(T) q_{\text{trans}}(V, T) q_{\text{rot}}(T) q_{\text{vib}}(T) \end{aligned} \quad (2.29)$$

When working at moderate temperatures, the degeneracy of the ground state is unity and the term $q_e(T)$ is easily evaluated using the ground state energy, obtained from solving the electronic Hamiltonian (equation 2.4). In practice, convention defines the ground state for each energy component with an energy of zero, resulting in $q_e(T) = 1$.

The translational contribution to the partition function is obtained by approximate the sum over the allowed energy levels (equation 2.18) as an integral over l :

$$q_{\text{trans}}(V, T) = \left(\frac{2\pi M k_B T}{h^2} \right)^{\frac{3}{2}} V \quad (2.30)$$

It should be noted that the translational partition function is dependent on the reference volume V derived from the ‘particle-in-a-box’ assumption. This volume is related to the reference state, which can theoretically be chosen completely arbitrarily. However, this typically based on either a pressure p of 1 bar for gas phase reactions, or on a concentration of 1 mol L^{-1} , for liquid phase reactions.

For non-linear molecules, the rotational contribution to the partition function is approximated³⁷ by:

$$q_{\text{rot}}(T) = \frac{\sqrt{\pi I_A I_B I_C}}{\sigma} \left(\frac{8\pi^2 k_B T}{h^2} \right)^{3/2} \quad (2.31)$$

Where I_A , I_B , and I_C are the principal moments of inertia, and σ is the symmetry number.

The vibrational contribution for a polyatomic molecule is evaluated based on the vibrational energies (equation 2.20). Under the harmonic oscillator approximation, and assuming the normal modes are all independent from one another, the following expression is obtained:

$$q_{\text{vib}}(T) = \prod_{n=1}^{n_{\text{vib}}} \left(\frac{1}{1 - e^{-\frac{h\nu_n}{k_B T}}} \right) \quad (2.32)$$

One may wonder what errors may be introduced in equation (2.32), by assuming a harmonic oscillator. In general, it is expected that the weakly hindered torsions are the least well described by the harmonic oscillator⁴⁰. These modes also exhibit the lowest frequencies and, hence, contribute most strongly to the partition function q . In this work, the non-imaginary frequencies below 30 cm^{-1} are therefore raised to this value in order to compensate for the failure of the harmonic oscillator in this region⁴¹.

2.5 Conventional transition state theory

Conventional transition state theory (CTST) is the most frequently used theory for obtaining theoretical rate coefficients. It is based on collision theory⁴², and was put forward by H. Eyring⁴³ and M. Polanyi⁴⁴. The important postulates of this theory are:

- The reacting molecules A and B must form an activated complex $[AB^\ddagger]$ before being converted to product C.
- The energy distribution among the reactant molecules is in accordance with the Boltzmann distribution. It is assumed that, even when the reactants A and B, and product C are not in equilibrium with each other, the activated complex $[AB^\ddagger]$ is in quasi-equilibrium with the reactants.
- Molecular systems that have just overcome the col at $[AB^\ddagger]$ in the direction of the products do not turn back and form reactant molecules again.

Considering the arbitrary reaction from reactants A and B to a product C, the Gibbs free energy as a function of the reaction coordinate is shown in Figure 2-1. In CTST, the situation at the col in the potential energy surface is of particular interest. Consider a dividing surface that passes through the col perpendicular to the reaction path. CTST is concerned with the rate at which systems pass through this dividing surface^c. Consider two parallel dividing surfaces separated by a very small distance δ , as drawn in Figure 2-1. Systems that are within this small distance are activated complexes, such as $[AB^\ddagger]$ in this example. Systems entering the region of thickness δ from the left hand side must exit into the product side and end up as products. Similarly, those entering from the product side must become reactants.

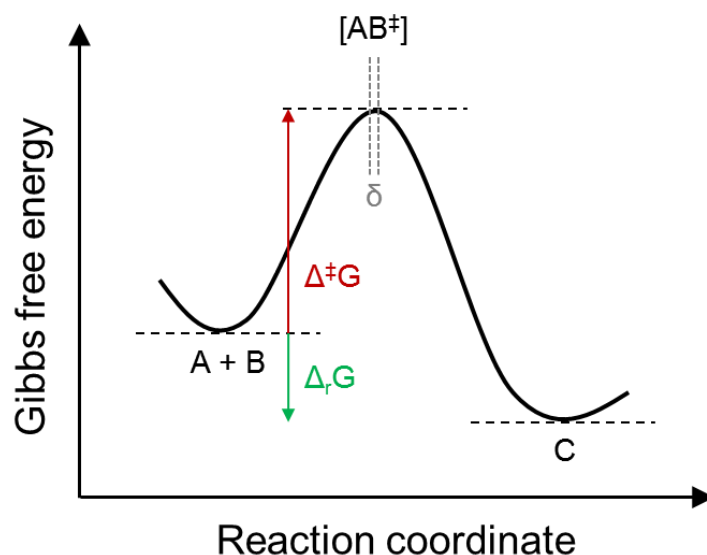


Figure 2-1: Gibbs free energy as function of the reaction coordinate for the reaction $A + B \rightarrow C$. Subscript r refers to the thermodynamic Gibbs free energy, superscript \ddagger refers to the transition state Gibbs free energy.

The equilibrium constant between reactants and transition state may be written as:

^c Contrary to CTST, in variational transition state theory, the position of this dividing surface is optimized to minimize the rate constant.

$$K^\ddagger = \frac{[AB^\ddagger]}{[A][B]} \quad (2.33)$$

The rate for the reaction may then be expressed as follows:

$$\text{Rate} = \nu [AB^\ddagger] = \nu K^\ddagger [A][B] = k [A][B] \quad (2.34)$$

With ν is the frequency of crossing the activation energy barrier and $[AB^\ddagger]$ the concentration of activated complex at the top of the barrier. It can be shown that $\nu = k_B T/h$, which ultimately leads to the Eyring equation (2.35):

$$k = \frac{k_B T}{h} e^{\frac{-\Delta^\ddagger G^\circ}{RT}} \quad (2.35)$$

With $\Delta^\ddagger G^\circ$ the Gibbs free activation energy, as displayed in Figure 2-1. Equation (2.35) is equivalent with equation (2.36) derived with the partition functions q :

$$k_+(T) = \frac{N_A k_B T}{h} \frac{q_{TS}}{\prod q_{\text{reactants}}} e^{\frac{-\Delta E_0}{RT}} \quad (2.36)$$

With ΔE_0 the electronic barrier, excluding zero point vibrational energy. Using the known reaction thermodynamic identity (2.35), $\Delta_r G^\circ$ in Figure 2-1, the reverse reaction rate (equation 2.38) can be derived accordingly.

$$K = e^{\frac{-\Delta_r G^\circ}{RT}} \quad (2.37)$$

$$k_- = \frac{k_+}{K} \quad (2.38)$$

2.6 Solvation effects

The experiments in this work are all performed in the liquid phase, while all computational modeling described above is developed for the gas phase. Modeling the solvent molecules explicitly could be performed to describe the liquid phase⁴⁵. However, due to computational limitations, this is only an option for molecular dynamics or Monte Carlo simulations. Because these simulations often utilize parameterized models, they lack the computational accuracy that is required for this work. Other methods, which can be coupled to high-level quantum mechanical calculations, have been developed to model the influence of the liquid phase on solute molecules.

2.6.1 Polarizable continuum models

The Polarizable Continuum Model (PCM) by Tomasi and coworkers⁴⁶ is one of the most commonly used continuum solvation methods. A calculation proceeds according to Figure 2-2, by first encapsulating the molecule of interest, called the solute. In this example, a spherical encapsulation is used. This shape is then embedded as a cavity in a homogeneous polarizable continuum with a fixed dielectric constant ϵ , which is step 1 in Figure 2-2. Next, the solute's charge distribution is placed in the cavity (step 2 in Figure 2-2). This polarizes the surrounding medium (step 3), which in turn causes a change in the polarization on the solute (step 4). Iteration to self-consistency of the polarization charges is then performed in step 4. This latter procedure is often referred to as a 'Self-Consistent Reaction Field' (SCRF) iteration.

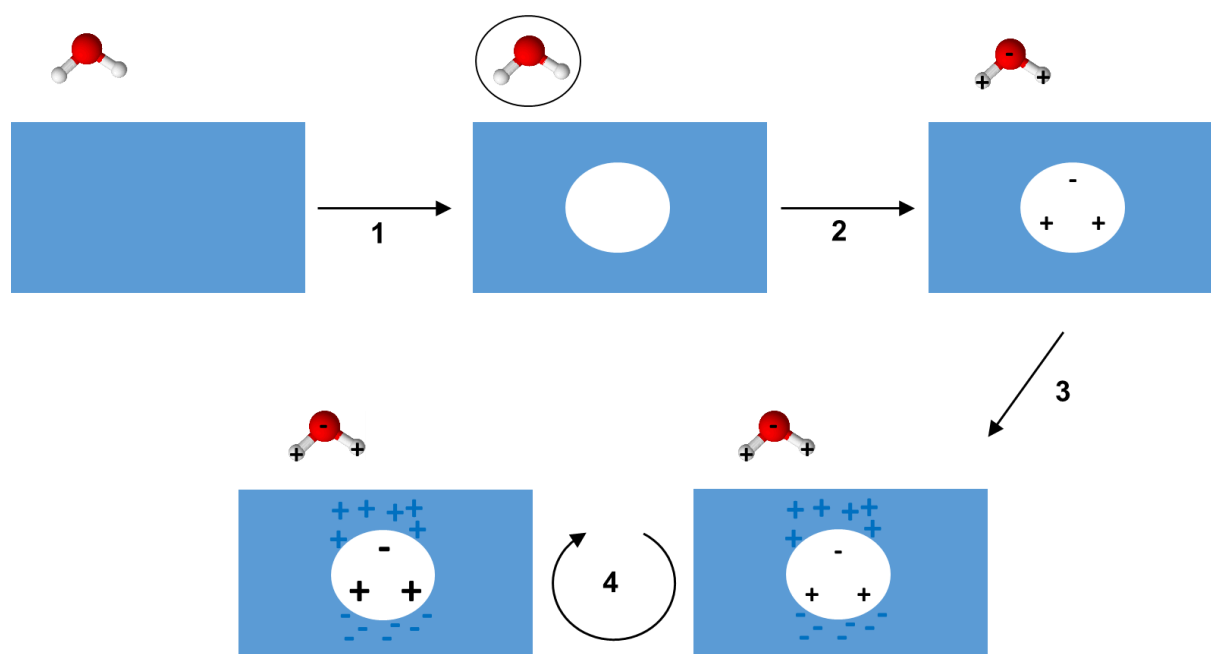


Figure 2-2: Schematic representation of moving a molecule from the gas phase to the liquid phase using the polarizable continuum model. Step 4 is iterated until self-consistency is obtained.

The key difference between PCM models is the choice of type and size of the solvent cavity. Several examples are shown in Figure 2-3, where a spherical or ellipsoidal cavity is the most coarse and simple approximation used by the Onsager model⁴⁷. A more improved version of PCM uses the VdW-surface around the molecules, which is constructed with spheres defined by empirical atomic radii⁴⁶. Another method called Isodensity PCM (IPCM)⁴⁸ uses an isosurface of electron density of the solute, which has the advantage that no empirical atomic radii are required. In the solvent-accessible surface area method, the accessible surface is

created by tracing a solvent probe sphere (Figure 2-3) as it rolls along the van der Waals surface. This smooths out sharp crevices and cusps inherent to the overlapping VdW spheres which would cause convergence issues.

Once a proper cavity has been defined, the polarization energy is then calculated as the interaction between the charge density of the solute and the electrostatic potential.

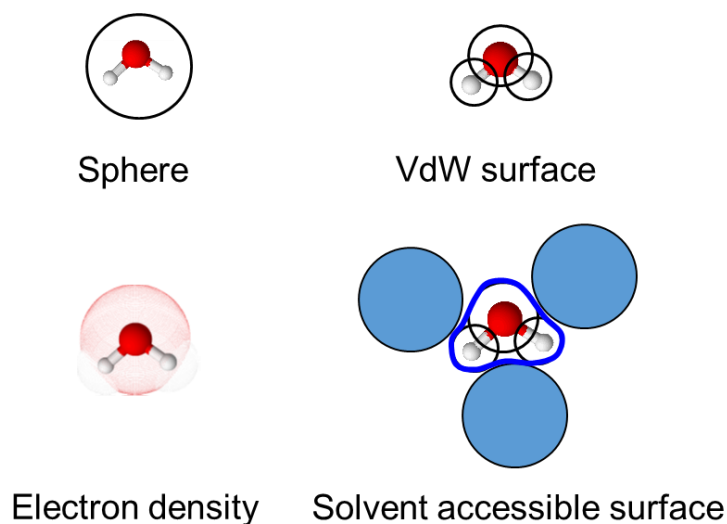


Figure 2-3: Multiple ways to construct the solvent cavity in polarizable continuum models

2.6.2 COSMO-RS

Instead of using the interaction of the solute with a continuum, the conductor-like screening for real solvent (COSMO-RS) model calculates the effects of solvation using the interaction of the molecular surface charges of solute and solvent via statistical thermodynamics starting from an ideal conductor reference frame⁴⁹.

The initial step is a quantum chemical COSMO calculation, which is basically a PCM calculation where the solute cavity is based on the solvent accessible surface, and the solvent is considered an ideal conductor ($\epsilon = \infty$). This allows to obtain a unique screening charge density (σ -profile) for each molecule, as displayed in Figure 2-4 for acetone. It is then assumed that the chemical potential μ in solution can be calculated from the interaction energies of pairwise contacts between surface segments.

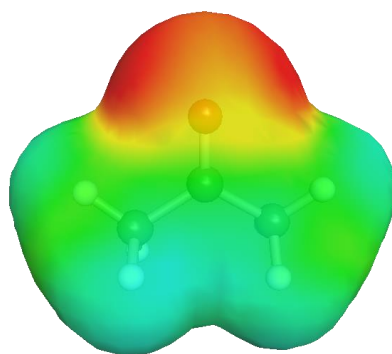


Figure 2-4: Screening charge density (σ -surface) of acetone as calculated by the COSMO method

Each molecule and mixture can be represented by the σ -profile $p(\sigma)$, as displayed in Figure 2-5. In case of a mixture, the σ -profile is the sum of the σ -profiles of the different components weighted with their respective molar fraction.

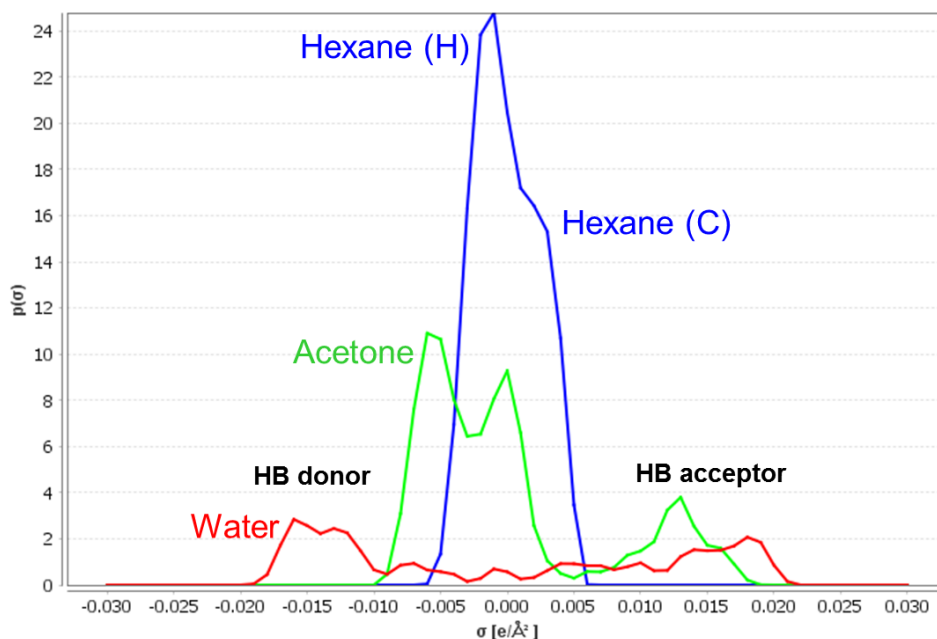


Figure 2-5: Example σ -profile for hexane (blue), acetone (green) and water (red).

Using the σ -profile $p(\sigma)$ of the noninteracting solvent molecules in the ideal conductor reference state, the sigma potential $\mu_S(\sigma)$ of an effective surface segment of area α_{eff} and polarity σ in the ensemble S can be calculated iteratively⁴⁹ according to:

$$\mu_S(\sigma) = -\frac{kT}{\alpha_{\text{eff}}} \ln \left[\int p(\sigma') \exp \left(-\frac{\alpha_{\text{eff}}}{kT} (E_{\text{int}}(\sigma, \sigma') - \mu_S(\sigma')) \right) d\sigma' \right] \quad (2.39)$$

With α_{eff} the effective contact area and E_{int} the pairwise interaction term for contacts between surface segments:

$$E_{\text{int}}(\sigma, \sigma') = E_{\text{misfit}}(\sigma, \sigma') + E_{\text{HB}}(\sigma, \sigma') + E_{\text{vdW}}(\sigma, \sigma') \quad (2.40)$$

Which is composed of

$$E_{\text{misfit}}(\sigma, \sigma') = \frac{\alpha'}{2} (\sigma + \sigma')^2 \quad (2.41)$$

$$E_{\text{HB}}(\sigma, \sigma') = c_{\text{HB}}(T) \min(0; \sigma\sigma' - \sigma_{\text{HB}}^2) \quad (2.42)$$

$$E_{\text{vdW}}(\sigma, \sigma') = \tau_{\text{vdW}} + \tau'_{\text{vdW}} \quad (2.43)$$

In simple words, this σ -potential is a characteristic function of a solvent, or mixture, which specifies how much it is attracted to a surface area of polarity σ . The misfit energy E_{misfit} represents the Coulomb interaction relative to the state in a perfect conductor and is composed of α , an adjustable parameter, and σ and σ' the screening charge densities of the two surface patches in contact. E_{HB} is an interaction energy term dealing with hydrogen-bonding, where σ_{acceptor} and σ_{donor} are the screening charge densities of the hydrogen bond acceptor and donor respectively, and the hydrogen bonding threshold σ_{HB} and the factor c_{HB} are adjustable parameters. Specifically the c_{HB} parameter is temperature dependent and describes the enthalpy gain and entropy loss that goes along with the formation of a hydrogen bond. As shown in Figure 2-5, a σ -profile that extends towards negative values of σ indicates possibility for hydrogen-bond acceptance, while a σ -profile that extends towards positive values of σ indicates possibility for hydrogen-bond donation. The $\min[\]$ construction ensures that the screening charge densities of the acceptor and donor exceeds the threshold for hydrogen bonding. Finally, Van der Waals interactions are taken into account by two element specific parameters τ_{vdW} and τ'_{vdW} .

The chemical potential of the solute X in solvent S is then finally obtained via integration of equation 2.39 over the full screening charge density:

$$\mu_X^S = \int p_X(\sigma) \mu_X(\sigma) d\sigma + kT \ln(\gamma_{\text{comb}}(X, S)) \quad (2.44)$$

where the second term on the right-hand side of the equation is a contribution describing the solute X and solvent S molecular size properties. These are often expressions based on surface areas and volumes of solutes and solvents⁵⁰. In COSMO-RS, this information is readily available from the COSMO cavities defined with the solvent-accessible-surface method.

An expression for the Gibbs free energy of solvation of the solute X is then obtained via taking the difference between the chemical potential in the ideal gas and in the liquid phase:

$$\Delta_{\text{solv}}G_X = \mu_X^S - \mu_X^G \quad (2.45)$$

where μ_X^G is the chemical potential for a molecule in the COSMO reference state (perfect conductor), and is composed of:

$$\mu_X^G = \Delta E_X^{\text{COSMO}} + \omega_{\text{ring}} n_{\text{ring},X} + \eta_{\text{ideal gas}}(T) \quad (2.46)$$

In this equation, the term $\Delta E_X^{\text{COSMO}}$ is the quantum chemical energy difference for going from the gas phase with a reference of 1 bar to the COSMO ideal conductor reference state. The vibrational, rotational and translational contributions to the free-energy were found to cancel out for the most part in the difference of gas- and liquid-phase free energies of molecules. A simple general correction term $\eta_{\text{ideal gas}}(T)$ appeared to be sufficient to account for any small discrepancies. However, for each ring structure an additional correction ω_{ring} of approximately 0.8 kJ mol^{-1} needs to be added.

Although the use of quantum chemical calculations reduces the need for empirical parameters in COSMO-RS, some fitting to experimental data is still required. The parameters that are empirically fitted are α , c_{hb} , σ_{hb} , τ_{vdw} and α_{eff} . All parameters are either general or element specific, which is a distinctive advantage of COSMO-RS as compared to other models for Gibbs free energy of solvation, such as group contribution methods.

One of the biggest disadvantages of the COSMO-RS method as described above is that it is based on a gas phase reference geometry. To overcome this, the Direct COSMO-RS method is developed which can be used during geometry optimization⁵¹. However, this method has a much higher computational demand.

2.7 References

1. Szabo, A.; Ostlund, N. S., *Modern quantum chemistry: introduction to advanced electronic structure theory*. Courier Corporation: 2012.
2. Parr, R. G., Density functional theory of atoms and molecules. In *Horizons of Quantum Chemistry*, Springer: 1980; pp 5-15.
3. Schrödinger, E., An undulatory theory of the mechanics of atoms and molecules. *Physical review* **1926**, 28 (6), 1049.
4. Cramer, C. J., *Computational Chemistry: Theories and Models*. John Wiley & Sons Chichester: 2004.
5. Born, M.; Oppenheimer, R., Zur quantentheorie der molekeln. *Annalen der physik* **1927**, 389 (20), 457-484.
6. Liehr, A. D., On the use of the Born-Oppenheimer approximation in molecular problems. *Annals of Physics* **1957**, 1 (3), 221-232.
7. Leach, A. R., *Molecular modelling: principles and applications*. Pearson education: 2001.
8. Slater, J. C., Note on Hartree's Method. *Physical Review* **1930**, 35 (2), 210-211.
9. Slater, J. C., The Self Consistent Field and the Structure of Atoms. *Physical Review* **1928**, 32 (3), 339-348.
10. Hartree, D. R., The Wave Mechanics of an Atom with a Non-Coulomb Central Field. Part I. Theory and Methods. *Mathematical Proceedings of the Cambridge Philosophical Society* **1928**, 24 (1), 89-110.
11. Gaunt, J. A., A Theory of Hartree's Atomic Fields. *Mathematical Proceedings of the Cambridge Philosophical Society* **1928**, 24 (2), 328-342.
12. Froese Fischer, C., General Hartree-Fock program. *Computer Physics Communications* **1987**, 43 (3), 355-365.
13. Hartree, D. R.; Hartree, W., Self-consistent field, with exchange, for beryllium. *Proceedings of the Royal Society of London. Series A-Mathematical and Physical Sciences* **1935**, 150 (869), 9-33.
14. Löwdin, P.-O., Quantum Theory of Many-Particle Systems. III. Extension of the Hartree-Fock Scheme to Include Degenerate Systems and Correlation Effects. *Physical Review* **1955**, 97 (6), 1509-1520.
15. McGuire, J. H., *Electron correlation dynamics in atomic collisions*. Cambridge University Press: 2005; Vol. 8.
16. Handy, N. C.; Cohen, A. J., Left-right correlation energy. *Molecular Physics* **2001**, 99 (5), 403-412.
17. David Sherrill, C.; Schaefer, H. F., The Configuration Interaction Method: Advances in Highly Correlated Approaches. In *Advances in Quantum Chemistry*, Löwdin, P.-O.; Sabin, J. R.; Zerner, M. C.; Brändas, E., Eds. Academic Press: 1999; Vol. 34, pp 143-269.
18. Møller, C.; Plesset, M. S., Note on an approximation treatment for many-electron systems. *Physical review* **1934**, 46 (7), 618.
19. Bartlett, R. J., Many-body perturbation theory and coupled cluster theory for electron correlation in molecules. *Annual review of physical chemistry* **1981**, 32 (1), 359-401.
20. Multiconfigurational SCF Theory. In *Multiconfigurational Quantum Chemistry*.
21. Koch, W.; Holthausen, M. C., *A chemist's guide to density functional theory*. Wiley Online Library: 2001; Vol. 2.
22. Hohenberg, P.; Kohn, W., Inhomogeneous electron gas. *Physical review* **1964**, 136 (3B), B864.
23. Kohn, W.; Sham, L. J., Self-consistent equations including exchange and correlation effects. *Physical review* **1965**, 140 (4A), A1133.
24. James, B.; Frisch, A., *Exploring chemistry with electronic structure methods*. Gaussian, Incorporated: 1996.
25. Perdew, J. P.; Burke, K.; Ernzerhof, M., Generalized gradient approximation made simple. *Physical review letters* **1996**, 77 (18), 3865.
26. Davidson, E. R.; Feller, D., Basis set selection for molecular calculations. *Chemical Reviews* **1986**, 86 (4), 681-696.

27. Jensen, F., Atomic orbital basis sets. *Wiley Interdisciplinary Reviews: Computational Molecular Science* **2013**, 3 (3), 273-295.
28. Jensen, F., Estimating the Hartree—Fock limit from finite basis set calculations. *Theoretical Chemistry Accounts* **2005**, 113 (5), 267-273.
29. Nyden, M. R.; Petersson, G., Complete basis set correlation energies. I. The asymptotic convergence of pair natural orbital expansions. *The Journal of Chemical Physics* **1981**, 75 (4), 1843-1862.
30. Hehre, W. J.; Ditchfield, R.; Pople, J. A., Self—consistent molecular orbital methods. XII. Further extensions of Gaussian—type basis sets for use in molecular orbital studies of organic molecules. *The Journal of Chemical Physics* **1972**, 56 (5), 2257-2261.
31. Bauschlicher, C. W.; Partridge, H., A comparison of correlation-consistent and Pople-type basis sets. *Chemical Physics Letters* **1995**, 245 (2), 158-164.
32. Kruse, H.; Goerigk, L.; Grimme, S., Why the Standard B3LYP/6-31G* Model Chemistry Should Not Be Used in DFT Calculations of Molecular Thermochemistry: Understanding and Correcting the Problem. *The Journal of Organic Chemistry* **2012**, 77 (23), 10824-10834.
33. Petersson, a.; Bennett, A.; Tensfeldt, T. G.; Al-Laham, M. A.; Shirley, W. A.; Mantzaris, J., A complete basis set model chemistry. I. The total energies of closed-shell atoms and hydrides of the first-row elements. *The Journal of chemical physics* **1988**, 89 (4), 2193-2218.
34. Karton, A., A computational chemist's guide to accurate thermochemistry for organic molecules. *Wiley Interdisciplinary Reviews: Computational Molecular Science* **2016**, 6 (3), 292-310.
35. Wheeler, S. E.; Moran, A.; Pieniazek, S. N.; Houk, K., Accurate reaction enthalpies and sources of error in DFT thermochemistry for aldol, Mannich, and α -aminooxylation reactions. *The Journal of Physical Chemistry A* **2009**, 113 (38), 10376-10384.
36. Desmet, G. B.; Sabbe, M. K.; D'hooge, D. R.; Espeel, P.; Celasun, S.; Marin, G. B.; Du Prez, F. E.; Reyniers, M.-F., Thiol-Michael addition in polar aprotic solvents: nucleophilic initiation or base catalysis? *Polymer Chemistry* **2017**, 8 (8), 1341-1352.
37. McQuarrie, D. A.; Cox, H.; Simon, J. D., *Physical chemistry: a molecular approach*. Sterling Publishing Company: 1997.
38. Gibbs, J. W., *Elementary principles in statistical mechanics*. Courier Corporation: 2014.
39. Greiner, W.; Neise, L.; Stöcker, H., *Thermodynamics and statistical mechanics*. Springer Science & Business Media: 2012.
40. Catlow, C. R. A.; Van Speybroeck, V.; van Santen, R., *Modelling and Simulation in the Science of Micro-and Meso-porous Materials*. Elsevier: 2017.
41. Desmet, G. B.; De Rybel, N.; Van Steenberge, P. H.; D'hooge, D. R.; Reyniers, M. F.; Marin, G. B., Ab-Initio-Based Kinetic Modeling to Understand RAFT Exchange: The Case of 2-Cyano-2-Propyl Dodecyl Trithiocarbonate and Styrene. *Macromolecular rapid communications* **2018**, 39 (2), 1700403.
42. Laidler, K. J., A glossary of terms used in chemical kinetics, including reaction dynamics (IUPAC Recommendations 1996). In *Pure and Applied Chemistry*, 1996; Vol. 68, p 149.
43. Eyring, H., The activated complex in chemical reactions. *The Journal of Chemical Physics* **1935**, 3 (2), 107-115.
44. Laidler, K. J.; King, M. C., Development of transition-state theory. *The Journal of Physical Chemistry* **1983**, 87 (15), 2657-2664.
45. Skyner, R.; McDonagh, J.; Groom, C.; Van Mourik, T.; Mitchell, J., A review of methods for the calculation of solution free energies and the modelling of systems in solution. *Physical Chemistry Chemical Physics* **2015**, 17 (9), 6174-6191.
46. Tomasi, J.; Mennucci, B.; Cammi, R., Quantum mechanical continuum solvation models. *Chemical reviews* **2005**, 105 (8), 2999-3094.
47. Onsager, L., Electric moments of molecules in liquids. *Journal of the American Chemical Society* **1936**, 58 (8), 1486-1493.
48. Foresman, J. B.; Keith, T. A.; Wiberg, K. B.; Snoonian, J.; Frisch, M. J., Solvent Effects. 5. Influence of Cavity Shape, Truncation of Electrostatics, and Electron Correlation on ab Initio Reaction Field Calculations. *The Journal of Physical Chemistry* **1996**, 100 (40), 16098-16104.
49. Klamt, A., *COSMO-RS: from quantum chemistry to fluid phase thermodynamics and drug design*. Elsevier: 2005.

50. Klamt, A., The COSMO and COSMO-RS solvation models. *Wiley Interdisciplinary Reviews: Computational Molecular Science* **2011**, *1* (5), 699-709.
51. Sinnecker, S.; Rajendran, A.; Klamt, A.; Diedenhofen, M.; Neese, F., Calculation of solvent shifts on electronic g-tensors with the conductor-like screening model (COSMO) and its self-consistent generalization to real solvents (direct COSMO-RS). *The Journal of Physical Chemistry A* **2006**, *110* (6), 2235-2245.

Chapter 3

Theoretical Assessment of Steric and Electronic Effects in Amines¹

The aldol reaction mechanisms in this work are catalyzed by either Lewis bases, Brønsted bases, or Brønsted acids. Whereas Brønsted acid or base catalysis involves a (de-)protonation reaction, Lewis base catalysis involves a nucleophilic attack on a substrate¹. The activity of the Brønsted base catalysts can thus be correlated to their relative proton affinity (PA) or proton basicity (PB) values, respectively defined by the enthalpy or Gibbs energy of dissociation of the protonated Lewis base (Reaction 1)². However, ranking the catalytic activity of Lewis base catalysts, such as amines, according to their proton affinity has proven to be unsuccessful³. One of the main reasons for this is the steric interaction encountered during the nucleophilic attack of the amine on a substrate, which are not simulated by the protonation reaction. The proton, which essentially comprises an empty 1s orbital, can be regarded as the “ideal” Lewis acid that forms strong covalent bonds with the Lewis base and has a minimal steric demand^{4, 5}. Several different Lewis acids have therefore been used to construct a basicity scale that is subject to steric interactions⁶⁻¹⁰. These Lewis acids include borane (BH₃)^{7, 11}, boron trifluoride (BF₃)¹²⁻¹⁷, trimethylborane (B(CH₃)₃)¹⁸⁻²², metal cations^{23, 24}, and several alkyl cations^{25, 26}, of which the methyl cation (CH₃⁺)^{3, 27-32} and the benzhydryl cations^{33, 34} have most often been investigated, both experimentally and computationally.

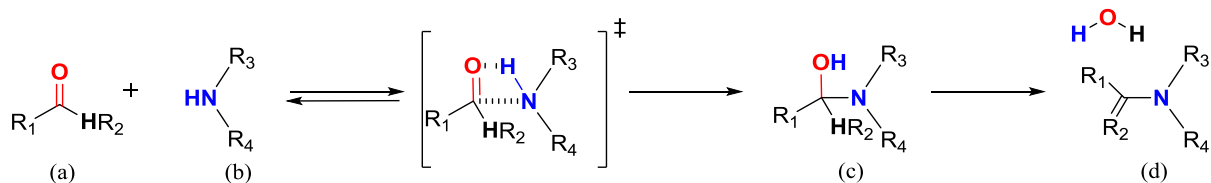
Specifically, the gas-phase methyl cation affinity (MCA) has been shown to correlate much better than the gas-phase proton affinity (PA) to the experimentally measured catalytic activity of tertiary amine catalysts in the nucleophile-induced addition reaction of methanol with acrylamide^{3, 35}. This shows that inclusion of steric effects in the gas-phase affinity scale already provides a much better correlation with experimentally measured catalytic activity, even for reactions that are performed in the liquid phase³.

¹ This chapter is published as: De Vylder, Anton et al. “Rational Design of Nucleophilic Amine Sites via Computational Probing of Steric and Electronic Effects.” *Catalysis Today* (2019)



Another reaction that is known to suffer from steric interactions around the nucleophilic active site is the amine-catalyzed aldol reaction of two carbonyl-containing species^{36, 37}. The generally accepted³⁸⁻⁴⁰ reaction mechanism proceeds via an enamine intermediate. The formation of this intermediate, as displayed in Scheme 3-1, starts with a nucleophilic attack of an amine (b) on the carbonyl moiety of an aldehyde or ketone (a) bearing an α -hydrogen. A carbinolamine (c) is subsequently formed that can dehydrate to the desired enamine intermediate (d). This enamine is nucleophilic enough to react with another aldehyde or ketone to produce a new carbon-carbon bond, after which a water-assisted desorption step releases the aldol product from the amine catalyst.

Too pronounced steric hindrance of substituents around the nitrogen active center has been suggested in previous work on the aldol reaction^{36, 37} to hinder the initial nucleophilic attack to such an extent that the desired enamine intermediate cannot be formed. Hence, a Lewis basicity scale is needed that also includes these steric effects, and can help to predict whether substituents around the nitrogen active center will cause the amine to be too sterically hindered for a nucleophilic attack on a carbonyl species.



Scheme 3-1: general pathway to the enamine formation via initial nucleophilic attack on the carbonyl group (a) by an amine catalyst (b), with the formation of a carbinolamine intermediate (c) and dehydration to the enamine (d). Severe steric hindrance around the amine will cause the rate of this first step to decrease and result in a negligible catalytic activity being observed.

Several steps in the amine catalyzed aldol reaction can be promoted by the cooperative effect of a hydrogen bond donor³⁹. This hydrogen-bond donor can be a carboxylic acid group, or a mildly acidic hydroxyl group, as is the case in respectively L-proline and L-prolinol^{37, 41}. In mesoporous silica supported amine catalysts, the mildly acidic surface silanol groups were found to be optimal hydrogen-bond promoters^{42, 43}. Intramolecular incorporation of a hydrogen-bond promoter, such as a hydroxyl group on the β -carbon of the organic amine function, has been suggested to eliminate the need for promoting surface silanol groups and thus allows a higher active site loading⁴⁴. However, the correct intramolecular placement of this hydroxyl

group is crucial to maximize the cooperative action with the amine while simultaneously avoiding additional steric hindrance around the nitrogen free electron pair⁴⁴.

In this work, a Lewis basicity scale is constructed based on gas-phase complexation of amine catalysts with the sterically demanding Lewis acid trimethylborane (TMB, Reaction 2). It will be shown that this TMB basicity scale can, as opposed to the proton basicity scale, correctly describe both the steric and electronic effect of substituents on the nucleophilic character of the amine site. Next, the TMB basicity scale is used as a tool to probe possible additional steric and electronic effects of placing an intramolecular promoting hydroxyl group around the nitrogen atom in the development of novel bifunctional amine-hydroxyl sites as application for new heterogeneous catalysts.

3.1 Computational methods

All of the electronic structure calculations were performed using the Gaussian 09 package⁴⁵. Global minimum energy conformations for reactants and complexes were determined in vacuo by a first scan of all freely rotating dihedral angles at the B3LYP/6-31G(d) level of theory. The CBS-QB3 composite model has been shown to provide reliable results for the calculation of proton affinity and gas-phase basicity of several acid-base catalysts⁴⁶, as well as the gas-phase BF₃ affinity scale⁴⁷. This quantum-chemical composite model was, hence, used for a full geometry optimization and free energy calculation of the lowest energy conformer of both the reactants and complexes. A tight optimization criterion and an ultrafine integration grid was used. Minimum energy conformations were confirmed to have zero imaginary frequency. Partition functions were calculated using statistical thermodynamics, based on the scaled B3LYP/CBSB7 frequency calculation in CBS-QB3. These were evaluated by using the rigid-rotor and harmonic oscillator (HO) approximation, assuming separability of translational, external rotational, rovibrational, and electronic contributions. All thermal contributions were calculated in the (quasi)harmonic oscillator approach, which means that any frequencies below 30 cm⁻¹ were raised to this value⁴⁸. Basis set superposition errors should be small with the complete basis set extrapolation and were therefore not specifically accounted for. The enthalpy and entropy of complex formation were calculated at 298.15 K and 1 atm, from which the Gibbs energy was derived at the same conditions.

It should be noted that there are two ways to thermodynamically quantify gas-phase base strength: either the enthalpy of reaction, often called affinity, or the Gibbs energy of reaction, often called basicity, is reported⁴. While the enthalpy of complexation is fundamentally closer

to the donor/acceptor bond energy, the Gibbs energy includes the entropy change of, for example, internal hydrogen bonding upon adduct formation. The protonation reaction is a special case because the very strong interaction with a proton leads to a relatively small entropic change compared to the enthalpy change. In this work, both affinity and basicity is reported and any pronounced differences in entropy is clarified. Furthermore, predicting a difference in kinetic performance based on thermodynamic basicity rankings is only done for small subsets of structurally similar Lewis bases that only differ in their nucleophilic character caused by differences in electronic or steric effects due to different substituents around the amine, and where it is expected that a linear free-energy relationship holds⁴⁹.

The proton basicity (PB) and proton affinity (PA), determined via respectively the Gibbs energy and the enthalpy of Reaction 1, were calculated according to Equation 1 and Equation 2 at 298.15 K and 1 atm. The trimethylborane basicity (TMBB) and affinity (TMBA) determined for Reaction 2 were calculated respectively according to Equation 3 and Equation 4, at 298.15 K and 1 atm.

$$\text{PB} = \Delta G^\circ_{\text{H}^+} + \Delta G^\circ_{\text{Base}} - \Delta G^\circ_{\text{HBase}^+} \quad \text{Equation 1}$$

$$\text{PA} = \Delta H^\circ_{\text{H}^+} + \Delta H^\circ_{\text{Base}} - \Delta H^\circ_{\text{HBase}^+} \quad \text{Equation 2}$$

$$\text{TMBB} = \Delta G^\circ_{\text{B(CH}_3)_3} + \Delta G^\circ_{\text{Base}} - \Delta G^\circ_{\text{B(CH}_3)_3\text{Base}} \quad \text{Equation 3}$$

$$\text{TMBA} = \Delta H^\circ_{\text{B(CH}_3)_3} + \Delta H^\circ_{\text{Base}} - \Delta H^\circ_{\text{B(CH}_3)_3\text{Base}} \quad \text{Equation 4}$$

3.2 Results and discussion

3.2.1 Validation of the computational method

To validate the ability of the computational method to describe experimentally observed steric effects in amines, the experimental gas-phase trimethylborane (TMB) basicity of 14 amines investigated by Brown et al.¹⁸⁻²² as displayed in Figure A-1 in Appendix A, is compared at 1 atm and 298.15 K to the values calculated with the CBS-QB3 composite model (TMBB_{CBS-QB3}), at the same conditions, in Figure A-2 in Appendix A. A maximum deviation of 2.10 kJ/mol from the experimental TMB basicity values is observed, with a mean absolute deviation of 1.10 kJ/mol. The gas-phase proton basicity (PB) of these amines is also calculated with the CBS-QB3 composite method, and is compared to the gas-phase values reported by Hunter and Lias⁵⁰. The parity plot of these results is included in Figure A-3 in Appendix A. The maximum

deviation of the experimental PB values is 4.40 kJ/mol, with a mean absolute deviation of 1.93 kJ/mol.

It can thus be concluded that the employed computational method can accurately describe the proton basicity of various amines, as well as describe the steric effects that lead to differences in relative order between the proton basicity scale and the TMB basicity scale.

3.2.2 Correlating the trimethylborane basicity of amine-based catalysts to their experimental activity in the aldol reaction

To validate the predictive behavior of the trimethylborane (TMB) basicity scale for steric effects that impact the initial nucleophilic attack of amine-based catalysts in the aldol reaction, several experimentally evaluated amine catalysts with different substituents are probed. Any deviations from the trend between the gas-phase proton basicity scale and the TMB basicity scale will indicate that not only electronic basicity effects, but also steric effects are an important factor to consider.

First, the homogeneous L-proline derivatives evaluated for the aldol reaction by Sakthivel et al.³⁷ will be ranked according to their TMB basicity and compared to their respective experimental activity. Next, heterogeneously supported catalytic amine sites with different sterically demanding substituents that were evaluated by Lauwaert et al.³⁶ for the same aldol reaction will also be probed with TMB.

3.2.2.1 Steric effect of substituents in L-proline derivatives

Sakthivel et al.³⁷ reported the experimental yield of several L-proline derivatives, with different substituents, for the aldol reaction of acetone with 4-nitrobenzaldehyde. They suggested that in catalysts with substitutions adjacent to the amino group, the acetone enamine formation can be disturbed by a combination of steric factors and a change in pKa³⁷. To investigate the electronic and steric effects of these substituents independently, the catalysts are ranked on both a TMB basicity scale as well as a proton basicity scale in Figure 3-1. The basicity, affinity, and entropy are given in Table 3-1, both for the gas-phase TMB complexation as well as the steric-free gas-phase protonation reaction. To ensure the promotional ability is equal in all the probed L-proline derivatives, from all the catalysts investigated by Sakthivel et al.³⁷, only the catalysts with carboxylic acids as promoting group are compared to each other in this paragraph.

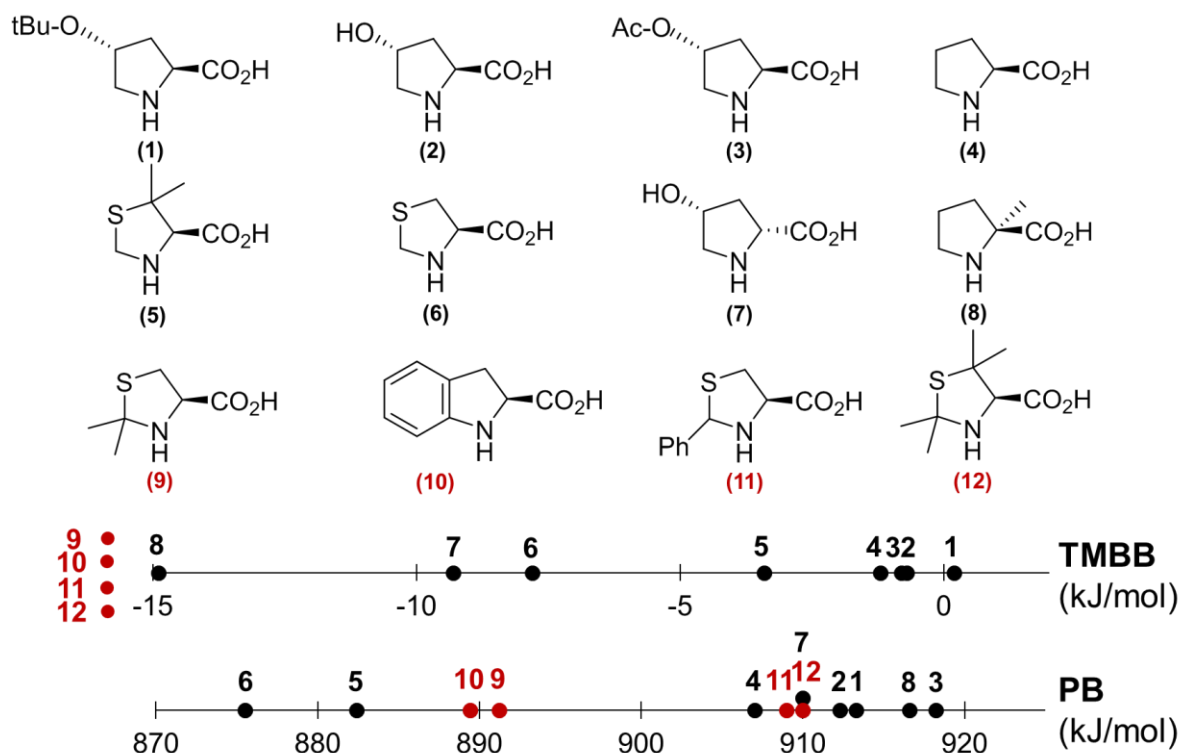


Figure 3-1: L-proline derivatives evaluated by Sakthivel et al.³⁷ in the aldol reaction of 4-nitrobenzaldehyde with acetone, ranked according to their TMB basicity (TMBB) and proton basicity (PB). Catalysts **9** to **12** (red) are too sterically hindered to form a stable complex with TMB and are also reported to be inactive in the aldol reaction³⁷.

Table 3-1: Affinity, entropy and basicity calculated at the CBS-QB3 level of theory at 298.15 K and 1 atm for reaction of L-proline derivatives 1 to 12 with the sterically demanding trimethylborane (TMB) or a steric-free proton.

Catalyst	TMB affinity (kJ mol ⁻¹)	TMB entropy (J K ⁻¹ mol ⁻¹)	TMB basicity (kJ mol ⁻¹)	Proton affinity (kJ mol ⁻¹)	Proton entropy (J K ⁻¹ mol ⁻¹)	Proton basicity (kJ mol ⁻¹)
1	67.1	224.3	0.2	944.1	103.5	913.3
2	65.3	221.3	-0.7	942.5	101.4	912.3
3	68.6	232.8	-0.8	951.8	112.7	918.2
4	63.1	215.8	-1.2	938.7	106.3	907.0
5	60.2	213.6	-3.4	918.9	106.4	887.1
6	56.3	215.1	-7.8	908.5	110.7	875.5
7	66.7	254.8	-9.3	940.8	103.5	910.0
8	50.6	219.9	-14.9	948.2	106.2	916.6
9	-	-	-	922.7	105.9	891.2
10	-	-	-	921.1	106.4	889.4
11	-	-	-	942.5	112.5	909.0
12	-	-	-	938.9	97.2	910.0

Substituents tert-butoxy (**1**), hydroxyl (**2**) or acetoxy (**3**) at the β -carbon in the 4-position *trans* to the carboxylic acid of L-proline (**4**) seem to slightly enhance its proton basicity. A

similar increase in the TMB basicity is also observed, which shows that the size and type of substituent at this position does not appear to have a detrimental steric effect on the amine. Experimentally, these substituents indeed do not hamper the catalytic activity, as compared to L-proline (**4**)³⁷. When the hydroxyl substituent is *cis* to the carboxylic acid function, as is the case in *cis*-4-hydroxy-D-proline (**7**), the calculated TMB basicity is severely decreased. This is mainly due to an increased entropic penalty, due to the formation of a hydrogen-bond between the hydrogen of the hydroxyl group and the oxygen of the carboxylic acid group, upon complexation with TMB as displayed in Figure A-4 in Appendix A. Hence, the TMB basicity decrease is not caused by an increased steric hindrance of the substituent. Experimentally, indeed no detrimental activity drop is reported for a hydroxyl group at this position³⁷. When the hydroxyl substituent is *trans* to the carboxylic acid, as is the case in catalyst **2**, this hydrogen bond does not exist in the complex formed with TMB, as is displayed in Figure A-5 in Appendix A.

Electron donating substituents at the α -carbon in 5-position (catalysts **9**, **11**, and **12**), increase the proton basicity of the nitrogen atom as compared to the “parent” catalyst 4-thiazolidinecarboxylic acid (**6**). However, no stable TMB adduct could be formed due to the severe steric hindrance of the substituents at this position. This is also the case for catalyst **10**, where the ring structure in the 5-position causes a detrimental steric effect. Additionally, the phenyl ring in catalyst **10** is conjugated with the nitrogen free-electron pair, which causes a decreased proton basicity. The experimental activity of catalysts **9**, **10**, **11** and **12** was reported to be minor³⁷. This clearly demonstrates that the proton basicity ranking cannot correlate to the experimentally observed activity while the TMB basicity based ranking can describe this trend.

A methyl substituent at the α -carbon in the 2-position, such as in 2-methyl-L-proline (**8**), results in an increased proton basicity due to the electron donating ability of the methyl group, as can be seen in Table 3-1. It, however, also causes an increase in steric hindrance, which can be seen as a reduced TMB basicity as compared to L-proline (**4**). Yet, the increase in steric hindrance is not as pronounced as in catalysts **9** to **12**, where no stable adduct was found. Indeed, experimentally, the activity of 2-methyl-L-proline (**8**) is reported as significantly lower than L-proline (**4**), but still higher than that of catalysts with substituents at the 5-position (catalysts **9** to **12**)³⁷.

Dimethyl substitution at the β -carbon in 3-position in 3,3-dimethyl-4-thiazolidinecarboxylic acid (**5**) increases the proton basicity, compared to 4-thiazolidinecarboxylic acid (**6**). The TMB basicity follows this increasing basicity trend,

indicating that the dimethyl groups at this position do not cause any steric interactions that decrease the catalytic activity, which was also experimentally reported³⁷.

It can, hence, be concluded that placing a substituent on the β -carbon in 3 position in 4-thiazolidinecarboxylic acid and 4 position of L-proline can increase the basicity of the amine without causing any prohibitive steric hindrance. However, substitution at the α -carbon in the 2 position of L-proline causes an increased steric hindrance and substitution at the α -carbon in the 5 position in L-proline or 4-thiazolidinecarboxylic acid will render the catalyst too sterically hindered for any reaction to take place. The experimentally observed trend in catalytic activity³⁷ can thus clearly be reproduced by the calculated gas-phase TMB basicity scale in Figure 3-1, whereas no such trend can be observed in the steric-free gas-phase proton basicity scale.

3.2.2.2 Effect of the ring conformation in cyclic amino acids and limitations of the TMB basicity scale

Although experimentally no difference in catalytic activity is observed when sulfur is incorporated at the 4-position in L-proline (**4**), the TMB and proton basicity of 4-thiazolidinecarboxylic acid (**6**) is lower than that of L-proline (**4**), as indicated in Figure 3-1. A change in the ring conformation due to the incorporation of sulfur, resulting in a higher pyramidalization angle of nitrogen, is responsible for this lower proton and TMB basicity. The higher experimental activity than expected based on the TMB basicity, indicates that relative comparison in the basicity scales should only be performed for structurally similar catalysts with the same heteroatoms. Since the goal of this work is probing possible steric effect of substituents in the initial nucleophilic attack, relative comparison between the derivatives of 4-thiazolidinecarboxylic acid (**6**) still allows to retrieve valuable information about the steric and electronic effect of substituent placement.

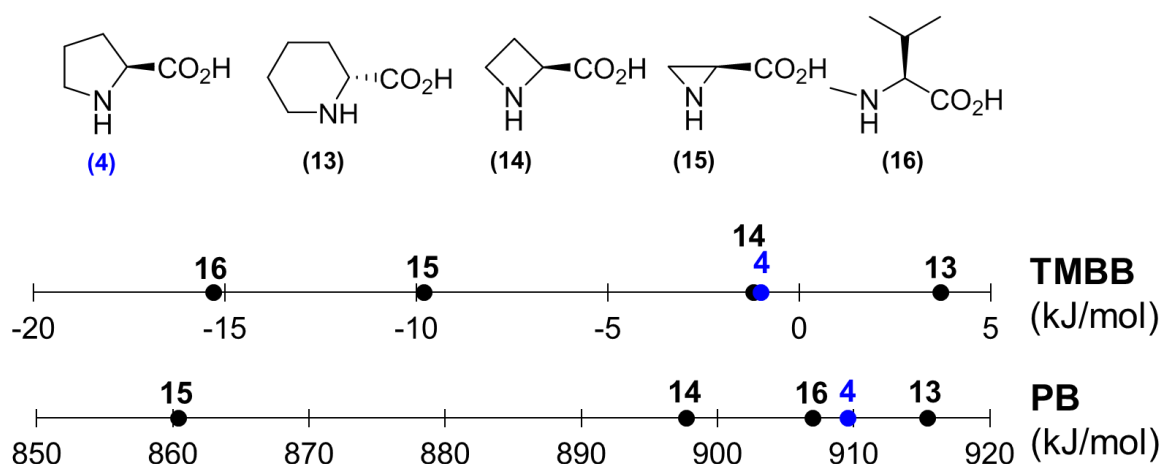


Figure 3-2: Effect of ring and ring size in (cyclic) amino acids on the TMB basicity (TMBB) and the proton basicity (PB). Catalysts **13**, **14** and **16** have been evaluated by Sakthivel et al.³⁷ for the amine catalyzed aldol reaction of acetone with 4-nitrobenzaldehyde.

Table 3-2: Affinity, entropy and basicity calculated at the CBS-QB3 level of theory at 298.15 K and 1 atm for reaction of L-proline derivatives **13** to **16** with the sterically demanding trimethylborane (TMB) or a steric-free proton.

Catalyst	TMB affinity (kJ mol ⁻¹)	TMB entropy (J K ⁻¹ mol ⁻¹)	TMB basicity (kJ mol ⁻¹)	Proton affinity (kJ mol ⁻¹)	Proton entropy (J K ⁻¹ mol ⁻¹)	Proton basicity (kJ mol ⁻¹)
13	67.3	213.5	3.7	943.5	94.0	915.4
14	63.6	216.5	-1.0	926.3	95.8	897.7
15	51.1	204.0	-9.8	891.4	104.0	860.4
16	54.6	234.4	-15.3	941.5	107.7	909.6

The cyclic 5-membered pyrrolidine structure of L-proline (**4**) yields a decrease in steric interactions when compared to the similar linear amino acid N-methyl-L-valine (**16**) that has a comparable proton basicity, as seen in Table 3-2 and Figure 3-2. Experimentally, the linear amino acid (**16**) is reported to be inactive³⁷, which could be related to these steric interactions encountered. The 6-membered R-pipecolic acid (**13**), however, has been reported as inactive in the aldol reaction³⁷ but exhibits the highest TMB and proton basicity of all the cyclic amino acids investigated. Hence, its inability to catalyze the aldol reaction does not seem to be due to more pronounced steric constraints in the initial nucleophilic attack but will be situated in a different step of the catalytic mechanism. Indeed, previous studies have shown that enamines derived from nucleophilic addition to a piperidine ring have a substantially lower nucleophilicity than enamines derived from nucleophilic addition to a pyrrolidine ring^{51,52}. This difference in reactivity is explained by a larger pyramidalization angle of nitrogen in the 6-membered piperidine-derived enamine, resulting in a reduced p-character of nitrogen, and a

reduction in the conjugation between the nitrogen lone pair and the double bond of the enamine^{52, 53}. Rather than a nucleophilicity reduction of the amine site, this will present itself in a nucleophilicity reduction of the resulting enamine, which could also be assessed with adequate computational tools.

The 4-membered 2-azetidine-carboxylic acid (**14**) has practically the same TMB basicity as L-proline (**4**), while its proton basicity is lower. Hence, it seems that the lower proton basicity is compensated for by the more compact ring structure. The catalyst is experimentally found to be slightly less active than L-proline (**4**)³⁷. The smallest cyclic amino acid, aziridine-2-carboxylic acid (**15**) has a low proton basicity and a low TMB basicity. This catalyst has not yet been tested in an aldol reaction but is expected to exhibit a low activity.

From the above results it can be concluded that the TMB basicity scale can correctly identify restrictive steric factors of substituents leading to the inability of an amino acid catalyst to initiate a nucleophilic attack. However, this also means that the TMB basicity scale cannot account for reactivity differences of the resulting enamine. The TMB basicity scale should thus only be used as a tool that, as opposed to the proton basicity, can warn for restrictive steric factors by substituents around the nitrogen atom during the nucleophilic attack of the amine moiety.

3.2.2.3 Amines supported on mesoporous silica

A range of acyclic secondary amines with substituents leading to different extents of steric constraints, supported on mesoporous silica, have been explored by Lauwaert et al³⁶. These monofunctional amine sites are connected via a propyl linker to mesoporous silica and are promoted by mildly acidic surface silanols. Because only the steric effect in the amine active site is assessed in this work, and not the cooperative action with the silica surface, as well as to keep the size of the computational model within a reasonable size, only the organic amine site is modeled, as is indicated in Figure 3-3. Because the employed methodology results in a relative ranking, it is crucial that only structurally similar sites are compared to each other. The TMB basicity results of homogeneous catalysts are therefore not to be directly compared to the results of the sites derived from the heterogeneous catalysts, and no conclusions regarding the effect of immobilization can be drawn from this work. It was reported³⁶ that increasing the substituent size from a methylgroup in the N-methylaminopropyl function (MAP, **18**) to an ethylgroup in the N-ethylaminopropyl function (EAP, **19**) reduces the catalytic activity. Moreover, an even larger substituent, such as a cyclohexyl group (CAP, **21**) completely hinders catalytic activity, which was suggested to be caused by a restrictive steric interaction in the

initial nucleophilic attack³⁶. As evident from Figure 3-3 and Table 3-3, this experimental reactivity order indeed agrees with the TMB basicity scale of the monofunctional amines in the gas-phase, while the reverse is found in the gas-phase proton basicity scale. The phenyl group in the N-phenylaminopropyl function (PAP, **20**) results in a lower proton basicity, and a TMB basicity that is comparable to that of the CAP function (**21**), due to conjugation effects of the free electron pair with the phenyl group. Previous work has indeed reported that the PAP (**20**) function exhibits an activity comparable to that of CAP (**21**)³⁶.

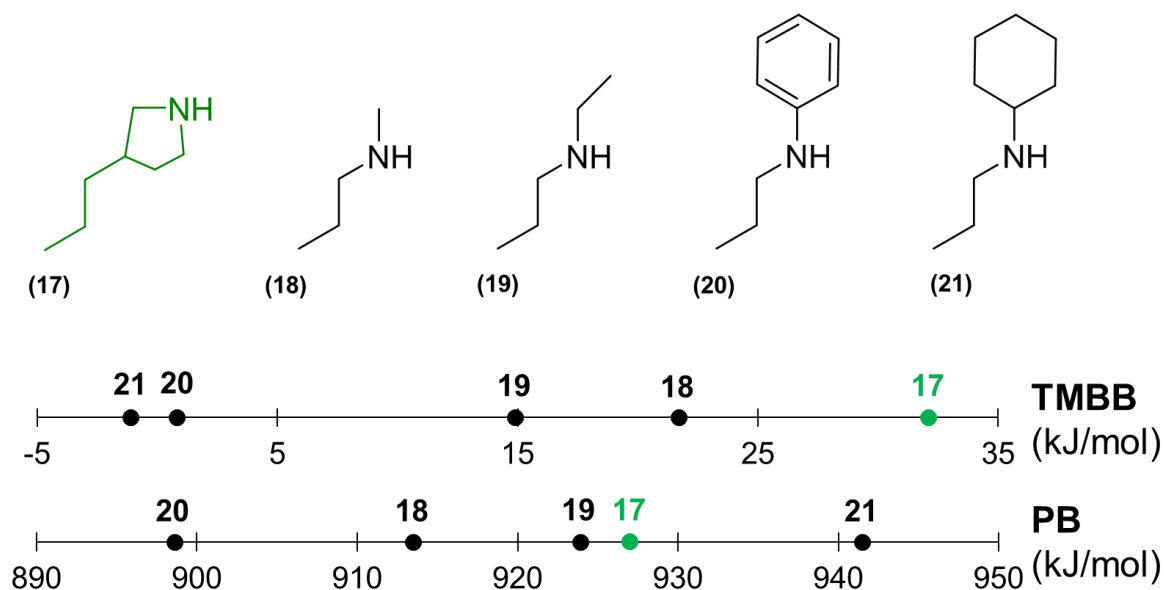


Figure 3-3: Monofunctional amine active sites (top, **18-21**) evaluated by Lauwaert et al.³⁶ for the aldol reaction of acetone with 4-nitrobenzaldehyde, ranked along their TMBB basicity (TMBB) and proton basicity (PB). Active site **17** (green) is suggested as a new optimal monofunctional amine that can be attached to mesoporous silica via a propyl linker.

To investigate the effect of intramolecular promotion by a hydrogen-bond donor, Lauwaert et al.⁴⁴ experimentally evaluated a heterogeneous mesoporous silica supported catalyst based on the bifunctional amine-hydroxyl **23**, without any promoting silanols. Its catalytic activity was found to be similar to the mesoporous silica catalyst based on the monofunctional EAP group (**19**), promoted by an excess of surface silanols, which proves that intramolecular promotion is equivalent to the randomly placed excess surface silanols⁴⁴. Computationally, the proton basicity of the bifunctional amine-hydroxyl active site **23** is found to be higher than the monofunctional EAP site (**19**). However, the calculated TMB basicity does not seem to follow this trend, and appears to be slightly lower for catalyst **23**, indicating that the hydroxyl group that is weakly hydrogen-bonded to the amine provides some additional steric crowding around the amine. Correct placement of the promoting hydroxyl group is thus critical to avoid additional steric hindrance around the amine.

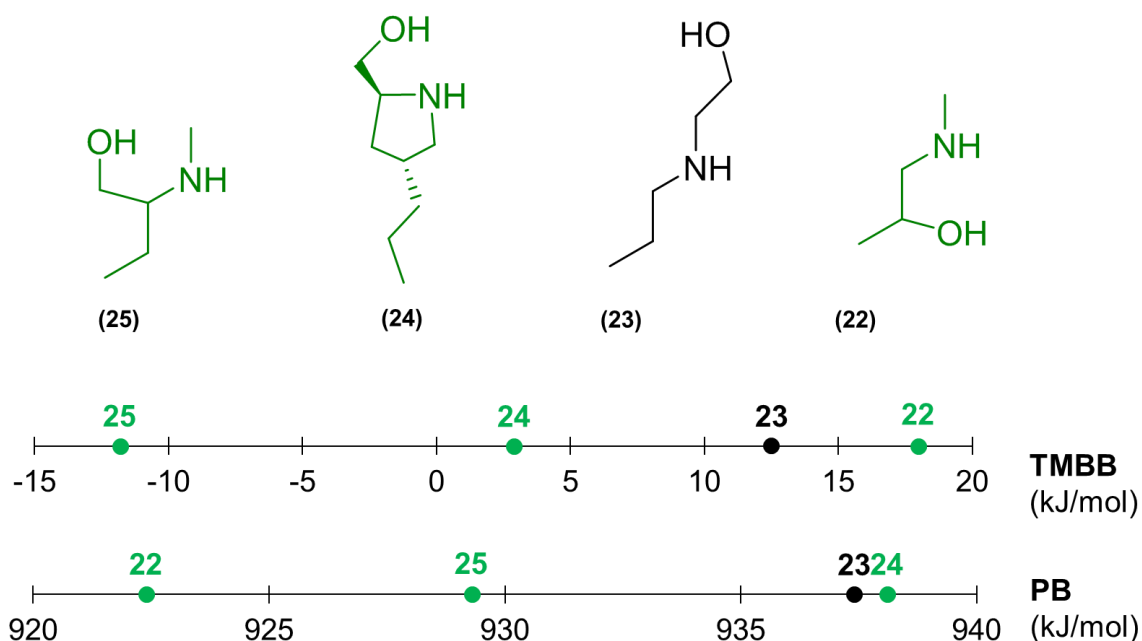


Figure 3-4: Bifunctional amine-hydroxyl functions that can be grafted on mesoporous silica ranked along their TMB basicity (TMBB) and proton basicity (PB). Groups **22**, **24** and **25** (green) are new amine-hydroxyl functions proposed for the aldol reaction, group **23** has already been experimentally tested by Lauwaert et al.⁴⁴

Table 3-3: Affinity, entropy and basicity calculated at the CBS-QB3 level of theory at 298.15 K and 1 atm for reaction of groups **17** to **25** with the sterically demanding trimethylborane (TMB) or a steric-free proton. Catalysts **17** to **21** are monofunctional amines, catalysts **22** to **25** are bifunctional amine-hydroxyls.

Catalyst	TMB affinity (kJ mol ⁻¹)	TMB entropy (J K ⁻¹ mol ⁻¹)	TMB basicity (kJ mol ⁻¹)	Proton affinity (kJ mol ⁻¹)	Proton entropy (J K ⁻¹ mol ⁻¹)	Proton basicity (kJ mol ⁻¹)
17	98.6	222.9	32.1	958.4	105.2	927.0
18	86.3	216.5	21.7	944.8	104.9	913.5
19	81.0	221.5	14.9	955.0	104.3	923.9
20	65.9	218.5	0.8	928.9	101.6	898.6
21	68.6	233.8	-1.1	972.4	103.7	941.5
22	82.7	217.0	18.0	953.4	103.8	922.4
23	77.8	218.9	12.5	970.4	110.7	937.4
24	72.1	232.2	2.9	969.5	105.3	938.1
25	58.5	235.8	-11.8	960.1	103.6	929.3

3.2.3 Design of a new monofunctional amine and bifunctional amine-hydroxyl site with a high TMB basicity

Calculating a priori the Lewis basicity of amine-based catalytic functions with adequate computational tools can assist in the development of catalysts with an optimal activity⁵⁴.

Especially since the development of novel heterogeneous amine catalysts is typically an arduous task, theoretical probing of the prospective amine function with trimethylborane can quickly yield valuable information about possible steric interactions that would limit their activity as a nucleophilic amine catalyst.

Currently, the best performing monofunctional heterogeneous amine catalyst for the aldol reaction of acetone with 4-nitrobenzaldehyde is a secondary amine with a small methyl group, connected with a propyl linker chain to the mesoporous silica surface, as modeled here by the N-methylaminopropyl group (**18**, MAP)³⁶. The length of a propyl linker has been shown to be optimal for promotion by an excess of surface silanol groups, with longer linkers having no adverse effects⁵⁵. Additionally, the active sites in Figure 3-3 and Figure 3-4 that were used to validate the computational method to experimental results all contain a propyl linker. Hence, the proposed new monofunctional group, based on the 5-membered pyrrolidine ring, is also designed with a propyl linker. This results in the 4-propyl-pyrrolidine group (**17**), which is found to yield a higher proton and TMB basicity than the, what was previously found as, best performing monofunctional MAP group (**18**). It is thus expected that a heterogeneously supported catalyst based on the 4-propyl-pyrrolidine function (**17**), promoted by an excess of surface silanol groups, will display an increased activity in the aldol reaction as compared to the previous experimentally evaluated monofunctional groups. It should be noted that, based on solely the proton basicity, a catalyst with a CAP function (**21**) would have been selected. However, this catalyst has already been shown experimentally³⁶ to exhibit a very low activity due to steric hindrance effects around the amine, which is correctly described by the TMB basicity scale.

Previous work by Lauwaert et al.⁴⁴ that did not include any steric effects, concluded that a bifunctional secondary amine-hydroxyl species, with a methyl substituent on the nitrogen atom and intramolecularly promoted by a hydroxyl group on a β -carbon, would be an optimal catalytic site. Correct intramolecular placement of this promotion hydroxyl group is, however, essential to obtain an efficient intramolecular promotion without causing additional steric hindrance. Several possibilities (**22** – **25**) are therefore ranked in Figure 3-4 according to their TMB basicity. Due to the intramolecular promotional ability of the amine-hydroxyl functions, the length of the linker connecting to the surface is not as critical here. However, for easy comparison with existing experimental work⁴⁴, a propyl linker is also chosen for the newly developed catalytic groups.

Based on the calculations performed for the monofunctional groups, an L-prolinol group with a propyl linker, is suggested as bifunctional amine-hydroxyl (**24**). This propyl linker is

attached at the 4-position, in order to not cause any additional steric hindrance. However, from the TMB basicity calculations in Table 3-3 it can be seen that introduction of a hydroxyl group in this position causes a large increase in steric hindrance around the nucleophilic nitrogen. This results in a TMB basicity that is lower than the already experimentally tested bifunctional group **23**, which shows a similar proton basicity. Hence, an alternative configuration with the least steric hindrance expected in the initial nucleophilic attack is the 1-(methylamino)propan-2-ol group (**22**) in Figure 3-4.

When comparing the monofunctional MAP group (**18**) with the proposed bifunctional amine-hydroxyl (**22**), it can be seen that introduction of this hydroxyl group at the β -carbon in the propyl linker chain causes the proton basicity to increase and the TMB basicity to drop. Hence, a small increase in steric hindrance is introduced by the addition of the hydroxyl group. This increase is, however, limited, which makes the 1-(methylamino)propan-2-ol group (**22**) the most preferred bifunctional amine-hydroxyl. This group actually appears to have the lowest proton basicity of all the bifunctional amine-hydroxyls that were investigated, which again proves that based on merely the proton basicity scale, a different optimal functional group would be selected than based on the TMB basicity scale that includes steric effects. To assess the difference between a secondary and a primary alcohol as promoting group, the bifunctional amine-hydroxyl **25** could be developed. However, the calculated TMB basicity readily indicates that in this catalyst a restrictive steric interaction around the amine site occurs and, quite likely, would render it inactive. Hence, it can be concluded that by incorporating the hydroxyl group on the β -carbon in the propyl linker connecting the active site to the silica surface, the increase in steric hindrance upon inclusion of an intramolecular promoting site can be minimized.

3.3 Conclusions

The overall catalytic activity of amine-based organocatalysts in a reaction starting with a nucleophilic attack on a carbon atom is generally difficult to correlate to the proton affinity or pKa value of the nucleophile due to the lack of steric interactions in the protonation reaction. In this work, a Lewis basicity scale using trimethylborane (TMB) as Lewis acid, which accounts for such steric effects, has been constructed for different amine based catalytic groups using the CBS-QB3 model chemistry. The computational model was successfully validated against experimentally measured gas-phase proton and TMB basicity values for several primary, secondary, and tertiary organic amines of varying steric demand.

Both a proton and a TMB basicity scale were constructed for L-proline derivatives with different substituents around the amine group, as well as for active sites of heterogeneously supported amine catalysts. Because the amine catalyzed aldol reaction starts with a nucleophilic attack of the amine on the carbonyl group, with the subsequent formation of an enamine, the TMB basicity scale is a potential indicator for the corresponding aldol reaction activity. This TMB basicity scale could indeed describe the experimentally observed activity trend much better than the steric-free proton basicity scale. This was particularly so for catalysts with substituents neighboring the amine. However, care should be taken when comparing structurally different organocatalysts, since the TMB basicity scale only provides information about the steric effects in the initial nucleophilic attack of the amine, and not about differences elsewhere in the catalytic mechanism such as the reactivity of the crucial enamine intermediate.

Taking these limitations in consideration, the developed gas-phase TMB basicity scale was then used to assess the steric hindrance in novel amine functions for heterogeneous catalysts, within the constraints desired for functionalization on heterogeneous silica-based supports. As least sterically hindered monofunctional group, promoted by an excess of surface silanols, 4-propyl-pyrrolidine is proposed. In a bifunctional amine-hydroxyl active site, the correct placement of the intramolecular promoting hydroxyl group on the β -carbon was shown to be crucial in limiting the steric hindrance around the nitrogen atom. From the obtained TMB basicity ranking, 1-(methylamino)propan-2-ol is proposed as a new unhindered bifunctional amine-hydroxyl active site for grafting on mesoporous silica. It should be noted that the synthesis of the proposed 1-(methylamino)propan-2-ol and 4-propyl-pyrrolidine groups will not be trivial. The strategic advantage of the methodology presented in this work is situated in the indications it gives with respect to the priorities that should be attached to the synthesis of the next generation of catalysts. The experimental focus can thus be laid on a limited number of active site designs that should be synthesized with priority.

3.4 References

1. Seayad, J.; List, B., Asymmetric organocatalysis. *Organic & Biomolecular Chemistry* **2005**, *3* (5), 719-724.
2. Maksic, Z. B.; Kovacevic, B.; Vianello, R., Advances in determining the absolute proton affinities of neutral organic molecules in the gas phase and their interpretation: a theoretical account. *Chemical reviews* **2012**, *112* (10), 5240-5270.
3. Wei, Y.; Sastry, G. N.; Zipse, H., Methyl cation affinities of commonly used organocatalysts. *Journal of the American Chemical Society* **2008**, *130* (11), 3473-3477.
4. Gal, J.-F., *Thermodynamic Treatments of Lewis Basicity*. Wiley-VCH Verlag GmbH & Co. KGaA: Weinheim, Germany, 2016.

5. Laurence, C.; Gal, J.-F., *Lewis basicity and affinity scales: data and measurement*. John Wiley & Sons: Chippingham, Wiltshire, United Kingdom, 2010.
6. Denmark, S. E.; Beutner, G. L., Lewis base catalysis in organic synthesis. *Angewandte Chemie International Edition* **2008**, *47* (9), 1560-1638.
7. Méndez, M.; Cedillo, A., Gas phase Lewis acidity and basicity scales for boranes, phosphines and amines based on the formation of donor–acceptor complexes. *Computational and Theoretical Chemistry* **2013**, *1011*, 44-56.
8. Hancock, R. D.; Nakani, B. S.; Marsicano, F., Relationship between Lewis acid-base behavior in the gas phase and in aqueous solution. 1. Role of inductive, polarizability, and steric effects in amine ligands. *Inorganic Chemistry* **1983**, *22* (18), 2531-2535.
9. Cypryk, M., Comparison of steric hindrance in silylenium and carbenium cations and their complexes: Natural steric analysis. *Journal of organometallic chemistry* **2003**, *686* (1-2), 164-174.
10. Bessac, F.; Frenking, G., Chemical bonding in phosphane and amine complexes of main group elements and transition metals. *Inorganic chemistry* **2006**, *45* (17), 6956-6964.
11. Staubitz, A.; Robertson, A. P.; Sloan, M. E.; Manners, I., Amine– and phosphine– borane adducts: new interest in old molecules. *Chemical reviews* **2010**, *110* (7), 4023-4078.
12. Rauk, A.; Hunt, I. R.; Keay, B. A., Lewis acidity and basicity: an ab initio study of proton and BF₃ affinities of oxygen-containing organic compounds. *The Journal of Organic Chemistry* **1994**, *59* (22), 6808-6816.
13. Maria, P. C.; Gal, J. F., A Lewis basicity scale for nonprotogenic solvents: enthalpies of complex formation with boron trifluoride in dichloromethane. *The Journal of Physical Chemistry* **1985**, *89* (7), 1296-1304.
14. Flores-Segura, H.; Torres, L. A., Enthalpies of formation of primary, secondary, and tertiary amineborane adducts in tetrahydrofuran solution. *Structural Chemistry* **1997**, *8* (3), 227-232.
15. McLaughlin, D. E.; Tamres, M.; Searles, S., The Addition Compounds of Cyclic Ethers with Boron Trifluoride. *Journal of the American Chemical Society* **1960**, *82* (21), 5621-5625.
16. Anane, H.; El Houssame, S.; El Guerraze, A.; Jarid, A.; Boutalib, A.; Nebot-Gil, I.; Tomás, F., Ab initio molecular orbital study of the substituent effect on ammonia and phosphine–borane complexes. *Journal of Molecular Structure: THEOCHEM* **2004**, *709* (1-3), 103-107.
17. Skancke, A.; Skancke, P., Density functional theory and perturbation calculations on some lewis acid– base complexes. A systematic study of substitution effects. *The Journal of Physical Chemistry* **1996**, *100* (37), 15079-15082.
18. Brown, H. C., Studies in Stereochemistry. VI. The Effect of F-Strain on the Relative Base Strengths of Ammonia and the Methylamines. *Journal of the American Chemical Society* **1945**, *67* (3), 378-380.
19. Brown, H. C., Studies in Stereochemistry. VII. The Effect of F-Strain on the Relative Base Strengths of Ammonia and the Ethylamines. *Journal of the American Chemical Society* **1945**, *67* (9), 1452-1455.
20. Brown, H. C.; Taylor, M. D., Dissociation of the Addition Compounds of Trimethylboron with the Ethylamines; Configuration of the Ethylamines. *Journal of the American Chemical Society* **1947**, *69* (6), 1332-1336.
21. Brown, H. C.; Taylor, M. D.; Sujishi, S., Dissociation of the Addition Compounds of Trimethylboron with the Normal Primary Aliphatic Amines; the Straight-chain Anomaly. *Journal of the American Chemical Society* **1951**, *73* (6), 2464-2467.
22. Brown, H. C.; Gerstein, M., Acid-base studies in gaseous systems. VII. Dissociation of the addition compounds of trimethylboron and cyclic imines; I-strain. *Journal of the American Chemical Society* **1950**, *72* (7), 2926-2933.
23. Gal, J.-F.; Maria, P.-C.; Massi, L.; Mayeux, C.; Burk, P.; Tammiku-Taul, J., Cesium cation affinities and basicities. *International Journal of Mass Spectrometry* **2007**, *267* (1-3), 7-23.
24. Oliveri, I. P.; Maccarrone, G.; Di Bella, S., A Lewis basicity scale in dichloromethane for amines and common nonprotogenic solvents using a zinc (II) Schiff-base complex as reference Lewis acid. *The Journal of organic chemistry* **2011**, *76* (21), 8879-8884.

25. Ruiz, J. M.; Mulder, R. J.; Guerra, C. F.; Bickelhaupt, F. M., Steric effects on alkyl cation affinities of maingroup-element hydrides. *Journal of computational chemistry* **2011**, *32* (4), 681-688.
26. Ruiz, J. M.; Fonseca Guerra, C. I.; Bickelhaupt, F. M., tert-Butyl Cation Affinities of Maingroup-Element Hydrides: Effect of Methyl Substituents at the Protophilic Center. *The Journal of Physical Chemistry A* **2011**, *115* (29), 8310-8315.
27. Lindner, C.; Maryasin, B.; Richter, F.; Zipse, H., Methyl cation affinity (MCA) values for phosphanes. *Journal of Physical Organic Chemistry* **2010**, *23* (11), 1036-1042.
28. Mulder, R. J.; Guerra, C. F.; Bickelhaupt, F. M., Methyl cation affinities of neutral and anionic maingroup-element hydrides: trends across the periodic table and correlation with proton affinities. *The Journal of Physical Chemistry A* **2010**, *114* (28), 7604-7608.
29. Lindner, C.; Tandon, R.; Maryasin, B.; Larionov, E.; Zipse, H., Cation affinity numbers of Lewis bases. *Beilstein journal of organic chemistry* **2012**, *8*, 1406.
30. Deakyne, C. A.; Meot-Ner, M., Methyl cation affinities of nitrogen atoms, oxygen atoms and carbon lone-pair donors. *Journal of Physical Chemistry* **1990**, *94* (1), 232-239.
31. Follet, E.; Zipse, H.; Lakhdar, S.; Ofial, A. R.; Berionni, G., Nucleophilicities and Lewis Basicities of Sterically Hindered Pyridines. *Synthesis* **2017**, *49* (15), 3495-3504.
32. Laurence, C.; Gal, J.-F., *Lewis basicity and affinity scales: data and measurement*. John Wiley & Sons: 2009.
33. Brotzel, F.; Kempf, B.; Singer, T.; Zipse, H.; Mayr, H., Nucleophilicities and carbon basicities of pyridines. *Chemistry-A European Journal* **2007**, *13* (1), 336-345.
34. Schindele, C.; Houk, K.; Mayr, H., Relationships between Carbocation stabilities and Electrophilic reactivity parameters, E: quantum mechanical studies of benzhydryl cation structures and stabilities. *Journal of the American Chemical Society* **2002**, *124* (37), 11208-11214.
35. Faltin, C.; Fleming, E. M.; Connon, S. J., Acrylamide in the Baylis– Hillman reaction: expanded reaction scope and the unexpected superiority of DABCO over more basic tertiary amine catalysts. *The Journal of organic chemistry* **2004**, *69* (19), 6496-6499.
36. Lauwaert, J.; De Canck, E.; Esquivel, D.; Van Der Voort, P.; Thybaut, J. W.; Marin, G. B., Effects of amine structure and base strength on acid–base cooperative aldol condensation. *Catalysis Today* **2015**, *246*, 35-45.
37. Sakthivel, K.; Notz, W.; Bui, T.; Barbas, C. F., Amino acid catalyzed direct asymmetric aldol reactions: a bioorganic approach to catalytic asymmetric carbon-carbon bond-forming reactions. *Journal of the American Chemical Society* **2001**, *123* (22), 5260-5267.
38. Shylesh, S.; Hanna, D.; Gomes, J.; Krishna, S.; Canlas, C. G.; Head-Gordon, M.; Bell, A. T., Tailoring the Cooperative Acid–Base Effects in Silica-Supported Amine Catalysts: Applications in the Continuous Gas-Phase Self-Condensation of n-Butanal. *ChemCatChem* **2014**, *6* (5), 1283-1290.
39. List, B.; Lerner, R. A.; Barbas, C. F., Proline-catalyzed direct asymmetric aldol reactions. *Journal of the American Chemical Society* **2000**, *122* (10), 2395-2396.
40. De Vylder, A.; Lauwaert, J.; Esquivel, D.; Poelman, D.; De Clercq, J.; Van Der Voort, P.; Thybaut, J. W., The role of water in the reusability of aminated silica catalysts for aldol reactions. *Journal of Catalysis* **2018**, *361*, 51-61.
41. Mase, N.; Nakai, Y.; Ohara, N.; Yoda, H.; Takabe, K.; Tanaka, F.; Barbas, C. F., Organocatalytic direct asymmetric aldol reactions in water. *Journal of the American Chemical Society* **2006**, *128* (3), 734-735.
42. Kubota, Y.; Yamaguchi, H.; Yamada, T.; Inagaki, S.; Sugi, Y.; Tatsumi, T., Further Investigations on the Promoting Effect of Mesoporous Silica on Base-Catalyzed Aldol Reaction. *Topics in Catalysis* **2010**, *53* (7-10), 492-499.
43. Brunelli, N. A.; Venkatasubbaiah, K.; Jones, C. W., Cooperative catalysis with acid–base bifunctional mesoporous silica: impact of grafting and co-condensation synthesis methods on material structure and catalytic properties. *Chemistry of Materials* **2012**, *24* (13), 2433-2442.
44. Lauwaert, J.; Moschetta, E. G.; Van Der Voort, P.; Thybaut, J. W.; Jones, C. W.; Marin, G. B., Spatial arrangement and acid strength effects on acid–base cooperatively catalyzed aldol condensation on aminosilica materials. *Journal of Catalysis* **2015**, *325*, 19-25.

45. Frisch, M. J.; Trucks, G. W.; Schlegel, H. B.; Scuseria, G. E.; Robb, M. A.; Cheeseman, J. R.; Scalmani, G.; Barone, V.; Mennucci, B.; Petersson, G. A.; Nakatsuji, H.; Caricato, M.; Li, X.; Hratchian, H. P.; Izmaylov, A. F.; Bloino, J.; Zheng, G.; Sonnenberg, J. L.; Hada, M.; Ehara, M.; Toyota, K.; Fukuda, R.; Hasegawa, J.; Ishida, M.; Nakajima, T.; Honda, Y.; Kitao, O.; Nakai, H.; Vreven, T.; Montgomery, J. A.; Peralta, J. E.; Ogliaro, F.; Bearpark, M.; Heyd, J. J.; Brothers, E.; Kudin, K. N.; Staroverov, V. N.; Kobayashi, R.; Normand, J.; Raghavachari, K.; Rendell, A.; Burant, J. C.; Iyengar, S. S.; Tomasi, J.; Cossi, M.; Rega, N.; Millam, J. M.; Klene, M.; Knox, J. E.; Cross, J. B.; Bakken, V.; Adamo, C.; Jaramillo, J.; Gomperts, R.; Stratmann, R. E.; Yazyev, O.; Austin, A. J.; Cammi, R.; Pomelli, C.; Ochterski, J. W.; Martin, R. L.; Morokuma, K.; Zakrzewski, V. G.; Voth, G. A.; Salvador, P.; Dannenberg, J. J.; Dapprich, S.; Daniels, A. D.; Farkas, Foresman, J. B.; Ortiz, J. V.; Cioslowski, J.; Fox, D. J., Gaussian 09, Revision B.01. Wallingford CT, 2009.
46. Moser, A.; Range, K.; York, D. M., Accurate proton affinity and gas-phase basicity values for molecules important in biocatalysis. *The Journal of Physical Chemistry B* **2010**, *114* (43), 13911-13921.
47. Burk, P.; Kutsar, M. In *Comparative calculations of complexation enthalpies between Lewis bases and borontrifluoride*, Proceedings of the Estonian Academy of Sciences, Chemistry, Estonian Academy Publishers: 2005; pp 154-164.
48. Desmet, G. B.; De Rybel, N.; Van Steenberge, P. H.; D'hooge, D. R.; Reyniers, M. F.; Marin, G. B., Ab-Initio-Based Kinetic Modeling to Understand RAFT Exchange: The Case of 2-Cyano-2-Propyl Dodecyl Trithiocarbonate and Styrene. *Macromolecular rapid communications* **2018**, *39* (2), 1700403.
49. Harris, J. M.; McManus, S. P., Introduction to Nucleophilic Reactivity. ACS Publications: Washington, DC, 1987.
50. Hunter, E. P.; Lias, S. G., Evaluated gas phase basicities and proton affinities of molecules: an update. *Journal of Physical and Chemical Reference Data* **1998**, *27* (3), 413-656.
51. Kempf, B.; Hampel, N.; Ofial, A. R.; Mayr, H., Structure–Nucleophilicity Relationships for Enamines. *Chemistry-A European Journal* **2003**, *9* (10), 2209-2218.
52. Hickmott, P. W., Enamines: recent advances in synthetic, spectroscopic, mechanistic, and stereochemical aspects. *Tetrahedron* **1982**, *38* (14), 1975-2050.
53. Alabugin, I. V., *Stereoelectronic Effects: a bridge between structure and reactivity*. John Wiley & Sons: Hoboken, NJ, 2016.
54. Larionov, E.; Zipse, H., Organocatalysis: acylation catalysts. *Wiley Interdisciplinary Reviews: Computational Molecular Science* **2011**, *1* (4), 601-619.
55. Brunelli, N. A.; Didas, S. A.; Venkatasubbaiah, K.; Jones, C. W., Tuning cooperativity by controlling the linker length of silica-supported amines in catalysis and CO₂ capture. *Journal of the American Chemical Society* **2012**, *134* (34), 13950-13953.

Chapter 4

The role of water in the reusability of aminated silica catalysts for aldol reactions¹

Not only the activity, but also stability is an important factor to take into account when assessing the commercial potential of a catalyst¹. This means that a catalyst should exhibit the same level of activity throughout its lifetime, or be easily regenerated to a similar activity level. Due to the nature of a batch reactor, deactivation cannot be observed separately from the normal time-evolution in the course of a single experiment. Hence, recycling of the spent catalyst in a subsequent experiment is performed in this chapter.

For aldol reactions using homogeneous L-proline, Zovota et al.² identified off-cycle species such as oxazolidinones and oxapyrrolizidines, which limit the catalytic activity, when insufficient water is present. Ouwehand et al.³ reported that an ethylene-bridged ordered periodic mesoporous organosilica material, functionalized with cysteine, exhibits a lower turnover frequency (TOF) in a recycle experiment. Shylesh et al.⁴ have performed gas-phase self-aldol reaction of butanal in a continuous-flow reactor on a cooperative acid-base mesoporous amorphous silica catalyst, but reported no information about catalyst deactivation with time on stream. Clearly, no detailed information about the deactivation behavior of aminated silica materials has been reported yet for aldol reactions.

In the present work, our aim is to systematically investigate the phenomena potentially involved in catalyst deactivation in heterogeneous amine catalyzed aldol reactions. To this end, consecutive experiments in a batch-type reactor have been performed. Using a variety of characterization techniques combined with mechanistic insights, conditions have been

¹ This chapter is published as **De Vylder, Anton, et al. "The role of water in the reusability of aminated silica catalysts for aldol reactions." *Journal of Catalysis* 361 (2018): 51-61.**

identified whereby the recyclability of the aminated mesoporous amorphous silica catalysts for the aldol reaction approaches 100%.

4.1 Experimental procedures

4.1.1 Synthesis of the cooperative acid-base catalyst and the monofunctional base catalyst

The procedure for grafting secondary amine functional groups on mesoporous amorphous silica, and the endcapping of the silanol groups with trimethylsilyl groups, was reported more elaborately before⁵ and is briefly summarized here. Silica gel 60 (grade 7734, Sigma-Aldrich) was used as a catalyst support material. A pellet size range between 63 μm and 210 μm was employed. The support material was first heated at a rate of 2 $^{\circ}\text{C}/\text{min}$ and calcined in air at 700 $^{\circ}\text{C}$ for 6 hours. After calcination, the material was maintained at a temperature of 150 $^{\circ}\text{C}$ to avoid adsorption of moisture. Next, 5 g of the hot support material was suspended in 30 mL of toluene (Sigma-Aldrich, anhydrous, 99.8%). The amine precursor, N-methylaminopropyltrimethoxysilane (MAPTMS, ABCR), was subsequently added with a molar ratio of precursor to free silanol groups of 0.25. The necessary volume of precursor is calculated assuming that, because of the employed calcination procedure, the number of free silanol groups is equal to 1.1 OH nm^{-2} ⁶. To ensure full promotion of each randomly grafted amine site by the silanol groups, at least 1.7 silanol groups are required per amine site⁷. Hence, in this work a ratio of 4 free silanol groups for each methylaminopropyl function was employed. After adding the precursor, the mixture was refluxed for 24 hours at 110 $^{\circ}\text{C}$ under an argon atmosphere. The obtained catalyst was then filtered and subsequently stirred in 250 mL chloroform (>99.8%, <50 ppm H_2O , Carl Roth) for 4 hours. After vacuum drying for 24 hours at room temperature, the cooperative acid–base catalyst was ready to be used in catalytic experiments. A desiccator was used for storage of the catalysts in order to avoid modifications due to the presence of atmospheric water vapor.

To obtain the monofunctional base catalyst, the silanol groups of the cooperative material were endcapped with trimethylsilyl groups^{7,8}. For this, 5 g of the dried cooperative acid-base catalyst was completely covered with 100 mL of 1,1,1,3,3,3-hexamethyldisilazane (99%, HMDS, ABCR). The mixture was then stirred at room temperature for 4 hours, subsequently filtered, and stirred in 250 mL chloroform (>99.8%, <50 ppm H_2O , Roth) for 4 hours. After

vacuum drying for 24 hours at room temperature, the monofunctional base catalyst was ready to be used in catalytic experiments. This catalyst was also stored in a desiccator.

4.1.2 Characterization of the fresh and spent catalysts

Nitrogen adsorption-desorption measurements were carried out at $-196\text{ }^{\circ}\text{C}$, using a Micromeritics Tristar II surface area and porosity analyzer. The specific surface area and pore volume were determined using the Brunauer–Emmett–Teller (BET) method. The average pore size and pore volume was obtained using the Barrett–Joyner–Halenda (BJH) method.

The concentration of amine groups was determined via elemental (CHN) analysis. These measurements were performed on a Thermo Flash 2000 elemental analyzer using V_2O_5 as catalyst, in order to ensure the total oxidation of the sample. The mass percent of nitrogen in the sample is obtained by referring the obtained peak area to a calibration curve of methionine (USP, 99%) that was obtained prior to the measurements. Conversion to the concentration of active sites, in mol per gram, was then performed with the molar mass of nitrogen.

The presence of organic species on the catalyst surface, both before and after reaction, was determined with Diffuse Reflectance Infrared Fourier Transform (DRIFT) spectroscopy, as well as Raman spectroscopy. The DRIFT spectra were recorded using a Nicolet 6700 by Thermo Scientific with a liquid nitrogen cooled MCT-A detector, using a Graseby Specac diffuse reactant cell, operating in vacuum at $140\text{ }^{\circ}\text{C}$. The Raman spectroscopy was performed on a NXR FT-Raman module of Thermo Scientific, with a laser of 1064 nm and an InGaAs detector. A resolution of 4 cm^{-1} was used on a total of 512 scans per sample at a laser intensity of 0.31 W.

The ^{13}C CP/MAS NMR spectra were recorded at 100.61 MHz on a Bruker Avance III HD 400 WB NMR spectrometer at room temperature. An overall of 1000 free induction decays were accumulated. The excitation pulse and recycle time were respectively 6 ms and 2 s. Chemical shifts were measured relative to tetramethylsilane standard. All samples were dried at $120\text{ }^{\circ}\text{C}$ for 24 hours prior to analysis.

UV-Vis diffuse reflection measurements were performed using a Varian Cary 500 UV-Vis-NIR spectrophotometer equipped with an internal BaSO_4 -coated integrating sphere.

4.1.3 Determination of the water content in stock organic solvents

To quantify the amount of water in the organic solvent dimethylsulfoxide (DMSO, $\geq 99\%$, FG, Sigma-Aldrich) and acetone (99.6%, Acros), Karl-Fischer titrations were performed on a

MKC-501 coulometric cell with diaphragm (Kyoto Electronics). For DMSO, anolyte solution Hydranal Coulomat AG (Sigma-Aldrich) and catholyte solution Hydranal Coulomat CG (Sigma-Aldrich) were used. For acetone, methanol-free anolyte solution Hydranal Coulomat AK (Sigma-Aldrich) and methanol-free catholyte solution Hydranal Coulomat CG-K (Sigma-Aldrich) were used.

Karl-Fischer titrations indicated an average water content in stock acetone of 0.31 ± 0.05 wt% and in DMSO of 0.09 ± 0.03 wt%. Both acetone and DMSO were stored under an argon atmosphere in order to minimize any absorption of ambient water. It was confirmed that storage under these circumstances during the course of the experimentation did not significantly change the amount of water in both DMSO as well as in acetone.

4.1.4 Drying of stock acetone

In order to further decrease the amount of water in the reactor, some experiments were performed with dried acetone. To remove water, 100 mL acetone was poured on 10 g freshly regenerated 3 Å molecular sieves (Sigma-Aldrich) and thoroughly mixed for one hour. This resulted in a 3-fold decrease in the water content to 0.09 ± 0.02 wt%.

4.1.5 Catalytic performance evaluation of the fresh and spent catalysts in the batch reactor

The catalyst performance was evaluated in a batch-type reactor (Parr 4560 mini, 300 mL). The detailed procedure has been reported previously⁵ and is also briefly summarized here. The considered benchmark reaction is the aldol reaction of acetone (99.6%, Acros) with 4-nitrobenzaldehyde (99%, Acros), resulting in 4-hydroxy-4-(4-nitrophenyl)butan-2-one as aldol product and 4-(4-nitrophenyl)-3-buten-2-one as enone product.

To start an experiment, the reactor was first loaded with an amount of catalyst equivalent with 0.1 mmol active amine sites, 51.7 g to 55.0 g DMSO as solvent, 0.5 g to 3 g water added (double deionized, Milli-Q[®]), and 0.25 g methyl 4-nitrobenzoate (> 99%, Sigma-Aldrich) as internal standard. This mixture was then heated to 55 °C, under constant stirring. Acetone (45 g) was separately heated to 55 °C and was used to dissolve 0.45 g 4-nitrobenzaldehyde before injecting in the reactor. Acetone was added in excess, in order to suppress the direct interaction of 4-nitrobenzaldehyde with the amine site. The amount of solvent was adapted according to the amount of water that is added to the reactor in order to avoid effects of a concentration change on the measured kinetics. The temperature in the reactor was maintained at 55 °C using

a PID-controller (CAL 9500P), with a thermocouple inside the reactor vessel. This PID controller steered both an electrical heating jacket as well as a cooling unit for an adequate temperature control. The reaction mixture was mechanically stirred at 600 rpm. The time of injection was taken as the start of the reaction ($t = 0$). The reaction was monitored for 4 hours by taking a sample (0.3 mL) of the reaction mixture every 15 minutes during the first hour, and subsequently every 30 minutes for the remaining 3 hours. For each experiment, the total decrease of reaction volume due to sampling was less than 5% whereby the effect of sampling on the kinetic data is considered to be negligible.

After the reaction, the spent catalyst was removed from the reactor, filtered, and stored in a desiccator, in order to avoid atmospheric water vapor from interacting with the catalyst. All recycling experiments were performed by repeating the procedures described above using the recovered spent catalyst within maximum 24 hours after the previous run. In order to characterize the surface intermediates on the spent catalysts with Raman spectroscopy and ^{13}C -NMR, the catalysts were additionally stirred in 100 mL chloroform (>99.8%, <50 ppm H_2O , Carl Roth) for 4 hours, filtered, and vacuum dried for 24 hours.

4.1.6 Sample analysis and defining the catalyst activity

The reaction samples were analyzed using a reversed-phase high-performance liquid chromatograph (RP-HPLC), from Agilent (1100 series) using the same procedure as reported before⁷. The HPLC Eclipse XDB-C18 column was operated at 30 °C using a gradient method with water (0.1% trifluoroacetic acid, Acros) and 30 v% to 62 v% acetonitrile (HPLC grade, Acros) as solvents. This method separates all the components in a period of 14 min. The components were identified using a UV-detector with a variable wavelength that has been programmed for an optimal absorption for each component. Quantification of the different components in the reaction mixture was performed by relating the surface areas of the component peaks to the amount of internal standard added to the reactor. The catalyst activity in the batch reactor was quantified by the TOF, which was determined from the slope of the initial linear part of the conversion of 4-nitrobenzaldehyde as a function of reaction time, the concentration of active amine sites and the initial concentration of 4-nitrobenzaldehyde. Repeat experiments have indicated that the experimental error calculated as the 95% confidence interval, was below 5%. With the rule of error propagation, it was determined that ratios of the TOF values in the batch reactor have an experimental error of about 10%.

4.2 Results and discussion

4.2.1 Catalyst characterization and validation of the synthesis procedure

The specific BET surface area, average pore size, and total pore volume of the silica gel support and the synthesized catalysts were determined from the nitrogen adsorption–desorption isotherms and are summarized in Table 4-1. The functionalization of the pristine support material, and further endcapping of the silanol groups with trimethylsilyl groups, caused a small decrease in surface area and pore volume. This decrease can be directly related to a decrease in free volume and an increase in catalyst mass, which is typically observed after the functionalization of these materials⁹. The catalyst, however, retained its mesoporous structure and average pore size of 5 nm after functionalization and endcapping of the silanol groups.

The presence of methylaminopropyl groups on the surface was verified with Diffuse Reflectance Infrared Fourier Transform (DRIFT) spectroscopy, as can be seen in Figure B-1 in Appendix B. In the pristine silica gel support material, a pronounced narrow peak at 3745 cm⁻¹ indicates the presence of free silanol groups on the surface. After reaction with N-methylaminopropyltrimethoxysilane (MAPTMS), several bands appeared in the region between 2800 cm⁻¹ and 3000 cm⁻¹, characteristic of the C-H stretching vibrations of the methylaminopropyl group attached to the surface⁷. At 3305 cm⁻¹ a small, broad peak indicates the presence of N-H vibrations. The peak that remains at 3745 cm⁻¹ confirms that free silanol groups were still present after grafting. When the catalyst was treated with HMDS to endcap the residual silanol groups, the peak at 3745 cm⁻¹ effectively disappeared. The endcapping of the silanol groups resulted in an increased intensity of the C-H stretching vibrations at 2960 cm⁻¹ from the trimethylsilyl groups that replaced the silanol groups. Using CHN analysis, the amine loading was determined to be 0.17 mmol/g. Using HMDS as a rough silanol titrator, the amount of silanol groups was estimated at 0.69 mmol/g. This indicates that there are at least 4 silanol groups available for each amine site in the cooperative acid-base catalyst, as was targeted during the catalyst synthesis.

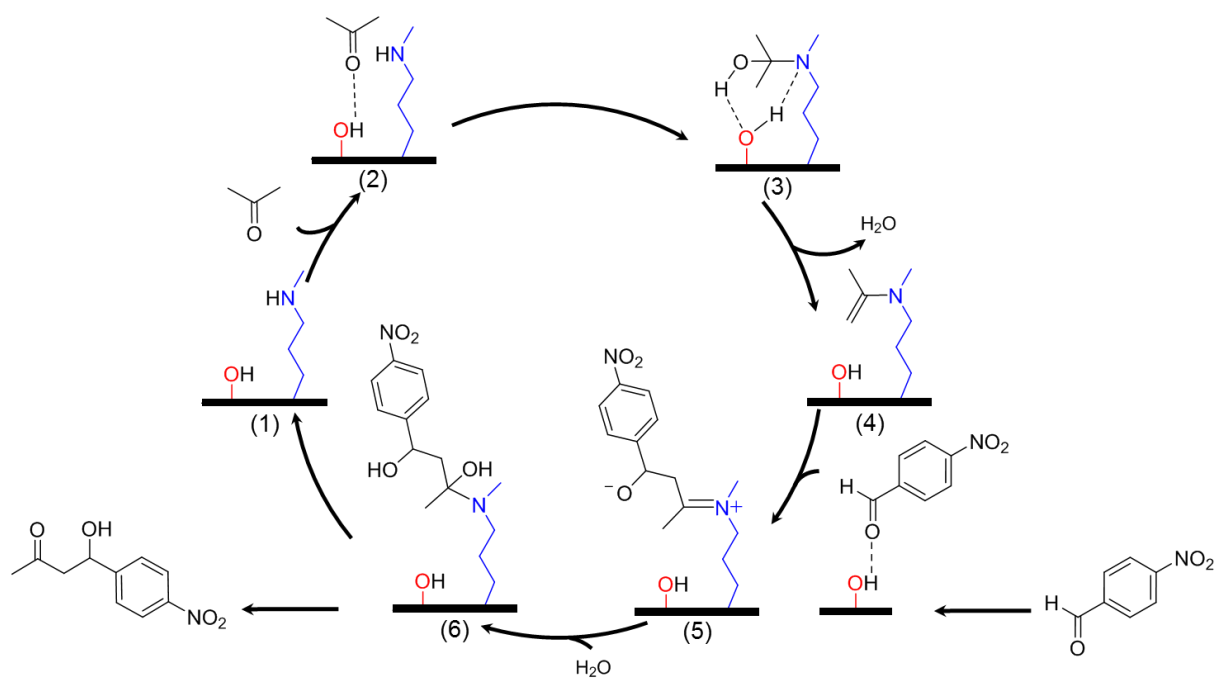
Table 4-1. Catalyst properties, for both the cooperative acid-base catalyst as well as the monofunctional base catalyst, fresh and spent in the aldol reaction of acetone with 4-nitrobenzaldehyde. BET surface area, pore size and pore volume are determined via nitrogen adsorption–desorption measurements.

	BET surface area ± 30 (m ² /g)	Pore size ±0.3 (nm)	Pore volume ± 0.04 (cm ³ /g)
Silica gel 60 support material	451	5.7	0.70
Cooperative acid-base catalyst			
Fresh	314	5.6	0.52
Spent	296	5.6	0.48
Monofunctional base catalyst			
Fresh	272	5.4	0.45
Spent	280	5.2	0.44

4.2.2 Catalytic performance in the aldol reaction of acetone with 4-nitrobenzaldehyde

The proposed reaction mechanism for the aldol reaction using a methyl substituted secondary amine promoted by surface silanol groups is given in Scheme 4-1. The catalytic cycle starts with the formation of a hydrogen bond between the free silanol group (**1**) and the oxygen of the carbonyl group of acetone (**2**). Next, the free electron pair of the amine attacks the activated carbonyl group of acetone, and a carbinolamine (**3**) is formed via a proton-transfer, assisted by the surface silanol group. This carbinolamine dehydrates, yielding an enamine intermediate (**4**), which then attacks the carbonyl group of an activated 4-nitrobenzaldehyde molecule and forms a new carbon-carbon bond. The formed iminium intermediate (**5**) is hydrolyzed towards the product carbinolamine (**6**) and, subsequently, desorbs from the active site as the aldol product. When the silanol groups are endcapped with trimethylsilyl groups, the initial activation by hydrogen-bonding, as well as the cooperativity in proton transfer reactions, are absent which results in a lower TOF.

A potential side-reaction for both the cooperative and monofunctional catalyst is the reaction of the amine with the carbonyl group of 4-nitrobenzaldehyde, which yields an iminium ion. This iminium can then react with acetone, via a Mannich type mechanism, and yield the enone as a primary product^{10, 11}. However, the direct interaction of 4-nitrobenzaldehyde with the amine is suppressed by using a 260 molar ratio excess of acetone.



Scheme 4-1. Proposed enamine catalytic reaction cycle of the aldol reaction of acetone with 4-nitrobenzaldehyde, catalyzed by a secondary cooperative aminated silica catalyst^{4, 7, 12}.

Preliminary experiments were performed at 55 °C using 45 g acetone in 55 g DMSO, with 0.1 mmol active amine sites, and 0.45 g 4-nitrobenzaldehyde. DMSO is chosen as solvent because of its full miscibility with water, allowing to investigate the effect of different amounts of water on the catalyst stability and activity. To adequately describe these effects, the initial water content in the organic solvents should also be known. Hence, using coulometric Karl-Fischer titration, the initial water content in the reactor, using stock acetone and DMSO, was determined at 0.19 wt%. Under these conditions, the cooperative acid-base catalyst exhibited a TOF of $7.04 \pm 0.40 \cdot 10^{-4} \text{ s}^{-1}$ in the aldol reaction. While, at the same reaction conditions, the monofunctional base catalyst exhibited a lower TOF of $2.56 \pm 0.13 \cdot 10^{-4} \text{ s}^{-1}$, as expected from previous research⁷. The aldol and enone product selectivity amounted to 73% and 27% respectively, for the cooperative acid-base catalyst and 77% and 23% respectively for the monofunctional base catalyst, and remained constant throughout the whole experiment. When reusing the spent catalyst in a second experiment, only 38% of the initial TOF was obtained for the cooperative acid-base catalyst while 77% of the initial TOF was retained for the monofunctional base catalyst.

To obtain insights in the cause of this reduction in initial TOF, characterization of the spent catalysts was performed. The specific BET surface areas, average pore sizes, and total pore volumes of the spent catalysts are also listed in Table 4-1. The spent catalysts exhibited a slight decrease in surface area and pore volume, but retained their average pore size of 5.0 nm.

However, the CHN elemental analysis indicated a nitrogen content increase of 60% for the spent cooperative acid-base catalyst and a 15% increase for the spent monofunctional base catalyst. Moreover, as will be discussed in more detail below, the originally white catalyst changed to dark yellow and retained this color even after additional stirring in chloroform and drying. This color change, together with the higher nitrogen content, indicates that the changes in catalytic behavior upon recycling may be caused by surface species that remain on the catalyst.

Raman spectroscopy of these spent catalysts was performed to identify the organic groups in the species remaining on the catalyst surface. The Raman spectrum is displayed in Figure 4-1a for the spent cooperative acid-base catalyst, and Figure 4-1b for the spent monofunctional base catalyst. The spectra for both catalysts exhibit sharp peaks at 1630 cm^{-1} , 1590 cm^{-1} , 1340 cm^{-1} and 1110 cm^{-1} . These correspond to, respectively, a C=C stretching band conjugated with an aromatic group, an aromatic C=C stretching, a symmetric NO_2 stretch and a weak band due to aromatic in-plane C-H deformation vibrations¹³. The bands below 300 cm^{-1} are characteristic of the lattice vibrations of the Si-O-Si network.

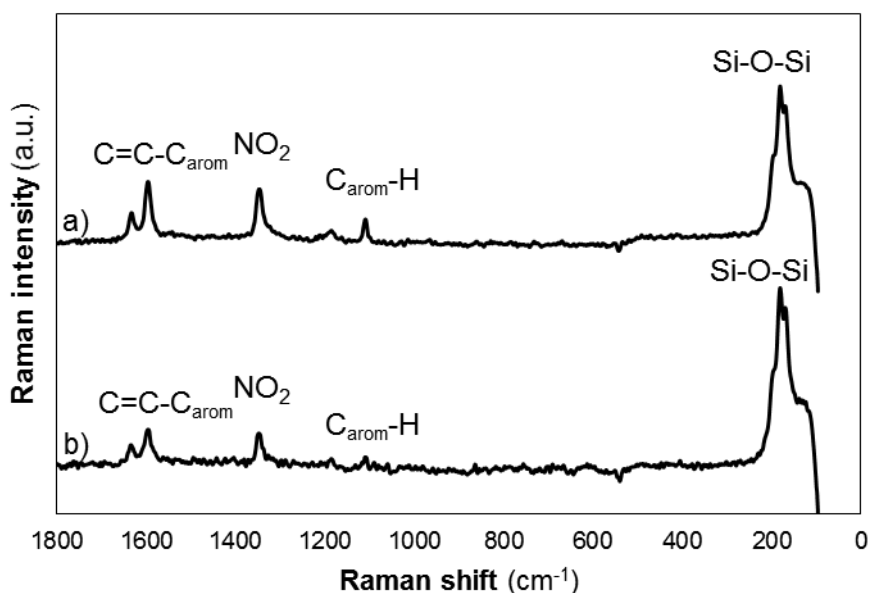


Figure 4-1. Raman spectrum of the spent cooperative acid-base catalyst (a) and spent monofunctional base catalyst (b).

Further characterization of the spent catalyst was performed with ^{13}C cross-polarization/magic-angle-spinning (CP/MAS) NMR spectroscopy. The spectrum is displayed in Figure 4-2 for the spent cooperative acid-base catalyst. The peak at 50 ppm can be associated with residual methoxy groups from the amine precursor that did not react with the surface silanol groups. The three peaks at 8, 22 and 49 ppm are associated with the sp^3 carbon atoms of the propyl chain and the peak at 33 ppm is associated with the methyl function of the secondary

amine. Additional bands are observed at 147 ppm (**b**), originating from an aromatic carbon attached to a nitro group and 127 ppm (**c**) and 123 ppm (**d**) from aromatic carbons. The shoulder peak at 150 ppm (**a**) can be assigned to the aromatic carbon in para-position of the nitro group when bounded to an sp^3 carbon. When bonded to a sp^2 carbon, the corresponding peak appears around 144 ppm and is indistinguishable from the large peak at 147 ppm. The small broad peak at 70 ppm could potentially be from an sp^3 carbon attached to both the aromatic ring and an alcohol function, while the small peak at 38 ppm could be assigned to an sp^3 carbon atom attached to the carbon atom at 70 ppm and an sp^2 carbon atom.

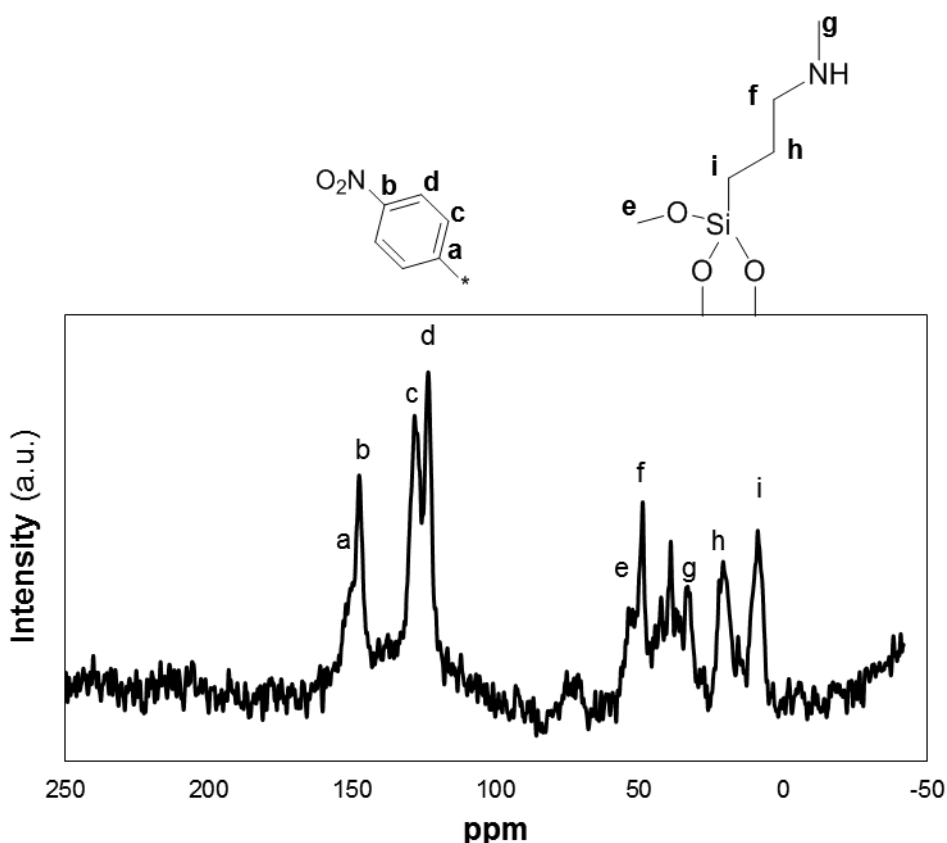


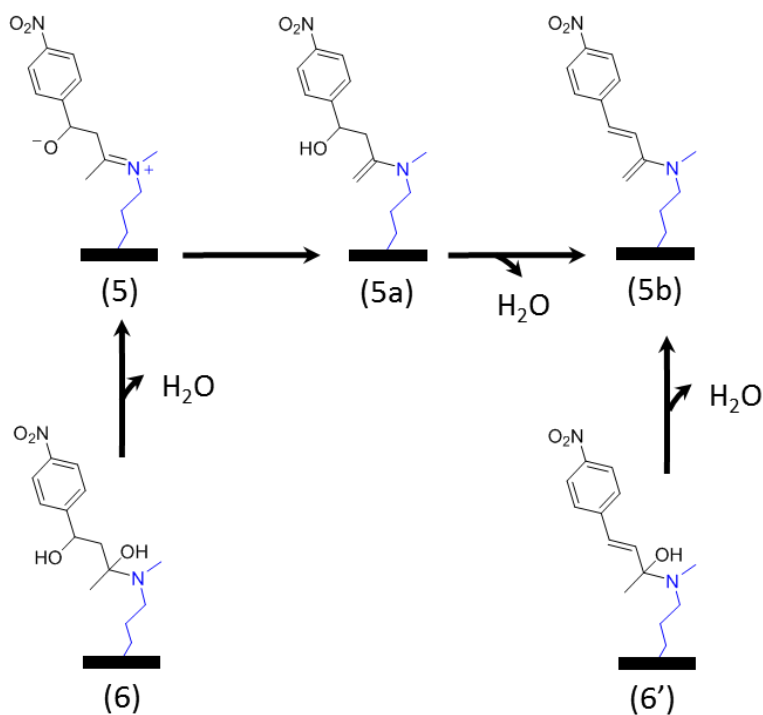
Figure 4-2. ^{13}C CP/MAS NMR spectrum of the spent cooperative acid-base catalyst. The grafted secondary amine can be identified in the spectrum, as well as the carbon atoms originating from the aromatic ring with a nitro substituent.

The Raman and ^{13}C -NMR spectra indicate that the species on the surface of the spent catalysts are derivatives of 4-nitrobenzaldehyde. Due to the absence of peaks in the ^{13}C -NMR between 170 ppm and 180 ppm and in the Raman spectrum at 1700 cm^{-1} , corresponding to carbonyl groups from aldehydes or ketones, physisorbed 4-nitrobenzaldehyde, or physisorbed products, can be excluded. Also, the direct addition of 4-nitrobenzaldehyde with the secondary amine did not lead to the observed Raman peaks. This is shown in Figure B-2 (Appendix B),

which is a Raman spectrum of a catalyst that was exposed to 4-nitrobenzaldehyde in DMSO, without acetone, under reaction conditions.

Several possible surface species, stemming from the iminium intermediate (**5** in Scheme 4-1), are proposed in Scheme 4-2. This iminium intermediate (**5**) is formed after the attack of the enamine on the carbonyl group of 4-nitrobenzaldehyde, or from the aldol product readsorption (**6**) and dehydration. It can subsequently rearrange towards the enamine form (**5a**). Upon dehydration of (**5a**), the enamine form of the condensation product (**5b**) is formed. This latter species can also be formed from the dehydration of the carbinolamine (**6'**).

Because charged species are unlikely to exist on a dried catalyst, the iminium intermediate is expected to only be stable under liquid-phase conditions. Any iminium intermediates that are on the surface of the catalyst after removal of the material from the reactor by filtration, are expected to convert to (**5a**), or directly dehydrate to (**5b**). The 4 different candidate species to be present on the surface of a spent catalyst correlating with the Raman spectroscopy and ^{13}C -NMR characterization results, are (**5a**), (**5b**), (**6**) and (**6'**) in Scheme 4-2. Recent computational research on the relative stability of enamines¹⁴ has shown that conjugated enamines, such as dienamines with phenyl groups, are thermodynamically stable due to their conjugation effects. Possibly, the enamine species (**5b**) thus blocks access to the catalytic site when recycling the catalyst in a subsequent experiment.



Scheme 4-2. Possible species on the surface of a spent catalyst corresponding with the characterization results and their proposed formation pathways. The iminium intermediate species (**5**) from the catalytic cycle in Scheme 4-1, or from the aldol product readsorption via (**6**), can further dehydrate into a conjugated species (**5b**) via its enamine intermediate (**5a**). Enone product readsorption via (**6'**) also yields the conjugated species (**5b**).

Water was co-fed in the reactor to enhance the hydrolysis of the iminium intermediate (5) in the catalytic cycle and, hence, prevent the formation of the site blocking species. In this work, the polar solvent DMSO was chosen because of its complete miscibility with water in a broad range of conditions. Even though this solvent does not yield the highest turnover frequencies (TOF) for amine catalyzed aldol reactions, it allows to perform a mechanistic investigation of the deactivation phenomena and the effect of co-feeding water.

4.2.3 Effect of water on the reusability of aminated silica catalysts for aldol reactions in the batch reactor

Several catalytic experiments were performed with a varying amount of water added to the starting mixture of the batch reactor. Care was taken that the amount of solvent, i.e., DMSO, was adapted to compensate for the volume of the water added to the system. Experiments were also performed with dried acetone, resulting in a total water content of 0.09 wt% in the reactor. After 4 hours of reaction, the spent catalysts were removed from the reactor, dried, and reused in a second experiment under identical operating conditions, or stored in a desiccator for further characterization.

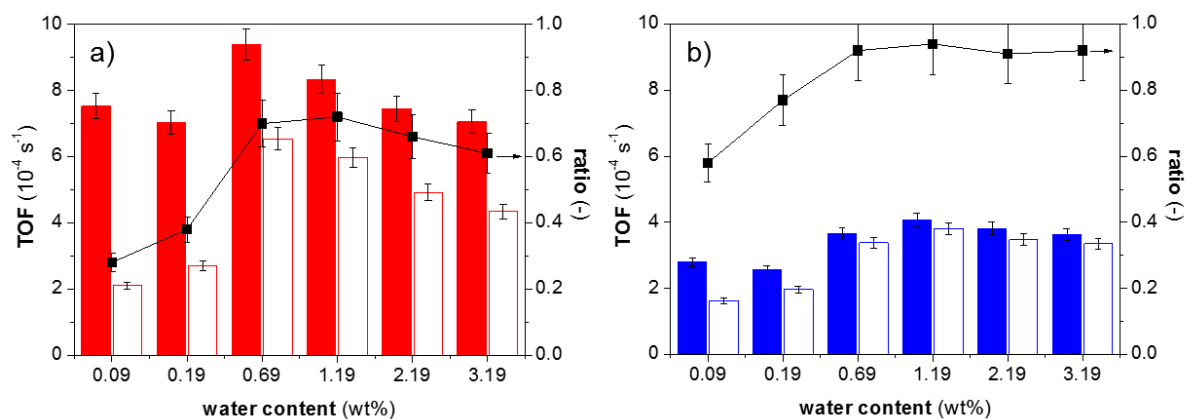


Figure 4-3. Turnover frequency (TOF – s^{-1}) for the aldol reaction of acetone with 4-nitrobenzaldehyde, using a cooperative acid-base catalyst (a, red) and a monofunctional base catalyst (b, blue) as a function of the amount of water in the reactor. Full bars represent the first run, empty bars the second run, and the right axis indicates the ratio between the TOF observed in the second and the first run. Lines are a guide for the eye. Absolute water content in the reactor has been determined with Karl-Fischer titrations. Error bars indicate a 95% confidence interval. ($T = 55\text{ }^{\circ}\text{C}$, 0.45 g 4-nitrobenzaldehyde, 45 g acetone, 52 g – 55 g DMSO, 0.20 g methyl 4-nitrobenzoate, 0.5 g to 3.0 g water added, 0.31 wt% water in stock acetone, 0.09 wt% water in dried acetone, 0.09 wt% water in stock DMSO)

The effect of water on the activity of the cooperative acid-base and the monofunctional base catalysts, as indicated by the TOF, is displayed in Figure 4-3a and Figure 4-3b respectively. When 0.69 wt% water was present in the reactor with the cooperative acid-base catalyst, the

TOF of the first run amounted to $9.38 \pm 0.47 \cdot 10^{-4} \text{ s}^{-1}$, compared to $7.04 \pm 0.35 \cdot 10^{-4} \text{ s}^{-1}$ without water addition. For the monofunctional base catalyst, an increase from $2.56 \pm 0.13 \cdot 10^{-4} \text{ s}^{-1}$ to $3.66 \pm 0.18 \cdot 10^{-4} \text{ s}^{-1}$ is observed. Such an enhancement in the reaction rate has also previously been observed when a small amount of water is co-fed when using homogeneous amino-acid catalysts¹⁵. This can be related to the increased hydration of the reactive iminium species on the catalytic surface, which leads to an increased product desorption rate. When the water amount was further increased up to 3.19 wt%, the TOF lowered again to $7.06 \pm 0.35 \cdot 10^{-4} \text{ s}^{-1}$ for the cooperative acid-base catalyst. This can be attributed to (i) an unfavorable shift in the carbinolamine-enamine equilibrium^{2, 10}, (ii) protonation of amine groups and (iii) hydrogen bonding of amine sites with surface silanol groups, assisted by water molecules¹⁶. The decrease in TOF with 3.19 wt% water also occurs for the monofunctional base catalyst, albeit to a lesser extent. This indicates that endcapping the silanol groups, and thereby increasing the hydrophobicity of the support, decreases its susceptibility to the negative effects of water.

During a single experiment, the selectivity rapidly converged to a constant value. Additionally, when more water was included in the starting mixture in the reactor, a pronounced shift in selectivity towards the aldol product was observed for both catalysts (Figure B-3 in Appendix B). Hence, it can be concluded that the aldol product and enone product are in equilibrium at the investigated conditions, and the addition of water shifts this equilibrium to the side of the aldol product.

The catalyst reusability ratios are calculated as the ratio of TOF in the second run to that in the first run, and are also displayed in Figure 4-3. The reusability of the cooperative acid-base catalyst increased from 28% with 0.09 wt% water to a maximum of 70% with 0.69 wt% water. Correspondingly, the reusability of the monofunctional base catalyst increased from 58% with 0.09 wt% water to 92% with 0.69 wt% water, and remained constant for higher water amounts. The presence of silanol groups in the cooperative acid-base catalyst therefore seems to limit the reusability that can be achieved. Yet, almost full reusability of the monofunctional base catalyst can be achieved with at least 0.69 wt% water. This demonstrates how deactivation of the amine active sites can be minimized by the addition of water. The catalyst characterization data in Table B-1 and Table B-2 (Appendix B) shows that, at the time scale of these batch experiments, structural degradation of the porous silica network is not a pronounced deactivation phenomenon for both types of catalyst.

It should further be noted that when a spent monofunctional base catalyst, after use under dry reaction conditions, was recycled for a second experiment with 2.19 wt%, only 70% reusability was achieved. This shows that, while such an amount of water can prevent the

deactivation of the amine active site by favoring the hydrolysis of the iminium intermediate during the first run, it cannot fully regenerate the already deactivated sites after a first run in which insufficient water was used.

Raman spectra were also recorded for each spent catalyst, and are plotted as a function of the water amount in the reactor in Figure 4-4. It can be seen that the peaks at 1630 cm^{-1} , 1600 cm^{-1} , 1340 cm^{-1} and 1110 cm^{-1} , associated with the aromatic species bearing a nitro group, gradually disappear when more water is present in the reactor.

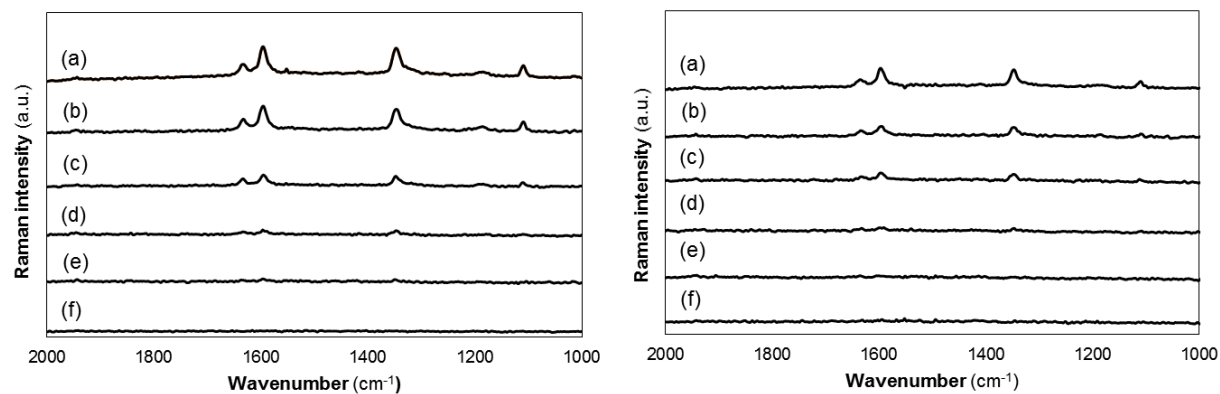


Figure 4-4. Raman spectrum of the spent cooperative acid-base catalyst (left) and the spent monofunctional base catalyst (right) (a: 0.09 wt% water, b: 0.19 wt% water, c: 0.69 wt% water, d: 1.19 wt% water, e: 2.19 wt% water and f: 3.19 wt% water).

Additionally, a ^{13}C -NMR spectrum was recorded for a cooperative acid-base catalyst that was spent in a reaction with 1.19 wt% water in the reactor and is displayed in Figure 4-5. Also here, the characteristic peaks of the nitro-containing aromatic species decreased considerably due to the addition of water.

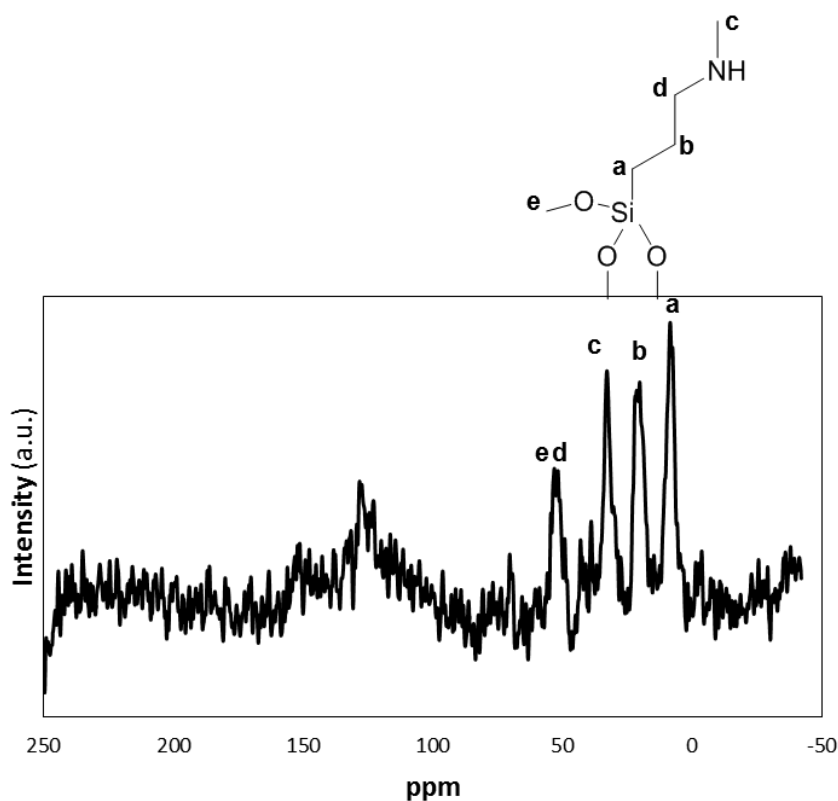


Figure 4-5 ^{13}C -NMR result of a cooperative acid-base catalyst, spent in the aldol reaction of 4-nitrobenzaldehyde with acetone, using 1.19 wt% water in the reactor.

As mentioned above, a distinct change in color of the spent catalyst was observed after reaction, which persisted after stirring the catalyst in chloroform. By co-feeding water, it appears that the colorization of the spent catalyst becomes less pronounced as a function of the amount of water, as is shown in Figure 4-6. Removing inherently present water from the stock acetone solution by drying caused the cooperative acid-base catalyst to appear dark red after being spent.

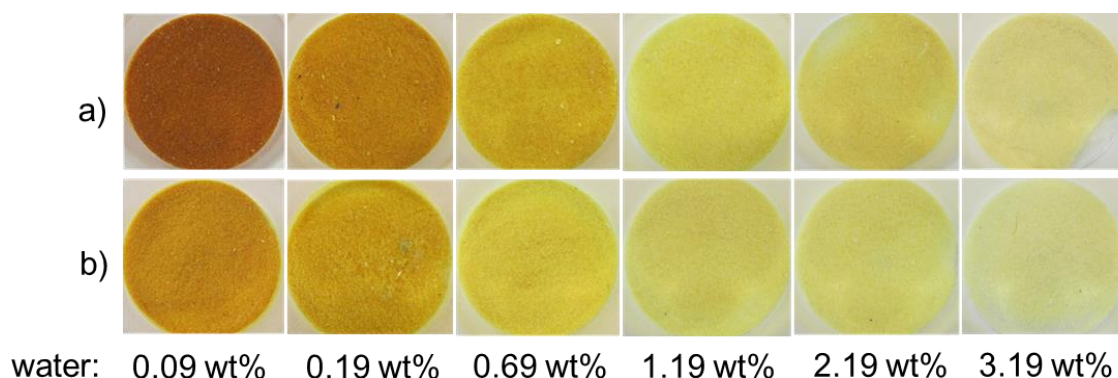


Figure 4-6. Spent catalyst color as a function of the water amount in the reactor. (a) Cooperative acid-base, (b) monofunctional base catalyst

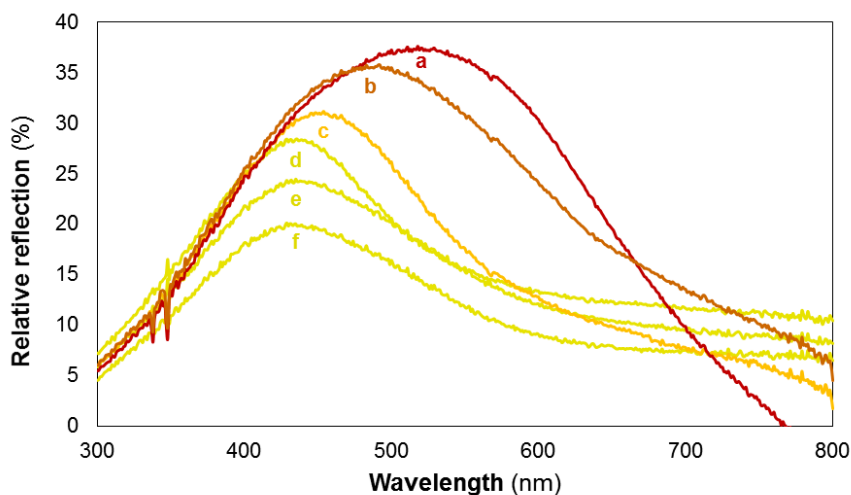


Figure 4-7: Percentage UV-Vis reflection as a function of wavelength of the spent cooperative acid-base catalysts, relative to a fresh catalyst (a: 0.09 wt% water, b: 0.19 wt% water, c: 0.69 wt% water, d: 1.19 wt% water, e: 2.19 wt% water and f: 3.19 wt% water).

UV-Vis reflection characterization of the spent cooperative acid-base catalysts was performed and is displayed in Figure 4-7. When more water was added to the reactor, the peak intensity of the spent catalyst is decreased. This indicates that less chromophoric surface species are present on a spent catalyst when more water is added to the reactor. The color variations of the spent monofunctional base catalyst seem to be shifted slightly towards the colors of the cooperative acid-base catalysts spent after having used a higher amount of water. Hence, the same trends are expected for the monofunctional base catalysts.

The peak maximum for the catalysts spent with 0.09 wt% of water is at 520 nm, while the peak maximum for the catalysts spent with at least 1.19 wt% of water is located at 432 nm. This shift to shorter wavelengths is a typical phenomenon that can be seen when the degree of conjugation in an organic compound decreases. Since this shift correlates with the increased reusability, a more highly conjugated species such as 5b (Scheme 4-2) is believed to be responsible for the deactivation of the catalyst. The possible chromophoric species at 432 nm, present on the spent catalysts after use with at least 1.19 wt% water, could then correspond to the more hydrated species 5a, 6 and 6' (Scheme 4-2).

As mentioned above, the nitrogen content on the spent catalyst was higher than that on the fresh catalyst. Hence, the catalysts spent using different amounts of water in the reactor were subject to CHNS elemental analysis. The observed amount of nitrogen on the spent catalyst as a function of the amount of water used in the experiment is expressed relative to the total amount of active sites on a fresh catalyst, and is defined as 'excess N' in Figure B-4 in Appendix B. Since possible leaching effects are masked by the increase in nitrogen content, it

has also been verified that there was no active site leaching by performing batch experiments with 4-chlorobenzaldehyde as a substrate, and ethyl-4-methylbenzoate as internal standard, under the same reaction conditions. These results are also included in the Appendix B, Figure B-4, and prove that leaching is not a significant deactivation factor at the investigated batch reactor conditions. The increase in the nitrogen content of the spent catalyst compared to the fresh catalyst can thus be used to quantify the fraction of sites that are covered with a nitrogen containing species, such as the ones proposed in Scheme 3. From the results in Figure 4S it is clear that, when using 0.09 wt% water, also denoted as ‘dry’ conditions, the fraction of covered sites is significantly larger (90%) on the spent cooperative acid-base catalyst than on the spent monofunctional base catalyst (40%). This could be the result of the relatively low amount of water with respect to active sites under these ‘dry’ conditions, i.e., with 0.09 wt% of water, only 5 mmol of water is available for 0.1 mmol amines and 0.4 mmol silanol groups. Hence, adsorption of several water molecules on the hydrophilic silanol groups can already significantly lower the amount of water molecules available for iminium ion hydrolysis. When no silanol groups are present for water adsorption, as is the case in the monofunctional base catalyst, more water is available for iminium ion hydrolysis. When a water excess is present, i.e. 0.69 wt% or more, this discrepancy between both catalysts disappears.

It can be concluded from the Raman spectra, the UV-Vis reflection spectra, the elemental CHNS analysis and the ^{13}C -NMR, that water reduces the amount of surface species that remain on a spent catalyst and increases the catalyst’s reusability. It however appears that, despite having no remaining surface species on the amine site, the activity of the cooperative acid-base catalyst can only be regained for 70% by adding water. To further investigate the deactivation behavior of the cooperative acid-base catalyst, experiments with a continuous-flow reactor are performed in Chapter 5.

4.3 Conclusions

For the first time, the reusability of aminated mesoporous amorphous silica catalysts was thoroughly investigated for the aldol reaction of 4-nitrobenzaldehyde with acetone in DMSO. It is found that, under ‘dry’ reaction conditions, both the cooperative acid-base catalyst, as well as the monofunctional base catalyst, exhibit a significantly poorer performance in consecutive batch experiments. Spent catalyst characterization using Raman spectroscopy, ^{13}C NMR, and UV-Vis characterization, allowed identifying site blocking species originating from the iminium intermediate in the catalytic cycle. To increase the hydration rate of this iminium

intermediate and, hence, reduce their conversion into site blocking species, water should be added to the batch reactor. This results in an increased reusability up to 70% for the cooperative acid-base catalyst and an almost complete reusability for the monofunctional base catalyst.

4.4 References

1. Hammond, C., Intensification studies of heterogeneous catalysts: probing and overcoming catalyst deactivation during liquid phase operation. *Green Chemistry* **2017**, *19*, 2711-2728.
2. Zotova, N.; Franzke, A.; Armstrong, A.; Blackmond, D. G., Clarification of the role of water in proline-mediated aldol reactions. *Journal of the American Chemical Society* **2007**, *129* (49), 15100-15101.
3. Ouwehand, J.; Lauwaert, J.; Esquivel, D.; Hendrickx, K.; Van Speybroeck, V.; Thybaut, J. W.; Van Der Voort, P., Facile Synthesis of Cooperative Acid–Base Catalysts by Clicking Cysteine and Cysteamine on an Ethylene-Bridged Periodic Mesoporous Organosilica. *European Journal of Inorganic Chemistry* **2016**.
4. Shylesh, S.; Hanna, D.; Gomes, J.; Krishna, S.; Canlas, C. G.; Head-Gordon, M.; Bell, A. T., Tailoring the Cooperative Acid–Base Effects in Silica-Supported Amine Catalysts: Applications in the Continuous Gas-Phase Self-Condensation of n-Butanal. *ChemCatChem* **2014**, *6* (5), 1283-1290.
5. Lauwaert, J.; De Canck, E.; Esquivel, D.; Van Der Voort, P.; Thybaut, J. W.; Marin, G. B., Effects of amine structure and base strength on acid–base cooperative aldol condensation. *Catalysis Today* **2015**, *246*, 35-45.
6. Der Voort, P. V.; Vansant, E., Silylation of the silica surface a review. *Journal of liquid chromatography & related technologies* **1996**, *19* (17-18), 2723-2752.
7. Lauwaert, J.; De Canck, E.; Esquivel, D.; Thybaut, J. W.; Van Der Voort, P.; Marin, G. B., Silanol-Assisted Aldol Condensation on Aminated Silica: Understanding the Arrangement of Functional Groups. *ChemCatChem* **2014**, *6* (1), 255-264.
8. Van Der Voort, P.; Vercauteren, S.; Peeters, K.; Vansant, E. F., Some precautions when determining the silanol number, using chemical modification with methylchlorosilanes. *Journal of colloid and interface science* **1993**, *157* (2), 518-519.
9. Lauwaert, J.; Ouwehand, J.; De Clercq, J.; Cool, P.; Van Der Voort, P.; Thybaut, J. W., Tuning component enrichment in amino acid functionalized (organo)silicas. *Catalysis Communications* **2017**, *88*, 85-89.
10. Kandel, K.; Althaus, S. M.; Peeraphatdit, C.; Kobayashi, T.; Trewyn, B. G.; Pruski, M.; Slowing, I. I., Solvent-Induced Reversal of Activities between Two Closely Related Heterogeneous Catalysts in the Aldol Reaction. *ACS Catalysis* **2013**, *3* (2), 265-271.
11. Nakadai, M.; Saito, S.; Yamamoto, H., Diversity-based strategy for discovery of environmentally benign organocatalyst: diamine–protonic acid catalysts for asymmetric direct aldol reaction. *Tetrahedron* **2002**, *58* (41), 8167-8177.
12. Kandel, K.; Althaus, S. M.; Peeraphatdit, C.; Kobayashi, T.; Trewyn, B. G.; Pruski, M.; Slowing, I. I., Substrate inhibition in the heterogeneous catalyzed aldol condensation: A mechanistic study of supported organocatalysts. *Journal of Catalysis* **2012**, *291*, 63-68.
13. Socrates, G., *Infrared and Raman characteristic group frequencies: tables and charts*. John Wiley & Sons: 2004.
14. Castro-Alvarez, A.; Carneros, H.; Costa, A. M.; Vilarrasa, J., Computer-Aided Insight into the Relative Stability of Enamines. *Synthesis* **2017**.
15. Amedjkouh, M., Primary amine catalyzed direct asymmetric aldol reaction assisted by water. *Tetrahedron: Asymmetry* **2005**, *16* (8), 1411-1414.
16. Paul, G.; Musso, G. E.; Bottinelli, E.; Cossi, M.; Marchese, L.; Berlier, G., Investigating the Interaction of Water Vapour with Aminopropyl Groups on the Surface of Mesoporous Silica Nanoparticles. *ChemPhysChem* **2017**, *18* (7), 839-849.

Chapter 5

Water and silanol assisted pathways in the amine catalyzed aldol reaction

Chapter 4 indicated both a rate-enhancing effect upon co-feeding small amounts of water in the amine catalyzed aldol reaction, as well as important effect of water on the stability of the methylaminopropyl (MAP) site. Without co-feeding water, several surface species stemming from a 4-nitrobenzaldehyde derived intermediate in the catalytic cycle were identified on the spent catalyst, and a low reusability was reported. However, when water was co-fed, the catalyst exhibited an increased reusability and these specific surface species were not detected on the spent catalyst anymore. It is, however, not yet clear what the exact pathway for the formation of these species is, and which species are exactly responsible for the low reusability of the catalyst. Hence, to obtain more information about the phenomena on the molecular scale, the full reaction mechanism is evaluated with computational chemistry.

5.1 Introduction

For primary and secondary amine functionalized mesoporous silica catalysts, it was experimentally observed that due to a cooperative interplay, the mildly acidic silanol groups, which are intrinsically present on the silica surface, increase the turnover frequency exhibited by the amine^{2,3}. These catalysts are thus denoted as cooperative acid-base catalysts. Replacing the silanol groups by stronger acids^{4,5}, or incorporating a strong acid in the grafted organic group⁶, was found to reduce the catalytic activity. This led to the conclusion that a good cooperativity between the acid and base group is based on the ability of the weak acid to form hydrogen-bonds with reactants and key intermediate species, without disturbing the acid-base protonation equilibrium⁶.

The promoting effect by silanol groups on the first step in the supported aminopropyl catalyzed aldol reaction, i.e., the formation of the carbinolamine intermediate from acetone, was investigated by de Lima Batista et al.⁷ using computational chemistry. Calculations with a minimal cluster model, consisting of free propylamine and an as small as possible silanol cluster

(H₃SiOH), revealed that the most likely reaction mechanism for the carbinolamine formation involved the active participation of a silanol group in transferring protons in the transition state. When multiple silanols were available in the vicinity of the amine site, which was modeled with a QM/MM surface model of β -cristobalite, a stepwise mechanism was found⁷. However, their conclusions regarding the preferred mechanism for promotion by a silanol group in the carbinolamine formation appeared irrespective of the model. Yet, possible promoting effects on the other steps in the reaction mechanism of the amine-catalyzed aldol reaction remain elusive, as well as possible solvent effects.

Similarly, Patil et al.⁸ employed gas-phase *ab initio* and density functional theory methods to investigate the mechanistic details of the carbinolamine and subsequent enamine formation between dimethylamine and propanal with methanol as a cooperative hydrogen-bond donating co-catalyst. Explicit inclusion of one or two methanol molecules as auxiliary species was found to stabilize the transition states, relative to the unassisted pathway by forming a relay for proton transfers.

Water molecules also can have a promoting effect as hydrogen-bond donor in the carbinolamine formation⁹⁻¹¹. Williams et al.^{10, 11} were the first to suggest this, using computational gas phase chemistry explicitly accounting for no, one or two water molecules in the addition reaction of ammonia and formaldehyde. Later, Hall et al.¹² performed high-level gas-phase *ab initio* calculations for the reaction of formaldehyde with methylamine, accounting for one or two water molecules in the transition state to explain the promoting effect of water as proton transfers for the carbinolamine and imine formation. Furthermore, Dickerson et al.¹³ modeled one promoting water molecule in the carbon-carbon bond formation step, and the water-assisted product desorption step, in the homogeneous normicotine catalyzed aqueous aldol reaction. Recently, Zhang et al.¹⁴ reported that using a polarized continuum model for either DMSO or water yields lower barriers in the histidine catalyzed aldol reaction of acetone with benzaldehyde. Yet, the effect of water and its possibility for hydrogen-bond promotion has not yet been computationally investigated for the complete amine-catalyzed aldol reaction mechanism.

From the aforementioned research, it is clear that both water and silanol groups enhance the reaction rate between a carbonyl containing species and an amine, by providing a proton relay in the transition state. Additionally, water seems to prevent the deactivation of the amine site during the aldol reaction by suppressing the formation of site-blocking species. In this work, a thorough mechanistic investigation of the promoting effect of water and silanol groups in the amine-catalyzed aldol reaction is performed for the first time using high-level computational

chemistry methods with liquid-phase corrections. Explicit inclusion of water molecules, or silanol moieties, can then account for hydrogen-bond stabilization, and proton transfer promotion in transition states. By considering both the entropic and enthalpic effect of promoting water molecules in the Gibbs free energy barriers of the transition state, the dominant reaction paths under “dry” and “wet” reaction conditions are determined and compared to experimental results¹. Changing the solvent model from a 50/50 vol% DMSO/acetone mixture to a 50/50 vol% hexane/acetone mixture then also yields insights into the effect of a change in solvent. The combination of these effects provides insight into the formation of deactivating species on the surface of the catalyst and offers guidelines for the selection of reaction conditions under which both catalytic activity and reusability can be maximized.

5.2 Computational details

5.2.1 Computational model construction

To keep the size of the computational model reasonable, and thus allow to use a high-level computational method including solvation effects, only the organic part of the mesoporous silica grafted N-methylpropylamine active site is modeled this work. The silanol groups that can assist the amine base in the cooperative acid-base catalyst are modeled as H₃SiOH clusters. Similar small clusters representing a silanol group have often been used in high-level computational studies^{7, 15-17}. Even though small cluster models cannot account for the long-range electrostatic effects of an extended lattice, they have turned out to be successful in simulating charge transfer properties and vibrational frequencies of silica interacting with water¹⁵ or ammonia¹⁸. The H₃SiOH cluster in particular has been successfully used in the computational investigation of glycine adsorption on amorphous silica^{19, 20}. However, it should be noted that the calculated acidity of this minimal silanol cluster was found to be lower than the experimentally observed one^{21, 22}. Hence, in this work, the reaction barriers involving promotion by the silanol group are expected to be slightly overestimated. However, this is not prohibitive for the identification of the dominant reaction pathways towards product liberation or catalyst deactivation.

5.2.2 Gas-phase calculations

Electronic structure calculations were performed using the Gaussian 16 package²³. The conformers were identified by evaluating the electronic energy at the B3LYP/6-31G(d) level of

theory for reactants, products and intermediates by rotating around all dihedral angles. All conformers within 5 kJ mol⁻¹ were subject to a Gibbs free energy calculation with the CBS-QB3 composite method, with tight optimization criteria, and an ultrafine integration grid^{24, 25}. The conformer with the lowest Gibbs free energy at this level of theory was then selected. Transition state structures were optimized using the Berny algorithm²⁶. All minimum energy conformers and transition state geometries were confirmed to, respectively, have zero and one imaginary frequency. Additionally, the reaction pathway on the potential energy surface has been monitored for all transition states by following the intrinsic reaction coordinate (IRC) pathway at the B3LYP/6-31G(d) level of theory. All thermal contributions were calculated with the quasiharmonic oscillator approach, which means that frequencies below 30 cm⁻¹ are artificially raised to this value to correct for the failure of the harmonic oscillator model at low-frequency vibrations^{27, 28}. Partition functions q were calculated using statistical thermodynamics²⁹, based on the B3LYP/CBSB7 frequency calculation with a default scaling factor of 0.99. The partition functions were evaluated using a rigid-rotor and harmonic oscillator approximation with separate translational, external rotational, rovibrational, and electronic contributions. To simulate the rigidity of a grafted N-methylpropylamine group, the external rotation and translational contributions to the partition function were removed for the active site and all intermediates occurring on it. The same procedure was done for the silanol groups that are modeled with the minimal silanol cluster.

Gibbs free energy is always calculated at 328.15 K, the typical experimental operating temperature for the aldol reaction¹. Reaction barriers are always with respect to the most stable reactant state. Decomposition of this Gibbs free energy barrier in an enthalpic and entropic part is performed where indicated.

5.2.3 Liquid-phase corrections

Gibbs free energy correction terms for the solvent mixture ($G_{\text{solvation}}$) are obtained via the COSMO-RS theory as implemented in the COSMOthermX18 software³⁰, and are added to the Gibbs free energy obtained from the completed gas-phase calculations. A detailed description is found in section C-6 in Appendix C. The input for COSMOtherm has been calculated with Gaussian 16, using the SCRF=COSMORS keyword based on the B3LYP/CBSB7 optimized structures that were recalculated at the B86/TZVP level of theory, for which COSMOthermX18 is parameterized. All molecules are considered at infinite dilution, i.e., relying on Henry's law. A solvent model of a 50/50 vol% DMSO/acetone is used, representative of the liquid phase

used during the experiments¹, with the solvent properties as implemented in the COSMOthermX18 software. For comparison to other experimental work, a 50/50 vol% hexane/acetone mixture⁶ was also considered. Water is not included in the continuum solvent model, as the water concentration was typically kept very low in the experiments¹, but water molecules are explicitly included during geometry optimization. All free energies are calculated with respect to a standard state of 1 mole per liter. Additionally, for the iminium ion assessment, geometry scans have been performed at the B3LYP/CBSB7 level of theory with an implicit SMD solvation model of DMSO ($\epsilon = 46.826$)³¹.

Solvation enthalpies and entropies were calculated at the typical experimental temperature¹ of 328.15 K by using the following thermodynamic functions²⁸:

$$\Delta H_{\text{solv}}(T) = -T^2 \frac{\partial \left(\frac{\Delta G_{\text{solv}}(T)}{T} \right)}{\partial T} \approx -T_1 T_2 \left(\frac{\left(\frac{\Delta G_{\text{solv}}(T_2)}{T_2} \right) - \left(\frac{\Delta G_{\text{solv}}(T_1)}{T_1} \right)}{T_2 - T_1} \right)$$

$$\Delta S_{\text{solv}}(T) = \frac{\Delta H_{\text{solv}}(T) - \Delta G_{\text{solv}}(T)}{T}$$

Interpolation was performed between $T_1 = 318.15$ K and $T_2 = 338.15$ K.

5.3 Results and discussion

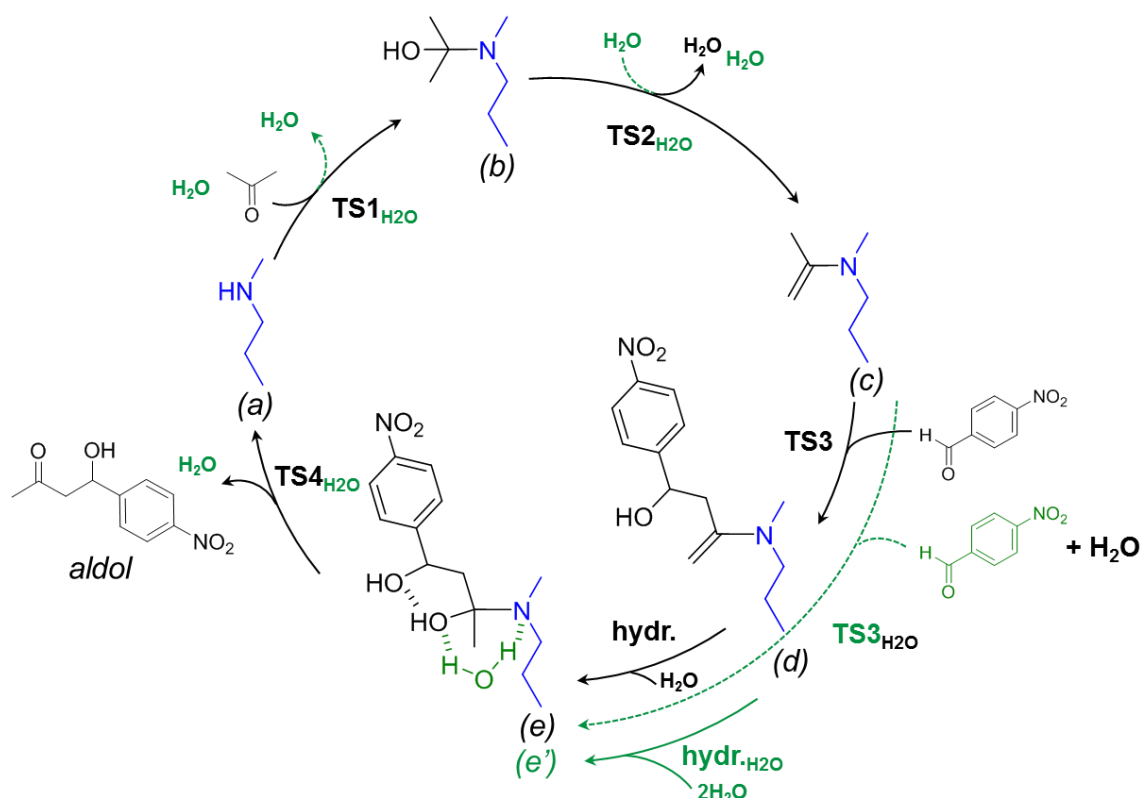
5.3.1 Amine-catalyzed aldol reaction assisted by water

By endcapping the surface silanol groups on aminated mesoporous silica catalysts with trimethylsilyl groups, their ability to act as a hydrogen-bond promotor towards the amine moiety disappears. While such a catalyst exhibits a significantly lower turnover frequency than the cooperative acid-base catalyst³² and, hence, has a lower application potential, it has been used in Chapter 4 to isolate the effect that water has on the amine site from its effect on the silanol groups¹. In this Chapter, it will serve as a base case for modeling the effect of water on the activity of the secondary amine site for a 50/50 vol% DMSO/acetone solvent mixture. Next, the promotional ability of water molecules is compared to the promoting ability of either isolated or vicinal silanol groups, and the aldol product dehydration towards the enone product is investigated. Lastly, by changing the solvent from a 50/50 vol% DMSO/acetone mixture to a 50/50 vol% hexane/acetone mixture, the effect of the nature of the solvent on the dominant reaction paths is discussed.

5.3.1.1 Zero versus one water molecule

The reaction mechanism, as catalyzed by N-methylpropylamine at 328.15 K, without any hydrogen-bond promotion, is represented in Scheme 5-1 by the black arrows. The Gibbs free energy barriers are reported in Table 5-1 and visualized in Figure 5-1. Thermodynamics of the different steps are reported in Table 5-2. The green arrows indicate the reaction pathway where one water molecule actively assists in proton transfers via a hydrogen-bond network. Passive stabilization by water molecules, i.e. where hydrogen-bonding only serves to stabilize charges in the transition state, is not considered in this work since previous work⁸ has already shown that the largest reduction in barrier height for the first two steps in the mechanism is obtained with active participation of hydrogen-bond donating molecules in proton transfers.

Only the reaction mechanism involving the enamine intermediate of acetone is considered in this work because the formation of an iminium of 4-nitrobenzaldehyde is limited under the typical experimental aldol reaction conditions^{1, 33}. Potential consecutive reactions of the products are not considered, except for the dehydration of the aldol product towards the enone product, as discussed in paragraph 5.3.3.



Scheme 5-1: Reaction mechanism of the aldol reaction of acetone with 4-nitrobenzaldehyde, catalyzed by an N-methylpropylamine catalyst (black pathway, no subscripts) or catalyzed by N-methylpropylamine, assisted by one water molecule (green pathway, H₂O subscript). Green water molecules are assisting, black water molecules are from the carbinolamine dehydration (TS2). Species (e) can occur as such without a complexed water molecule, or as (e') with one complexed water molecule.

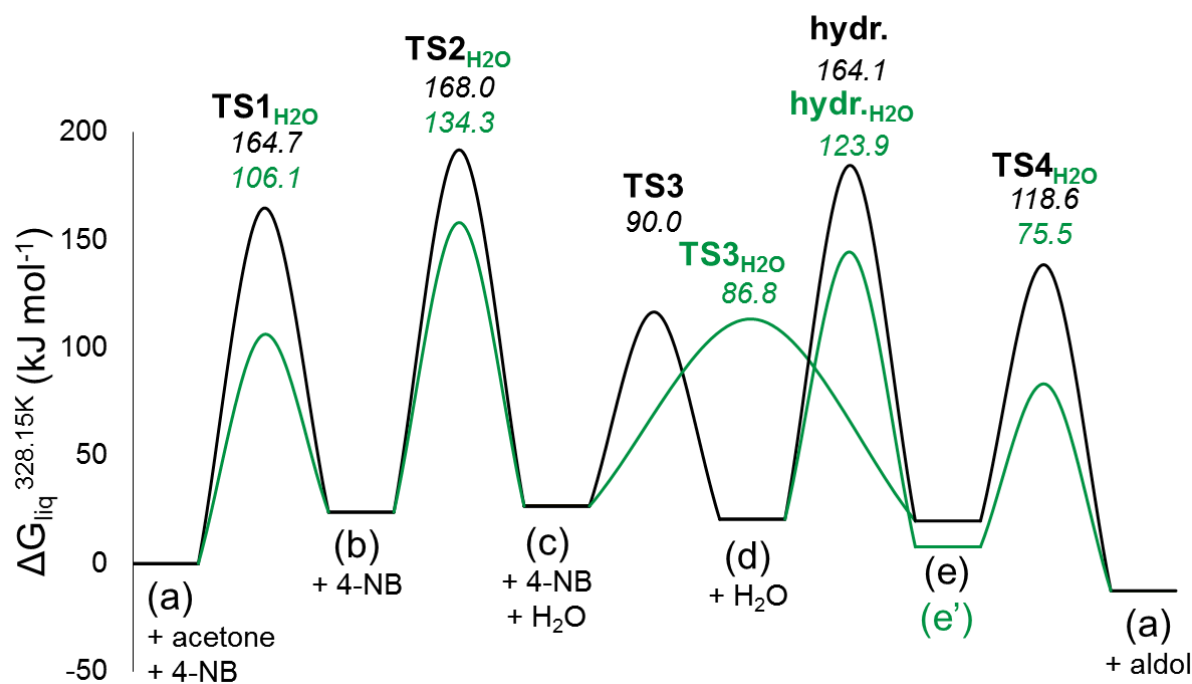


Figure 5-1: Gibbs free energy diagram for the aldol reaction of acetone with 4-nitrobenzaldehyde at 328.15 K catalyzed by an N-methylpropylamine catalyst (black pathway, no subscript) and catalyzed by N-methylpropylamine, assisted by one water molecule (green pathway, H₂O subscript). The numbers indicate the $\Delta^\ddagger G_{\text{forward}}$ for the considered reaction. The Gibbs free energy includes a correction term for a 50/50 vol% DMSO/acetone liquid phase, as experimentally employed in Chapter 4.

The reaction mechanism of the aldol reaction, catalyzed by N-methylpropylamine is shown in Scheme 5-1 and starts with acetone reacting with the amine site (**TS1**) resulting in a carbinolamine intermediate (**b**). This carbinolamine (**b**) then dehydrates (**TS2**) to an enamine intermediate (**c**), which has a nucleophilic nature. The actual carbon-carbon bond formation step comprises the attack of the nucleophilic carbon in the enamine on the carbonyl group of 4-nitrobenzaldehyde (**TS3**), which can occur either *si* or *re* faced, yielding two possible enantiomers. Due to the achiral character of the catalyst, the energetics for the formation of both the (*R*) and (*S*) enantiomers is the same. Hence, only the (*S*) enantiomer is considered in this work. Hydration of the resulting (*S*) product enamine (**d**) can also occur either *si* or *re* faced, and will yield two possible diastereomers (*S,S*) and (*R,S*). Because diastereomers can differ in reactivity, both have been considered. The route through the (*R,S*) diastereomer generally displays the lowest reaction barriers and is thus reported here, the route through the (*S,S*) diastereomer is reported in the Appendix C. It should be emphasized that the differences in reaction barrier and thermodynamic stability between both diastereomers is minor, and leads to the same conclusions regarding the promoting effect of water or silanol groups.

It appears from Figure 5-1 that both the barriers for **TS1**, as well as **TS2**, can be significantly reduced by the addition of one water molecule as a proton relay. As can be seen in Figure C-1 and Figure C-2 in the Appendix C, one water molecule transforms the 4-membered transition state of **TS1** and **TS2** into a 6-membered one (respectively **TS1_{H2O}** and **TS2_{H2O}**). The proton transfer then occurs in a concerted manner. This is similar to what Patil et al.⁸ reported when using methanol as a co-catalyst for the enamine formation of dimethylamine and propanal. The entropic penalty due to the introduction of an additional auxiliary species in the transition state, as is clear from Table 5-1, is compensated for by the decrease in the enthalpy barrier due to a reduced strain.

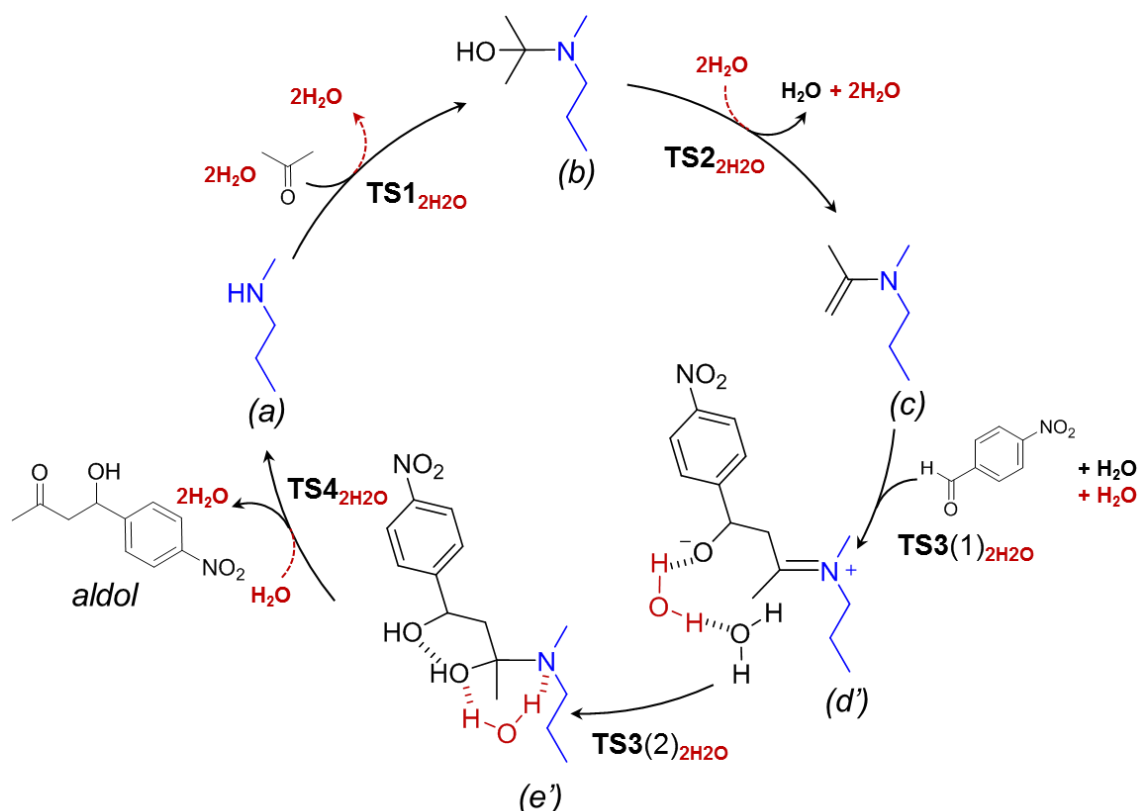
In the carbon-carbon bond formation step, water can be introduced in a concerted (**TS3_{H2O}**) or a stepwise manner (**TS3** and then **hydr.**), as displayed in Scheme 5-1. It is expected that, under dry reaction conditions, where the only water molecules in the reaction medium are from the carbinolamine dehydration (**TS2**), the stepwise mechanism will dominate over the concerted addition-hydration mechanism, and thereby yield the enamine of the aldol product (**d**) via an intramolecular proton transfer. The subsequent hydration (**hydr.**) of this enamine species (**d**) towards (**e**), however, has a high barrier, as shown in Figure 5-1. This is the case even when an additional water molecule is available to assist in the hydration (**hydr._{H2O}**). Hence, when working with low water concentrations, this hydration step could become rate-determining and the intermediate **d** can then be abundantly present on the catalyst surface, as has indeed been experimentally observed from spent catalyst characterization in Chapter 4. Reusing the catalyst under exactly the same reaction conditions will then yield a lower turnover frequency as compared to the first run, due to active site blocking by this enamine species (**d**). It also appears from the reaction barriers in Figure 5-1, that a higher water concentration is required to fully hydrate the site-blocking species (via step **hydr.** or **hydr._{H2O}**) than the amount that would have been required to prevent its formation in the first place (**TS3_{H2O}**).

If the water concentration in the reaction is sufficiently high, it is thus expected that the concerted addition-hydration step (**TS3_{H2O}** in Scheme 5-1) will prevail over the stepwise mechanism (**TS3**) and, hence, reduce the formation of the site-blocking species **d**, which will result in an increased catalyst reusability. Additionally, because acetone is experimentally added in excess, at the beginning of the reaction the rate-determining step with a sufficient amount of water is most likely situated in the dehydration of the carbinolamine **b** towards the enamine **c** via **TS2**. Because in a typical aldol reaction the conversion of 4-nitrobenzaldehyde is measured in an excess of acetone, this results in a zero order reaction being observed under sufficiently “wet” reaction conditions.

After the carbon-carbon bond formation step, which occurs either concerted with water (**TS3_{H2O}**) or stepwise (**TS3** and then **hydr.**), a carbinolamine of the aldol product (**e**) is formed on the active site. Upon introducing one water molecule in the system, the intermediate (**e**) was found to be lower in Gibbs free energy when one water molecule was hydrogen bonded to both the hydroxyl group of the carbinolamine and the amine (**e'**), as summarized in Table 5-2. No other intermediates were found to be complexed with water molecules. Similar to one assisting water molecule in the first step of the mechanism (**TS1_{H2O}**), the barrier for the aldol product desorption with one assisting water molecule (**TS4_{H2O}**) also appears to be lower than without (**TS4**).

5.3.1.2 Multiple water molecules

Scheme 5-2 and Figure 5-2, respectively, indicate the reaction mechanism and Gibbs free energy barriers for the amine-catalyzed aldol reaction assisted by two water molecules in the transition state. The reaction barriers are summarized in Table 5-1 and the thermodynamics of the intermediates are summarized in Table 5-2.



Scheme 5-2: Reaction mechanism of the aldol reaction of acetone with 4-nitrobenzaldehyde catalyzed by a monofunctional N-methylpropylamine catalyst, assisted by two water molecules (red subscript 2H₂O).

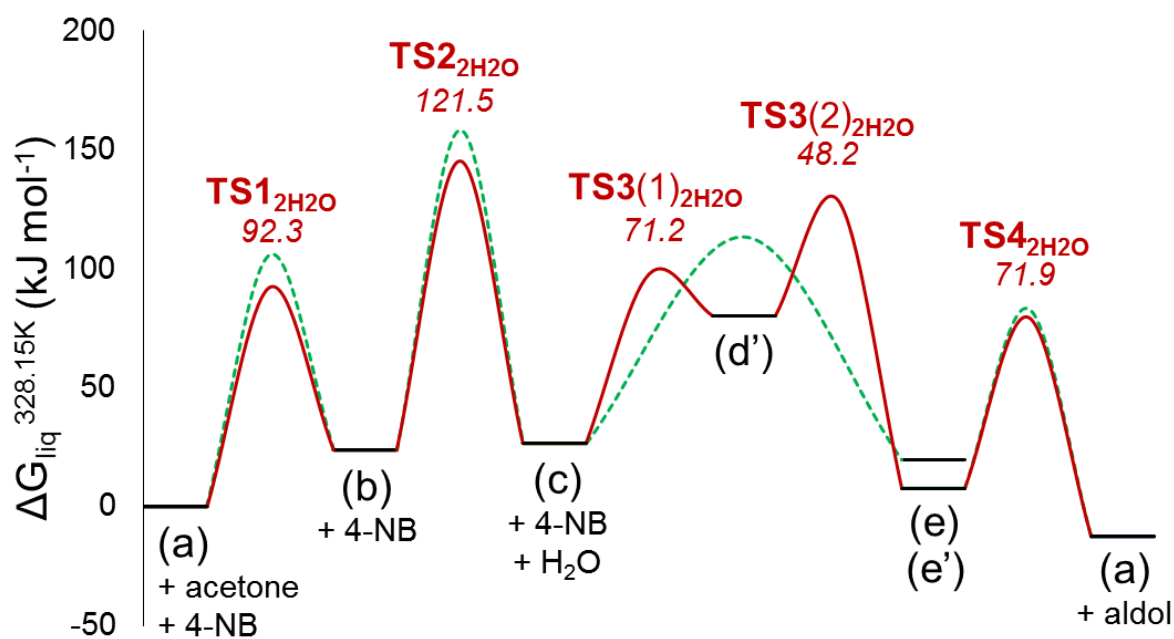


Figure 5-2: Gibbs free energy diagram and reaction barriers of the aldol reaction of acetone with 4-nitrobenzaldehyde at 328.15 K catalyzed by N-methylpropylamine, assisted by two water molecules (red, subscript 2H₂O). The dashed green line indicates the promotion by one water molecule, as reported in Figure 5-1. The numbers indicate the $\Delta^\ddagger G_{\text{forward}}$ for the considered reaction. The Gibbs free energy includes a correction term for a 50/50 vol% DMSO/acetone liquid phase, as experimentally employed in Chapter 4.

When two water molecules are available to interact with the transition state species, the barriers **TS1_{2H2O}** and **TS2_{2H2O}** appear slightly reduced, as displayed in Figure 5-2, compared to those when interaction is possible with only a single water molecule (Figure 5-1). **TS1_{2H2O}** is now an 8-membered transition state, as can be seen in Figure C-1 in Appendix C. Introduction of a third water molecule (**TS1_{3H2O}**) was found to increase the Gibbs free energy reaction barrier due to an increased entropic penalty, as reported in Table 5-1. As displayed in Figure C-1 in Appendix C, **TS2_{2H2O}** remains a 6-membered transition state, with the second water molecule hydrogen-bonding to the hydroxyl group and not actively assisting in the proton transfer. The presence of three assisting water molecules (**TS2_{3H2O}**) leads to a stepwise mechanism, where an iminium intermediate is found, as displayed in Figure C-3 in Appendix C. The composite Gibbs free energy barrier for this reaction (**TS2_{3H2O}**) is reported in Table 5-1 and amounts to 131.3 kJ mol⁻¹, which is higher than in the case of two water molecules (**TS2_{2H2O}**) due to the increased entropic penalty of introducing three water molecules in the transition state.

The carbon-carbon coupling step, assisted by two water molecules (**TS3_{2H2O}**) is, contrary to one assisting water molecule (**TS3_{H2O}**), now a stepwise mechanism with an iminium intermediate (**d'**). It, however, raises the question whether the iminium intermediate (**d'**) could also have been found as a stable intermediate during geometry optimization, without explicit

promoting water molecules, but in a polar continuum rather than the gas phase. To investigate this, reaction coordinate scans of 4-nitrobenzaldehyde reacting with the enamine **c** towards the enamine **d** were performed, both in the gas phase as well as in DMSO ($\epsilon = 46.826$) as polar continuum. As displayed in Figure C-6 in Appendix C, in the gas phase no stable iminium intermediate (**d'**) is found, while in the polar continuum model, (**d'**) is identified with an energy barrier below 2 kJ mol^{-1} towards the reactant side. From this it can be concluded that the iminium intermediate (**d'**) is only sufficiently stabilized when there is hydrogen-bond stabilization by at least two hydrogen-bond donors, and cannot be stabilized by merely the polarized continuum. The composite reaction barrier, which includes the iminium formation (**TS3(1)2H2O**) and its hydration (**TS3(2)2H2O**), as reported in Table 5-1, amounts to $114.5 \text{ kJ mol}^{-1}$. Surprisingly, this composite Gibbs free energy barrier is higher than when the carbon-carbon bond formation occurs in a concerted manner with the hydration (**TS3H2O**). It, hence, appears that in the carbon-carbon coupling step, an assisting water molecule as hydrogen-bond donor is not beneficial.

The Gibbs free energy barrier for the liberation of the aldol product from the catalyst, assisted by two water molecules (**TS42H2O**) appears to be lower than in the case of a single water molecule (**TS4H2O**). Also in this case, the introduction of a third water molecule (**TS43H2O**) imposes a too large entropic penalty and results in a higher Gibbs free energy barrier than when two water molecules are considered, as summarized in Table 5-1.

Table 5-1: Reaction Gibbs free energy barriers for the aldol reaction of acetone with 4-nitrobenzaldehyde in 50/50 vol% solvent/acetone mixture, catalyzed by N-methylpropylamine. Transition states are assisted by one, two or three water molecules or one isolated silanol group or two vicinal silanol groups. Gibbs free energy diagrams are displayed in Figure 5-1, Figure 5-2, Figure 5-3 and Figure 5-4. Thermodynamics of the considered reaction steps are reported in Table 5-2 and Table 5-3. (* indicates that the composite barrier is reported)

	Assisted by	50 vol% DMSO			50 vol% hexane		
		$\Delta^\ddagger H_{\text{liq}}^{328\text{K}}$ kJ mol ⁻¹	$\Delta^\ddagger S_{\text{liq}}^{328\text{K}}$ J K ⁻¹ mol ⁻¹	$\Delta^\ddagger G_{\text{liq}}^{328\text{K}}$ kJ mol ⁻¹	$\Delta^\ddagger H_{\text{liq}}^{328\text{K}}$ kJ mol ⁻¹	$\Delta^\ddagger S_{\text{liq}}^{328\text{K}}$ J K ⁻¹ mol ⁻¹	$\Delta^\ddagger G_{\text{liq}}^{328\text{K}}$ kJ mol ⁻¹
TS1	-	106.3	-177.9	164.7	105.3	-179.0	164.0
	H ₂ O	29.6	-233.3	106.1	16.5	-249.9	98.5
	2H ₂ O	-0.7	-283.3	92.3	-23.4	-311.8	78.9
	3H ₂ O	2.9	-331.2	111.6	-29.5	-371.0	92.2
	H ₃ SiOH	13.4	-189.1	75.5	12.2	-189.3	74.3
	2H ₃ SiOH	-29.9	-198.3	35.2	-28.9	-197.1	35.8
TS2	-	180.1	37.0	168.0	177.3	24.6	169.3
	H ₂ O	133.2	-3.4	134.3	117.2	-32.6	127.9
	2H ₂ O	109.9	-35.4	121.5	82.7	-76.8	107.9
	3H ₂ O*	105.6	-78.5	131.3	68.1	-133.3	111.8
	H ₃ SiOH (1)	63.4	-2.3	64.1	68.7	-1.2	69.1
	H ₃ SiOH (2)	10.4	-8.4	13.2	9.8	-5.2	11.5
	2H ₃ SiOH (1)	58.2	0.7	57.9	64.0	5.1	62.3
	2H ₃ SiOH (2)	34.3	-2.1	35.0	34.4	1.4	33.9
TS3	-	35.7	-165.7	90.0	34.0	-170.6	90.0
	H ₂ O	16.6	-214.2	86.8	2.4	-234.8	79.5
	2H ₂ O (1)	-8.4	-242.4	71.2	-29.2	-265.9	58.0
	2H ₂ O (2)	45.4	-8.7	48.2	39.4	-18.6	45.5
	H ₃ SiOH (1)	-57.5	-199.7	8.0	-55.9	-199.1	9.4
	H ₃ SiOH (2)	31.2	-7.7	33.7	29.9	-7.0	38.0
	2H ₃ SiOH (1)	-19.3	-175.1	38.1	-20.9	-177.7	37.4
	2H ₃ SiOH (2)	45.6	8.2	42.9	43.5	8.2	40.8
TS4	-	127.6	27.6	118.6	121.9	11.1	118.3
	H ₂ O	70.0	-16.8	75.5	67.8	-24.7	75.9
	2H ₂ O	46.5	-77.5	71.9	36.6	-94.0	67.4
	3H ₂ O	53.3	-126.7	94.8	33.2	-155.6	84.3
	H ₃ SiOH	12.3	-24.2	20.2	15.0	-24.8	23.2
	2H ₃ SiOH	1.5	-8.7	4.4	-2.5	-31.7	7.9
hydr.	-	130.3	-103.0	164.1	130.2	-104.1	164.4
	H ₂ O	74.8	-149.5	123.9	61.7	-166.7	116.3
	H ₃ SiOH	47.1	-26.3	55.7	24.5	-66.0	46.1
	2H ₃ SiOH	67.8	20.6	61.0	28.9	-70.6	52.0

It can be concluded that water molecules play an important role in the reduction of the Gibbs free energy barriers in the reaction mechanism of the N-methylpropylamine catalyzed aldol reaction of acetone with 4-nitrobenzaldehyde and, hence, affect the measured reaction rate positively. More importantly, in the carbon-carbon formation step, a concerted addition-

hydration (**TS3H₂O**) will yield the carbinolamine of the aldol product (**e**), which can relatively easily desorb from the active site as the aldol product, whereas the unassisted addition of 4-nitrobenzaldehyde (**TS3**) yields an enamine (**d**). Hydrating this enamine (**d**) towards the product carbinolamine (**e**) appears to have a high barrier and can thus be the cause of active-site blocking under dry reaction conditions, as was indeed experimentally found in Chapter 4.

Table 5-2: Thermodynamics of the intermediates in the mechanisms displayed in Figure 5-1 and Figure 5-2.

	50 vol% DMSO			50 vol% hexane		
	$\Delta_r H_{liq}^{328K}$ kJ mol ⁻¹	$\Delta_r S_{liq}^{328K}$ J K ⁻¹ mol ⁻¹	$\Delta_r G_{liq}^{328K}$ kJ mol ⁻¹	$\Delta_r H_{liq}^{328K}$ kJ mol ⁻¹	$\Delta_r S_{liq}^{328K}$ J K ⁻¹ mol ⁻¹	$\Delta_r G_{liq}^{328K}$ kJ mol ⁻¹
a + acetone → b	-40.4	-195.4	23.8	-37.5	-183.3	22.6
b → c + H ₂ O	26.8	73.2	2.8	36.8	83.4	9.5
c + 4-NB → d	-57.5	-156.6	-6.1	-58.9	-154.6	-8.2
d + H ₂ O → e	-28.8	-85.1	-0.8	-37.2	-92.2	-6.9
e → a + aldol	41.9	226.0	-32.3	38.5	212.8	-31.4
e + H ₂ O → e'	-20.6	-26.4	-11.9	-34.4	-46.9	-19.0
c + 2H ₂ O + 4-NB → d'	-24.2	-237.4	53.7	-45.0	-262.4	41.2
d' → e'	-82.7	-30.8	-72.6	-85.5	-31.3	-75.2
e' → a + aldol + H ₂ O	62.5	252.5	-20.3	72.8	259.7	-12.4
acetone+4-NB → aldol	-57.9	-137.9	-12.6	-58.29	-133.9	-14.3

5.3.2 Amine-catalyzed aldol reaction assisted by silanol groups

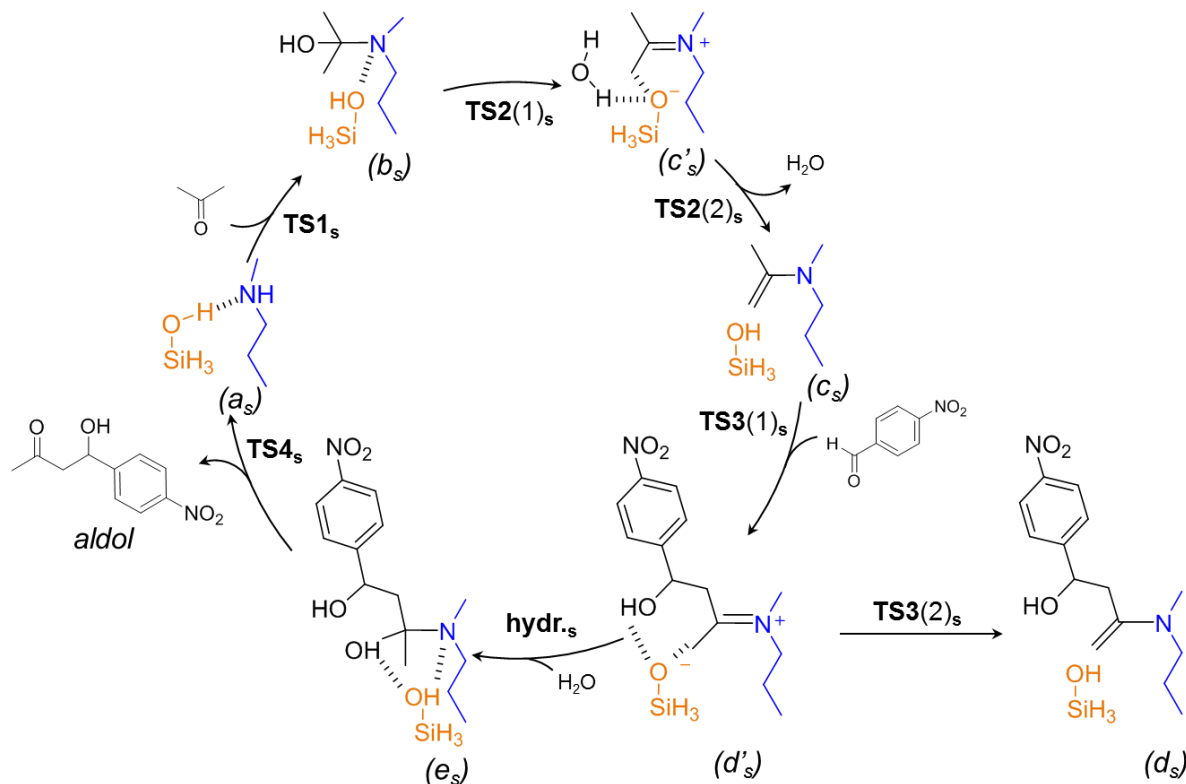
Silanol groups on a silica surface can occur either in an isolated, geminal or vicinal position with respect to each other³⁴. A silanol group is denoted as “isolated” when the distance to the closest other silanol groups is such that they cannot be involved in mutual hydrogen-bond interactions. This is typically at least 3.3 Å. Vicinal silanol groups are closer to each other than 3 Å, are not on the same silicon atom, and can form hydrogen-bonds with each other. Geminal silanol groups are linked to the same surface silicon atom and are hydrogen-bonded. The cooperative aminated mesoporous silica catalysts typically employed for the aldol reaction are calcined prior to functionalization and, hence, primarily contain isolated silanol groups^{1, 32}. In this work, isolated silanol groups are modeled as H₃SiOH moieties. Rehydration of the silica surface under ambient conditions would yield a sharp increase in vicinal silanol groups, which are modeled by two hydrogen-bonded H₃SiOH molecules. Geminal silanol groups only occur to a limited extent on these materials³⁴ and, hence, are not further addressed. During optimization, no constraint was imposed on any silanol position in the minimal cluster model. Although silanol groups on a silica surface do not have such a freedom of motion, this procedure should allow to identify the “best possible” configuration of the silanol group(s) in the transition

states and intermediates. The feasibility of the minimal cluster model geometries is then verified by optimization of all the intermediates on a periodic silica surface slab of the (111) surface of β -cristobalite and the (100) surface of α -quartz, as a representative surface model for respectively isolated³⁵ and vicinal silanol groups³⁶. The geometries in the minimal cluster models and the surface models are remarkably similar, as can be seen in section C-4 in Appendix C.

The case of a simultaneous promotion by surface silanol groups and water was considered less relevant and, hence, was not further explored in detail in our calculations. The promoting effect of silanol groups has experimentally been found to decrease in the presence of a large amount of water, most likely due to the silanols being covered by water molecules which then take over the hydrogen-bond promotion¹.

5.3.2.1 Isolated silanols

The reaction mechanism for the aldol reaction of 4-nitrobenzaldehyde with acetone, catalyzed by N-methylpropylamine, and assisted by an isolated silanol group (H_3SiOH), is displayed in Scheme 5-3. The reaction barriers are visualized in Figure 5-3 and reported in Table 5-1.



Scheme 5-3: Reaction mechanism of the aldol reaction of acetone with 4-nitrobenzaldehyde catalyzed by N-methylpropylamine, assisted by one isolated silanol group (subscript s).

The mechanism of hydrogen-bond promotion by a silanol group (Scheme 5-3) is remarkably similar to the promotion by one water molecule (Scheme 5-1). However, the more pronounced acidity of the silanol group as compared to water causes both the iminium ions of acetone (\mathbf{c}_s') and the aldol product (\mathbf{d}_s') to be found as intermediates. Moreover, all the reported Gibbs free energy barriers for the reactions assisted by isolated silanol groups, summarized in Table 5-1, are significantly lower than in the case one or two assisting water molecules. This proves that the mildly acidic silanol groups are intrinsically better amine promoters than water molecules.

In Scheme 5-3 it can be seen that deprotonation of the iminium \mathbf{c}_s' via $\mathbf{TS2}(2)_s$ towards the enamine \mathbf{c}_s , the hydrogen-bond between water and the silanol group is lost. This results in an entropy increase, as reported in Table 5-3. It should be noted that this entropy increase is likely overestimated, because on a silica surface water could remain hydrogen-bonded to a nearby silanol group in the pores of the material. It will, however, not remain hydrogen-bonded to the silanol group that is catalytically active in $\mathbf{TS3}$, because this results in a much higher Gibbs free energy barrier of 39.7 kJ mol⁻¹ for $\mathbf{TS3}(1)_s$. Hence, the transition state $\mathbf{TS3}(1)_s$ proceeds without any water molecule and results in the iminium ion \mathbf{d}_s' being formed. It is expected that this iminium ion \mathbf{d}_s' will be abundantly present under dry reaction conditions, i.e., where the hydration of this species is the rate-determining step. This iminium \mathbf{d}_s' could undergo a unimolecular proton transfer ($\mathbf{TS3}(2)_s$) towards species \mathbf{d}_s , which has been observed on a catalyst spent under dry reaction conditions¹. On the other hand, when the water concentration is sufficiently high, the iminium intermediate \mathbf{d}_s' will undergo rapid hydration (**hydr.**) towards the product carbinolamine \mathbf{e}_s . This product carbinolamine \mathbf{e}_s is subsequently released ($\mathbf{TS4}_s$) from the amine as the aldol product. Similarly to the case of the monofunctional amine site, when the concentration of water is high enough, the formation of the site-blocking enamine \mathbf{d}_s will be low. However, it is also important to note that a high water concentration was experimentally found to deactivate the promoting ability of the silanol groups¹, which eventually leads to a lower activity and reusability.

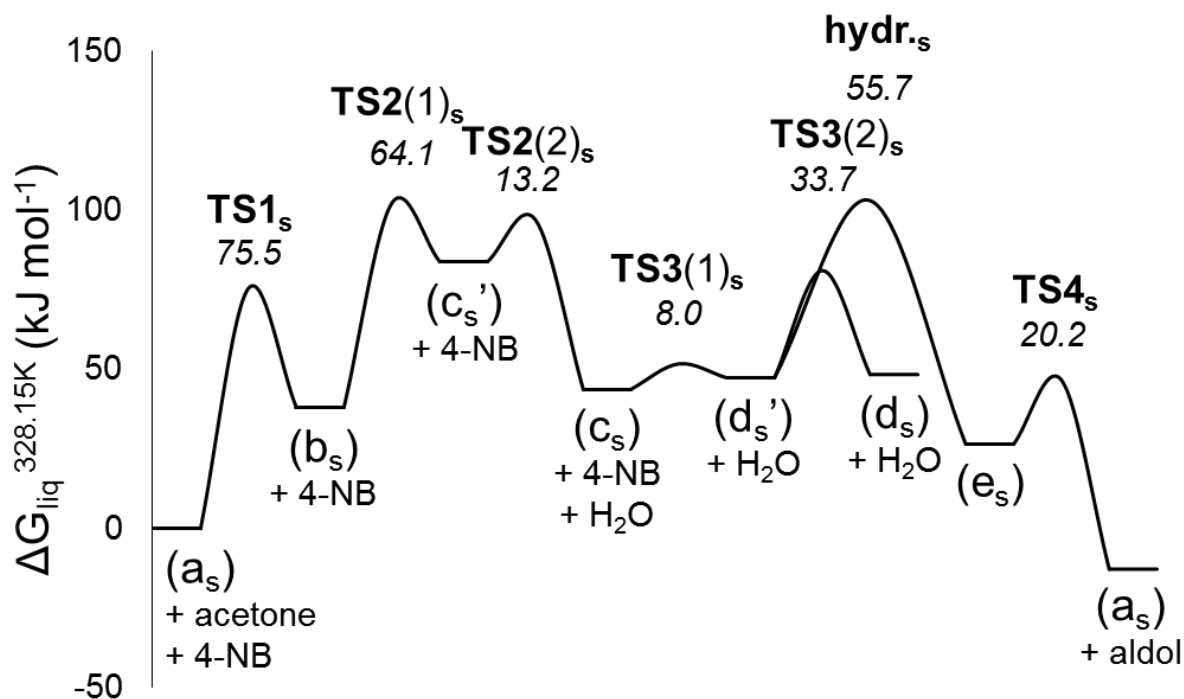


Figure 5-3: Gibbs free energy diagram for the aldol reaction of acetone with 4-nitrobenzaldehyde at 328.15 K catalyzed by N-methylpropylamine, assisted by one isolated silanol group (subscript s). The numbers indicate the $\Delta^{\ddagger}G_{\text{forward}}$ for the considered reaction. The Gibbs free energy includes a correction term for a 50/50 vol% DMSO/acetone liquid phase, as experimentally employed¹.

5.3.2.2 Vicinal silanols

The Gibbs free energy diagram for the aldol reaction catalyzed by N-methylpropylamine, assisted by two hydrogen-bonded silanols (2 H₃SiOH), is displayed in Figure 5-4.

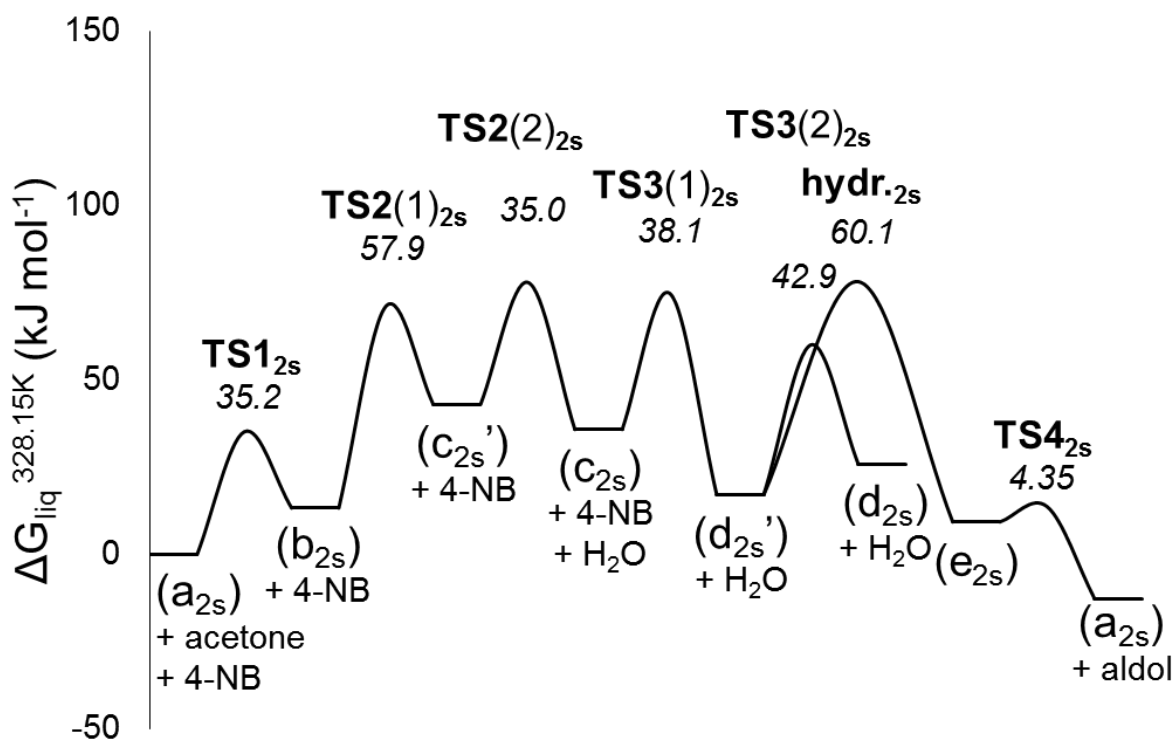


Figure 5-4: Gibbs free energy diagram for the aldol reaction of acetone with 4-nitrobenzaldehyde catalyzed by N-methylpropylamine, assisted by two vicinal silanols (subscript 2s). The numbers indicate the $\Delta^\ddagger G_{\text{forward}}$ for the considered reaction. The Gibbs free energy includes a correction term for a 50/50 vol% DMSO and acetone liquid phase, as experimentally employed¹.

The stable reaction intermediates identified in the case of two promoting vicinal silanol groups are the same as in the case of a single promoting silanol group and are, hence, included in Appendix C (Scheme C-2). A minor difference between assistance by one isolated silanol or two vicinal silanols is for the position of the protons in the carbinolamine (**b**_{2s}) intermediate, which appears as a zwitterionic intermediate in the latter case, similar to what de Lima Batista et al.⁷ found.

The iminium intermediates **c**_{2s}' and **d**_{2s}' are, however, found to be better stabilized than in the case of a single promoting silanol group, as can be seen from Table 5-3, which results in higher barriers for both **TS2(2)**_{2s}, **TS3(2)**_{2s} and **hydr.**, as reported in Table 5-1. Also the initial carbon-carbon bond formation step **TS3(1)**_{2s} towards the iminium intermediate **d**_{2s}' appears to have a higher barrier than when a single silanol group is involved (**TS3(1)**_s). This is consistent with the previous result where also the promotion by a single water molecule (**TS3H₂O**) was found to be optimal for this step. The carbinolamine formation (**TS1**_{2s}), iminium ion formation (**TS2(1)**_{2s}) and aldol product release (**TS4**_{2s}), however, do seem to benefit from the additional promoting silanol group. This results in a flatter Gibbs free energy diagram, which will lead to

a higher overall reaction rate in the case of promotion by two vicinal silanols as compared to isolated silanols.

Table 5-3: Thermodynamics of the intermediates for the aldol reaction of acetone and 4-nitrobenzaldehyde, catalyzed by N-methylpropylamine and assisted by one or two silanol groups (respectively subscript s and 2s). The Gibbs free energy includes a correction term for a 50/50 vol% solvent/acetone liquid phase.

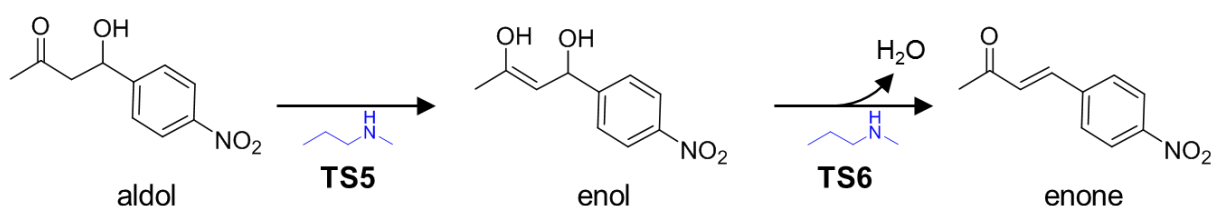
	50 vol% DMSO			50 vol% hexane		
	$\Delta_r H_{liq}^{328K}$ kJ mol ⁻¹	$\Delta_r S_{liq}^{328K}$ J K ⁻¹ mol ⁻¹	$\Delta_r G_{liq}^{328K}$ kJ mol ⁻¹	$\Delta_r H_{liq}^{328K}$ kJ mol ⁻¹	$\Delta_r S_{liq}^{328K}$ J K ⁻¹ mol ⁻¹	$\Delta_r G_{liq}^{328K}$ kJ mol ⁻¹
Isolated silanol						
$a_s + \text{acetone} \rightarrow b_s$	-19.6	-176.3	38.2	-22.5	-174.0	34.6
$b_s \rightarrow c_s'$	52.5	20.5	45.8	58.1	21.2	51.1
$c_s' \rightarrow c_s + H_2O$	-21.2	57.5	-40.1	-12.6	74.8	-37.2
$c_s + 4\text{-NB} \rightarrow d_s'$	-60.3	-194.7	3.6	-57.8	-193.7	5.8
$d_s' \rightarrow d_s$	4.6	21.7	-2.5	-0.3	22.3	-7.6
$d_s' + H_2O \rightarrow e_s$	-24.4	-10.6	-20.9	-51.5	-53.3	-34.0
$e_s \rightarrow \text{aldol} + a_s$	15.1	165.6	-39.2	28.0	191.0	-34.7
Vicinal silanols						
$a_{2s} + \text{acetone} \rightarrow b_{2s}$	-48.9	-189.3	13.3	-49.4	-186.8	11.9
$b_{2s} \rightarrow c_{2s}'$	34.3	14.0	29.7	40.8	18.2	34.8
$c_{2s}' \rightarrow c_{2s} + H_2O$	14.9	67.4	-7.2	22.7	83.4	-4.7
$c_{2s} + 4\text{-NB} \rightarrow d_{2s}'$	-86.4	-206.6	-18.6	-83.6	-205.9	-16.1
$d_{2s}' \rightarrow d_{2s}$	24.2	47.4	8.7	19.6	47.8	3.9
$d_{2s}' + H_2O \rightarrow e_{2s}$	-17.0	-27.9	-7.9	-36.4	-48.0	-20.6
$e_{2s} \rightarrow \text{aldol} + a_{2s}$	45.1	204.5	-22.0	50.1	236.8	-27.6

5.3.3 Aldol product dehydration to the enone product and readsorption

The pathway towards the site-blocking enamine species (**d** or **d_s**), which has been experimentally identified on a spent catalyst surface, was elucidated in the previous section. Another species that was identified on a spent catalyst¹ is the conjugated enamine **h_s**, displayed in Scheme 5-5. Direct dehydration of the surface intermediates **d_s** or **d_s'** towards **h_s**, was in Chapter 4 suggested as possible pathway. This route, however, was found to have a Gibbs free energy barrier of 198.0 kJ mol⁻¹, which is prohibitively large for the reaction to occur under the investigated reaction conditions. A more likely pathway towards **h_s** occurs via readsorption of the enone product on the amine.

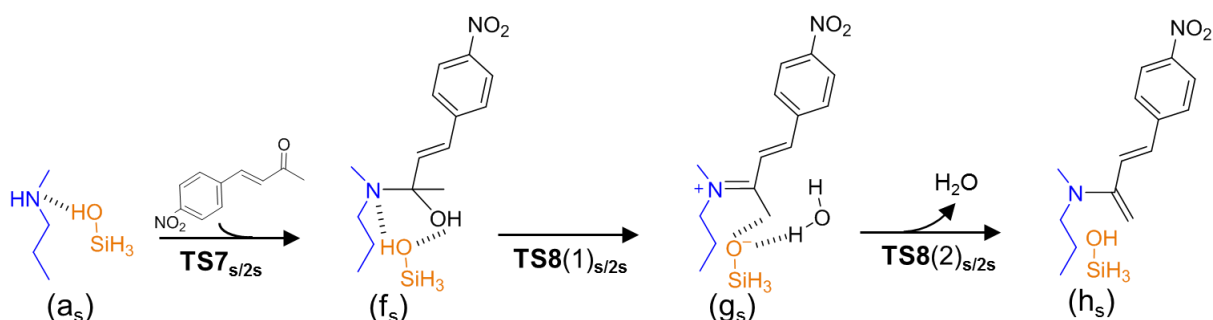
Experimentally, it was observed that the formation of the enone product occurs via dehydration of the primary aldol product^{3,32}. Scheme 5-4 indicates that the reaction mechanism towards this dehydrated enone product is catalyzed by the weakly basic amine catalyst. The

reaction starts with the enolization of the aldol product (**TS5**), which can be either unassisted or assisted by silanol groups. The Gibbs free energy barriers are reported in Table 5-4, and are visualized in Figure 5-5. Assistance by one or two water molecules did not lower the reaction barriers and is thus not reported. The resulting enol is 41.6 kJ mol⁻¹ less stable than the aldol product, as summarized in Table 5-5, and can dehydrate spontaneously, or assisted by the amine site with zero, one or two silanol groups (**TS6**), to the enone product. It was previously found in Chapter 4 that, at the investigated experimental conditions, the aldol product and dehydrated enone product are at thermodynamic equilibrium.



Scheme 5-4: Amine catalyzed aldol product isomerization to its enol form and subsequent amine catalyzed or uncatalyzed dehydration to the enone product, with the release of water. The N-methylpropylamine catalyst only binds to the transition states and not to the reagents, intermediates, or products.

Readsorption of the enone product on the active site occurs via **TS7_s**, as displayed in Scheme 5-5. The carbinolamine intermediate (**f_s**) is then dehydrated via **TS8(1)_s** to its iminium intermediate (**g_s**). A proton transfer between the iminium ion and the silanol group then occurs, and water is released (**TS8(2)_s**), resulting in the conjugated enamine species **h_s**. Promotion by water molecules is not considered for this reaction, because adding water to the reaction was experimentally found to shift the selectivity away from enone product, thereby limiting its possibility for readsorption¹.



Scheme 5-5: Enone product readsorption and dehydration to the conjugated enamine **h_s**

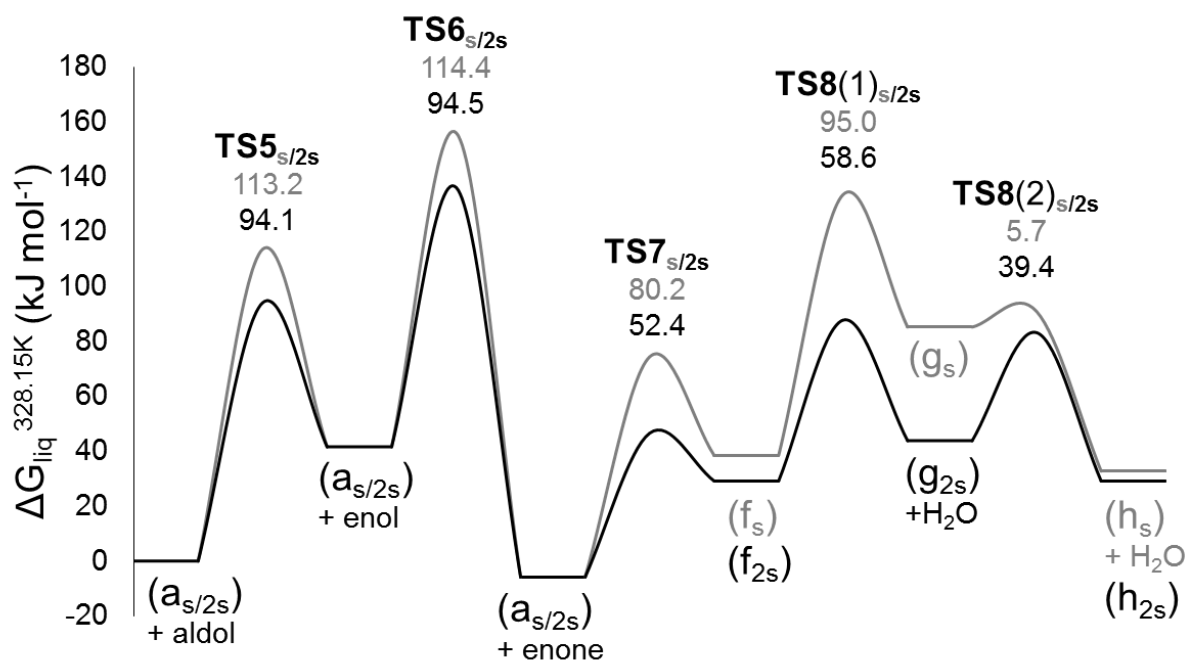


Figure 5-5: Gibbs free energy reaction barriers for the aldol product dehydration to the enone product, readsorption on the N-methylpropylamine site, and dehydration, assisted by one isolated silanol (grey, subscript s) or two vicinal silanols (black, subscript 2s). The numbers indicate the $\Delta^\ddagger G_{\text{forward}}$ for the considered reaction. The Gibbs free energy includes a correction term for a 50/50 vol% DMSO/acetone liquid phase, as experimentally employed ¹.

The Gibbs free energy diagram in Figure 5-5 indicates that the formation of the conjugated enamine **h_s** can be assisted by an isolated silanol or by vicinal silanol groups. It, however, appears thermodynamically not favored, largely due to the entropy loss upon readsorption of a free enone molecule from the bulk of the solvent to the amine site (**TS7**). Nonetheless, this work is able to demonstrate that the dominant reaction path to the experimentally observed conjugated enamine **h_s** on a cooperative catalyst, under dry reaction conditions, is via the enone product readsorption and subsequent dehydration.

Table 5-4: Gibbs free energy barriers for the reactions displayed in Scheme 5-4 and Scheme 5-5. The Gibbs free energy includes a correction term for a 50/50 vol% solvent/acetone liquid phase.

		50 vol% DMSO			50 vol% hexane		
Assisted by		$\Delta^\ddagger H_{\text{liq}}^{328\text{K}}$ kJ mol ⁻¹	$\Delta^\ddagger S_{\text{liq}}^{328\text{K}}$ J K ⁻¹ mol ⁻¹	$\Delta^\ddagger G_{\text{liq}}^{328\text{K}}$ kJ mol ⁻¹	$\Delta^\ddagger H_{\text{liq}}^{328\text{K}}$ kJ mol ⁻¹	$\Delta^\ddagger S_{\text{liq}}^{328\text{K}}$ J K ⁻¹ mol ⁻¹	$\Delta^\ddagger G_{\text{liq}}^{328\text{K}}$ kJ mol ⁻¹
TS5	-	68.1	-158.8	120.2	60.0	-182.5	119.9
	H ₃ SiOH	68.8	-135.2	113.2	56.0	-162.3	109.2
	2H ₃ SiOH	45.8	-147.1	94.1	35.3	-172.9	92.0
TS6	(<i>uncatalyzed</i>)	120.1	31.9	109.6	112.6	15.5	107.5
	-	91.3	-90.1	120.8	79.0	-111.8	115.6
	H ₃ SiOH	90.1	-74.0	114.4	73.2	-99.8	105.9
	2H ₃ SiOH	67.0	-83.9	94.5	52.8	-109.0	88.6
TS7	H ₃ SiOH	19.6	-184.5	80.2	9.7	-211.2	79.0
	2H ₃ SiOH	-11.1	-193.5	52.4	-18.5	-218.4	53.1
TS8	H ₃ SiOH (1)	75.7	-37.3	88.0	67.9	-70.2	91.0
	H ₃ SiOH (2)	3.9	-5.3	5.7	9.9	-10.2	13.2
	2H ₃ SiOH (1)	56.2	-7.3	58.6	65.8	10.1	62.4
	2H ₃ SiOH (2)	41.6	6.8	39.4	36.6	-1.5	37.1

Table 5-5: Thermodynamics for the intermediates in Scheme 5-4 and Scheme 5-5. The Gibbs free energy includes a correction term for a 50/50 vol% solvent/acetone liquid phase.

	50 vol% DMSO			50 vol% hexane		
	$\Delta H_{\text{liq}}^{328\text{K}}$ kJ mol ⁻¹	$\Delta S_{\text{liq}}^{328\text{K}}$ J K ⁻¹ mol ⁻¹	$\Delta G_{\text{liq}}^{328\text{K}}$ kJ mol ⁻¹	$\Delta H_{\text{liq}}^{328\text{K}}$ kJ mol ⁻¹	$\Delta S_{\text{liq}}^{328\text{K}}$ J K ⁻¹ mol ⁻¹	$\Delta G_{\text{liq}}^{328\text{K}}$ kJ mol ⁻¹
Isolated silanol						
a_s + enone → f_s	-2.6	-164.5	51.4	-14.35	-189.6	47.9
f_s → g_s	42.5	9.0	39.6	49.04	15.3	44.0
g_s → h_s + H₂O	-36.3	49.2	-52.4	-28.84	59.7	-48.4
Vicinal silanols						
a_{2s} + enone → f_{2s}	-22.3	-174.4	35.0	-32.1	-199.9	33.5
f_{2s} → g_{2s}	13.4	-3.8	14.7	26.2	15.3	21.2
g_{2s} → h_{2s} + H₂O	4.9	59.7	-14.7	6.0	49.4	-10.2
aldol → enol	25.2	-50.1	41.6	30.4	-48.9	46.4
enol → enone + H₂O	-15.64	96.9	-47.4	-6.35	115.3	-44.2
aldol → enone + H₂O	9.54	46.8	-5.8	24.03	66.4	2.2

5.3.4 Effect of solvent on reaction barriers and intermediates

The experimental work of Kandel et al.³³ highlighted the possibility of inhibition of the secondary amine sites by stable iminium ions when polar solvents are employed. Specifically, the iminium ion of 4-nitrobenzaldehyde was suggested as a stable intermediate on secondary amine catalysts in polar media. In this work, iminium ions only appeared as intermediates when they are stabilized by hydrogen-bonding with water molecules, or silanol groups, but they are found to be too reactive to be considered inhibiting species. It is, however, plausible that when water is used as solvent³³, instead of being co-fed in small amounts, these iminium ions will indeed be stabilized sufficiently to inhibit the secondary amine site and result in a lower reaction rate as compared to an apolar solvent. Water as solvent is, however, not considered in this work.

The reaction barriers determined in the paragraphs above are for a 50/50 vol% DMSO/acetone mixture, as was experimentally employed to investigate the reusability of the aminated silica catalysts¹. A mixture of 50/50 vol% hexane/acetone has also been experimentally used, and is reported to yield the highest overall reaction rates⁶. Because in this work the solvation Gibbs free energy is calculated with COSMO-RS theory, based on the gas-phase optimized geometries, changing the solvent mixture can be performed without recalculating the computationally expensive CBS-QB3 energies.

When switching from a 50/50 vol% DMSO/acetone to a 50/50 vol% hexane/acetone mixture, the Gibbs free energy barriers in the pathway without any promoting species are the same, as reported in Table 5-1. The Gibbs free energy thermodynamic stability of the intermediate species with hexane as solvent, reported in Table 5-2, only slightly differs from DMSO when water is either a product or reagent in the reaction. This difference is primarily caused by the less negative solvation Gibbs free energy for water in hexane, as compared to DMSO. This effect also causes the reaction barriers for the water-assisted transition states to be considerably lower in hexane, as compared to DMSO. Of particular interest is the water assisted carbon-carbon coupling step **TS3_{H2O}**, which has a Gibbs free energy barrier of 79.5 kJ mol⁻¹ in hexane as compared to 86.8 kJ mol⁻¹ in DMSO. Because the equivalent unassisted **TS3** barrier, leading to the site-blocking species (**d**), is the same in both solvents, using hexane as solvent will result in a less pronounced site blocking, given that the concentration of water is the same in both solvents.

The reaction barriers for the case of one or two promoting silanol groups is not considerably different in both solvents, as reported in Table 5-1, with a maximum difference of 4.9 kJ mol⁻¹ in the case where an isolated silanol group is deprotonated in the transition state

(TS2(1)_{s/2s}) and, hence, slightly better stabilized in the polar DMSO. The thermodynamic stability of the intermediates, reported in Table 5-2 and Table 5-3, is only slightly different in hexane when water is involved as product or reagent.

The Gibbs free energy barriers for the aldol dehydration towards the enone, and readsorption on the active site with one or two promoting silanol groups, is the same in both solvents, as reported in Table 5-4. However, the dehydration of the aldol product towards the enone product, with the release of water, is thermodynamically less favored in hexane.

It thus appears that all the Gibbs free energy barriers for reactions that involve water as reactant, or water aiding in the transition state, are lower when using hexane as solvent. This means that, for the same concentration of water, the promoting effect of water will be more pronounced in hexane, and a lower amount of water will be required to completely prevent the formation of site-blocking species on the surface of the catalyst. It should, however, be noted that the computational approach used considers water as infinitely diluted in the solvent mixture. When the water content increases substantially, particularly in the case of apolar solvents, the solubility of water will also start to play an important role.

5.4 Conclusions

Gibbs free energy calculations for transition states, and surface intermediates, using the CBS-QB3 model chemistry demonstrate that water plays an important role in reducing reaction barriers and preventing the formation of site-blocking species in the liquid-phase amine-catalyzed aldol reaction. The presence of one or two water molecules in the transition state reduces the barrier for reactions that involve a proton transfer, i.e., the carbinolamine and enamine formation, and the aldol product liberation. Promotion by two water molecules was found to be optimal in these steps, whereas the involvement of a third water molecule led to a too pronounced entropic penalty. The presence of one water molecule in the carbon-carbon bond formation step is found to be crucial for avoiding the formation of a site-blocking enamine species. The presence of two water molecules in this step was found to again increase the reaction barrier.

Isolated silanol groups were found to assist in the amine-catalyzed aldol reaction in a similar way as a water molecule does, but with lower reaction barriers for all steps. This proves that silanol groups are more efficient promoters than water molecules. The more pronounced acidity of the silanol group, as compared to water, leads to iminium ions as stable intermediates. Also in this case, the absence of water will lead to abundant formation of the site-blocking

enamine species. Vicinal silanols stabilize the iminium ion intermediates more, leading to higher Gibbs free energy barriers for reactions with these iminium ions. However, generally, a flatter energy diagram is obtained, which indicates that the overall reaction rate will be higher for promotion by two vicinal silanols.

Dehydration of the aldol product towards the enone product was found to occur via a two-step base catalyzed mechanism involving enolization followed by dehydration. Enone product readsorption on the amine, and dehydration, assisted by isolated or vicinal silanols, causes the formation of a conjugated enamine species which was experimentally observed in previous work on a cooperative catalyst spent under dry reaction conditions.

Switching the solvent from a 50/50 vol% DMSO/acetone to a 50/50 vol% hexane/acetone mixture mainly resulted in a less negative Gibbs free energy of solvation of water and thereby lowered the reaction barriers for all the transition states where water is involved as reagent or auxiliary species in the transition state. This also means that less water will be required to prevent the formation of site-blocking species when an apolar solvent such as hexane is used. Care should, however, be taken that the optimal water concentration is still fully miscible in this mixture.

5.5 References

1. De Vylder, A.; Lauwaert, J.; Esquivel, D.; Poelman, D.; De Clercq, J.; Van Der Voort, P.; Thybaut, J. W., The role of water in the reusability of aminated silica catalysts for aldol reactions. *Journal of Catalysis* **2018**, *361*, 51-61.
2. Kubota, Y.; Yamaguchi, H.; Yamada, T.; Inagaki, S.; Sugi, Y.; Tatsumi, T., Further Investigations on the Promoting Effect of Mesoporous Silica on Base-Catalyzed Aldol Reaction. *Topics in Catalysis* **2010**, *53* (7-10), 492-499.
3. Kandel, K.; Althaus, S. M.; Peeraphatdit, C.; Kobayashi, T.; Trewyn, B. G.; Pruski, M.; Slowing, I. I., Substrate inhibition in the heterogeneous catalyzed aldol condensation: A mechanistic study of supported organocatalysts. *Journal of Catalysis* **2012**, *291*, 63-68.
4. Brunelli, N. A.; Venkatasubbaiah, K.; Jones, C. W., Cooperative catalysis with acid–base bifunctional mesoporous silica: impact of grafting and co-condensation synthesis methods on material structure and catalytic properties. *Chemistry of Materials* **2012**, *24* (13), 2433-2442.
5. Zeidan, R. K.; Davis, M. E., The effect of acid–base pairing on catalysis: An efficient acid–base functionalized catalyst for aldol condensation. *Journal of Catalysis* **2007**, *247* (2), 379-382.
6. Lauwaert, J.; Moschetta, E. G.; Van Der Voort, P.; Thybaut, J. W.; Jones, C. W.; Marin, G. B., Spatial arrangement and acid strength effects on acid–base cooperatively catalyzed aldol condensation on aminosilica materials. *Journal of Catalysis* **2015**, *325*, 19-25.
7. de Lima Batista, A. P.; Zahariev, F.; Slowing, I. I.; Braga, A. A. C.; Ornellas, F. R.; Gordon, M. S., Silanol-Assisted Carbinolamine Formation in an Amine-Functionalized Mesoporous Silica Surface: Theoretical Investigation by Fragmentation Methods. *The Journal of Physical Chemistry B* **2016**, *120* (8), 1660-1669.
8. Patil, M. P.; Sunoj, R. B., Insights on co-catalyst-promoted enamine formation between dimethylamine and propanal through ab initio and density functional theory study. *The Journal of organic chemistry* **2007**, *72* (22), 8202-8215.

9. Louie, M. K.; Francisco, J. S.; Verdicchio, M.; Klippenstein, S. J.; Sinha, A., Dimethylamine addition to formaldehyde catalyzed by a single water molecule: a facile route for atmospheric carbinolamine formation and potential promoter of aerosol growth. *The Journal of Physical Chemistry A* **2015**, *120* (9), 1358-1368.
10. Williams, I. H., Theoretical modelling of specific solvation effects upon carbonyl addition. *Journal of the American Chemical Society* **1987**, *109* (21), 6299-6307.
11. Williams, I. H.; Spangler, D.; Femec, D. A.; Maggiora, G. M.; Schowen, R. L., Theoretical models for solvation and catalysis in carbonyl addition. *Journal of the American Chemical Society* **1983**, *105* (1), 31-40.
12. Hall, N. E.; Smith, B. J., High-level ab initio molecular orbital calculations of imine formation. *The Journal of Physical Chemistry A* **1998**, *102* (25), 4930-4938.
13. Dickerson, T. J.; Lovell, T.; Meijler, M. M.; Noodleman, L.; Janda, K. D., Nicotinic Aqueous Aldol Reactions: Synthetic and Theoretical Investigations into the Origins of Catalysis. *The Journal of Organic Chemistry* **2004**, *69* (20), 6603-6609.
14. Zhang, P.-H.; Pu, M.; Gao, Y.; Zhang, Y.-F.; Lei, M.; Yang, Z.-Y., Theoretical Study of the Histidine-catalyzed Asymmetric Aldol Reaction of Acetone and Benzaldehyde. *The Journal of Physical Chemistry A* **2018**, *122* (39), 7842-7851.
15. Ugliengo, P.; Saunders, V.; Garrone, E., Silanol as a model for the free hydroxyl of amorphous silica: ab-initio calculations of the interaction with water. *Journal of Physical Chemistry* **1990**, *94* (6), 2260-2267.
16. Civalleri, B.; Garrone, E.; Ugliengo, P., Vibrational modes of isolated hydroxyls of silica computed ab initio in a cluster approach. *Chemical physics letters* **1998**, *294* (1-3), 103-108.
17. Sahai, N.; Rosso, K. M., Computational molecular basis for improved silica surface complexation models. *Surface Complexation Modeling, Elsevier* **2006**, *11*, 359-396.
18. Civalleri, B.; Garrone, E.; Ugliengo, P., Cage-like clusters as models for the isolated hydroxyls of silica: Ab initio B3-LYP calculations of the interaction with ammonia. *Langmuir* **1999**, *15* (18), 5829-5835.
19. Lomenech, C.; Bery, G.; Costa, D.; Stievano, L.; Lambert, J.-F., Theoretical and experimental study of the adsorption of neutral glycine on silica from the gas phase. *ChemPhysChem* **2005**, *6* (6), 1061-1070.
20. Costa, D.; Lomenech, C.; Meng, M.; Stievano, L.; Lambert, J.-F., Microsolvation of glycine by silanol ligands: A DFT study. *Journal of Molecular Structure: Theochem* **2007**, *806* (1-3), 253-259.
21. Civalleri, B.; Garrone, E.; Ugliengo, P., Ab initio study of the adducts of small molecules with the isolated hydroxyl of silica and the brønsted site in zeolites: A comparison between B3-LYP and MP2 methods. *The Journal of Physical Chemistry B* **1998**, *102* (13), 2373-2382.
22. Sauer, J.; Hill, J.-R., The acidity of surface silanol groups. A theoretical estimate based on ab initio calculations on a model surface. *Chemical physics letters* **1994**, *218* (4), 333-337.
23. Frisch, M. J.; Trucks, G. W.; Schlegel, H. B.; Scuseria, G. E.; Robb, M. A.; Cheeseman, J. R.; Scalmani, G.; Barone, V.; Petersson, G. A.; Nakatsuji, H.; Li, X.; Caricato, M.; Marenich, A. V.; Bloino, J.; Janesko, B. G.; Gomperts, R.; Mennucci, B.; Hratchian, H. P.; Ortiz, J. V.; Izmaylov, A. F.; Sonnenberg, J. L.; Williams; Ding, F.; Lipparini, F.; Egidi, F.; Goings, J.; Peng, B.; Petrone, A.; Henderson, T.; Ranasinghe, D.; Zakrzewski, V. G.; Gao, J.; Rega, N.; Zheng, G.; Liang, W.; Hada, M.; Ehara, M.; Toyota, K.; Fukuda, R.; Hasegawa, J.; Ishida, M.; Nakajima, T.; Honda, Y.; Kitao, O.; Nakai, H.; Vreven, T.; Throssell, K.; Montgomery Jr., J. A.; Peralta, J. E.; Ogliaro, F.; Bearpark, M. J.; Heyd, J. J.; Brothers, E. N.; Kudin, K. N.; Staroverov, V. N.; Keith, T. A.; Kobayashi, R.; Normand, J.; Raghavachari, K.; Rendell, A. P.; Burant, J. C.; Iyengar, S. S.; Tomasi, J.; Cossi, M.; Millam, J. M.; Klene, M.; Adamo, C.; Cammi, R.; Ochterski, J. W.; Martin, R. L.; Morokuma, K.; Farkas, O.; Foresman, J. B.; Fox, D. J. *Gaussian 16*, Wallingford, CT, 2016.
24. Montgomery Jr, J. A.; Frisch, M. J.; Ochterski, J. W.; Petersson, G. A., A complete basis set model chemistry. VI. Use of density functional geometries and frequencies. *The Journal of chemical physics* **1999**, *110* (6), 2822-2827.

25. Wheeler, S. E.; Moran, A.; Pieniazek, S. N.; Houk, K., Accurate reaction enthalpies and sources of error in DFT thermochemistry for aldol, Mannich, and α -aminoxylation reactions. *The Journal of Physical Chemistry A* **2009**, *113* (38), 10376-10384.
26. Schlegel, H. B., Optimization of equilibrium geometries and transition structures. *Journal of Computational Chemistry* **1982**, *3* (2), 214-218.
27. De Vylder, A.; Lauwaert, J.; Sabbe, M. K.; Reyniers, M.-F.; De Clercq, J.; Van Der Voort, P.; Thybaut, J. W., Rational Design of Nucleophilic Amine Sites via Computational Probing of Steric and Electronic Effects. *Catalysis Today* **2019**.
28. Desmet, G. B.; Sabbe, M. K.; D'hooge, D. R.; Espeel, P.; Celasun, S.; Marin, G. B.; Du Prez, F. E.; Reyniers, M.-F., Thiol-Michael addition in polar aprotic solvents: nucleophilic initiation or base catalysis? *Polymer Chemistry* **2017**, *8* (8), 1341-1352.
29. McQuarrie, D. A.; Cox, H.; Simon, J. D., *Physical chemistry: a molecular approach*. Sterling Publishing Company: 1997.
30. Klamt, A.; Eckert, F., COSMO-RS: a novel and efficient method for the a priori prediction of thermophysical data of liquids. *Fluid Phase Equilibria* **2000**, *172* (1), 43-72.
31. Marenich, A. V.; Cramer, C. J.; Truhlar, D. G., Universal Solvation Model Based on Solute Electron Density and on a Continuum Model of the Solvent Defined by the Bulk Dielectric Constant and Atomic Surface Tensions. *The Journal of Physical Chemistry B* **2009**, *113* (18), 6378-6396.
32. Lauwaert, J.; De Canck, E.; Esquivel, D.; Thybaut, J. W.; Van Der Voort, P.; Marin, G. B., Silanol-Assisted Aldol Condensation on Aminated Silica: Understanding the Arrangement of Functional Groups. *ChemCatChem* **2014**, *6* (1), 255-264.
33. Kandel, K.; Althaus, S. M.; Peeraphatdit, C.; Kobayashi, T.; Trewyn, B. G.; Pruski, M.; Slowing, I. I., Solvent-Induced Reversal of Activities between Two Closely Related Heterogeneous Catalysts in the Aldol Reaction. *ACS Catalysis* **2013**, *3* (2), 265-271.
34. Der Voort, P. V.; Vansant, E., Silylation of the silica surface a review. *Journal of liquid chromatography & related technologies* **1996**, *19* (17-18), 2723-2752.
35. Ceresoli, D.; Bernasconi, M.; Iarlori, S.; Parrinello, M.; Tosatti, E., Two-membered silicon rings on the dehydroxylated surface of silica. *Physical review letters* **2000**, *84* (17), 3887.
36. Cho, M.; Park, J.; Yavuz, C. T.; Jung, Y. J. P. C. C. P., A catalytic role of surface silanol groups in CO₂ capture on the amine-anchored silica support. **2018**, *20* (17), 12149-12156.

Chapter 6

Continuous-flow aldol reactions¹

Opposed to a batch-type reactor, a continuous-flow type reactor provides a direct means to observe catalyst deactivation phenomena by measuring the catalytic performance as a function of the time-on-stream. This allows for more detailed insights into the specific deactivation behavior of the heterogeneous catalyst. In the present chapter, a new reactor set-up for measuring the kinetics of liquid-phase reactions is designed and built to assess the long term catalyst stability in the aldol reaction between acetone and 4-nitrobenzaldehyde. The “intrinsic kinetics” character of the rate data is then assessed, both via correlations and with experimental tests. Subsequently, the aminated silica catalysts that were evaluated in a batch reactor, see Chapter 4, are now evaluated for their long-term stability with time on stream using different solvents and solvent mixtures.

6.1 Design of a Liquid-Solid Lab-Scale (LS)² plug flow reactor

A lab-scale liquid phase plug flow reactor is developed. This reactor is commonly referred to as the “Liquid-Solid Lab-Scale reactor”, or the “(LS)²-reactor”. The (LS)² reactor is specifically designed with the goal of measuring intrinsic kinetics in liquid phase reactions on a heterogeneous catalyst and is schematically displayed in Figure 6-1. To determine whether it is possible to operate the aldol reaction between acetone and 4-nitrobenzaldehyde catalyzed by aminated silica catalysts in an intrinsic way, standard correlations for internal and external heat and mass transfer limitations were verified¹. From the detailed calculations as reported Appendix D, it can be concluded that the reaction can indeed be operated in the intrinsic kinetics regime for a variety of solvents, such as hexane, DMSO, and acetone.

¹ Part of this chapter is published as **De Vylder, Anton, et al. "Catalyst Stability Assessment in a Lab-Scale Liquid Solid (LS)² Plug-Flow Reactor" Catalysts (2019).**

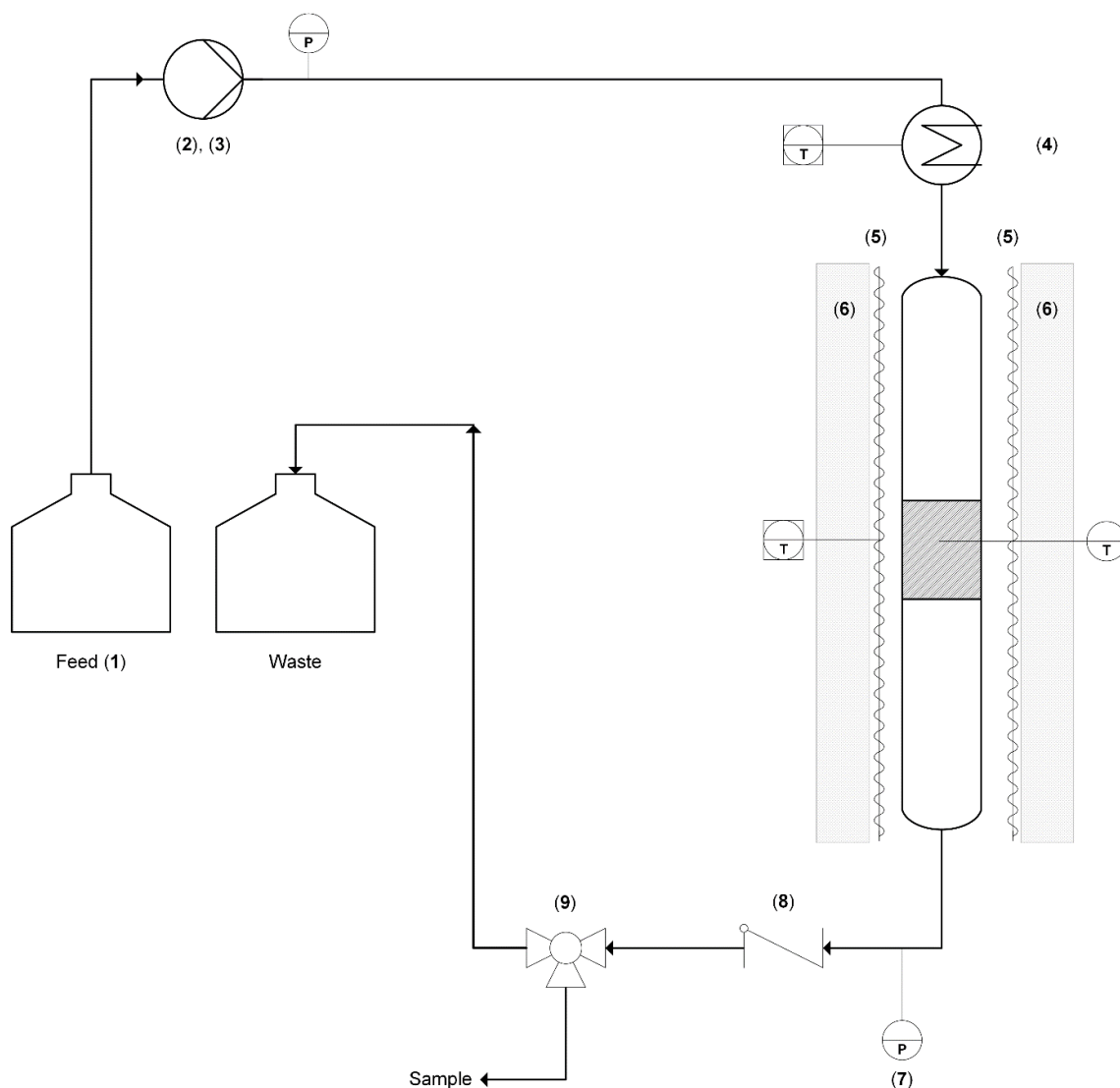


Figure 6-1: Schematic representation of the (LS)² reactor with the feed vessel (1), the positive displacement pump (2) with pulsation damper (3), the pre-heating (4), the reactor heating (5) and insulation (6), the outlet pressure gauge (7), the check valve (8) and three-way valve (9)

6.1.1 Feed section

The feed section essentially comprises a flask with the reactant mixture (1 in Figure 6-2) connected to an Eldex 2SMP plunger pump (2 in Figure 6-2). The flask is gently stirred to avoid the development of concentration gradients. The positive displacement pump can deliver flow rates between 0.01 and 10 mL/min with discharge pressures up to 400 bar. To reduce flow fluctuations, a pulsation damper (3 in Figure 6-2) is installed. A manometer is coupled to this damper, which measures the pump discharge pressure and is able to impose a high-pressure limit above which the pump operation is stopped. As this pump is used to feed different reactant mixtures to the reactor, it is important to verify the chemical compatibility of the internal parts for all the chemicals used, see Table 6-1. The piston is made from sapphire, and the inlet and

outlet valves incorporate sapphire seats with ruby balls. The piston seal material is made from graphite fiber reinforced polytetrafluoroethylene (PTFE) and all the tubing is made of type 316 stainless. Sealings are either a chlorotrifluoroethylene (CTFE) or Kal-Rez[®] type.



Figure 6-2: Continuously stirred reagent vessel (1), plunger pump Eldex 2SMP (2) with pulsation damper (3).

Table 6-1: ‘Wetted parts’ in the Eldex 2SMP pump and their chemical compatibility with the solvents used in this work²

<i>Part</i>	<i>Acetone</i>	<i>Hexane</i>	<i>DMSO</i>
Stainless steel (316)	✓	✓	✓
Sapphire	✓	✓	✓
Ruby	✓	✓	✓
PTFE	✓	✓	✓
CTFE	To 40 °C	To 100 °C	To 50 °C
Kal-Rez	✓	✓	✓

To also ensure chemical compatibility between the construction materials and the employed chemicals in the rest of the setup, all the tubing is made either of stainless steel 316 or of PTFE, and all ferrules and fittings are made of PTFE.

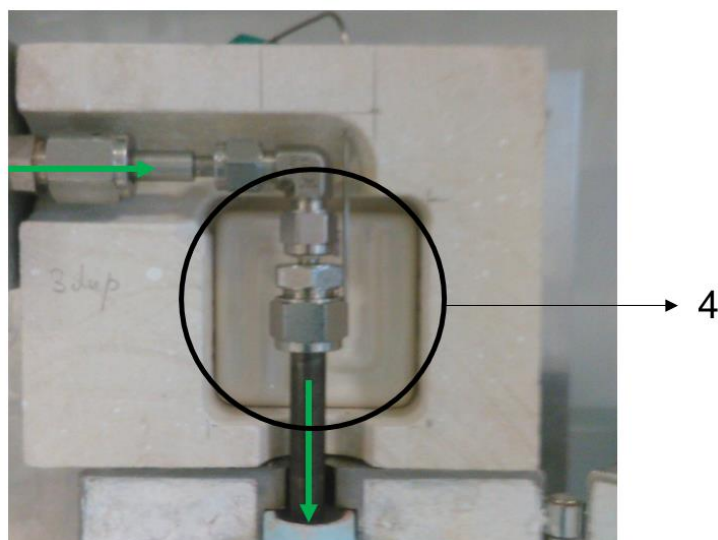


Figure 6-3: Heating element (4) of 125 W to pre-heat the feed before it enters the reactor. The green arrow indicates the direction of flow.

To ensure that the reactant mixture is fed at the right temperature upon reaching the catalyst bed for a variety of flow rates, the option for additional pre-heating before the reactor inlet is available. As seen on Figure 6-3, the preheater is an insulated box around the feed tube with a radiation heater of 125 W (4). The box itself is made of thermally insulating material ‘FACT01 PROMASIL 1100 super’. A thermocouple is placed on the inside of the box in order to measure and control the temperature with an Omron e5ck PID controller.

6.1.2 Reaction section

The actual reactor is a stainless steel 316 tube with an inner diameter of 0.75 cm and a length of 30 cm. At 10 cm from the bottom of the reactor, there is mesh which prevents the packing and catalyst from leaving the reactor, as schematically drawn in Figure 6-4. The reactor tube is surrounded by a heating coat to bring the reactor to the desired reaction temperature, controlled with an Omron e5ck PID controller. The whole of reactor and heating wire is insulated in order to keep the reactor isothermal (6 in Figure 6-4).

For intrinsic kinetics assessment, no radial temperature gradient should occur in the reactor. This means that the temperature which is controlled at the outside of the reactor has to be equal to the temperature measured inside of the reactor. The external thermocouple is attached to the reactor tube, between the heating wire and the outside of the tube. The internal thermocouple is located in the middle of the catalyst bed. The schematic representation in Figure 6-4 shows the placement of both thermocouples.

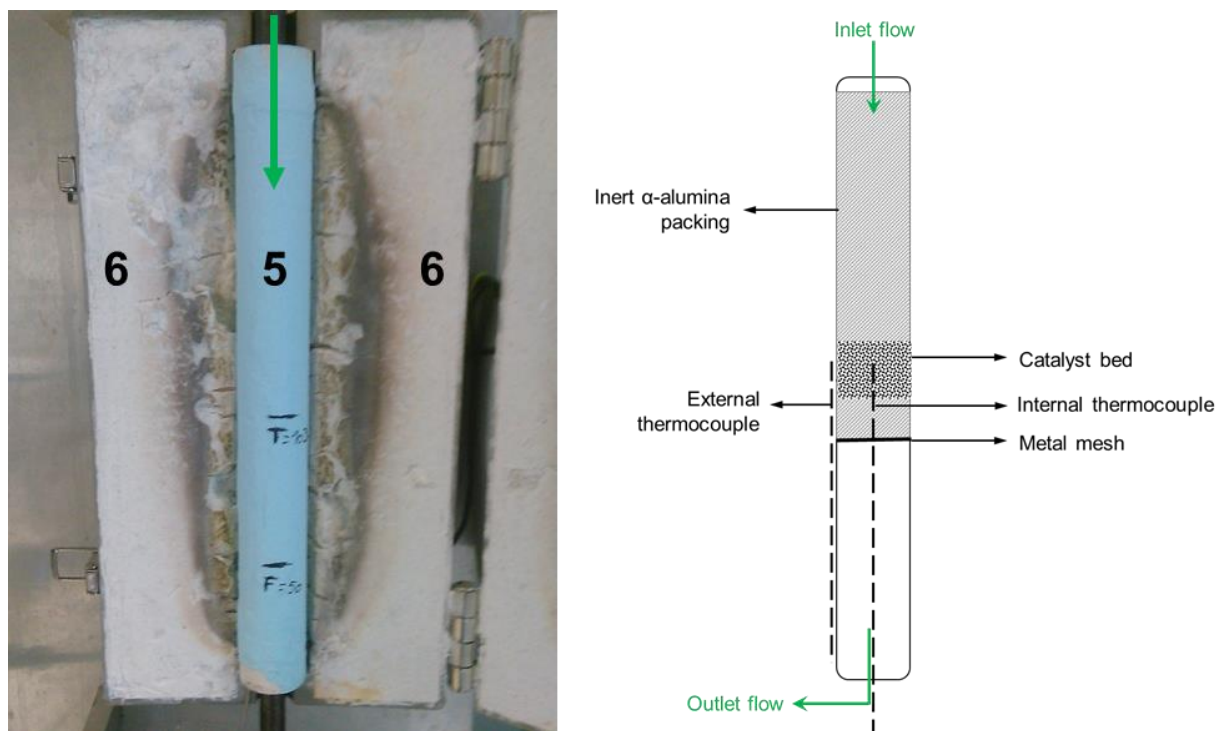


Figure 6-4: Heating cone for the reactor tube (5), surrounded by insulation (6). Indication ‘F’ is the mesh location at 50 mm from the bottom of the heating coat, indication ‘T’ is the height of the internal thermocouple at 103 mm from the bottom of the heating coat. The green arrow indicates the direction of flow.

6.1.3 Outlet collection and sampling

The heated sections of the (LS)² reactor should be at a constant pressure, which is maintained slightly above atmospheric pressure to avoid vaporization. The outlet pressure can be monitored on the pressure gauge which is installed immediately after the reactor outlet (7 in Figure 6-5). To create a back-pressure, a check valve (8 in Figure 6-5) is installed with a spring that opens at a pressure of 1.8 barg. The difference between this backpressure and the pump outlet pressure gives an indication of the pressure drop over the entire setup.

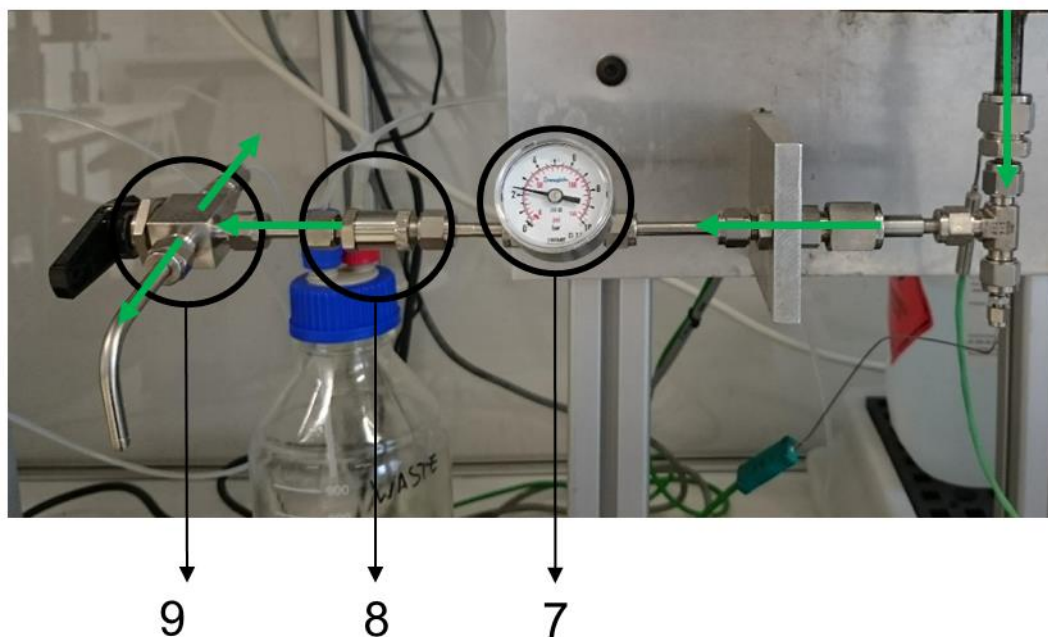


Figure 6-5: Outlet of the reactor, with the outlet pressure manometer (7), the backpressure check valve (8) and the three-way valve (9) with one line for drawing samples and the other line going to the waste bottle. The green arrow indicates the direction of flow.

Samples of the reactor outlet can be drawn by switching the three-way valve (9 in Figure 6-5). This allows to take samples in an easy and safe way. When no sample is being taken, the reactor effluent is collected in a waste vessel that is placed on a balance. This balance is used to verify the mass balance.

6.1.4 Safety considerations

To ensure safe operation of the reactor, several safety precautions were installed. A drip tray was placed underneath the entire setup to avoid spilling solvent to the environment in case a leak should occur. Additionally, a hydrocarbon detector was installed, which is triggered upon detection of any hydrocarbon partial pressure and then reacts by increasing the room ventilation and shutting down both the feed pump and the heating elements.

6.2 Procedure for catalyst stability assessment

The methylaminopropyl (MAP) functionalized mesoporous silica catalyst used in the continuous flow (LS)² reactor is synthesized according to the procedures as described in Chapter 4, with the exception that a larger pellet diameter range (250 – 500 μm) is chosen to avoid a significant pressure drop over the catalyst bed.

The experiments described in the present chapter are all conducted at 328.15 K, with a feed mixture equivalent to the one used in the batch experiments reported in Chapter 4. This mixture contains 50 vol% acetone and 50 vol% of a selected solvent. A molar acetone excess with respect to 4-nitrobenzaldehyde amounting to 100 was employed. The amount of catalyst is determined such that all the experiments are performed at the same site time, which is defined as space time $\left(\frac{W}{F_{4\text{-NB}}^0}\right)$, multiplied with the active site concentration C_{site} . With W the catalyst mass (kg_{cat}) and $F_{4\text{-NB}}^0$ the molar inlet feed of 4-nitrobenzaldehyde $\left(\frac{\text{mol}_{4\text{-NB}}}{\text{s}}\right)$ and C_{site} $\left(\frac{\text{mol}_{\text{site}}}{\text{kg}_{\text{cat}}}\right)$ determined with CHNS analysis. The site time, hence, has units $\frac{\text{mol}_{\text{site}} \text{ s}}{\text{mol}_{4\text{-NB}}}$.

The time on stream measurement is started when the feed pump is started and at certain time intervals samples are taken. Sampling was only started after 30 min on stream because no steady-state operation with respect to the hydrodynamics and isothermicity was obtained in the first 30 minutes of reaction.

6.3 Catalyst stability with time on stream

In this section, the long-term stability of the monofunctional methylaminopropyl (MAP) mesoporous silica catalyst as described in Chapter 4 is evaluated for a variety of solvents and solvent mixtures.

6.3.1 Hexane as solvent

Figure 6-6 indicates that in 50 vol% hexane, without any water added, a slow decrease in conversion as a function of time on stream can be observed. This decrease amounts to 2.1% over the course of 3.5 hours on stream and is likely related to the formation of site-blocking species under dry reaction conditions, as discussed in Chapter 4.

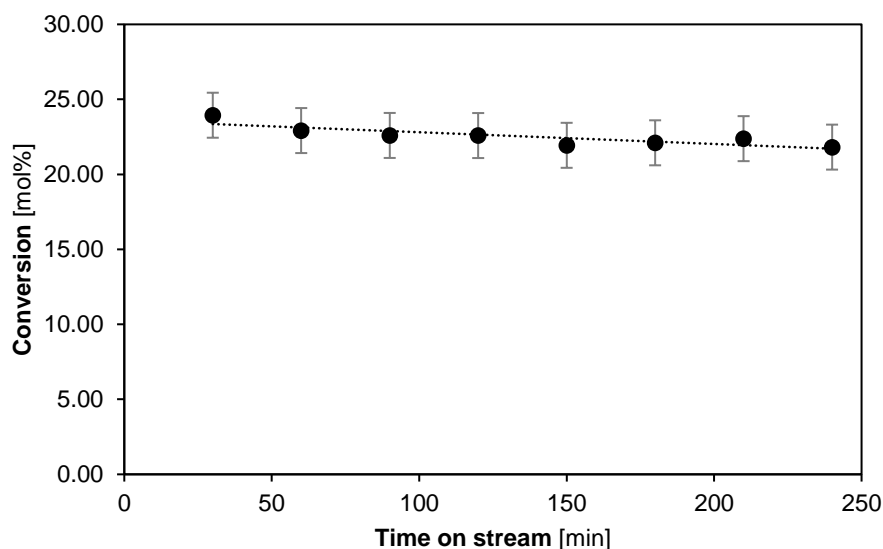


Figure 6-6: Conversion as function of time on stream for the aldol reaction between acetone and 4-nitrobenzaldehyde using hexane as a solvent, catalyzed by a monofunctional MAP catalyst. ($T = 328.15 \text{ K}$, $P_{\text{tot}} = 180 \text{ kPa}$, site time = $165.1 \text{ mol}_{\text{site}} \cdot \text{s} \cdot \text{mol}_{4\text{-NB}}^{-1}$, 0.45 wt% 4-nitrobenzaldehyde, 55.8 wt% acetone, 43.5 wt% hexane, 0.25 wt% IS). Line is a guide for the eye.

6.3.2 Acetone as solvent

When the reaction is performed solvent-free, i.e., with acetone both as excess reagent and as a solvent, a more pronounced decrease in activity is noted as a function of time on stream. A conversion decrease of 5% occurred during the first 3.5 hours on stream. Further sampling shows that the deactivation appears to asymptotically stabilize. It should be noted that the acetone used in this experiment is so-called “stock” acetone with a water content amounting to $0.31 \pm 0.05 \text{ wt\%}$. The lower overall activity when using acetone as solvent, as compared to hexane, could be an indication of a change in concentration of either 4-nitrobenzaldehyde or water around the active sites in the pores of the catalyst.

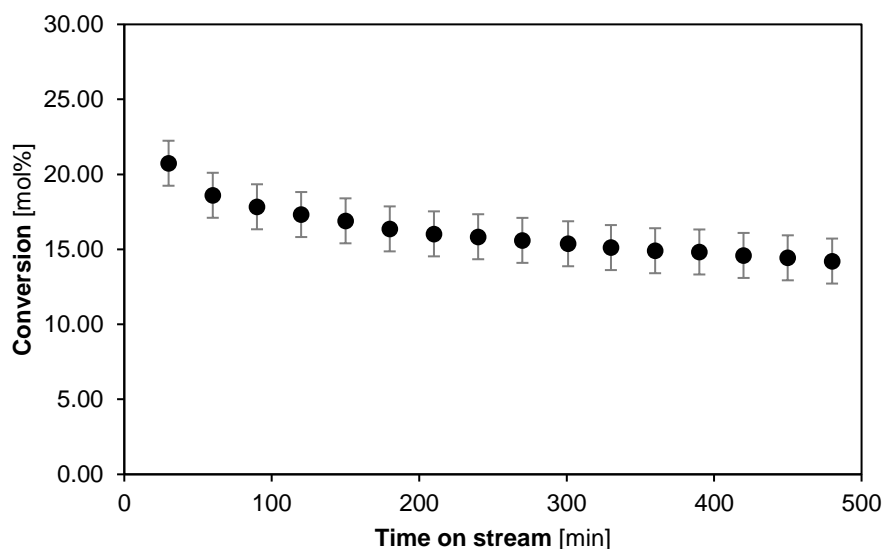


Figure 6-7: Conversion as a function of time on stream for the aldol reaction between acetone and 4-nitrobenzaldehyde using acetone as solvent, catalyzed by a monofunctional MAP catalyst. ($T = 328.15 \text{ K}$, $P = 180 \text{ kPa}$, site time = $165.1 \text{ mol}_{\text{site}} \cdot \text{s} \cdot \text{mol}^{-1}$, 0.45 wt% 4-nitrobenzaldehyde, 99.3 wt% acetone, 0.25 wt% IS.)

6.3.3 DMSO as solvent

In the previous chapter, DMSO was selected as solvent because of its miscibility with acetone in all concentrations, including various amounts of water. Complete reusability was achieved when at least 0.5 wt% water was co-fed to the reaction catalyzed by a monofunctional MAP catalyst. In Figure 6-8, the stability with time on stream of this catalyst is evaluated for DMSO as solvent with respectively 0 wt%, 1 wt% and 2 wt% of water added. The amount of DMSO is adapted to ensure that no concentration differences arise from co-feeding water. In Figure 6-8, the same trend in stability as a function of the added water amount can be noted as with the batch reactor: when no water is added, the catalyst deactivates with 3.6% during 4 hours on stream. When 1 wt% water is added, a more flat conversion profile is obtained with only 1% decrease in activity during 4 hours on stream, which is within the experimental error margin of 1.5%. However, with 2 wt% of water added, the conversion profile as a function of time on stream appears to be stable for at least 4 hours on stream. These conditions are, hence, selected for a longer experiment.

The long-term stability of both the monofunctional MAP and cooperative MAP catalyst, using DMSO as solvent with 2 wt% water, is assessed in Figure 6-9. Samples were drawn every hour during 28 hours on stream. It can be seen from Figure 6-9 that the monofunctional MAP catalyst slowly decreases in activity during this period. The cooperative MAP catalyst, however, exhibits two deactivation regions. Till 7 hours on stream, the cooperative MAP catalyst exhibits a higher activity than the monofunctional base catalyst. This agrees well with

the observations made in the batch reactor, see Chapter 4, where the cooperative MAP catalyst exhibited a higher activity than the monofunctional MAP catalyst at the same operating conditions. However, after 7 hours on-stream, the activity of the cooperative catalyst has dropped to the same level as the monofunctional catalyst, which has only slightly deactivated. This first, and most rapid, deactivation of the cooperative catalyst can be attributed to the loss of the cooperativity between the silanol groups and the amine active sites. Indeed, when the cooperative ability has been completely lost after 7 hours on stream, only the activity of the isolated amine site remains, whereby the activity of the cooperative MAP catalyst has been reduced to that of the monofunctional MAP catalyst. The silanol groups, that are responsible for this cooperative effect, seem to quickly lose their hydrogen-bonding ability towards the carbonyl substrates. This could be due to water deprotonating the silanol groups, or forming an extensive multilayer coverage on the surface of the silica gel³, which limits access to the silanol groups for the carbonyl substrates. This silanol deactivation also explains why the cooperative catalysts employed in the Chapter 4 were not reusable in a batch reactor under the same conditions where the monofunctional base catalyst was reusable, and the addition of larger amounts of water seems to even decrease the reusability ratio, even though the amine site itself can be made fully reusable.

After 8 hours on-stream, the slope of the evolution of the conversion with time-on-stream for the cooperative MAP catalyst changes. The deactivation occurs at a reduced rate, yet, it remains faster than the decrease in conversion with the time-on-stream exhibited by the monofunctional MAP catalyst. In this regime of prolonged exposure to the aqueous feed, the deactivation is most likely caused by hydrolysis reactions of the silica material that cause aminosilane leaching, structural degradation of the support material and silica dissolution⁴. The slower deactivation rate of the monofunctional MAP catalyst in this region could be the result of the end-capping of the silanol groups with trimethylsilyl groups, which introduced a more hydrophobic surface environment^{5, 6}.

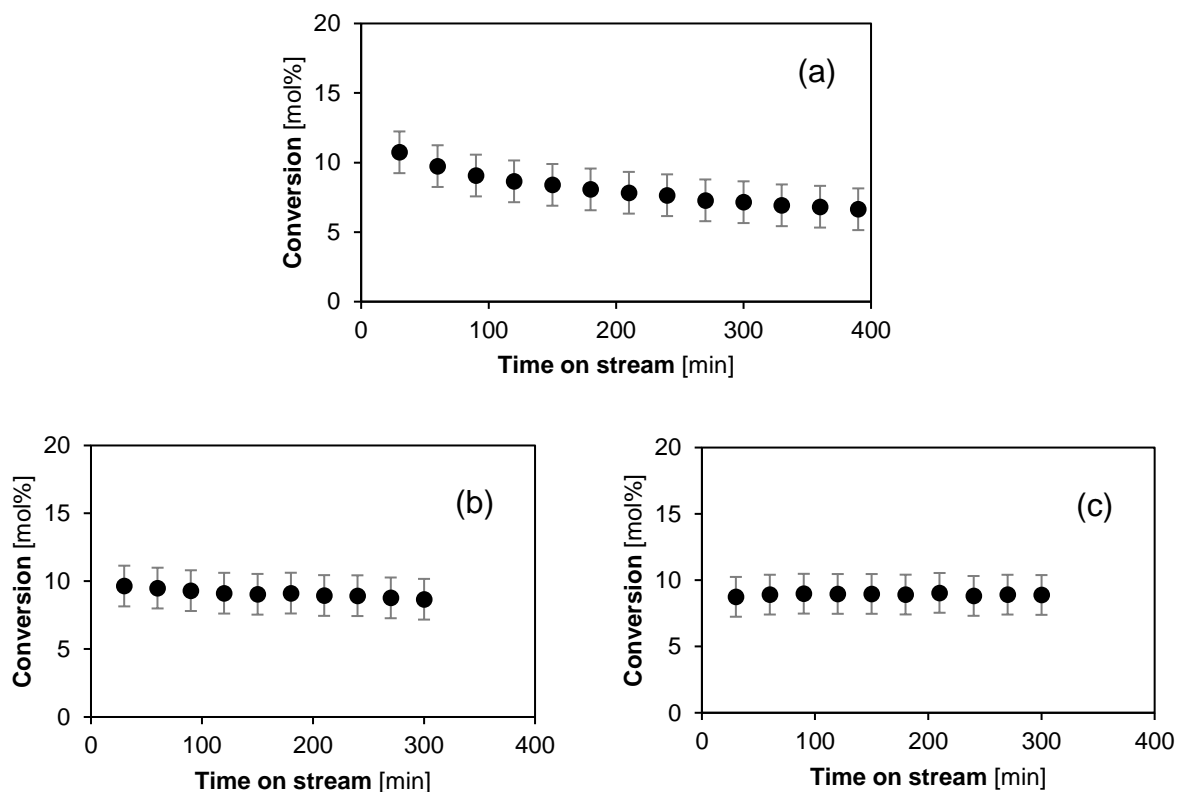


Figure 6-8: Conversion as a function of time on stream for the aldol reaction between acetone and 4-nitrobenzaldehyde using DMSO as a solvent with varying amounts of water. (a): no added water, (b): 1 wt% water added, (c): 2 wt% water added. ($T = 328.15$ K, $P = 180$ kPa, site time = $165.1 \text{ mol}_{\text{site}} \cdot \text{s} \cdot \text{mol}^{-1}$, 0.45 wt% 4-nitrobenzaldehyde, 44.6 wt% acetone, 52.5 – 55.0 wt% DMSO, 0.25 wt% IS.)

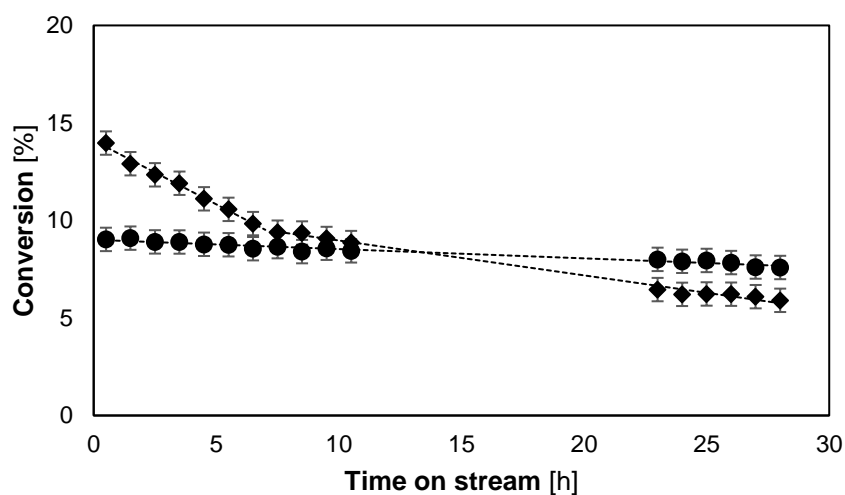


Figure 6-9. Stability of the cooperative MAP catalyst (♦) and the monofunctional MAP catalyst (●) with time-on-stream for 28 hours. ($T = 328.15$ K, $P_{\text{tot}} = 180$ kPa, site time = $165.1 \text{ mol}_{\text{site}} \cdot \text{s} \cdot \text{mol}_{4\text{-nitrobenzaldehyde}}^{-1}$, 0.45 wt% 4-nitrobenzaldehyde, 44.6 wt% acetone, 52.5 wt% DMSO, 2.19 wt% water, 0.25 wt% IS). Lines are a guide to the eye.

6.4 Experimental intrinsic kinetics assessment

The design conditions of the (LS)² reactor were determined using standard correlations for the absence of concentration and temperature gradients, based on the reaction rate measured in a batch reactor. The results of these correlations are, of course, only valid when the same reaction rate is indeed measured in the (LS)² reactor. Additionally, experimental tests are performed to ensure the absence of internal and external concentration gradients, and radial temperature gradients.

6.4.1 Reaction rate equivalence with a batch-type reactor

The turnover frequency (TOF) for a known catalyst is determined in the (LS)² reactor and is then compared to the value obtained in the Parr[®] batch reactor, for which the intrinsic character of the measured kinetics was verified in earlier work⁷. Due to the equivalence between a batch reactor and a plug flow reactor, the same TOF should be obtained when the observed rate is intrinsic⁸.

Hexane is selected as solvent, because it has been the standard solvent in previous research^{7,9} and exhibits the highest activity for the MAP catalysts. The activity is, however, not stable as a function of time on stream, as displayed in Figure 6-6. Hence, the points measured for the kinetic profile in Figure 6-10 are all determined in the range of 30 to 240 minutes on stream, where the decrease in catalyst activity is limited to 2.1%. From the slope of the conversion versus site time plot in Figure 6-10, a turnover frequency (TOF) of $1.2 \cdot 10^{-3} \text{ s}^{-1}$ is measured. The literature reported⁹ TOF in the batch reactor for the monofunctional MAP catalyst in hexane amounts to $1.0 \cdot 10^{-3} \text{ s}^{-1}$. The TOF is 20% higher in the continuous flow (LS)² reactor which could be related to a different timescale of catalyst deactivation in both reactors. This issue is, however, not in the scope of present work and will not be elaborated upon further. The correlations in Appendix D were also evaluated for this slightly higher TOF and still indicate the possibility for intrinsic kinetics.

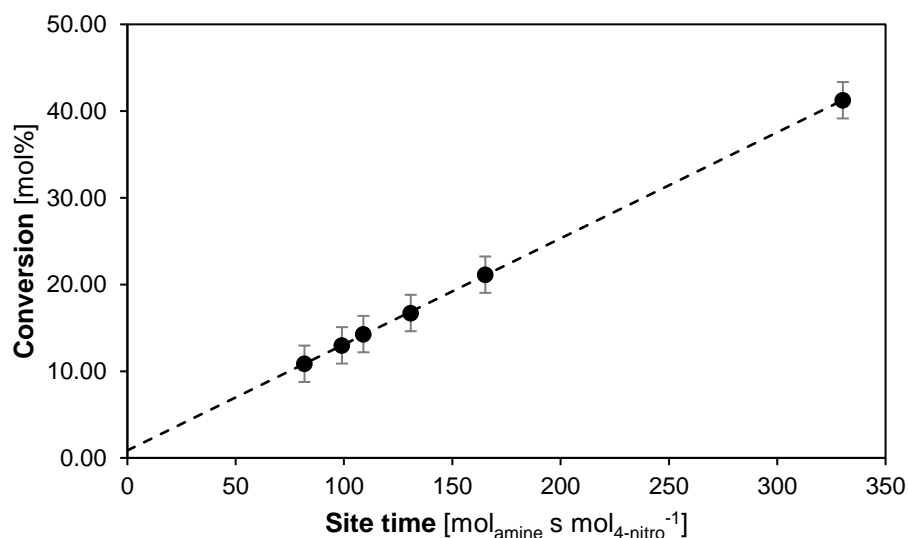


Figure 6-10: Conversion as function of site time of a monofunctional MAPS catalyst for the aldol reaction between acetone and 4-nitrobenzaldehyde using hexane as solvent. ($T = 328.15 \text{ K}$, $P_{\text{tot}} = 180 \text{ kPa}$, site time = $81.75 - 330.3 \text{ mol}_{\text{site}} \cdot \text{s} \cdot \text{mol}^{-1}$, 0.45 wt% 4-nitrobenzaldehyde, 55.8 wt% acetone, 43.5 wt% hexane, 0.25 wt% IS. Fixed error of 2.1 %)

6.4.2 Experimental verification of heat and mass transfer limitations

6.4.2.1 Radial temperature gradient

Comparison of the temperature measured by the internal thermocouple and external thermocouple, at the height of the catalyst bed, allows to determine whether a radial temperature gradient exists. Throughout all the experiments, the temperature of the two thermocouples was identical, so no indication of any radial temperature gradient was obtained.

6.4.2.2 External concentration gradients in the catalyst pellet

External concentration gradients can be evaluated by performing experiments with identical site times but different flow rates. This correlates to a different liquid velocity¹. If there are no external concentration gradients, than there will be no difference in conversion. The latter thus being necessary for working in the intrinsic regime. As can be seen in Table 6-2, the absence of external concentration gradients is confirmed with these experiments.

Table 6-2: Conversion of 2 different experiments with an identical site time but different flow rate. Hexane was used as solvent.

Site time ($\text{mol}_{\text{site}} \cdot \text{s} \cdot \text{mol}^{-1}$)	165.1	165.1
Flowrate (ml min^{-1})	1.5	2
Conversion (mol%)	22 ± 1.5	21 ± 1.5

6.4.2.3 Internal concentration gradients in the catalyst pellet

The occurrence of internal concentration gradients is assessed by performing experiments using catalysts with different particle diameters. If there are no internal concentration gradients, then the conversion obtained making use of these catalysts of different size at the same site time will be identical. Table 6-3 indicates that, within the experimental error margin, the same conversion level is reached. It should be noted that, due to the inability to pelletize the mesoporous silica material, a catalyst with the smaller pellet diameter was independently synthesized. The determination of its amine loading also contributes to an experimental error, but is not included in the error margin.

Table 6-3: Conversion of 2 different experiments at $149.3 \text{ mol}_{\text{site}} \text{ s mol}^{-1}$ but different pellet sizes. Hexane was used as solvent.

Particle diameter (μm)	63 - 210	250 - 500
Conversion (mol%)	16 ± 1.5	19 ± 1.5

6.5 Conclusions

A lab-scale continuous flow reactor, which can be operated under the same conditions as the Parr[®] batch reactor, was designed and built. It is commonly referred to as the (LS)² reactor, i.e., the liquid-solid lab-scale reactor. A high accuracy positive displacement pump with pulsation damper and discharge pressure readout was installed at the feed line. An optional pre-heating element was added, which allows to isothermally feed high flow rates of reagents. The reaction section is heated by a heating coat, the temperature of which is controlled by an external thermocouple. An internal thermocouple measures the temperature of the catalyst bed and allows to ensure no radial temperature gradients develop. At the reactor outlet, backpressure is created with a check valve of 1.8 barg before the feed passes through a three-way valve. This three-way valve can be switched to either the organic waste bottle or a sample point.

One of the most significant advantages of a continuous-flow reactor is the ability to directly measure the long-term catalyst stability as a function of time on stream. Using hexane or acetone as solvent in the aldol reaction of acetone with 4-nitrobenzaldehyde, catalyzed by a monofunctional MAP catalyst, indicated that deactivation with time on stream could not be avoided. DMSO, without any water added, also caused the monofunctional MAP catalyst to deactivate. However, adding 1 wt% of water significantly reduced the extent of deactivation, while including 2 wt% of water in the feed appeared to be a sufficient to obtain a stable

conversion during 4 hours on stream. Even longer-term stability tests do indicate that both the cooperative MAP as well as the monofunctional MAP catalyst deactivate with time on stream. In the first instance, a relatively rapid loss of the cooperative ability of the cooperative MAP catalyst is observed, which is most likely due to the local buildup of water, or the deprotonation of the silanol groups by water. With a longer time-on-stream, the activity of both the cooperative as well as the monofunctional catalyst further decreases more moderately, which can be related to hydrolysis reactions of the silica network that lead to aminosilane leaching, support degradation, and silica dissolution. This deactivation being less pronounced for the monofunctional base catalyst than for the cooperative one, is attributed to its more pronounced hydrophobicity owing to the trimethylsilyl groups used for endcapping.

Intrinsic kinetics were verified for the aldol reaction, employing either DMSO or hexane as solvent, using the appropriate correlations. Specifically for the case of hexane as solvent, the intrinsic kinetics were also verified by determining a turnover frequency at the same reaction conditions as the batch reactor. Additionally, two experimental checks were performed that verified the absence of internal and external concentration gradients around the catalyst pellet.

6.6 References

1. Berger, R. J.; Stitt, E. H.; Marin, G. B.; Kapteijn, F.; Moulijn, J. A., Eurokin. Chemical reaction kinetics in practice. *Cattech* **2001**, 5 (1), 36-60.
2. Thermo Fisher Scientific Chemical Compatibility Guide <http://tools.thermofisher.com/content/sfs/brochures/D20480.pdf>.
3. Scott, R. P.; Kucera, P., Solute-solvent interactions on the surface of silica gel. *Journal of Chromatography A* **1978**, 149, 93-110.
4. Etienne, M.; Walcarius, A., Analytical investigation of the chemical reactivity and stability of aminopropyl-grafted silica in aqueous medium. *Talanta* **2003**, 59 (6), 1173-1188.
5. Koyano, K.; Tatsumi, T.; Tanaka, Y.; Nakata, S., Stabilization of mesoporous molecular sieves by trimethylsilylation. *The Journal of Physical Chemistry B* **1997**, 101 (46), 9436-9440.
6. Takei, T.; Yamazaki, A.; Watanabe, T.; Chikazawa, M., Water adsorption properties on porous silica glass surface modified by trimethylsilyl groups. *Journal of colloid and interface science* **1997**, 188 (2), 409-414.
7. Lauwaert, J.; De Canck, E.; Esquivel, D.; Thybaut, J. W.; Van Der Voort, P.; Marin, G. B., Silanol-Assisted Aldol Condensation on Aminated Silica: Understanding the Arrangement of Functional Groups. *ChemCatChem* **2014**, 6 (1), 255-264.
8. Marin, G.; Yablonsky, G. S., *Kinetics of chemical reactions*. John Wiley & Sons: 2011.
9. Lauwaert, J.; De Canck, E.; Esquivel, D.; Van Der Voort, P.; Thybaut, J. W.; Marin, G. B., Effects of amine structure and base strength on acid-base cooperative aldol condensation. *Catalysis Today* **2015**, 246, 35-45.

Chapter 7

Chitosan as a Sustainable Catalyst in the Aqueous Aldol reaction¹

Chitin is one of the most abundant biopolymers in nature, obtained from crab- and shrimp shell waste, and is composed almost entirely of β -(1-4)-N-acetyl-D-glucosamine units¹. Partial deacetylation of chitin yields a copolymer consisting of both β -(1-4)-N-acetyl-D-glucosamine and D-glucosamine units, called chitosan, as displayed in Figure 7-1. The primary amines that are made accessible have proven their use for a variety of applications, e.g., for their chelating ability in removal of heavy metal ions from aqueous streams², their biocompatibility for nanofibrous pH sensors³, and their antibacterial and antifungal properties⁴. Moreover, they have also served as catalytic sites for various organic reactions, such as the aldol⁵⁻⁹, nitroaldol⁸ and Knoevenagel reaction^{5, 8}, or for anchoring novel catalytic sites¹⁰⁻¹².

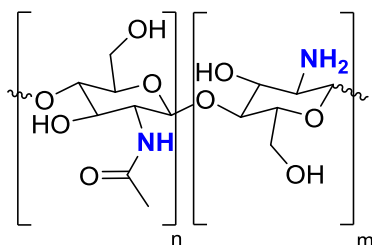


Figure 7-1: Structure of chitosan, consisting of n β -(1-4)-N-acetyl-D-glucosamine units and m D-glucosamine units.

7.1 Introduction

This work focuses on the aldol reaction, which is an important carbon-carbon coupling reaction that has applications in the pharmaceutical industry¹³, fine-chemical synthesis^{14, 15}, and in the production of biomass-derived hydrocarbon fuels^{16, 17}. Nowadays, at the commercial scale, these processes are typically performed in the presence of an organic solvent, while more

¹ This chapter is published as De Vylder, Anton, et al. "Kinetic evaluation of chitosan-derived catalysts for the aldol reaction in water" *Reaction Chemistry & Engineering* (2019).

sustainable solutions with either water as solvent or solvent-free are being pursued^{18,19}. Another focus is the development of heterogeneous catalysts that can replace the frequently employed homogeneous catalysts. Related advantages are a reduced energy cost for separating the catalyst from the product stream, a longer catalyst lifetime, and reduced equipment corrosion^{20,21}. In this chapter, the biopolymer chitosan is evaluated as a potential heterogeneous catalyst for the aldol reaction.

Both primary and secondary amines on silica catalyze the aldol reaction through an enamine intermediate²². However, in organic solvents, primary amines form stable imines that inhibit the catalytic activity. Secondary amines cannot form these imines and are therefore typically found to exhibit a higher catalytic activity, provided that the access to the amine site is not sterically hindered²³⁻²⁵. Although it does appear that this activity order can be reversed when using water as a solvent due to water shifting the equilibrium away from the inhibiting imine²⁶. For amine functionalized mesoporous silica catalysts, it has reported noted that the residual silanol groups on the surface of the support act cooperatively with the grafted amines, thereby increasing the turnover frequency^{22,27}. More recent work demonstrated that the reusability of these grafted amine sites could be significantly enhanced if a few percentages of water are added to the aldol reaction mixture²⁸. However, larger amounts of water lead to hydrolysis of the silica support and subsequent loss of the active sites^{28,29}. Hence, improvement of the support stability in an aqueous reaction environment is an important next step in the development of a stable heterogeneous amine catalyst for the aldol reaction. Amines immobilized on organic polymers, as is the case in chitosan, thus present themselves as ideal candidate catalysts.

The mechanism of the often investigated model aldol reaction of acetone with 4-nitrobenzaldehyde, catalyzed by primary amines, is shown in Figure 7-2^{22,30}. It starts with the addition of acetone to the primary amine (**1**) and subsequent formation of a carbinolamine intermediate (**2**). This carbinolamine then dehydrates towards an imine intermediate (**3**), which is in equilibrium with its enamine form (**4**) via an intramolecular proton transfer. The enamine is sufficiently nucleophilic to bind an incoming 4-nitrobenzaldehyde species and form a new carbon-carbon bond, resulting in the formation of an imine intermediate (**5**). Hydration of this imine intermediate (**5**) yields a carbinolamine (**6**) that detaches from the active site as the aldol product (**7**), thereby restoring the catalytic site (**1**). A possible side-reaction is the formation of an imine species originating from 4-nitrobenzaldehyde (**8**)²⁴, as represented by the grey arrows.

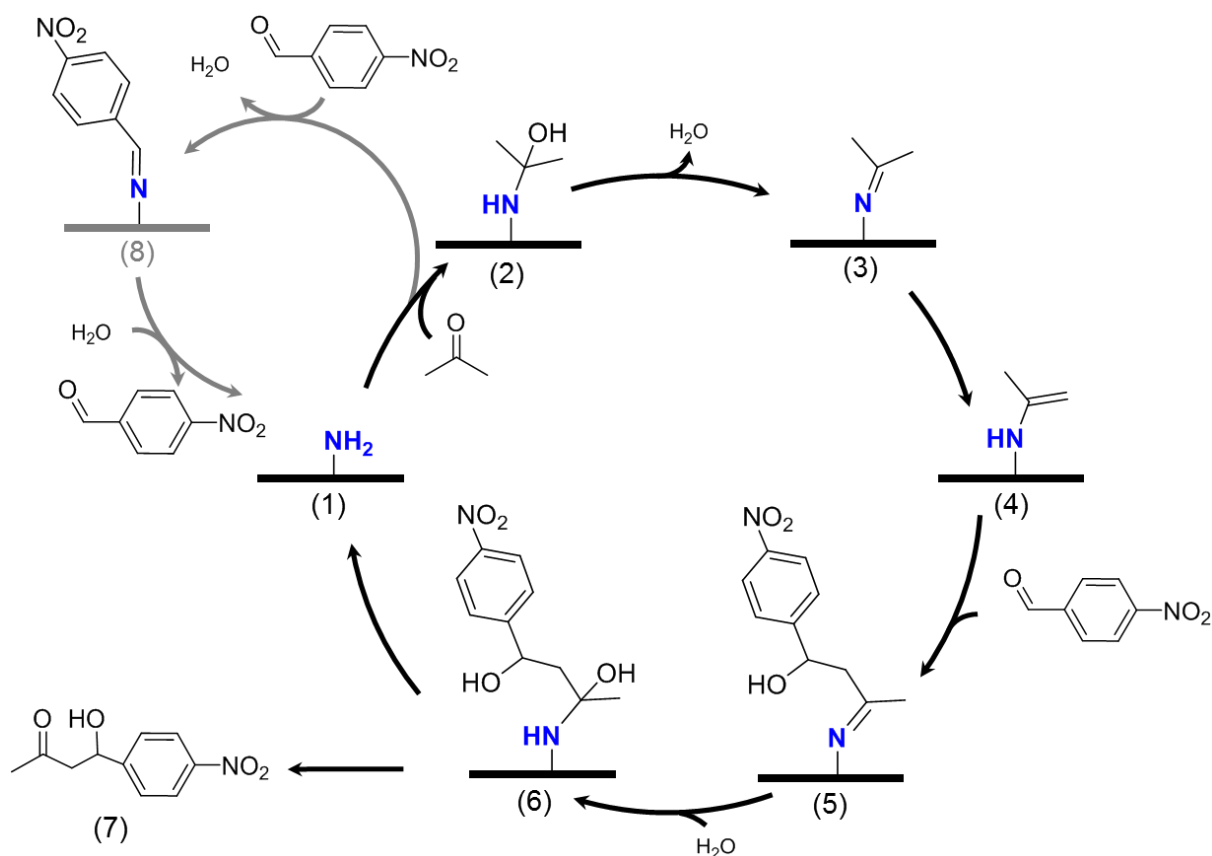


Figure 7-2: Reaction mechanism for the aldol reaction of acetone with 4-nitrobenzaldehyde on the primary amines of chitosan catalysts, based on reference ²².

In recent years, the chitosan catalyzed aldol reaction has been extensively investigated using crude, hydrogel-, or aerogel-based chitosan. Kantam et al.⁵ reported complete conversion in the aldol condensation of 4-nitrobenzaldehyde with acetone with chitosan hydrogels, using dimethylsulfoxide (DMSO) as solvent. No conversion was observed when chitosan powder was employed under the same reaction conditions. Quignard et al.^{6, 7} were the first to recognize the need of water as solvent to obtain meaningful conversion levels in the aldol reaction catalyzed by crude chitosan and chitosan aerogels. They concluded that, when using water as solvent, comparable conversion levels can be reached with both the hydrogel, aerogel and crude form of chitosan⁶. Diaz et al.⁸ were unable to reproduce these conversion levels and highlighted the importance of a meticulous washing procedure of the chitosan hydrogels to avoid residual hydroxide ions catalyzing the aldol reaction. Kayser et al.⁹ reported that chitosan aerogels are catalytically active in the aldol reaction of furfural and acetone, provided that water is present, and obtained complete conversion in 4 hours. Hence, a considerable amount of work has already been performed by these research groups on the potential of chitosan, and its hydro- and aerogel

form, for reaching high conversion levels in the aldol reaction. However, no dedicated kinetics or reusability ratio has yet been measured for chitosan as a catalyst in the aldol reaction.

Meanwhile, it has become clear that the beneficial effect of using water as solvent in the chitosan catalyzed aldol reaction can be attributed to the molecular structure of chitosan³¹. Because of the abundant presence of amino and hydroxyl groups in the polymer chain of both chitin and chitosan, a hydrogen-bond network is formed between these moieties in an organic solvent, leading to partial crystallization and poor accessibility of the amine sites on the polymer¹¹. Water can break this intramolecular hydrogen-bond network, and allows both chitin³² and chitosan to swell^{11,33}. This improved accessibility leads to a higher catalytic activity being observed when chitosan is used in the aqueous aldol reaction⁶ or when hydrogels are used⁵. Therefore, in combination with previous work performed on the beneficial effect of water on the amine site stability in the aldol reaction^{24,26,28}, water will be employed as solvent in this work.

The catalytic activity of chitosan, which is an important feature to evaluate its potential industrial viability, is evaluated in this work in an initial and a consecutive run in a batch reactor³⁴. This allows assessing the activity of chitosan as heterogeneous catalyst in the aldol reaction, and comparing it with existing heterogeneous amine catalysts. Its reusability ratio and active site inhibition by imine formation, is also quantified and compared to existing silica-based heterogeneous amine catalysts²³. Finally, the long-term stability under reaction conditions is evaluated with time on stream in a continuous-flow setup.

7.2 Procedures

7.2.1 Catalyst synthesis

Crude low-molecular weight chitosan (Sigma Aldrich, low molecular weight = 50000 - 190000 Da, degree of deacetylation $\geq 75\%$) and crude chitin (Sigma Aldrich, practical grade, coarse flakes, from shrimp shells) were used as received without further purification. The hydrogel form was synthesized by first dissolving five grams of low molecular weight chitosan powder in 200 mL of an acetic-acid solution (50 mM in water) and stirring for 24 hours. The resulting solution was then added dropwise into a 4 M NaOH-solution with a syringe equipped with a needle (\varnothing 0,08 mm) leading to reprecipitated hydrogels with a diameter of ± 2 mm. Previous research has shown that this procedure results in chitosan hydrogels with a crystallinity that is comparable to hydrated chitosan.³⁵ After 10 hours of hardening, the formed

hydrogels were filtered on a Buchner filter and washed with double deionized water. For the complete removal of the entrapped NaOH, the hydrogels were placed in 1 L double deionized water and gently stirred at 60 rpm for 4 hours before being filtered off. This washing step was repeated until the pH-value of the washing water was neutral and then, to ensure no NaOH remained entrapped in the pores⁸, this was repeated three more times. To determine the water content in the hydrogels, part of the hydrogel beads were dried overnight at 120 °C and the correspondingly obtained dry mass was then compared to the wet mass. Aerogels were prepared by freezing the hydrogels to -80 °C and then placing them for 24 hours in a freeze-dryer (Alpha 1-2 LDplus), operating at 0.12 mbar.

Chitosan with different degrees-of-deacetylation was synthesized according to literature³⁶. The coarse chitin flakes were first pulverized, after which they were immersed in a 12.5 M NaOH-solution, employing a volumetric solid-to-solvent ratio of 1:5, at 100 °C. The reaction times were varied between 2 and 24 hours to obtain a range of deacetylation degrees. To completely remove all residual NaOH, the same washing procedure as described above for the hydrogels was applied. Afterwards, the chitosan was dried at 70 °C for 24 hours.

7.2.2 Catalyst characterization

Elemental CHN analysis was used to quantify the degree-of-deacetylation (DDA) of the chitosan samples, as it is one of the few accurate methods that are applicable in the full deacetylation range³⁷⁻³⁹. These experiments were performed on a Thermo Flash 2000 elemental analyzer. The DDA was calculated from the carbon/nitrogen ratio (C/N), which varies from 5.145 in completely deacetylated chitosan (C₆H₁₁O₄N) to 6.861 in fully acetylated chitin (C₈H₁₃O₅N) according to formula (7.1).

$$\text{DDA} = 1 - \left(\frac{C/N - 5.145}{6.861 - 5.145} \right) \quad (7-1)$$

Infrared spectroscopy on crude chitosan and spent chitosan was performed on a Tensor II (Bruker). Background correction was performed with KBr (Sigma-Aldrich, FR-IR grade, >99%). The sample was measured between 600 cm⁻¹ and 4000 cm⁻¹. Before analysis, the spent chitosan was washed and filtered twice using 1 L of double deionized water, to remove reaction products and unreacted reagents from the pores.

7.2.3 Performance evaluation

The same aldol reaction as in Chapter 4 of acetone (99.6%, Acros) with 4-nitrobenzaldehyde (99%, Acros), yielding 4-hydroxy-4-(4-nitrophenyl)butan-2-one as aldol adduct and 4-(4-nitrophenyl)-3-buten-2-one as enone product, was selected as the model reaction. Two batch reactors have been used to measure the kinetics of this reaction, i.e., a Parr reactor and a glass flask. Consecutive batch experiments with recycled chitosan were performed for the hydrogel and aerogel type. No recycle experiments were performed with crude chitosan as a catalyst, because of difficulties in filtering the fine powder. Instead, the catalytic stability of crude chitosan was evaluated in a packed-bed continuous-flow reactor.

A limited, non-heterogeneously catalyzed conversion of 4-nitrobenzaldehyde towards the aldol reaction products occurred when using water as solvent, as displayed in Figure E-1 in Appendix E. This has also been observed by other research groups^{40, 41}. In this work, the amount of catalyst is determined such that the obtained yields are always significantly higher than this background reaction in water.

7.2.3.1 Batch reactor

The detailed procedure for operating the Parr[®] 4560 mini reactor has been reported previously²⁸ and is briefly summarized here. The reactor was first loaded with 0.26 g crude chitosan, 55.0 g water as solvent (double deionized, Milli-Q[®]), and 0.25 g methyl 4-nitrobenzoate (> 99%, Sigma-Aldrich) as internal standard. This mixture was then heated to 55 °C, under constant stirring at 400 rpm. Acetone (45 g) was separately heated to 55 °C and was used to dissolve 0.45 g 4-nitrobenzaldehyde before injecting in the reactor. The temperature in the reactor was maintained at 55 °C. The time of injection of the acetone and 4-nitrobenzaldehyde mixture in the reactor was taken as the start of the reaction ($t = 0$). The reaction was monitored for 4 hours by taking a sample (0.3 mL) of the reaction mixture every 30 minutes. For each experiment, the total decrease of reaction volume due to sampling was less than 5% whereby the effect of sampling on the kinetic data is considered to be negligible.

To avoid breaking the hydrogel beads by vigorous mechanical stirring, smaller scale experiments in glassware were also performed for the chitosan hydrogel beads. It was verified that changing the scale of the reaction did not alter the measured kinetics. For these experiments, 22.5 g acetone, 27.5 g double deionized water, 0.23 g 4-nitrobenzaldehyde, 0.11 g methyl 4-nitrobenzoate were added to a 250 mL flask and stirred at 250 rpm in an oil bath at 55 °C. The temperature in the oil bath is controlled by a thermocouple (ETS-D5 IKA RCT) and a water

cooled reflux condenser is used to seal the flask. The mixture was allowed to reach the isothermal reaction temperature during 30 minutes, after which the catalyst is added. This time is taken as $t = 0$. Samples (0.3 mL) were drawn from the reaction mixture every hour for 4 hours. For each experiment, the total decrease of reaction volume due to sampling was less than 5% whereby the effect of sampling on the kinetic data is considered to be negligible.

7.2.3.2 *Continuous-flow reactor*

Stability tests were performed in the in-house developed liquid-phase packed-bed (LS)² reactor, loaded with 1 g of crude chitosan. The feed mixture was fed at the top of the reactor at a rate of 1.5 ml min⁻¹. The feed composition was equivalent to the batch reactor feed composition, consisting of 0.45 wt% 4-nitrobenzaldehyde, 44.6 wt% acetone, 54.5 wt% water and 0.25 wt% methyl 4-nitrobenzoate as internal standard. The non-heterogeneously catalyzed product yield at these conditions was determined at 1.69 % and is subtracted from the results. The reactor itself is electrically heated, with its temperature being controlled at 55 °C by an outer thermocouple. The temperature in the catalyst bed was measured with an internal thermocouple to confirm the absence of radial temperature gradients. A backpressure of 1.8 barg is used for all experiments.

7.2.3.3 *Sample analysis*

The reaction samples were analyzed using a reversed-phase high-performance liquid chromatograph (RP-HPLC) from Agilent (1100 series) using the same procedure as reported in Chapter 4.

7.2.3.4 *Determination of catalytic activity and 4-nitrobenzaldehyde molar balance*

The product yield is defined by the sum of the aldol and dehydrated enone product concentration divided by the initial concentration of 4-nitrobenzaldehyde. The specific catalytic activity ($\text{mol}_{\text{product}} \text{g}_{\text{catalyst}}^{-1} \text{s}^{-1}$) was determined by considering the slope of the stable linear part in the graph of the total product yield as a function of reaction time multiplied by the amount of catalyst. The site-time yield ($\text{mol}_{\text{product}} \text{mol}_{\text{sites}}^{-1} \text{s}^{-1}$) was defined by dividing the specific catalytic activity by active site concentration ($\text{mol}_{\text{sites}} \text{g}_{\text{catalyst}}^{-1}$), as determined from elemental analysis. The 4-nitrobenzaldehyde molar balance (Δ) at time t was defined for each sample by relating the sum of the concentration of 4-nitrobenzaldehyde, aldol product, and enone product to the initially added concentration of 4-nitrobenzaldehyde (7-2).

$$\Delta(t) = \frac{C_{4-NB,t} + C_{aldol,t} + C_{enone,t}}{C_{4-NB,0}} \quad (7-2)$$

7.3 Results and Discussion

The catalytic activity of chitosan in its crude form, as hydrogel and as aerogel is evaluated in a batch reactor for the aldol reaction of acetone with 4-nitrobenzaldehyde using water as solvent. To assess the stability of the catalyst, a repeat experiment is performed with the recycled catalysts. Additionally, the catalyst stability is also evaluated by measuring the product yield as a function of time on stream in the continuous-flow (LS)² reactor. Finally, the activity of the primary amine sites as a function of the degree of deacetylation is investigated, and guidelines are provided for further catalyst improvement.

7.3.1 Kinetic investigation of chitosan in a batch reactor

7.3.1.1 Crude chitosan

The measured total product yield obtained with crude low-molecular weight chitosan as catalyst in the aldol reaction of acetone with 4-nitrobenzaldehyde, as a function of time, is displayed in Figure 7-3. Two different regions, indicated by grey and black symbols, can be distinguished. Initially, the slope of the curve decreases up to 2 hours of reaction, after which it appears to remain constant. This trend is not expected for a simple reaction in a batch reactor, which should exhibit a linear trend initially followed by a gradually decreasing slope at higher conversions. This deviating trend indicates that specific phenomena occur initially, leading to a decrease in the reaction rate, until a constant residual reaction rate remains, e.g., because the phenomenon has been equilibrated.

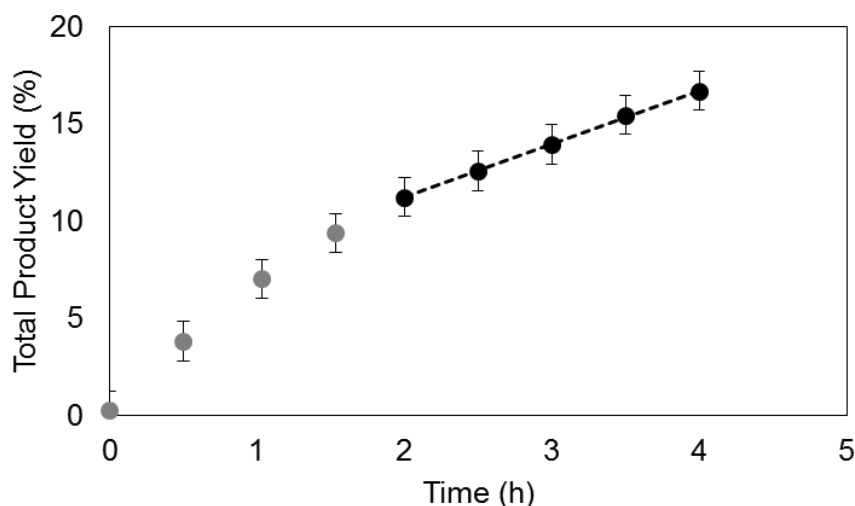


Figure 7-3: Measured total product yield versus reaction time for crude low-molecular weight chitosan as catalyst in the aldol reaction of acetone with 4-nitrobenzaldehyde. ($T = 55\text{ }^{\circ}\text{C}$, $m_{\text{acetone}} = 45\text{ g}$, $m_{4\text{NB}} = 0.45\text{ g}$, $m_{\text{water}} = 55\text{ g}$, $m_{\text{chitosan}} = 0.26\text{ g}$)

The 4-nitrobenzaldehyde molar balance for the liquid phase in this experiment, shown in Appendix E in Figure E-2, decreased from 100% at the start of the reaction asymptotically to 78%. This means that 22% of the 4-nitrobenzaldehyde fed in the reaction is converted to other products than the reaction products. Because no additional products have been detected in the liquid phase during HPLC analysis, it is likely that part of the 4-nitrobenzaldehyde remains adsorbed on the active sites. Previously, it has been suggested that stable imines derived from 4-nitrobenzaldehyde can form on primary amines and inhibit the aldol reaction²⁴. In the considered reaction mechanism, displayed in Figure 7-2, two different imines involving 4-nitrobenzaldehyde occur, i.e. species 5 and species 8. The latter is more stable towards hydration due to conjugation with the aromatic ring and is, hence, expected to act as an inhibiting species. Reactions that consume this imine intermediate (**8**), such as Mannich-type addition reactions, would require activating acetone towards its enol or enolate intermediate with a strong homogeneous acid or base and, hence, are expected to be of minor importance at the investigated reaction conditions²⁶. The formation of imine species 8 thus allows rationalizing the primary amine site inhibition.

It is indeed generally known that the primary amines on chitosan can form imines, with the release of water, when reacting with aldehydes or ketones^{9, 42, 43}. It is, however, assumed that hydrolysis of the imine is fast in aqueous conditions, and thereby shifts the equilibrium away from the imine^{24, 44}. Figure 7-4 shows an FTIR spectrum of fresh and spent crude chitosan used in the aldol reaction from which it does appear that, under the employed reaction conditions, a stable imine of a 4-nitrobenzaldehyde containing species can form on the primary

amines. Three small peaks appear in the spectrum of the spent catalyst in the region of 700 cm^{-1} to 900 cm^{-1} , indicative of the C-H vibrations in aromatic molecules. The large peak at 1529 cm^{-1} and the shoulder at 1620 cm^{-1} further indicates aromatic species, while the peak at 1356 cm^{-1} can be attributed to an NO_2 group attached to the aromatic ring. A small shoulder at 1690 cm^{-1} , next to the known amide stretch peak, indicates the C-N stretch of an imine. The small peak at 2460 cm^{-1} is due to the N-H^+ stretch of a protonated imine or amine species. While peaks that signify the presence of an imine are close to those that indicate the presence of aldehyde groups, it is unlikely that the aldehyde form of 4-nitrobenzaldehyde as such is present on the material because the spent chitosan was washed twice in deionized water before analysis.

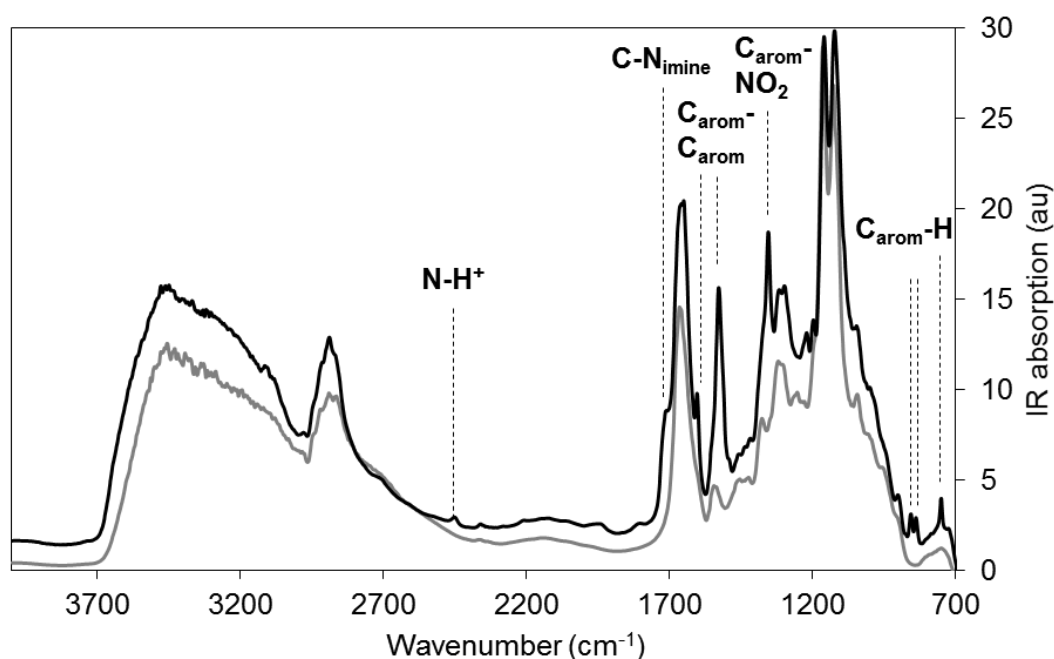


Figure 7-4: FT-IR spectrum of fresh (grey) and spent (black) chitosan for the aldol reaction of acetone with 4-nitrobenzaldehyde employing water as solvent. ($T = 55\text{ }^\circ\text{C}$, $m_{\text{acetone}} = 45\text{ g}$, $m_{4\text{NB}} = 0.45\text{ g}$, $m_{\text{water}} = 55\text{ g}$, $m_{\text{chitosan}} = 0.26\text{ g}$)

Under the employed reaction conditions in the batch reactor, the decrease of the 4-nitrobenzaldehyde molar balance equilibrates at 78%, which amounts to 0.60 mmol of 4-nitrobenzaldehyde-containing species being adsorbed as imines. This amounts to 52% of the primary amine sites on chitosan that have been inhibited by an imine of 4-nitrobenzaldehyde. A 24 hour 4-nitrobenzaldehyde adsorption equilibrium test was also performed with crude chitosan, under exactly the same conditions as the catalytic experiments, except that acetone was replaced by DMSO. It was calculated from the decrease in the liquid phase 4-nitrobenzaldehyde concentration that adsorption had occurred on almost half of the primary amine sites. The FTIR spectrum of this chitosan catalyst is added in Appendix E, Figure E-4,

and exhibits the same characteristic peaks as the ones observed in Figure 7-4. This further points into the direction that the species detected on the spent catalyst is indeed species **8** which is formed by interaction of 4-nitrobenzaldehyde with the primary amine.

The reaction rate measured for crude chitosan in the linear regime observed in Figure 7-3, where it is assumed that the inhibition phenomena have been equilibrated, amounts to $8.87 \pm 0.09 \cdot 10^{-5} \text{ mol}_{\text{products}} \text{ kg}_{\text{chitosan}}^{-1} \text{ s}^{-1}$, as displayed in Table 7-1. Elemental analysis indicated a degree-of-deacetylation of $70.5 \pm 3.5 \%$, which results in an average site-time yield of $2.18 \pm 0.05 \cdot 10^{-5} \text{ mol}_{\text{product}} \text{ mol}_{\text{amine}}^{-1} \text{ s}^{-1}$ considering all primary amine sites, i.e., including the inhibited sites.

7.3.1.2 Chitosan hydrogel and aerogel

Chitosan hydrogels of ± 2 mm diameter are synthesized according to known literature procedures⁸, and have also been evaluated in the aldol reaction of acetone with 4-nitrobenzaldehyde. In these catalytic performance tests, the chitosan mass is the same as with crude chitosan. The total product yield as a function of reaction time is given in Figure 7-5 for a first and a consecutive run. The first catalytic run exhibited the same behavior as crude chitosan, i.e., a decrease in slope until 2 hours of reaction after which the slope remained constant until the end of the reaction. The reaction rate measured in this linear regime amounts to $8.96 \pm 0.21 \cdot 10^{-5} \text{ mol}_{\text{product}} \text{ kg}_{\text{chitosan}}^{-1} \text{ s}^{-1}$ and the corresponding site-time yield to $2.21 \pm 0.18 \cdot 10^{-5} \text{ s}^{-1}$, see Table 7-1. The catalytic activity of chitosan hydrogels, calculated based on the equivalent of chitosan in the hydrogel, is thus found to be identical as that of crude chitosan. The second run exhibited a linear evolution over the entire duration of the experiment, indicating that in the second run, the inhibitory imine formation on the surface is equilibrated from the start of the experiment. Even though much lower yields were obtained in a second run, the slope of the yield versus time curve is approximately identical to the slope at higher conversions observed during the first run. Comparing these slopes, a reusability ratio of 82% is found. However, it should be noted that the mechanical stirring in the Parr[®] reactor caused the hydrogel beads to break. Hence, a smaller scale experiment in glassware was also conducted, under less severe stirring, for which a reaction rate of $2.16 \pm 0.09 \cdot 10^{-5} \text{ mol}_{\text{product}} \text{ mol}_{\text{amine}}^{-1} \text{ s}^{-1}$ was found and a $95 \pm 10 \%$ reusability ratio. The product yield curve versus time for this experiment is displayed in Figure E-3 in Appendix E.

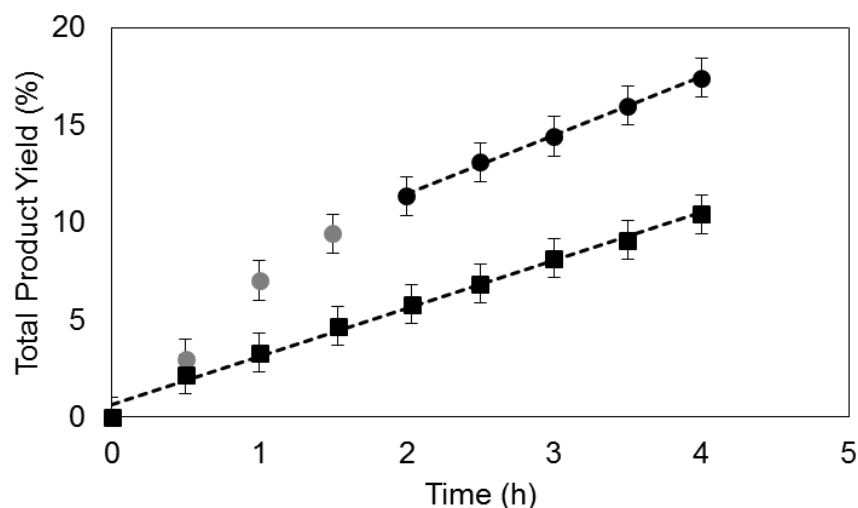


Figure 7-5: Measured total product yield versus reaction time for hydrogels of low-molecular weight chitosan as catalyst in the aldol reaction of acetone with 4-nitrobenzaldehyde. First run (●) second run (■). ($T = 55\text{ }^{\circ}\text{C}$, $m_{\text{acetone}} = 45\text{ g}$, $m_{4\text{NB}} = 0.45\text{ g}$, $m_{\text{water}} = 55\text{ g}$, $m_{\text{chitosan}} = 0.26\text{ g}$)

Chitosan aerogels were synthesized by lyophilization of the hydrogel beads. Again, in Figure 7-6, the same behavior in the product yield versus reaction time is observed, i.e., a gradually decreasing slope until 2 hours of reaction, after which a more stable regime is reached. The slope of the linear part of the yield versus time graph for the chitosan aerogels results in an activity of $8.51 \pm 0.43 \cdot 10^{-5} \text{ mol}_{\text{product}} \text{ kg}_{\text{chitosan}}^{-1} \text{ s}^{-1}$ and a site-time yield of $2.09 \pm 0.11 \cdot 10^{-5} \text{ mol}_{\text{product}} \text{ mol}_{\text{amine}}^{-1} \text{ s}^{-1}$. Also, in this case the reaction rate appears to be the same, within the experimental error margin, as compared to crude chitosan in water and chitosan hydrogels. All values are summarized in Table 7-1. The second run in the Parr reactor using chitosan aerogels resulted in a reusability ratio of $90 \pm 10\%$.

The above observations indicate that the catalytic activity in the linear regime of the yield versus time curve of the first run can be reproduced in the second one and, hence, that hydrogel and aerogel catalysts are reusable without quantifiable activity losses.

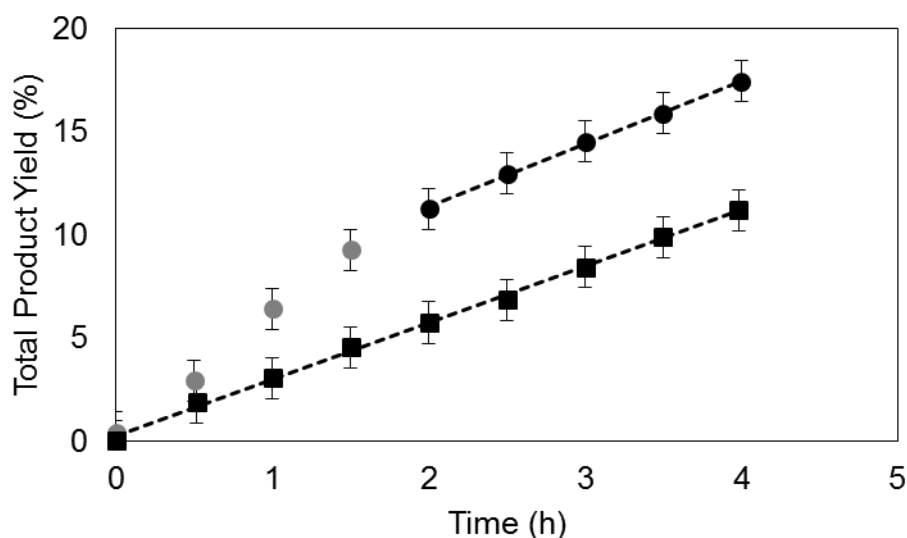


Figure 7-6: Measured total product yield versus reaction time for aerogels of low-molecular weight chitosan as catalyst in the aldol reaction of acetone with 4-nitrobenzaldehyde. First run (●) second run (■). ($T = 55\text{ }^{\circ}\text{C}$, $m_{\text{acetone}} = 45\text{ g}$, $m_{\text{4NB}} = 0.45\text{ g}$, $m_{\text{water}} = 55\text{ g}$, $m_{\text{chitosan}} = 0.26\text{ g}$)

Table 7-1: Summary of the reaction rate, site-time yield and reusability in a second 4 hour run for the different chitosan catalysts. (*reusability was evaluated in smaller glass batch-type reactor)

Chitosan Catalyst	Reaction rate $10^{-5} (\text{mol}_{\text{product}} \text{kg}_{\text{chitosan}}^{-1} \text{s}^{-1})$	Site-time yield $10^{-5} (\text{mol}_{\text{product}} \text{mol}_{\text{amine}}^{-1} \text{s}^{-1})$	Reusability (%)
Crude	8.87 ± 0.21	2.18 ± 0.05	-
Hydrogel	8.96 ± 0.74	2.21 ± 0.18	* 95 ± 10
Aerogel	8.51 ± 0.43	2.09 ± 0.11	90 ± 10

7.3.2 Continuous-flow stability of crude chitosan

It was described in section 3.1 how the chitosan hydrogel and aerogel catalyst were recycled for a second run in a batch reactor and the original activity could be reproduced. To assess the long-term stability of crude chitosan under reaction conditions, without filtering and recycling the catalyst after each run, a continuous-flow reactor loaded with a packed bed has been employed under exactly the same operating conditions as in the batch reactor.

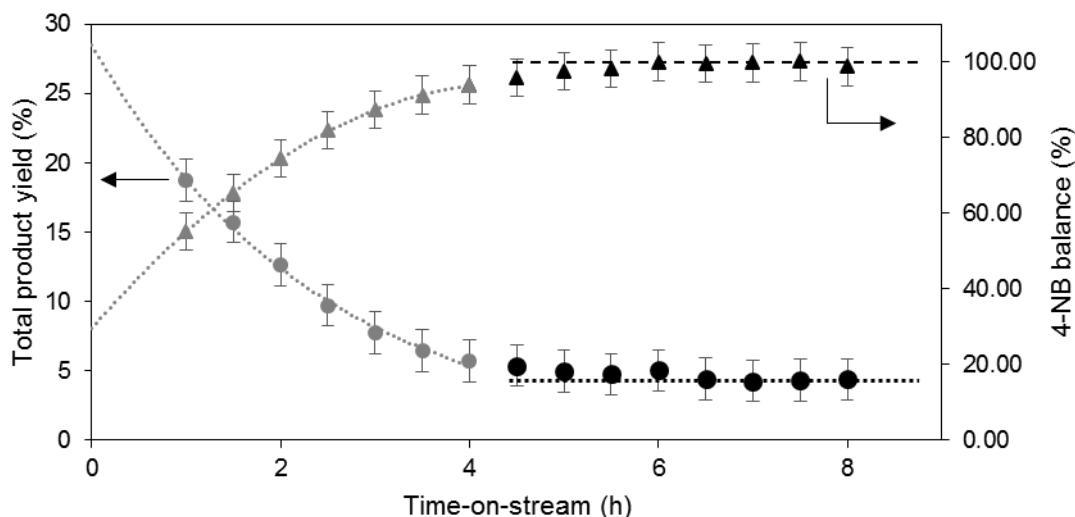


Figure 7-7: Total product yield (●, left axis) and 4-nitrobenzaldehyde molar balance (▲, right axis) as a function of time-on-stream in the continuous-flow reactor using crude chitosan as catalyst. ($W/F_{4\text{-NB}}^0 = 1510 \text{ kg}_{\text{cat}} \text{ s mol}^{-1}_{4\text{-NB}}$, 44.7 m% acetone, 54.6 m% water, 0.45 m% 4-nitrobenzaldehyde, 0.20 m% methyl-4-nitrobenzoate, $T = 55 \text{ }^\circ\text{C}$).

The total product yield for the aldol reaction in the continuous-flow reactor is given as a function of the time-on-stream in Figure 7-7. Sampling was only started after 1h on stream because, from the reactor hydrodynamics point of view, no steady-state operation was obtained in this first hour of reaction. From 1 hour on-stream up to 4.5 hours on-stream, the total product yield decreased gradually. This is attributed to the formation of stable imines derived from 4-nitrobenzaldehyde, in line with the observations made in the batch reactor. From 4.5 hours on-stream onwards, the inhibitory phenomena have stabilized and a stable total product yield is obtained. The 4-nitrobenzaldehyde molar balance also equilibrated after 4.5 hours on stream around 100%. This indicates that the adsorption of 4-nitrobenzaldehyde as imine species on the surface has reached an equilibrium.

These results indicate that, even though the imine formation is inhibiting active sites on chitosan and leading to a lower observed product yield, a stable operating regime can be reached in the continuous-flow aldol reaction with water as solvent. This is in contrast with the aminated mesoporous silica catalysts that were found to continuously deactivate due to silica hydrolysis and leaching caused by water^{28, 29}.

7.3.3 Amine activity as a function of the degree-of-deacetylation

Chitin was found to possess a degree-of-deacetylation (DDA) of $2.6 \pm 3.5\%$ and was also evaluated for the aldol reaction. The primary amines in chitin yielded a site-time yield of 15.40

$\pm 0.07 \cdot 10^{-5} \text{ mol}_{\text{product}} \text{ mol}_{\text{amine}}^{-1} \text{ s}^{-1}$, which exceeds that observed by the chitosan catalysts with a DDA of $70.4 \pm 3.5 \%$ by almost a factor 8. Additionally, in-house synthesized chitosan catalysts, in powder form, with a DDA varying between $13.1 \pm 3.5 \%$ and $76.8 \pm 3.5 \%$ were also evaluated. Their site-time yield (STY) was determined in the region between 2 hours and 4 hours of reaction and is shown in Figure 7-8 as a function of DDA.

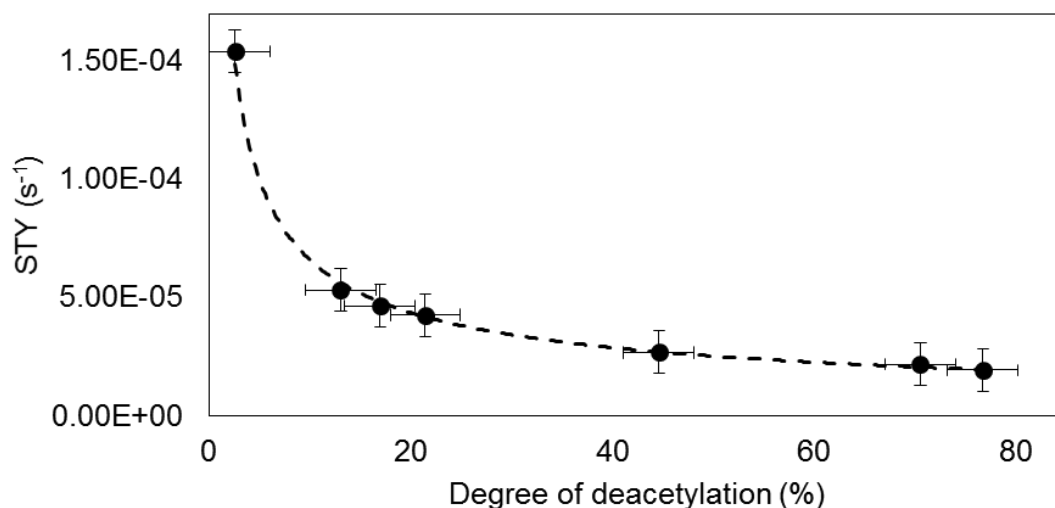


Figure 7-8: Site-time yield for primary amines in deacetylated chitin from 2.6% to 76.8% deacetylation. Line is a guide for the eye. ($T = 55 \text{ }^\circ\text{C}$, $m_{\text{acetone}} = 45 \text{ g}$, $m_{4\text{NB}} = 0.45 \text{ g}$, $m_{\text{water}} = 55 \text{ g}$, $m_{\text{chitosan}} = 0.26 \text{ g}$, Parr reactor)

As the DDA increased, the primary amine concentration increased, and the site time yield decreased, as displayed in Figure 7-8. Table 7-2 indicates that the increase in active site concentration appears to compensate for the loss in site time yield and therefore results in an increasing catalytic activity on a mass basis. This site time yield decrease with increasing DDA can be attributed to a decrease in the primary amine basicity from a pKa of 10.44, when chitosan is almost fully acetylated, to a pKa of 5.44 upon full deacetylation⁴⁵. The increased hydrophobicity upon acetylation has been deemed responsible for differences in electrostatic properties, leading, in turn, to this change in amine pKa with DDA⁴⁵. The amine sites in chitosan with a low DDA, hence, appear to exhibit a basicity close to that of a simple primary amine with a short alkyl chain, such as those typically grafted on mesoporous silica²³.

Table 7-2: Summary of reaction rate and site-time yield for chitosan with a different degree-of-deacetylation.

DDA (%) $\pm 3.5 \%$	Primary amines (mmol/g)	Reaction rate $10^{-5} (\text{mol}_{\text{product}} \text{kg}_{\text{chitosan}}^{-1} \text{s}^{-1})$	Site-time yield $10^{-5} (\text{mol}_{\text{product}} \text{mol}_{\text{amine}}^{-1} \text{s}^{-1})$
2.6	0.13	1.97 ± 0.18	15.40 ± 1.39
13.1	0.66	3.48 ± 0.31	5.31 ± 0.48
17.0	0.87	4.03 ± 0.36	4.64 ± 0.42
21.5	1.11	4.55 ± 0.41	4.25 ± 0.38
44.6	2.42	6.53 ± 0.59	2.66 ± 0.24
76.7	4.49	8.83 ± 0.79	1.92 ± 0.17

Primary amine grafted mesoporous silica catalysts, evaluated using hexane as solvent, exhibited a site-time yield of $78.0 \cdot 10^{-5} \text{ s}^{-1}$ in the presence of an excess of cooperative silanol groups and $20.0 \cdot 10^{-5} \text{ s}^{-1}$ without such silanol groups²³. While comparison should be performed carefully because of differences in solvent and catalyst morphology can lead to a different sorption behavior⁴⁶, the value of the unpromoted primary aminated silica catalysts appears to be in the same order of magnitude as the value reported in Table 7-2 for chitosan with the lowest DDA.

These results indicate that further improvement of the catalytic activity of chitosan is possible by tuning the electrostatic properties of the material, such that the pKa of the amine sites is increased. Combined with the high loadings that are possible on these materials, and their stability in an aqueous environment, promising new heterogeneous catalysts can be developed for the aldol reaction.

7.4 Conclusions

Commercial chitosan with a degree-of-deacetylation (DDA) of 70.4% has been kinetically evaluated in the aldol reaction of acetone with 4-nitrobenzaldehyde, using water as a solvent. During the first 2 hours in the batch reactor, stable imines derived from 4-nitrobenzaldehyde are formed on the primary amine sites, which block access to the active site and decrease the observed catalytic activity. When the imine formation has equilibrated, a stable catalytic activity of $2.18 \pm 0.05 \cdot 10^{-5} \text{ mol}_{\text{product}} \text{mol}_{\text{amine}}^{-1} \text{ s}^{-1}$ is obtained. Changing the morphology of the catalyst to a hydrogel, or an aerogel via lyophilization, did not affect the intrinsic catalytic activity of the primary amine in the catalyst. Chitosan hydrogels and aerogels were recycled in the batch reactor and allowed reproducing the original activity when the inhibitory phenomena were equilibrated. Crude chitosan was evaluated in a continuous-flow reactor, under the same reaction conditions as the batch reactor, and showed first an exponential decrease in activity due to imine formation that is then followed by a stable activity regime.

This remarkable catalytic stability makes chitosan a desirable heterogeneous catalyst for the aqueous aldol reaction.

The site time yield of the primary amines in commercial chitin with a DDA of 2.6% amounted to $15.40 \pm 1.39 \cdot 10^{-5} \text{ mol}_{\text{product}} \text{ mol}_{\text{amine}}^{-1} \text{ s}^{-1}$, which is in the same order of magnitude as the unpromoted primary amine functionalized silica catalysts evaluated in hexane. Increasing the degree of deacetylation, however, causes a decrease in the site time yield due to a corresponding decrease in amine pKa. Further catalyst improvement is thus situated in the development of amine sites with a high pKa, which is independent from the amine loading on the polymer backbone.

7.5 References

1. El Kadib, A., Chitosan as a sustainable organocatalyst: a concise overview. *ChemSusChem* **2015**, *8* (2), 217-244.
2. Asere, T. G.; Mincke, S.; De Clercq, J.; Verbeken, K.; Tessema, D. A.; Fufa, F.; Stevens, C. V.; Du Laing, G., Removal of arsenic (V) from aqueous solutions using chitosan–red scoria and chitosan–pumice blends. *International journal of environmental research and public health* **2017**, *14* (8), 895.
3. Schoolaert, E.; Steyaert, I.; Vancoillie, G.; Geltmeyer, J.; Lava, K.; Hoogenboom, R.; De Clerck, K., Blend electrospinning of dye-functionalized chitosan and poly (ϵ -caprolactone): towards biocompatible pH-sensors. *Journal of Materials Chemistry B* **2016**, *4* (26), 4507-4516.
4. Verlee, A.; Mincke, S.; Stevens, C. V., Recent developments in antibacterial and antifungal chitosan and its derivatives. *Carbohydrate polymers* **2017**, *164*, 268-283.
5. Reddy, K. R.; Rajgopal, K.; Maheswari, C. U.; Kantam, M. L., Chitosan hydrogel: A green and recyclable biopolymer catalyst for aldol and Knoevenagel reactions. *New journal of chemistry* **2006**, *30* (11), 1549-1552.
6. Gioia, C.; Ricci, A.; Bernardi, L.; Bourahla, K.; Tanchoux, N.; Robitzer, M.; Quignard, F., Chitosan aerogel beads as a heterogeneous organocatalyst for the asymmetric aldol reaction in the presence of water: an assessment of the effect of additives. *European Journal of Organic Chemistry* **2013**, *2013* (3), 588-594.
7. Ricci, A.; Bernardi, L.; Gioia, C.; Vierucci, S.; Robitzer, M.; Quignard, F., Chitosan aerogel: A recyclable, heterogeneous organocatalyst for the asymmetric direct aldol reaction in water. *Chemical communications* **2010**, *46* (34), 6288-6290.
8. Kühbeck, D.; Saidulu, G.; Reddy, K. R.; Díaz, D. D., Critical assessment of the efficiency of chitosan biohydrogel beads as recyclable and heterogeneous organocatalyst for C–C bond formation. *Green chemistry* **2012**, *14* (2), 378-392.
9. Kayser, H.; Müller, C. R.; García-González, C. A.; Smirnova, I.; Leitner, W.; de María, P. D., Dried chitosan-gels as organocatalysts for the production of biomass-derived platform chemicals. *Applied Catalysis A: General* **2012**, *445*, 180-186.
10. Mahé, O.; Brière, J. F.; Dez, I., Chitosan: An upgraded polysaccharide waste for organocatalysis. *European Journal of Organic Chemistry* **2015**, *2015* (12), 2559-2578.
11. Zhang, H.; Zhao, W.; Zou, J.; Liu, Y.; Li, R.; Cui, Y., Aldol reaction catalyzed by a hydrophilic catalyst in aqueous micelle as an enzyme mimic system. *Chirality: The*

- Pharmacological, Biological, and Chemical Consequences of Molecular Asymmetry* **2009**, 21 (5), 492-496.
12. Jose, T.; Sudheesh, N.; Shukla, R. S., Amino functionalized chitosan as a catalyst for selective solvent-free self-condensation of linear aldehydes. *Journal of Molecular Catalysis A: Chemical* **2010**, 333 (1-2), 158-166.
 13. Suwito, H.; Jumina; Mustofa; Kristanti, A. N.; Puspaningsih, N. N. T., Chalcones: Synthesis, structure diversity and pharmacological aspects. *Journal of Chemical and Pharmaceutical Research* **2014**, 6 (5), 1076-1088.
 14. Kelly, G.; King, F.; Kett, M., Waste elimination in condensation reactions of industrial importance. *Green Chemistry* **2002**, 4 (4), 392-399.
 15. Cheng, S.; Wang, X.; Chen, S.-Y., Applications of amine-functionalized mesoporous silica in fine chemical synthesis. *Topics in Catalysis* **2009**, 52 (6-7), 681-687.
 16. Chheda, J. N.; Dumesic, J. A., An overview of dehydration, aldol-condensation and hydrogenation processes for production of liquid alkanes from biomass-derived carbohydrates. *Catalysis Today* **2007**, 123 (1), 59-70.
 17. Xie, J.; Zhang, L.; Zhang, X.; Han, P.; Xie, J.; Pan, L.; Zou, D.-R.; Liu, S.-H.; Zou, J.-J., Synthesis of high-density and low-freezing-point jet fuel using lignocellulose-derived isophorone and furanic aldehydes. *Sustainable Energy & Fuels* **2018**, 2 (8), 1863-1869.
 18. Xing, R.; Subrahmanyam, A. V.; Olcay, H.; Qi, W.; van Walsum, G. P.; Pendse, H.; Huber, G. W., Production of jet and diesel fuel range alkanes from waste hemicellulose-derived aqueous solutions. *Green Chemistry* **2010**, 12 (11), 1933-1946.
 19. Deng, Q.; Xu, J.; Han, P.; Pan, L.; Wang, L.; Zhang, X.; Zou, J.-J., Efficient synthesis of high-density aviation biofuel via solvent-free aldol condensation of cyclic ketones and furanic aldehydes. *Fuel Processing Technology* **2016**, 148, 361-366.
 20. Lucarelli, C.; Vaccari, A., Examples of heterogeneous catalytic processes for fine chemistry. *Green Chemistry* **2011**, 13 (8), 1941-1949.
 21. Price, P. M.; Clark, J. H.; Macquarrie, D. J., Modified silicas for clean technology. *Journal of the Chemical Society, Dalton Transactions* **2000**, (2), 101-110.
 22. Lauwaert, J.; De Canck, E.; Esquivel, D.; Thybaut, J. W.; Van Der Voort, P.; Marin, G. B., Silanol-Assisted Aldol Condensation on Aminated Silica: Understanding the Arrangement of Functional Groups. *ChemCatChem* **2014**, 6 (1), 255-264.
 23. Lauwaert, J.; De Canck, E.; Esquivel, D.; Van Der Voort, P.; Thybaut, J. W.; Marin, G. B., Effects of amine structure and base strength on acid–base cooperative aldol condensation. *Catalysis Today* **2015**, 246, 35-45.
 24. Kandel, K.; Althaus, S. M.; Peeraphatdit, C.; Kobayashi, T.; Trewyn, B. G.; Pruski, M.; Slowing, I. I., Substrate inhibition in the heterogeneous catalyzed aldol condensation: A mechanistic study of supported organocatalysts. *Journal of Catalysis* **2012**, 291, 63-68.
 25. De Vylder, A.; Lauwaert, J.; Sabbe, M. K.; Reyniers, M.-F.; De Clercq, J.; Van Der Voort, P.; Thybaut, J. W., Rational Design of Nucleophilic Amine Sites via Computational Probing of Steric and Electronic Effects. *Catalysis Today* **2019**.
 26. Kandel, K.; Althaus, S. M.; Peeraphatdit, C.; Kobayashi, T.; Trewyn, B. G.; Pruski, M.; Slowing, I. I., Solvent-Induced Reversal of Activities between Two Closely Related Heterogeneous Catalysts in the Aldol Reaction. *ACS Catalysis* **2013**, 3 (2), 265-271.
 27. Brunelli, N. A.; Venkatasubbaiah, K.; Jones, C. W., Cooperative catalysis with acid–base bifunctional mesoporous silica: impact of grafting and co-condensation synthesis methods on material structure and catalytic properties. *Chemistry of Materials* **2012**, 24 (13), 2433-2442.

28. De Vylder, A.; Lauwaert, J.; Esquivel, D.; Poelman, D.; De Clercq, J.; Van Der Voort, P.; Thybaut, J. W., The role of water in the reusability of aminated silica catalysts for aldol reactions. *Journal of Catalysis* **2018**, *361*, 51-61.
29. Etienne, M.; Walcarius, A., Analytical investigation of the chemical reactivity and stability of aminopropyl-grafted silica in aqueous medium. *Talanta* **2003**, *59* (6), 1173-1188.
30. Bahmanyar, S.; Houk, K., Transition states of amine-catalyzed aldol reactions involving enamine intermediates: theoretical studies of mechanism, reactivity, and stereoselectivity. *Journal of the American Chemical Society* **2001**, *123* (45), 11273-11283.
31. Okuyama, K.; Noguchi, K.; Miyazawa, T.; Yui, T.; Ogawa, K., Molecular and crystal structure of hydrated chitosan. *Macromolecules* **1997**, *30* (19), 5849-5855.
32. Rinaudo, M., Chitin and chitosan: properties and applications. *Progress in polymer science* **2006**, *31* (7), 603-632.
33. Franca, E. F.; Lins, R. D.; Freitas, L. C.; Straatsma, T., Characterization of chitin and chitosan molecular structure in aqueous solution. *Journal of Chemical Theory and Computation* **2008**, *4* (12), 2141-2149.
34. Hammond, C., Intensification studies of heterogeneous catalysts: probing and overcoming catalyst deactivation during liquid phase operation. *Green Chemistry* **2017**, *19*, 2711-2728.
35. Ogawa, K.; Yui, T.; Miya, M., Dependence on the preparation procedure of the polymorphism and crystallinity of chitosan membranes. *Bioscience, biotechnology, and biochemistry* **1992**, *56* (6), 858-862.
36. Mohammed, M. H.; Williams, P. A.; Tverezovskaya, O., Extraction of chitin from prawn shells and conversion to low molecular mass chitosan. *Food Hydrocolloids* **2013**, *31* (2), 166-171.
37. Kasaai, M. R.; Arul, J.; Charlet, G., Intrinsic viscosity–molecular weight relationship for chitosan. *Journal of Polymer Science Part B: Polymer Physics* **2000**, *38* (19), 2591-2598.
38. Gupta, K.; Jabrail, F. H., Effects of degree of deacetylation and cross-linking on physical characteristics, swelling and release behavior of chitosan microspheres. *Carbohydrate Polymers* **2006**, *66* (1), 43-54.
39. Dos Santos, Z.; Caroni, A.; Pereira, M.; Da Silva, D.; Fonseca, J., Determination of deacetylation degree of chitosan: a comparison between conductometric titration and CHN elemental analysis. *Carbohydrate Research* **2009**, *344* (18), 2591-2595.
40. Ellebracht, N. C.; Jones, C. W., Amine functionalization of cellulose nanocrystals for acid–base organocatalysis: surface chemistry, cross-linking, and solvent effects. *Cellulose* **2018**, *25* (11), 6495-6512.
41. Zhang, X.; Houk, K. N., Acid/Base Catalysis by Pure Water: The Aldol Reaction. *The Journal of Organic Chemistry* **2005**, *70* (24), 9712-9716.
42. Marin, L.; Simionescu, B.; Barboiu, M., Imino-chitosan biodynamers. *Chemical Communications* **2012**, *48* (70), 8778-8780.
43. dos Santos, J. E.; Dockal, E. R.; Cavalheiro, É. T. G., Synthesis and characterization of Schiff bases from chitosan and salicylaldehyde derivatives. *Carbohydrate Polymers* **2005**, *60* (3), 277-282.
44. Yao, K. d.; Peng, T.; Xu, M. x.; Yuan, C.; Goosen, M. F.; Zhang, Q. q.; Ren, L., pH-dependent hydrolysis and drug release of chitosan/polyether interpenetrating polymer network hydrogel. *Polymer international* **1994**, *34* (2), 213-219.

45. Sorlier, P.; Denuzière, A.; Viton, C.; Domard, A., Relation between the degree of acetylation and the electrostatic properties of chitin and chitosan. *Biomacromolecules* **2001**, *2* (3), 765-772.
46. Lauwaert, J.; Ouwehand, J.; De Clercq, J.; Cool, P.; Van Der Voort, P.; Thybaut, J. W., Tuning component enrichment in amino acid functionalized (organo)silicas. *Catalysis Communications* **2017**, *88*, 85-89.

Chapter 8

Stable aldol reaction catalysts under continuous-flow

8.1 Introduction and goal

It has been shown that co-feeding water has a positive effect on the stability and activity of the amine site in the aldol reaction between acetone and 4-nitrobenzaldehyde, but has a detrimental effect on the stability of the silica support material, see also Chapter 4. Therefore, a logical next step is to focus on the development of more hydrothermally stable support materials. In this regard, Periodic Mesoporous Organosilica (PMO) materials¹⁻⁴ present themselves as promising candidate materials due to the incorporation of hydrophobic organic groups into the (siliceous) material wall. However, the surface of these organosilica materials still comprises many silanol groups, which possess a hydrophilic character. Therefore, the hydrophobicity and, hence, the hydrothermal stability, of the support material will be further enhanced by endcapping these silanol groups with HMDS. It is hypothesized that aminated PMO catalysts are stable in an aqueous environment and, hence, in the first part of this chapter, PMO materials are investigated to unravel their potential as supports for aldol reaction catalysts.

The natural biopolymer “chitosan” has been identified as an inherently stable heterogeneous primary amine catalyst in the aqueous aldol reaction of acetone with 4-nitrobenzaldehyde, see also Chapter 7. Due to the absence of bonds that are sensitive to hydrolysis under the aldol reaction conditions, no leaching of active sites occurred. However, the catalytic activity of the amine sites was found to be very low compared to the current state-of-the-art silica-based catalysts. Hence, in a second part of this chapter, a new hydrothermally stable resin is developed with more active primary, or secondary, amines as catalytic sites. Special attention is paid to the ability of the resin to swell in a typical reaction mixture containing water as solvent and acetone as excess reagent.

8.1.1 PMO supported amine catalysts

PMO supported amine catalysts with different primary amine sites have already been investigated for the aldol reaction using both hexane and water as solvent^{4, 5}. Lauwaert et al.⁶ reported a remarkable interplay between the liquid phase and the support properties leading to selective enrichment of components in the pores of the material. However, to the best of our knowledge, PMO supported amine catalysts have not yet been evaluated for their reusability or longer term stability in the aqueous aldol reaction.

To assess the effect of the support on the catalyst stability, different PMO catalysts are synthesized. A 100% Ethane-PMO material (Figure 8-1, left) is used as a support for grafting the N-methylaminopropyltrimethoxysilane (MAPTMS) active site, in a similar way as was done on mesoporous silica gel in Chapter 4, i.e., on silanol groups belonging to the siliceous part of the material. This leads to the Amine-Ethane-PMO catalyst, displayed in Figure 8-2. End capping the remaining silanol groups with HMDS then leads to the HMDS-Amine-Ethane-PMO catalyst, which is also displayed in Figure 8-2.

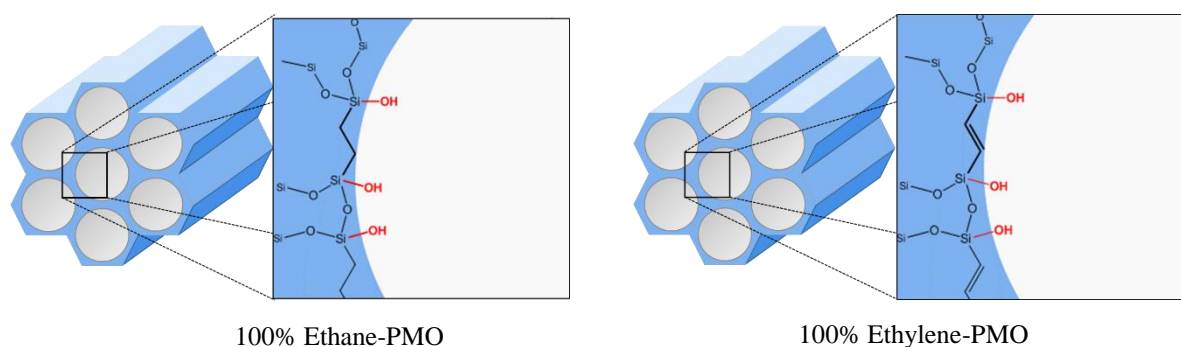


Figure 8-1: Two different PMO materials that will serve as support for the amine catalyst.

It should be noted that the Si-O-Si bond connecting the amine site to the PMO support material in the Amine-Ethane-PMO catalyst can still be subject to hydrolysis. Hence, also a second type of catalyst is synthesized, based on a 100% Ethylene-PMO material (Figure 8-1, right). In these catalysts, the reactive ethylene group is used for anchoring the secondary amine site via a thiol-ene click reaction leading to the Amine-Ethylene-PMO catalyst (Figure 8-2). This makes that the active site is connected to the support material by a hydrothermally stable thioether bond. However, these catalysts, of course, still contain Si-O-Si bonds connecting the individual organobissilanes to each other. These connections still lead to the presence of surface silanol groups. Endcapping these silanol groups with HMDS then leads to the HMDS-Amine-Ethylene-PMO catalyst, as seen in Figure 8-2.

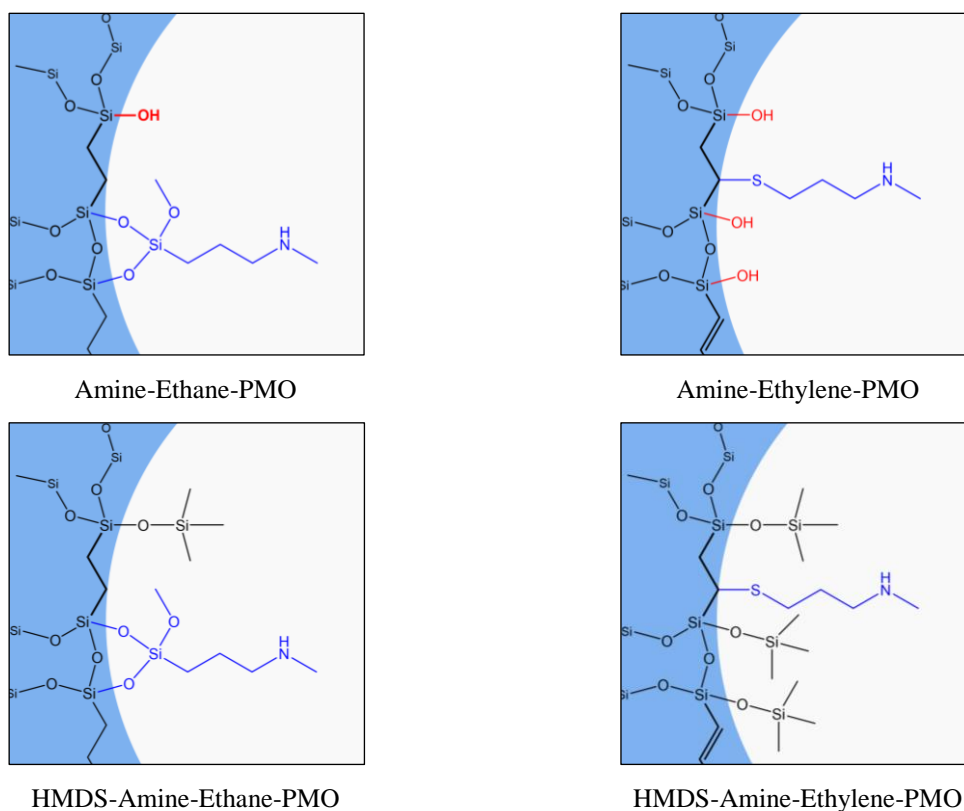


Figure 8-2: Four different amine-PMO catalysts that are synthesized in this work, based on the supports in Figure 8-1.

8.1.2 PEGMA catalysts

Organic resin catalysts do not contain any Si-O-Si bonds and, hence, will not be subject to the hydrolysis reactions to which PMO materials are susceptible. In this work, a lightly crosslinked organic resin is aimed at, so as to ensure that the polymer will not completely dissolve in the reaction mixture and still has the possibility to swell in a compatible solvent. As discussed in Chapter 1, this swelling behavior is one of the key properties of a resin catalyst⁷. The catalysts that are developed are based on poly(ethylene glycol) (PEG), which is described as a “chameleon type” polymer, because it has both hydrophobic and hydrophilic properties⁸. As a crosslinked resin, it will swell in water, acetone, ethanol as well as toluene, methylene chloride, and many organic solvents⁸. This versatile swelling behavior allows to efficiently synthesize the catalyst in a dry organic solvent, while making use of its catalytic properties in the aqueous aldol reaction. Combined with its stability under the typical reaction conditions used in the aldol reaction, and easy functionalization, PEG derived catalysts appear very attractive.

Several commercial PEG based resins are available, such as methacrylates substituted with PEG groups, called poly(ethylene glycol) methacrylate (PEGMA), which can be polymerized via a free-radical methacrylate polymerization⁹. In this work, a PEGMA monomer

with 6 PEG units is chosen. Cross-linking is achieved with a PEG dimethacrylate of 9 PEG units. A suspension polymerization is then performed, to obtain small polymer beads in the order of 100 μm . The endgroups of these polymers are hydroxyl groups, which are partly converted to amine sites to obtain a primary amine catalyst (PEGMA-EDA) or a secondary amine catalyst (PEGMA-DED and PEGMA-MA), as displayed in Figure 8-3. Complete replacement of all hydroxyl groups with amine sites is not desired, as this would lead to steric hindrance of the closely grafted active sites, leading to a lower activity of the sites.

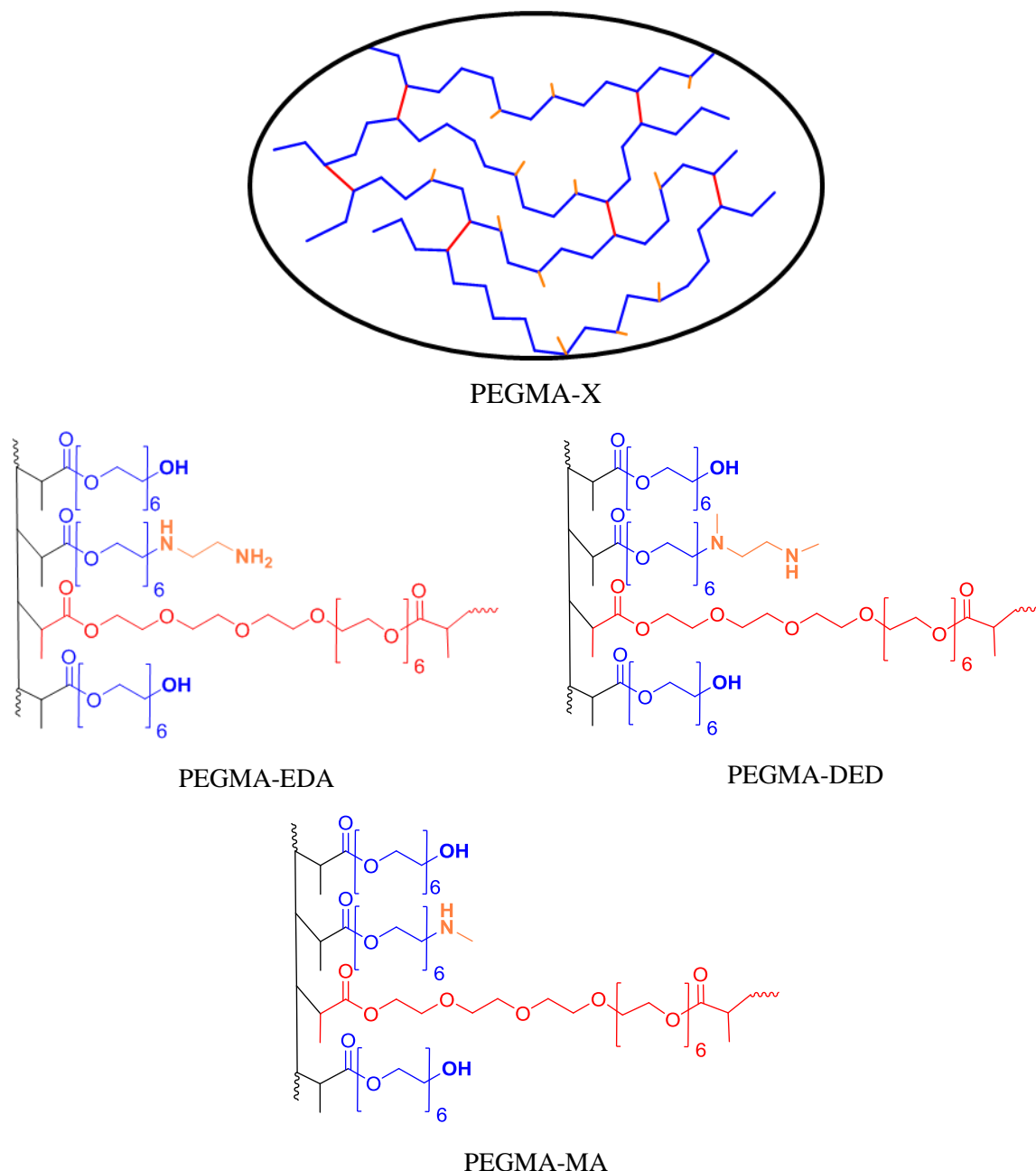


Figure 8-3: Cross-linked resin catalysts based on a poly(ethylene glycol) methacrylate (PEGMA-X), functionalized with ethylenediamine (PEGMA-EDA), N,N'-dimethylethylenediamine (PEGMA-DED) or methylamine (PEGMA-MA)

8.2 Procedures

8.2.1 Periodic Mesoporous Organosilica (PMO) catalyst synthesis

Both ethane and ethylene bridged PMO catalysts have been synthesized, the main distinctive feature being the anchoring point of the amine functional groups. While on the ethane bridged PMO the organosilanes are grafted on silanol groups, i.e., on the siliceous fraction of the material, the ethylene bridges in the alternative PMO material provide an opportunity for anchoring the amines via non hydrolysable organic bonds.

The synthesis procedure for the ethane-bridged PMO is based on the work of Burleigh et al.¹⁰ The PMO synthesis starts with dissolving 3.0 g of the surfactant Brij[®] S10 (Sigma Aldrich) in acidified water, which is a solution of 10 ml concentrated HCl (Carl Roth, 12 mol l⁻¹) in 138 ml deionized water (double deionized, 18.20 mΩ cm). This solution is stirred in a three-neck round-bottom flask at 50 °C at 1000 rpm for at least 4 hours with a 2.7 mm stirrer, in order to completely dissolve the surfactant. When the surfactant is fully dissolved, the 1,2-bis(triethoxysilyl)ethane (BTEE, abcr, 97%) organosilica precursor is added dropwise to the clear solution. The amount of precursor added is adjusted in order to get a total silicon content of 0.025 mol and can be calculated with equation (8.1).

$$V_{\text{prec}} = \frac{n_{\text{Si}} \cdot \text{MM}_{\text{prec}}}{x \cdot p \cdot \rho_{\text{prec}}} \quad (8.1)$$

With:

n_{Si}	Silicon content (= 0.025 mol)	[mol]
MM_{prec}	Precursor molar mass ($\text{MM}_{\text{BTEE}} = 354.59 \text{ g mol}^{-1}$)	[g mol ⁻¹]
x	Number of silicon atoms introduced per precursor ($x = 2$)	[-]
p	Precursor purity ($p_{\text{BTEE}} = 0.97$)	[-]
ρ_{prec}	Precursor density ($\rho_{\text{BTEE}} = 0.975 \text{ g ml}^{-1}$)	[g ml ⁻¹]

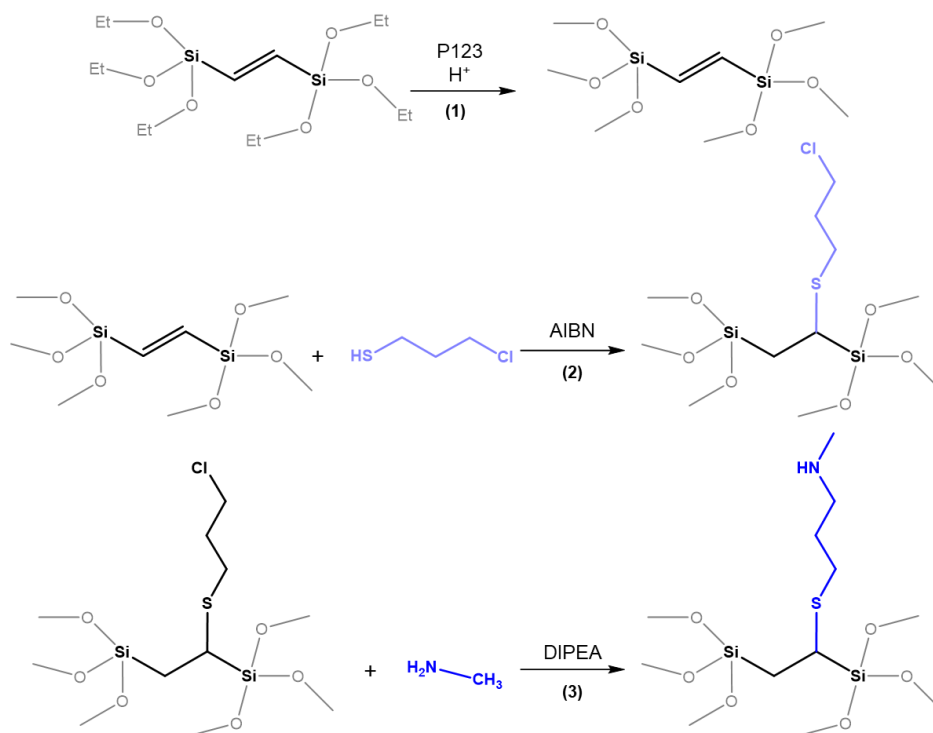
The synthesis mixture is intensely stirred at 50 °C at 1000 rpm for 24 hours. Afterwards, the mixture is aged at 90 °C for another 24 hours under static conditions (no stirring). Then, the mixture is filtered over a glass filter (por. 4) and shortly rinsed with deionized water. The surfactant is extracted by washing the material repeatedly in acidified absolute ethanol (0.24 mol L⁻¹ HCl) at 80 °C, three times in 24 hours. After three washing steps, the product is recovered by filtration over a glass filter, rinsed with acetone (Acros, ACS reagent, 99.6%) and dried under vacuum at 120 °C for 24 hours.

Using the silanol groups as anchoring points, amine active sites are incorporated in the ethane-bridged PMO by grafting. For functionalisation, 1.7 g of PMO material is submersed in 30 mL toluene (Fischer Scientific, Synthesis grade $\geq 99.5\%$) in a one neck flask. A volume of 258 μL N-methyl-1,3-aminopropyltrimethoxysilane (MAPTMS), amounting to 1.3 mmol, is then added to the solution. Before reaction, the reaction set-up is flushed with argon. For the reaction to proceed, the mixture is stirred at 110 $^{\circ}\text{C}$ under argon atmosphere at 300 rpm for 24 hours. Then, the catalyst is recovered by filtration over a glass filter and washed with chloroform (Chem-Lab, $\geq 99.8\%$) at 400 rpm at room temperature for 3 hours. After filtering, the recovered material is dried under vacuum conditions at room temperature for 24 hours and is then ready for use as catalyst. Endcapping of the surface silanol groups with trimethylsilyl groups was performed in the same way as for aminated mesoporous silica catalyst reported in Chapter 4.

Characterization of the obtained catalyst was performed with CHN analysis, nitrogen sorption and DRIFTS for which the procedures are discussed in Chapter 4.

The ethylene-bridged PMO catalyst synthesis procedure starts with the condensation of the precursor 1,2-bis(triethoxysilyl)ethylene around a template (Pluronic[®] P-123) under acidic conditions, followed by removal of the template as displayed in Scheme 8-1 (1). An as-synthesised ethylene-bridged PMO material was already available from dr. Judith Ouwehand⁸ to start with. In the synthesis of this PMO material, the surfactant Pluronic[®] P-123 was used. The synthesis procedure of this ethylene-bridged PMO is described by Vercaemst et al.⁷ and Ouwehand et al.⁸

A synthesis strategy as presented in Scheme 8-1 was further followed to anchor the amine sites to the support via hydrothermally stable thiol bonds. The ethylene bridges of the organosilica, rather than the silanol groups, were utilized in a thiol-ene click reaction with 3-chloro-1-propanethiol (Sigma-Aldrich, 98%) (2) for the incorporation of the desired functional group. First, 0.25 g of the ethylene-PMO is dissolved in 40 ml of dry toluene in a three-neck round-bottom flask, while bubbling argon through the mixture for 5 minutes, to avoid the presence of oxygen. To start the reaction, 0.8 g of recrystallized thermal initiator 2,2'-azobis(2-methylpropionitrile) (AIBN, Sigma-Aldrich, 98%) and 0.25 ml of the reagent 3-chloro-1-propanethiol are added to the mixture. The reaction mixture is stirred at 90 $^{\circ}\text{C}$ under argon atmosphere at 400 rpm for 24 hours. Afterwards, the mixture is filtered over a glass filter (por. 4) and the solids are recovered.



Scheme 8-1: Synthesis pathway, involving condensation of ethylene-bridged PMO (**1**), a thiol-ene click reaction (**2**) and an S_N2 nucleophilic substitution reaction (**3**).

In a final step in Scheme 8-1, the amine function is introduced via a nucleophilic substitution reaction with methylamine (in solution, 2 M in THF, Sigma-Aldrich) in a basic environment (**3**). The recovered solids from the previous step are dissolved in 25 ml tetrahydrofuran (THF, Chem-Lab, HPLC grade, $\geq 99.8\%$) and 6 ml N,N-diisopropylethylamine (DIPEA, Sigma-Aldrich, Reagent grade, $\geq 99\%$) is added as a non-nucleophilic strong base. As a reagent, 10 ml of the methylamine solution in THF is added and the reaction mixture is stirred at room temperature under argon atmosphere at 600 rpm for 24 hours. The reaction mixture is then filtered over a glass filter. Subsequently, the recovered solids are washed in 50 ml chloroform at room temperature at 400 rpm for 3 hours and filtered again. After drying under vacuum at room temperature for 24 hours, the catalyst is ready to be used. Endcapping of the surface silanol groups with trimethylsilyl groups was performed in the same way as for aminated mesoporous silica catalyst reported in Chapter 4.

Characterization of the catalysts was performed with CHN analysis, nitrogen sorption and DRIFTS for which the procedures are discussed in Chapter 4.

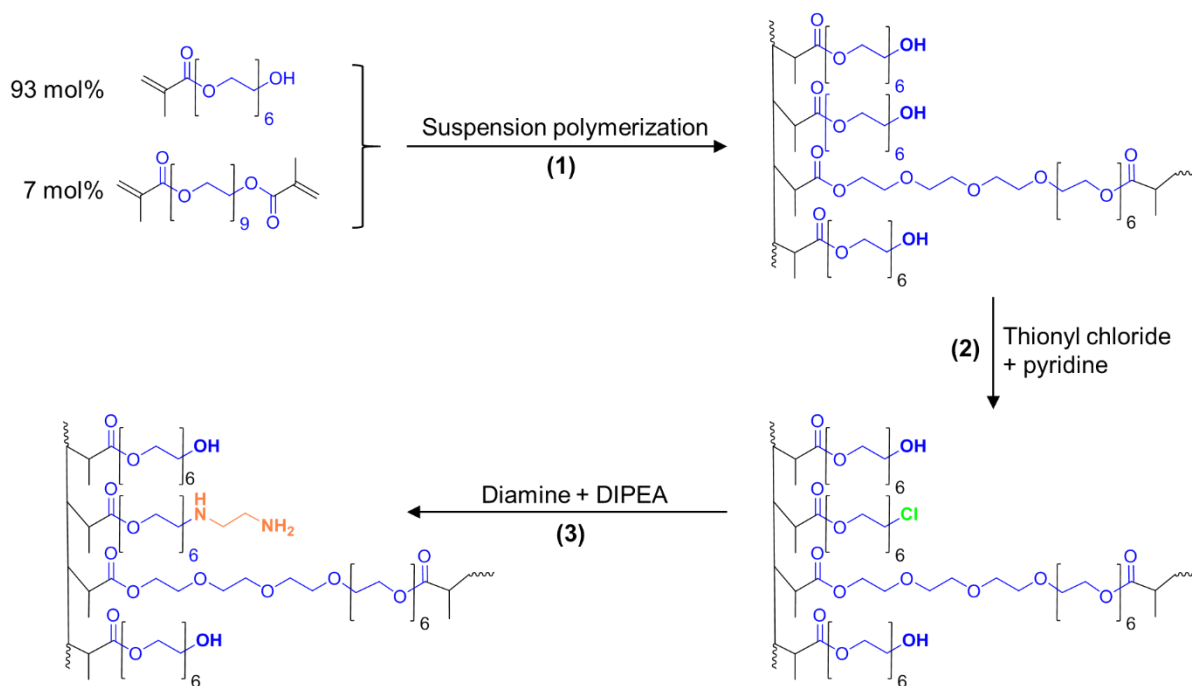
8.2.2 Synthesis and characterization of PEGMA catalysts

The synthesis of cross-linked poly(ethylene glycol) methacrylate hydrogels displayed in Scheme 8-2 occurs via suspension polymerization, and is adapted from Tuncel et al.⁹ The stabilizer, PVP (Sigma-Aldrich, K30, MW 40000) is dissolved in 40 mL deionized water for the preparation of the continuous phase. The disperse phase was prepared by mixing 5.5 mL cyclohexanol (Sigma-Aldrich, ReagentPlus, 99%) with 2.0 mL octanol (Acros, 99%), 4.0 mL poly(ethylene glycol) methacrylate (Sigma-Aldrich, average Mn 360) and 0.6 mL Polyethylene glycol dimethacrylate (Sigma-Aldrich, average Mn 750). The initiator BPO (0.12 g, Luperox® A98, reagent grade, $\geq 98\%$) was then dissolved in this homogeneous solution. The disperse phase was added to the continuous phase in a 50 mL glass flask and stirred at 450 rpm for 4 hours at 85 °C and for 1 hour at 90 °C. After completion, swellable hydrogel beads were obtained which were washed twice with acetone (VWR, 99.5%) and dried overnight on a high vacuum line at 50 °C.

In the next step, 30% of the hydroxyl groups on the material are replaced with chlorine groups, as displayed in Scheme 8-2. The dried hydrogel beads were covered completely with 40 mL dry toluene (Sigma-Aldrich, anhydrous, 99.8%), 0.3 mL of thionyl chloride (Sigma-Aldrich, $>99\%$, ReagentPlus) was added and 0.33 mL pyridine (JT Baker, ACS Reagent, 100%). This mixture was stirred for 4 hours at 75 °C before being filtered off and washed twice in ethanol (Koptec, 200 proof).

Finally, in the last step in Scheme 8-2, amine groups are introduced on the material by S_N2 nucleophilic substitution of the chlorine group. For this, either 5 mL ethylenediamine (Sigma-Aldrich, 99%, ReagentPlus) or 3 mL N,N' -dimethylethylenediamine (Alfa Aesar, 95%) or 15 mL methylamine (2.0 M in THF, Sigma Aldrich) is added to the hydrogels dissolved in dry toluene. An equivalent molar amount of di-isopropylethylamine (DIPEA, Sigma-Aldrich, $>99\%$, ReagentPlus) is added to deprotonate the diamine before nucleophilic substitution. Grafting of the diamines is performed at reflux temperature (110 °C) for 24 hours, grafting of methylamine is performed at 40 °C for 48 hours. Afterwards, the obtained catalysts are washed twice in 200 mL ethanol and dried at 50 °C on a high vacuum.

CHN analysis of PEGMA catalysts was performed by Atlantic MicroLabs. Non-spinning Direct Polarization (DP) ^{13}C NMR spectra were recorded at 60 °C with a Bruker AVIII-300. Fourier Transform-Infrared (FT-IR) transmission spectroscopy was performed with a Nicolet iS10 Spectrometer.



Scheme 8-2: Synthesis procedure of PEGMA catalysts, in this example functionalized with a primary ethylenediamine (PEGMA-EDA). Other amines or diamines can also be used.

8.2.3 Performance Evaluation

All catalysts are evaluated in the Parr[®] batch type reactor for the aldol reaction between acetone and 4-nitrobenzaldehyde using water as solvent, under the same conditions as described in Chapter 7. A catalyst amount corresponding to 0.1 mmol active amine sites was added in the reactor for evaluation of the PMO materials, similar to the silica catalysts evaluated in Chapter 4. The PEGMA catalysts, however, were evaluated with 0.06 mmol active amine sites in the reactor, due to the limited catalyst loading and limited amount of catalyst synthesized. The stability of the PEGMA-EDA catalyst was evaluated in the (LS)² reactor with a site time of 544 mol_{site} s mol_{4NB}⁻¹.

8.3 Results and discussion

8.3.1 Characterization results

The nitrogen adsorption-desorption isotherms for the Ethane-bridged PMO materials and the Ethylene-bridged PMO materials are presented in, respectively, Figure 8-4 and Figure 8-5. They all exhibit type IV isotherms with H1 type hysteresis loops at relative pressures in the range of 0.4 to 0.5, indicative of mesopores with a narrow pore size distribution. The specific

surface area (S_{BET}), the total pore volume (V_{p}) and average pore size (d_{p}) of all the synthesized PMO materials are summarized in Table 8-1. The pristine Ethane-bridged PMO has a surface area of $1064 \text{ m}^2 \text{ g}^{-1}$. After functionalization and endcapping, the specific surface area respectively decreased with 11% and 13%. The pore volume respectively decreased with 14% and 12%. This is attributed to a decrease in free volume and an increase in catalyst mass, which is typically observed after functionalisation⁶. The pristine Ethylene-bridged PMO material has a surface area of $826 \text{ m}^2 \text{ g}^{-1}$, which severely decreased by 53% upon anchoring active sites on the ethylene moiety and endcapping. A similarly large decrease in surface area was noted by Ouwehand et al.⁵ upon clicking cysteamine on an ethylene-bridged PMO. The pore volume (V_{p}) and average pore diameter (d_{p}), reported in Table 8-1, however, indicate that the mesoporous structure is still intact. The original mesostructure in both materials thus remains unchanged, with an average pore size in the range of 3.5 to 4.2 nm. These pore sizes depend on the surfactant used, here Brij[®] S10 for the Ethane-bridged PMO and Pluronic[®] P-123 for the Ethylene-bridged PMO, and are only slightly smaller than the pore sizes reported in literature^{5, 10}.

Elemental CHN analysis indicated an amine loading of $0.76 \pm 0.08 \text{ mmol g}^{-1}$ for the Amine-Ethane-PMO and $0.35 \pm 0.04 \text{ mmol g}^{-1}$ for the Amine-Ethylene-PMO.

Table 8-1: Structural properties obtained via nitrogen sorption of the Ethane-bridged and Ethylene-bridged PMO material and catalysts.

	$S_{\text{BET}} [\text{m}^2 \text{ g}^{-1}] \pm 7\%$	$V_{\text{p}} [\text{cm}^3 \text{ g}^{-1}] \pm 6\%$	$d_{\text{p}} [\text{nm}] \pm 5\%$
Ethane-PMO	1064	1.11	3.6
Amine-Ethane-PMO	951	0.95	3.5
HMDS-Amine-Ethane-PMO	832	0.84	3.5
Spent Amine-Ethane-PMO	995	1.04	3.7
Spent HMDS-Amine-Ethane-PMO	871	0.93	3.6
Ethylene-PMO	826	0.42	4.5
Amine-Ethylene-PMO	384	0.43	4.2
HMDS-Amine-Ethylene-PMO	304	0.31	3.8
Spent Amine-Ethylene-PMO	528	0.54	4.5
Spent HMDS-Amine-Ethylene-PMO	353	0.34	3.9

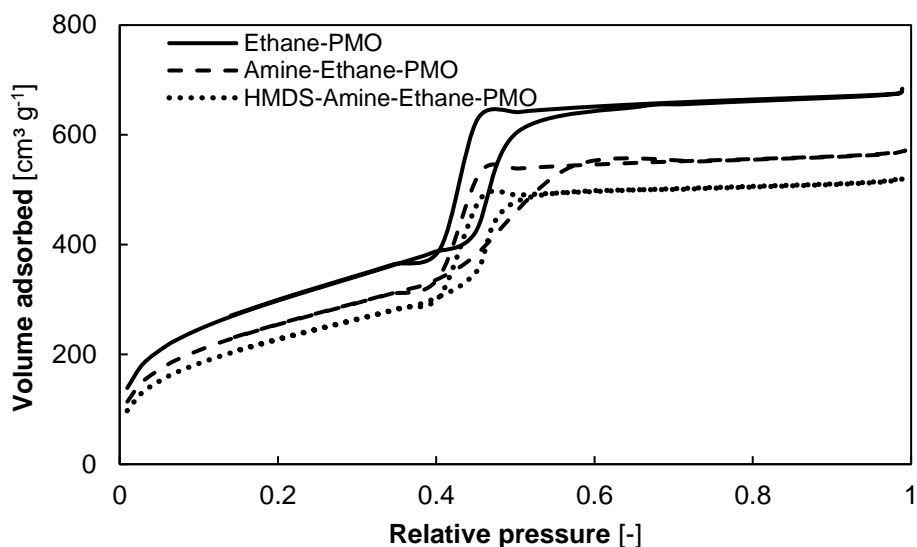


Figure 8-4: Nitrogen sorption isotherms for the Ethane-bridged PMO material and the catalysts derived from it

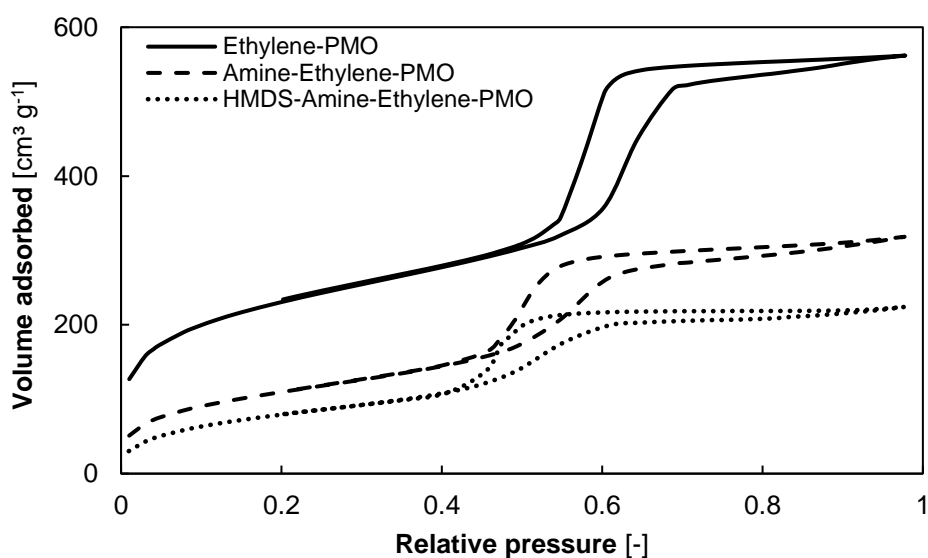


Figure 8-5: Nitrogen sorption isotherms for the Ethylene-bridged PMO material and the catalysts derived from it

DRIFTS measurements were performed on both PMO materials in the various steps of the synthesis. The spectra are provided in Appendix F. A narrow peak at 3745 cm^{-1} indicates the presence of free silanol groups. The N-H vibrations of the secondary amine in the amine functionalized catalysts should appear at 3305 cm^{-1} , but cannot be distinguished in the spectra. This is most probably due to the relatively low amine loading, as well as the generally low intensity of N-H vibrations from secondary amines in DRIFTS. The peaks between 3000 cm^{-1} and 2850 cm^{-1} correspond to the C-H stretch of the organic alkane linkers and the HMDS

moieties. A peak between 1700 and 1600 cm^{-1} corresponds with the C=C stretch and decreases in intensity when the click-reaction is performed on the ethylene-PMO material.

The broad peak between 3600 cm^{-1} and 3200 cm^{-1} on both materials could correspond to water molecules bonded to the silanol groups, which indicates that the drying procedure of the catalysts did not completely remove hydrogen-bonded water molecules. However, treatment with an excess of HMDS removes a large part of this surface-bound water. Subsequent elemental analysis of the HMDS-Amine-Ethane-PMO catalyst indicated that this causes no decrease in amine loading, ensuring that the desired silane grafting occurred on the silanol groups and not on the hydrogen-bonded water molecules.

It should also be noted that the endcapping of the surface silanols on the HMDS-Amine-Ethane-PMO catalyst appears not to be complete. This is most likely related to sterically hindered silanol groups which cannot be reached by the bulky HMDS molecules¹¹.

The PEGMA hydrogels and their functionalized counterparts are subject to Direct Polarization (DP) ^{13}C -NMR, FT-IR, and elemental analysis. The DP ^{13}C -NMR of the pristine hydrogels exhibits all the characteristic peaks of polymerized PEGMA, as indicated in Figure 8-6(a). The first functionalization step is the reaction with thionylchloride, which, as can be observed in Figure 8-6(b), reduces the intensity of the peak at 61.3 ppm, corresponding to the hydroxyl groups, and increases the peak around 44.8 ppm, corresponding to a carbon attached to Cl. There is some overlap with the peak related to the polymerized methacrylate carbon atom at 46.8 ppm, but a clear shift in the maximum and intensity was found after chlorination. No other peaks have shifted, or appeared, indicating that only the desired reaction took place. To compare, the ^{13}C -NMR spectrum of a 100% chlorinated PEGMA material is displayed in Figure F-3, where the complete disappearance of the hydroxyl peak at 61.3 ppm is visible in favor of a larger peak at 44.8 ppm corresponding to C-Cl. While such a highly functionalized material is not used for catalytic purposes, it indicates that the resin can sufficiently swell in dry toluene to allow access to all the active sites.

The FT-IR spectrum in Figure 8-7 supports the conclusions drawn above. The characteristic peaks associated with the C-H, C=O and C-O vibrations in the polymerized PEGMA molecule are the most intense and respectively appear at 2900 cm^{-1} , 1720 cm^{-1} and 1100 cm^{-1} . The spectrum of the chlorinated PEGMA shows that the peak associated with hydroxyl groups in PEGMA, around 3500 cm^{-1} , reduces upon reaction with thionyl chloride in favor of a C-Cl peak at 660 cm^{-1} . The spectrum of a 100% chlorinated PEGMA material, indicates a complete loss of the hydroxyl groups in PEGMA, around 3500 cm^{-1} and an increase in the C-Cl peak at 660 cm^{-1} as displayed in Figure F-4 in Appendix F. Furthermore, no other

peaks have appeared or changed shape. There is, hence, no obvious indication that any other than the desired reaction occurred.

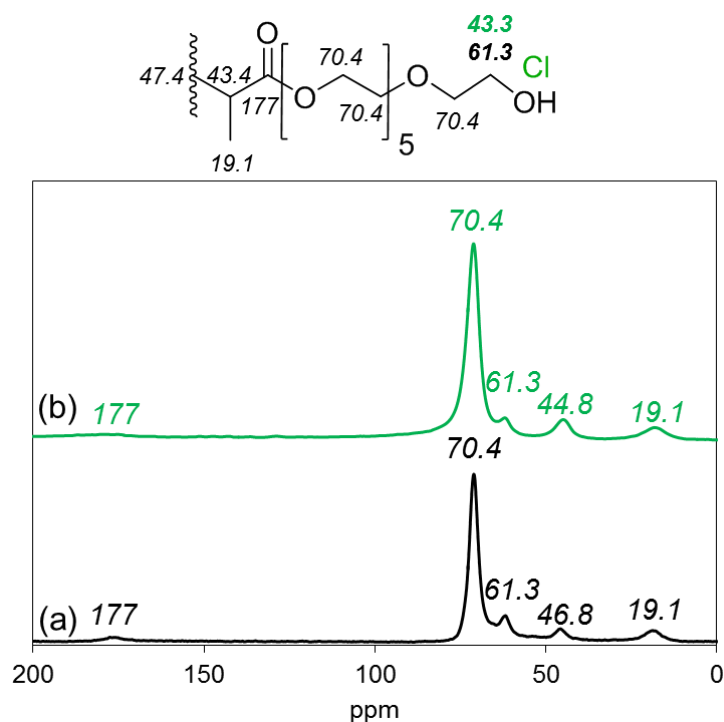


Figure 8-6: DP ^{13}C -NMR at 60°C of PEGMA hydrogel (a) and chlorine functionalized PEGMA (b)

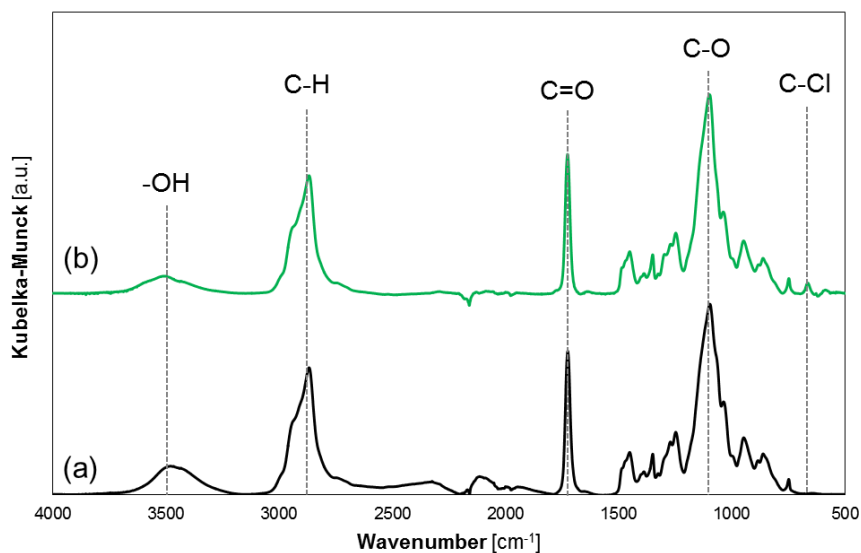


Figure 8-7: FT-IR spectrum of PEGMA hydrogel (a) and chlorine functionalized PEGMA (b)

Next, the chlorine functionalized PEGMA materials are subject to nucleophilic substitution with a symmetrical diamine to produce the desired catalysts. Their loading is reported in Table 8-2. Figure 8-8 and Figure 8-9 respectively indicate the DP ^{13}C -NMR results of the PEGMA-EDA and PEGMA-DED catalysts including the peak assignment to the

functionalized groups. The different individual peaks in the ^{13}C -NMR profile are difficult to assign independently due to their low intensity. This is due to the relatively low diamine loading on the catalysts. The same issue causes the FT-IR spectra of the PEGMA-EDA and PEGMA-DED catalysts to be indistinguishable from the unfunctionalized PEGMA material, as displayed in Figure F-5. However, characterization results of a high-loaded PEGMA-EDA, with 88% of the available hydroxyl groups replaced with EDA, is displayed in Figure F-6 and Figure F-7. The peaks associated with the primary diamine are clearly visible in the ^{13}C -NMR and FT-IR spectrum. Even though this latter material is not evaluated for its catalytic activity, it indicates that the desired functionalization indeed occurs under the used experimental conditions and no undesired side-reactions are taking place.

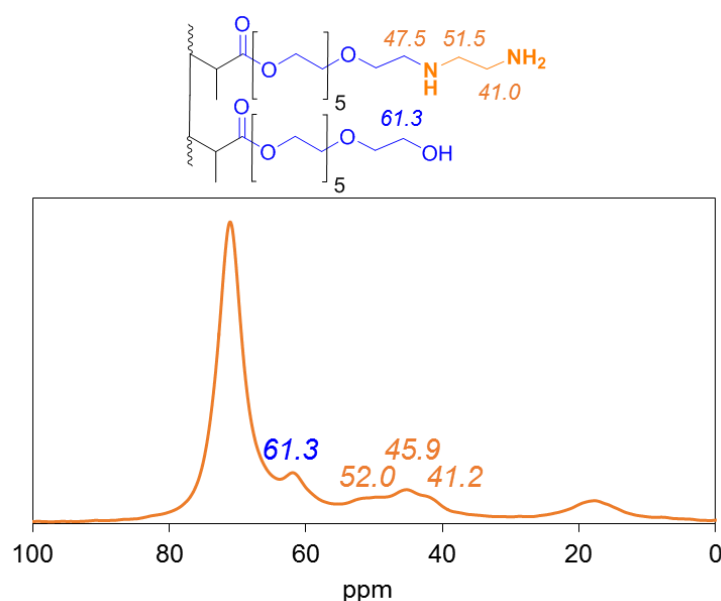


Figure 8-8: 60 °C DP ^{13}C -NMR of the PEGMA-EDA catalyst

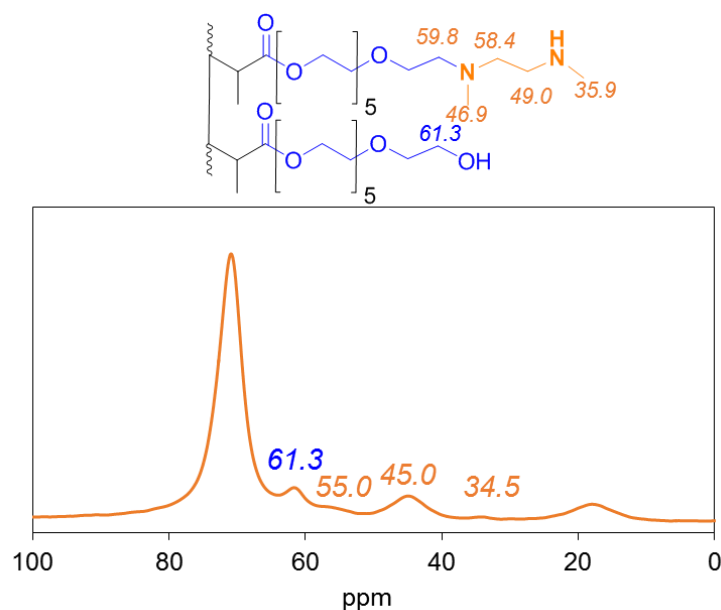


Figure 8-9: 60 °C DP ^{13}C -NMR of the PEGMA-DED catalyst

In order to investigate the possible catalytic activity of the secondary amine in the EDA chain of the PEGMA-EDA catalyst, functionalization with methylamine is also performed to produce PEGMA-MA. In the DP ^{13}C -NMR and FT-IR spectra corresponding to this material, no clear peaks relating to the methylamine group can be distinguished due to the low mass percentage of methylamine and the low intensity of secondary amine vibrations in FT-IR. However, its loading as determined from the nitrogen elemental analysis is reported in Table 8-2 and proves that amine functionalization has occurred.

Table 8-2: Diamine loading for the different PEGMA catalysts.

Sample	Diamine loading ^a ± 5% (mmol g ⁻¹)
PEGMA-EDA	0.43
PEGMA-DED	0.28
PEGMA-MA	0.24

The diamine loading, as reported in Table 8-2, is specifically kept low to ensure as much as possible isolated amine sites. The chlorine substitution degree was targeted at 30% of the hydroxyl sites, which amounts to a chlorine content of 0.72 mmol g⁻¹. The lower diamine

^a The diamine loading corresponds to the total nitrogen content obtained from CHN analysis divided by 2.

loading shows that either the chlorination reaction or the nucleophilic substitution was not complete.

8.3.2 Catalytic performance evaluation

All catalysts are evaluated in a batch experiment using 50 vol% water as solvent and 50 vol% acetone as excess reagent. The obtained turnover frequency (TOF), determined from the initial linear part of the conversion versus reaction time plot, are reported to compare the intrinsic amine activity for the different catalysts. Subsequently, the PMO catalysts are filtered and recycled for a second batch experiment to assess their reusability. Finally, the stability of the best performing PEGMA catalyst is evaluated in the continuous-flow (LS)² reactor.

The TOF of a first and second run of the PMO catalysts is displayed in Figure 8-10. The Amine-Ethane-PMO catalyst, where the amines are grafted on surface silanols, exhibits a TOF amounting to $3.6 \cdot 10^{-3} \text{ s}^{-1}$, while the equivalent endcapped HMDS-Amine-Ethane-PMO exhibits a TOF of $4.7 \cdot 10^{-3} \text{ s}^{-1}$. These values are higher than the highest TOF values previously reported with aminated silica catalysts, using hexane as solvent¹². It also appears that, when working with water as solvent, endcapping silanol groups does not have a negative influence on the activity of the catalyst. This indicates that promotion by surface silanol groups is losing relevance when water is used as solvent. Indeed, the endcapped catalyst, HMDS-Amine-Ethane-PMO, even exhibits a slightly higher TOF value, which could be related to the more hydrophobic environment around the active site¹³. Significant activity losses were observed when determining the reusability of these materials: only about 20% of the activity could be achieved in the second run of both catalysts.

The catalysts obtained by the thiol-ene click reaction, Amine-Ethylene-PMO and HMDS-Amine-Ethylene-PMO, exhibit a TOF amounting to respectively $8.6 \cdot 10^{-4} \text{ s}^{-1}$ and $7.1 \cdot 10^{-4} \text{ s}^{-1}$. These values are much lower than those obtained with the Amine-Ethane-PMO catalysts. As previously reported in literature, this difference might be related to the organic linker used in the PMO material, which can induce selective absorption behavior in the pores of the catalyst⁶. Or this could be caused by an unknown number of unfunctionalized 'clicked' chlorine-containing groups influencing the reaction environment. However, this was not further investigated because the Amine-Ethylene-PMO catalysts exhibited a similar, poor reusability of only 20% as the Amine-Ethane-PMO catalysts.

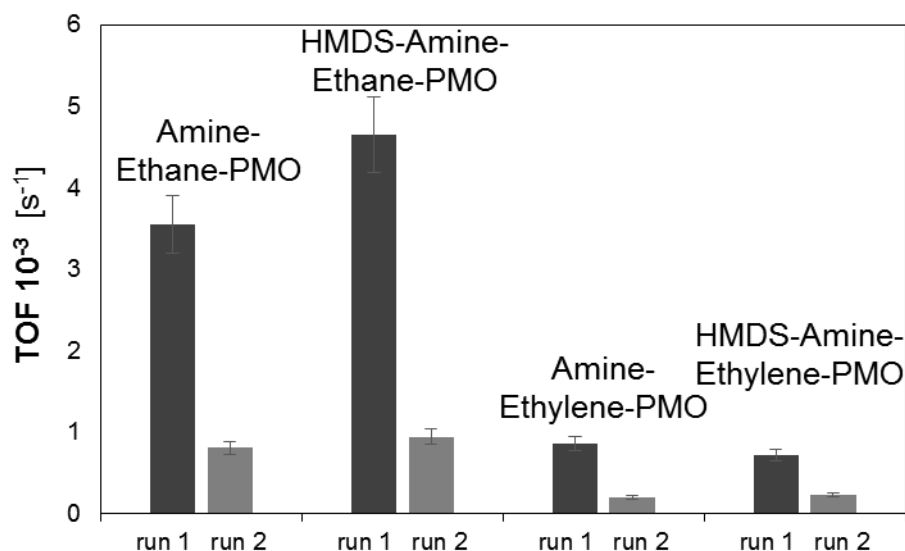


Figure 8-10: Turnover frequency for the PMO catalysts, determined in the Parr[®] batch reactor, for the aldol reaction of acetone with 4-nitrobenzaldehyde. ($T = 55\text{ }^{\circ}\text{C}$, $m_{\text{acetone}} = 45\text{ g}$, $m_{4\text{NB}} = 0.45\text{ g}$, $m_{\text{water}} = 55\text{ g}$, 0.1 mmol amine sites)

Because the poor reusability of the PMO catalysts is likely related to hydrolysis reactions, possible mechanisms of catalyst deactivation for the Ethane-PMO and Ethylene-PMO catalysts are displayed in, respectively, Figure 8-11 and Figure 8-12. It should be noted that in both cases the basic amine groups itself can bend towards the surface of the PMO and catalyze hydrolysis reactions of any Si-O-Si bond, leading to active site leaching and PMO degradation¹⁴⁻¹⁶.

From elemental analysis of the spent catalysts, a loss of $79\% \pm 8\%$ of active sites is observed for the Amine-Ethane-PMO after run 2. Similarly, for the HMDS-Amine-Ethane-PMO, this loss amounts to $77\% \pm 8\%$ after run 2. The loss of grafted active sites occurs hand in hand with an increase in surface area and pore volume, as reported in Table 8-1, indicating that free volume is gained.

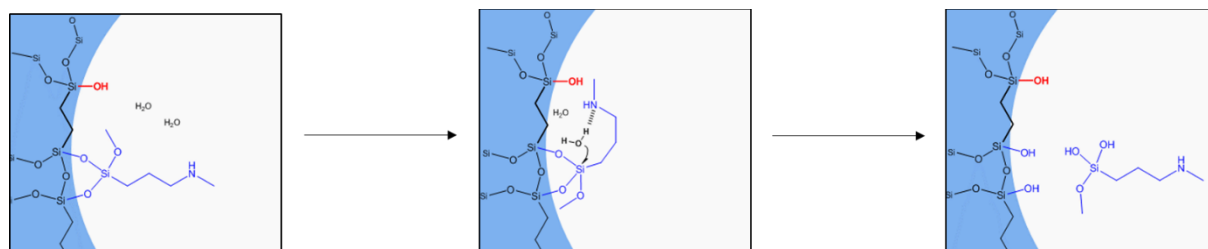


Figure 8-11 Leaching of the amine sites in the Amine-Ethane-PMO catalyst through amine catalyzed hydrolysis of the siloxane bonds¹⁴.

On the Amine-Ethylene-PMO catalysts, the active sites are incorporated by clicking on the organic backbone, leading to a very stable covalent thioether bond. Leaching of the active site itself by hydrolysis of these bonds is thus unlikely. However, as displayed in Figure 8-12,

the PMO support could suffer from degradation by hydrolysis reactions, as it is, next to organic linkers, also composed of siloxane bonds. This hypothesis is confirmed by nitrogen sorption measurements of the spent catalysts, as summarized in Table 8-1, that indicate an increase in surface area and pore volume. However, the amine loading only appeared to decrease by $7\% \pm 1\%$ for the Amine-Ethylene-PMO material and by $23\% \pm 2\%$ for the HMDS-Amine-Ethylene-PMO. This decrease indicates loss of active sites in some way. However, more research is required to investigate the mechanism in detail.

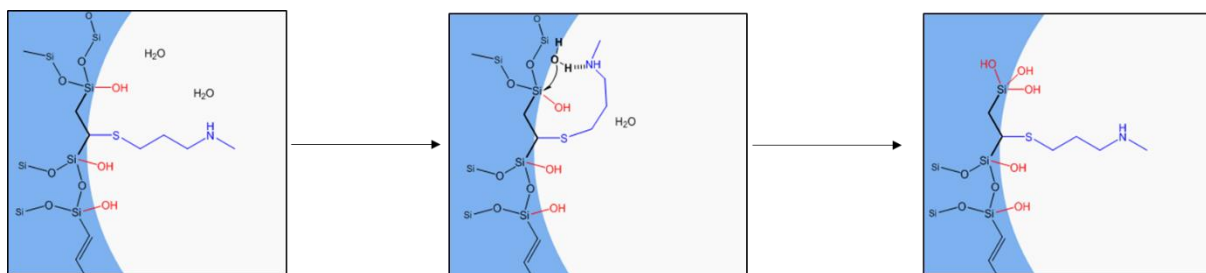


Figure 8-12 Structural degradation of the PMO material through hydrolysis of the siloxane bonds, catalyzed by the amine site can lead to structural degradation.

From the evaluation of the above aminated PMO catalysts, it is clear that no stable catalyst is obtained for the aqueous aldol reaction when a methylaminopropyl active site, such as on silica gel in Chapter 4, is employed. Both the grafted as well as the clicked amine-PMO catalysts exhibited a large and irreversible deactivation behavior. This is likely caused by hydrolysis reactions of Si-O-Si bonds, catalyzed by the amine which is attached to the surface with a flexible propyl linker. An improvement in stability could be achieved by employing a shorter linker connecting the amine site to the surface, which does not allow the active site to bend towards the Si-O-Si bonds. Previous research has shown that limiting the linker length also limits promoting effects with silanol groups¹⁷, but Figure 8-10 shows that these promoting effects are limited when working with water as solvent.

Both the PEGMA-EDA and PEGMA-DED catalysts are evaluated for the aldol reaction and their activity is summarized in Figure 8-13. The TOF exhibited by the secondary amine functionalized PEGMA-DED amounts to $3.1 \cdot 10^{-4} \text{ s}^{-1}$, which is inferior to that obtained with the Ethane-PMO catalysts. This could be a consequence of the difference in local polarity environment¹³, in this case the difference between PEG chains and hydrophobic organic groups in the PMO material, which can cause a selective absorption behavior¹⁸. The TOF obtained with PEGMA-EDA amounts to $6.3 \cdot 10^{-4} \text{ s}^{-1}$, which suggests that, contrary to working with hexane as solvent^{12, 19}, primary amine sites are more active with water as solvent than the secondary amine sites²⁰. This has been reported previously by Kandel et al.²⁰ and is attributed to the presence of

water, shifting the equilibrium away from the inhibiting imine on primary amines. Experiments with methylamine functionalized PEGMA-MA yielded no measurable 4-nitrobenzaldehyde conversion, which indicates that the secondary amine that is formed in PEGMA-EDA is not catalytically active. This is possibly related to the severe steric hindrance.

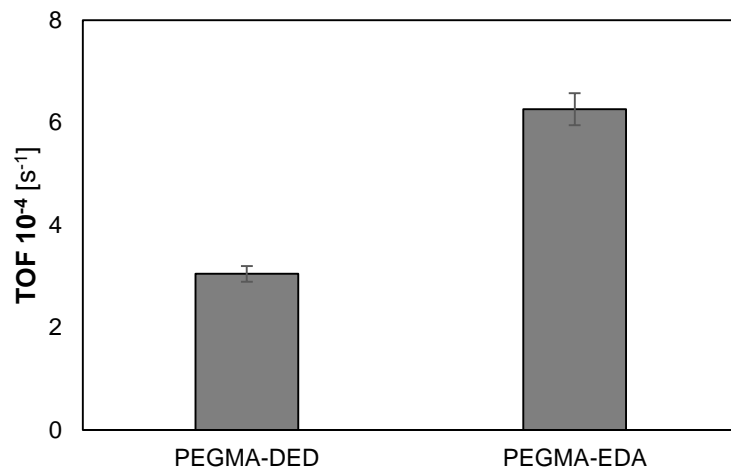


Figure 8-13: Turnover frequency for the PEGMA catalysts, determined in the Parr[®] batch reactor, for the aldol reaction of acetone with 4-nitrobenzaldehyde. ($T = 55$ °C, $m_{\text{acetone}} = 45$ g, $m_{4\text{NB}} = 0.45$ g, $m_{\text{water}} = 55$ g, 0.1 mmol amine sites)

Reusability was not evaluated in the Parr[®] batch reactor because the small resin beads were difficult to recover after a first run. To avoid errors while filtering and recycling a catalyst in a batch reaction, the stability of the PEGMA-EDA catalyst is evaluated in the continuous-flow (LS)² reactor. The conversion versus time on stream graph is displayed in Figure 8-14 and indicates stable catalyst operation for the aldol reaction during at least 8 hours on stream.

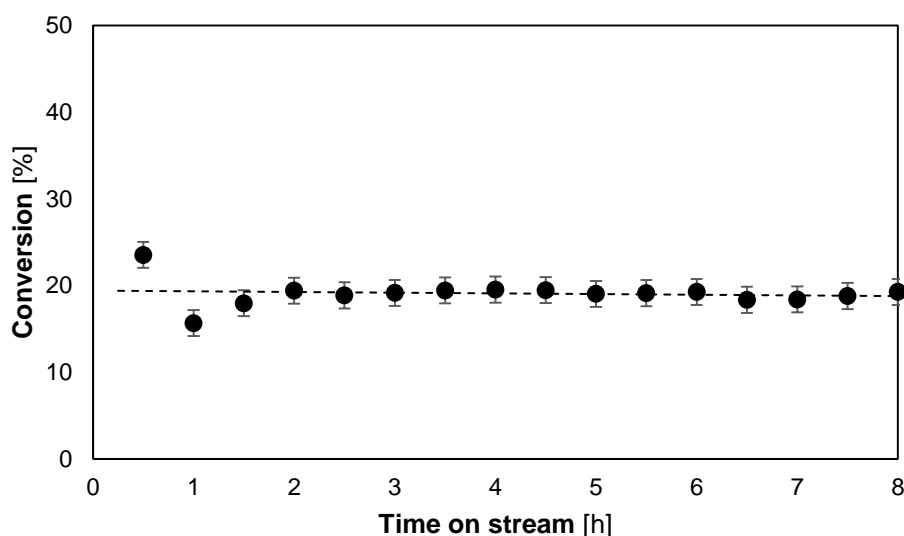


Figure 8-14: Conversion as a function of time on stream for the PEGMA-EDA catalyst in the aldol reaction of acetone with 4-nitrobenzaldehyde. ($T = 328.15$ K, $P = 180$ kPa, site time = $544 \text{ mol}_{\text{site}} \cdot \text{s} \cdot \text{mol}^{-1}$, 0.45 wt% 4-nitrobenzaldehyde, 44.6 wt% acetone, 54.5 wt% water, 0.25 wt% IS.)

The constant conversion as a function of time on stream in Figure 8-14 shows that the developed PEGMA-EDA catalyst exhibits the same stability as the chitosan derived catalysts from Chapter 7, and has an activity that is at least 4 times higher than the most active chitosan catalyst.

8.4 Conclusions

Two different kinds of catalysts were developed with organic groups incorporated in the support material. On the one hand, periodic mesoporous organosilica (PMO) materials were synthesized by condensation of either ethane or ethylene bridged bisilanes. On the other hand, (poly ethyleneglycol) methacrylate (PEGMA) organic hydrogels, without any silicon atoms, were synthesized via free radical suspension polymerization. The ethane-PMO was functionalized with methylaminopropyltrimethoxysilane (MAPTMS) via grafting on the free silanol groups. The ethylene-PMO was functionalized with the same active site by a thiol-ene click reaction on the ethylene functionality, which provides a hydrothermally stable thioether bond. The PEGMA catalysts were functionalized by nucleophilic substitution of different diamines and amines on chlorine functionalized PEGMA.

The stability of the catalysts was evaluated for the aldol reaction of acetone with 4-nitrobenzaldehyde using water as solvent. Recycle experiments in a batch reactor indicated poor reusability of all PMO catalysts, most likely due to amine catalyzed hydrolysis reactions of various Si-O-Si bonds. These are the bonds that connect the active MAPTMS site to the Ethane-PMO support, and connect the different organobisilanes to each other in both the Ethane-PMO and the Ethylene-PMO. However, the most active PEGMA catalyst, i.e. the PEGMA-EDA catalyst, was found to exhibit a stable conversion with time on stream in the continuous-flow (LS)² reactor, indicating no catalyst deactivation occurs.

Compared to chitosan, the amine sites in the developed PEGMA-EDA exhibit an activity that is 4 times higher. With a 3 times higher loading than the corresponding chitosan catalyst, and an equal stability with time on stream, PEGMA-EDA appears as a very attractive potential new catalyst for the aqueous aldol reaction.

8.5 References

1. Asefa, T.; MacLachlan, M. J.; Coombs, N.; Ozin, G. A., Periodic mesoporous organosilicas with organic groups inside the channel walls. *Nature* **1999**, *402* (6764), 867.
2. Inagaki, S.; Guan, S.; Fukushima, Y.; Ohsuna, T.; Terasaki, O., Novel mesoporous materials with a uniform distribution of organic groups and inorganic oxide in their frameworks. *Journal of the American Chemical Society* **1999**, *121* (41), 9611-9614.
3. Van Der Voort, P.; Esquivel, D.; De Canck, E.; Goethals, F.; Van Driessche, I.; Romero-Salguero, F. J., Periodic mesoporous organosilicas: from simple to complex bridges; a comprehensive overview of functions, morphologies and applications. *Chemical Society Reviews* **2013**, *42* (9), 3913-3955.
4. Huybrechts, W.; Lauwaert, J.; De Vylder, A.; Mertens, M.; Mali, G.; Thybaut, J. W.; Van Der Voort, P.; Cool, P., Synthesis of L-serine modified benzene bridged periodic mesoporous organosilica and its catalytic performance towards aldol condensations. *Microporous and Mesoporous Materials* **2017**, *251*, 1-8.
5. Ouwehand, J.; Lauwaert, J.; Esquivel, D.; Hendrickx, K.; Van Speybroeck, V.; Thybaut, J. W.; Van Der Voort, P., Facile Synthesis of Cooperative Acid–Base Catalysts by Clicking Cysteine and Cysteamine on an Ethylene-Bridged Periodic Mesoporous Organosilica. *European Journal of Inorganic Chemistry* **2016**.
6. Lauwaert, J.; Ouwehand, J.; De Clercq, J.; Cool, P.; Van Der Voort, P.; Thybaut, J. W., Tuning component enrichment in amino acid functionalized (organo)silicas. *Catalysis Communications* **2017**, *88*, 85-89.
7. Van de Steene, E.; De Clercq, J.; Thybaut, J. W., Ion-exchange resin catalyzed transesterification of ethyl acetate with methanol: Gel versus macroporous resins. *Chemical Engineering Journal* **2014**, *242*, 170-179.
8. Harris, J. M., Introduction to biotechnical and biomedical applications of poly (ethylene glycol). In *Poly (ethylene glycol) Chemistry*, Springer: 1992; pp 1-14.
9. Tuncel, A., Suspension polymerization of poly (ethylene glycol) methacrylate: a route for swellable spherical gel beads with controlled hydrophilicity and functionality. *Colloid and Polymer Science* **2000**, *278* (12), 1126-1138.
10. Burleigh, M. C.; Jayasundera, S.; Thomas, C. W.; Spector, M. S.; Markowitz, M. A.; Gaber, B. P., A versatile synthetic approach to periodic mesoporous organosilicas. *Colloid and Polymer Science* **2004**, *282* (7), 728-733.
11. Takei, T.; Yamazaki, A.; Watanabe, T.; Chikazawa, M., Water adsorption properties on porous silica glass surface modified by trimethylsilyl groups. *Journal of colloid and interface science* **1997**, *188* (2), 409-414.
12. Lauwaert, J.; De Canck, E.; Esquivel, D.; Van Der Voort, P.; Thybaut, J. W.; Marin, G. B., Effects of amine structure and base strength on acid–base cooperative aldol condensation. *Catalysis Today* **2015**, *246*, 35-45.
13. Singappuli-Arachchige, D.; Kobayashi, T.; Wang, Z.; Burkhov, S. J.; Smith, E. A.; Pruski, M.; Slowing, I. I., Interfacial Control of Catalytic Activity in the Aldol Condensation: Combining the Effects of Hydrophobic Environments and Water. *ACS Catalysis* **2019**.
14. Etienne, M.; Walcarius, A., Analytical investigation of the chemical reactivity and stability of aminopropyl-grafted silica in aqueous medium. *Talanta* **2003**, *59* (6), 1173-1188.
15. Asenath Smith, E.; Chen, W., How to prevent the loss of surface functionality derived from aminosilanes. *Langmuir* **2008**, *24* (21), 12405-12409.
16. Krumpfer, J. W.; Fadeev, A. Y., Displacement reactions of covalently attached organosilicon monolayers on Si. *Langmuir* **2006**, *22* (20), 8271-8272.
17. Brunelli, N. A.; Didas, S. A.; Venkatasubbaiah, K.; Jones, C. W., Tuning cooperativity by controlling the linker length of silica-supported amines in catalysis and CO₂ capture. *Journal of the American Chemical Society* **2012**, *134* (34), 13950-13953.
18. Sainio, T.; Laatikainen, M.; Paatero, E., Phase equilibria in solvent mixture–ion exchange resin catalyst systems. *Fluid Phase Equilibria* **2004**, *218* (2), 269-283.

19. Kandel, K.; Althaus, S. M.; Peeraphatdit, C.; Kobayashi, T.; Trewyn, B. G.; Pruski, M.; Slowing, I. I., Substrate inhibition in the heterogeneous catalyzed aldol condensation: A mechanistic study of supported organocatalysts. *Journal of Catalysis* **2012**, *291*, 63-68.
20. Kandel, K.; Althaus, S. M.; Peeraphatdit, C.; Kobayashi, T.; Trewyn, B. G.; Pruski, M.; Slowing, I. I., Solvent-Induced Reversal of Activities between Two Closely Related Heterogeneous Catalysts in the Aldol Reaction. *ACS Catalysis* **2013**, *3* (2), 265-271.

Chapter 9

Conclusions and perspectives

9.1 Conclusions

Aldol reactions are widely used in the pharmaceutical industry, as well as for the preparation of fine chemicals. Moreover, aldol reactions of renewable lignocellulosic biomass derived components offer promising perspectives for the production of sustainable liquid hydrocarbon fuels. In present-day commercial processes a homogenous, strong base catalyst, such as NaOH, is used to catalyze this type of reactions. However, in a search for more sustainable chemicals production, heterogeneous alternatives for these homogenous catalysts are being pursued. Inspired by previous work on aminated mesoporous silica catalysts, this work aimed at the further development of supported amine catalysts.

Steric hindrance experienced during interactions with supported amine sites severely limits the catalytic activity that can be achieved. As a result, among the secondary propylamines grafted on mesoporous silica, the one with a small substituent such as a methyl group was found to exhibit the highest activity. In this work, a computational basicity scale was developed to indicate which sites are the least sterically hindered and, hence, appear as the most attractive catalytic sites for the aldol reaction. As least sterically hindered monofunctional group, 4-propyl-pyrrolidine was proposed. For intramolecular cooperativity, the correct placement of the promoting hydroxyl group on the β -carbon with respect to the amine function was shown to be crucial in limiting the steric hindrance. Hence, 1-(methylamino)propan-2-ol was proposed as a potential new bifunctional amine-hydroxyl site. Using this methodology, it is possible to focus the experimental effort on a limited number of active site designs that should be synthesized with high priority.

Not only the activity, but also the stability is an important factor in the assessment of the commercial potential of a catalyst. Hence, the reusability of the most active aminated mesoporous silica catalyst, bearing the N-methylaminopropyl (MAP) active site, was experimentally investigated for the model aldol reaction of 4-nitrobenzaldehyde with acetone using dimethylsulfoxide (DMSO) as solvent. Both the cooperative acid-base catalyst, i.e. where

the amine sites are promoted by silanol groups on the silica surface, as well as the monofunctional base catalysts, i.e. where the silanol groups have been endcapped with trimethylsilyl groups, were evaluated. It was found that, without co-feeding of water, both the cooperative acid-base catalyst, as well as the monofunctional base catalyst, exhibit a significantly lower activity in consecutive batch experiments. Thorough characterization of the spent catalysts using nitrogen sorption, CHN analysis, Raman spectroscopy, ^{13}C NMR, and UV-Vis characterization lead to the identification of site blocking species that were related to the iminium intermediate in the catalytic cycle. To enhance the hydration of this iminium intermediate and, hence, reduce their conversion into site blocking species, it sufficed to feed 0.69 wt% of water. This resulted in an increased reusability of up to 70% for the cooperative acid-base catalyst, and an almost complete reusability for the monofunctional base catalyst.

To investigate the reusability of the cooperative acid-base catalyst in a more straightforward manner, a packed-bed plug-flow reactor has been developed called the “Liquid-Solid Lab-Scale” or (LS)² reactor. Long term stability tests indicated that both the cooperative as well as the monofunctional MAP catalyst deactivated with time on stream. In the first instance, a relatively rapid loss of the promoting ability of the silanol groups in the cooperative catalyst was observed, which is most likely due to the local buildup of water, or the deprotonation of the silanol groups by water. With a longer time on stream, the activity of both the cooperative as well as the monofunctional catalyst further decreased, albeit more moderately, which can be related to hydrolysis reactions of the silica network that lead to aminosilane leaching, support degradation, and silica dissolution. This deactivation being less pronounced for the monofunctional base catalyst than for the cooperative one, was attributed to its more pronounced hydrophobicity owing to the trimethylsilyl groups used for endcapping.

Further insight into the role of water on a molecular level was achieved by modeling the elementary steps on the MAP site using the CBS-QB3 level of theory. The presence of one or two water molecules in the transition state was found to reduce the barrier for reactions that involve a proton transfer, i.e., the carbinolamine and enamine formation, and the aldol product liberation. Promotion by two water molecules was found to be optimal in these steps, whereas the involvement of a third water molecule led to a too pronounced entropic penalty. The presence of one water molecule in the carbon-carbon bond formation step was found to be crucial for avoiding the formation of a site-blocking enamine species. The presence of two water molecules in this step was found to again increase the reaction barrier. Changing the solvent mixture from a 50/50 vol% DMSO/acetone to a 50/50 vol% hexane/acetone mixture lowered the reaction barriers for all the transition states where water is involved as reagent or

auxiliary species in the transition state. This means that less water will be required to prevent the formation of site-blocking species when an apolar solvent such as hexane is used, as opposed to DMSO.

These insights open up perspectives for using water as a solvent in the aldol reaction. However, the aminated mesoporous silica catalysts are not stable under these conditions due to the easy hydrolysis of Si-O-Si bonds. Hence, an alternative catalyst design is pursued. The biopolymer chitosan, which does contain primary amine sites and no bonds prone to hydrolysis, was evaluated for its catalytic activity in the aldol reaction using water as solvent. It was found that during the first 2 hours in the batch reactor, stable imines derived from 4-nitrobenzaldehyde were formed on the primary amine sites, which led to a decreased catalytic activity. When this imine formation equilibrated, a stable catalytic activity was obtained which could be reproduced in a recycle experiment. However, the overall activity was inferior to that of the cooperative primary amine functionalized mesoporous silica catalysts by more than an order of magnitude. The catalyst stability was also confirmed by the stable conversion as a function of time on stream in the packed-bed plug-flow (LS)² reactor. Despite its unacceptably low activity, the remarkable stability of chitosan as an aldol reaction catalyst in an aqueous environment provides inspiration for further catalyst design.

Inspired by the positive effect of water in preventing the amine deactivation, and the stability of the organic biopolymer chitosan, more water resistant support materials are aimed at. In the first instance, amine functionalized Periodic Mesoporous Organosilica (PMO) catalysts were developed. However, despite the increased hydrothermal stability of the PMO support material, degradation via hydrolysis reactions still occurred at the Si-O-Si bonds connecting the individual organic groups. Hence, an entirely organic resin catalyst based on aminated poly(ethylene glycol) methacrylate (PEGMA) was developed. The versatile swelling behavior of this resin catalyst allowed to efficiently synthesize the catalyst in an organic solvent under dry reaction conditions and also apply it in the aqueous aldol reaction. These PEGMA catalysts were found to be equally stable with time on stream as chitosan and exhibited 81% of the activity measured with the cooperative primary amine functionalized mesoporous silica catalyst using hexane as solvent.

9.2 Perspectives

This work has shown that the interplay between the amine function, catalyst support and solvent can be tuned for an optimized catalytic activity and stability in the aldol reaction.

Further improvements along these lines are still possible. For example, the sterically least hindered amine site, such as based on pyrrolidine, could be attached to the PEGMA support materials to increase their catalytic activity. Furthermore, the PEGMA support materials can be tuned for an optimized uptake of the reagents in the pores of the catalyst by altering the composition of the copolymer. Many different methacrylate monomers, both with hydrophilic PEG groups or without, are commercially available and can be employed. Depending on the rate-determining step in the elementary reaction mechanism, preferentially sorbing either water, acetone, or 4-nitrobenzaldehyde can enhance the catalytic activity. To find out which steps are rate-determining in specific reaction conditions, the reaction barriers and thermodynamics as calculated in this work could be supplied to a kinetic model. Next, determining the activity coefficients of the species absorbed in the pores of the swollen resin catalyst can also help to optimize the solvent ratios to be used in experiments.

Further catalytic evaluation of the developed stable PEGMA catalyst should focus on a more complex aldol reaction that is closer to a potential application. For example, the aldol reaction between acetone and furfural is a typical reaction that can be performed in the bio-based industry to increase the carbon chain length of the biomass-derived components to that desired for application as fuel. More specifically, the stability of the PEGMA catalyst in both an aqueous environment and organic solvent can be of particular interest in this application. The selective addition of acetone to furfural, without further oligomerization to too high carbon chain lengths, will then be a challenge to be addressed. Moreover, in the real carbonyl containing feedstock obtained from aqueous-phase reforming of biomass, a significant portion of carboxylic acid components can be present. These carboxylic acids can neutralize the amine sites and should therefore be prevented from interaction with the active site in the catalyst by, e.g., restricting their uptake in the pores.

Appendix A

A.1 Experimental Nucleophilicity of Amines

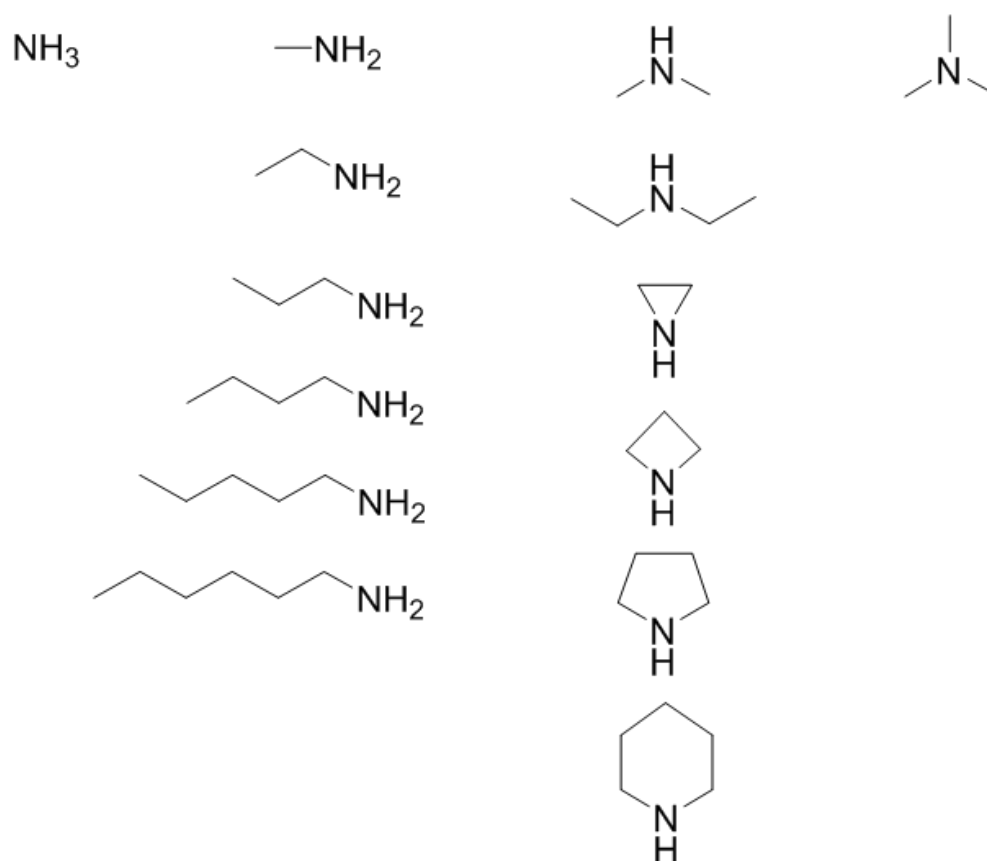


Figure A-1: Amines with different steric requirements experimentally investigated by Brown et al.¹⁻⁵

Table A-1: CBS-QB3 computational results at 298.15 K and 1 atm of the TMB complexation and the protonation with the amines displayed in Figure A-1.

CBS-QB3 calculations	TMB affinity (kJ mol⁻¹)	TMB entropy (J K⁻¹ mol⁻¹)	TMB basicity (kJ mol⁻¹)
NH ₃	65.1	198.4	5.9
CH ₃ NH ₂	84.0	207.6	22.1
CH ₃ CH ₂ NH ₂	85.1	206.8	23.4
CH ₃ (CH ₂) ₂ NH ₂	85.7	206.5	24.1
CH ₃ (CH ₂) ₃ NH ₂	86.2	206.7	24.5
CH ₃ (CH ₂) ₄ NH ₂	86.3	206.6	24.7
CH ₃ (CH ₂) ₅ NH ₂	86.5	206.7	24.8
(CH ₃) ₂ NH	89.2	214.1	25.4
(CH ₃ CH ₂) ₂ NH	78.9	220.9	13.1
AZIRIDINE	85.8	207.3	24.1
AZETIDINE	98.5	205.0	37.4
PYRROLIDINE	95.5	214.9	31.4
PIPERIDINE	90.6	215.2	26.5
(CH ₃) ₃ N	83.1	226.6	15.5

CBS-QB3 calculations	Proton affinity (kJ mol⁻¹)	Proton entropy (J K⁻¹ mol⁻¹)	Proton basicity (kJ mol⁻¹)
NH ₃	854.3	103.8	823.4
CH ₃ NH ₂	899.4	106.1	867.8
CH ₃ CH ₂ NH ₂	912.5	105.0	881.1
CH ₃ (CH ₂) ₂ NH ₂	917.3	104.6	886.1
CH ₃ (CH ₂) ₃ NH ₂	920.4	104.5	889.3
CH ₃ (CH ₂) ₄ NH ₂	922.0	104.4	890.9
CH ₃ (CH ₂) ₅ NH ₂	922.9	104.3	891.8
(CH ₃) ₂ NH	928.5	105.7	897.0
(CH ₃ CH ₂) ₂ NH	950.4	104.4	919.3
AZIRIDINE	906.1	106.6	874.3
AZETIDINE	938.7	103.1	907.9
PYRROLIDINE	948.3	106.3	916.6
PIPERIDINE	951.4	105.8	919.9
(CH ₃) ₃ N	946.5	104.9	915.3

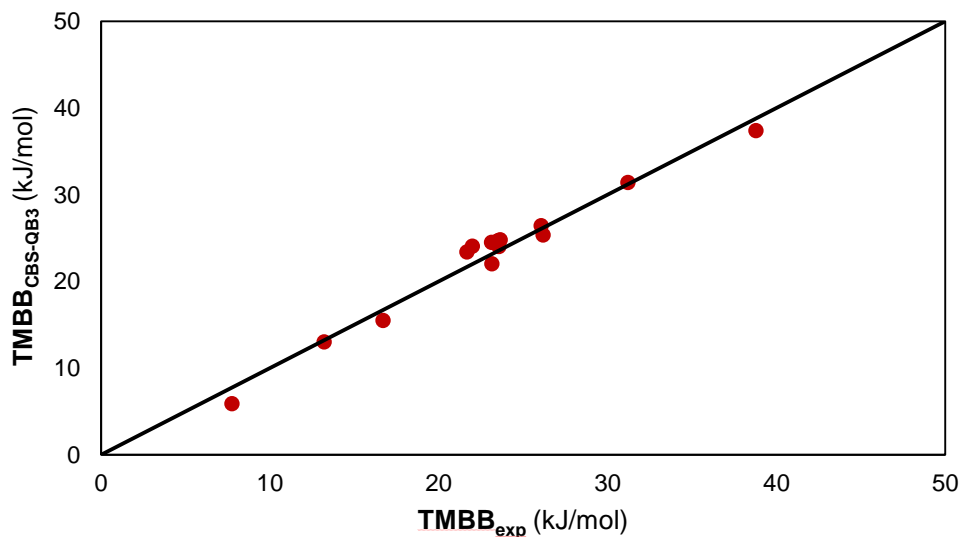


Figure A-2: comparison of the gas-phase experimental trimethylborane basicity (TMBB) by Brown et al.¹⁻⁵ for the amines displayed in Figure A-1, compared to the gas-phase TMBB values calculated with the CBS-QB3 model chemistry, at 298.15 K and 1 atm.

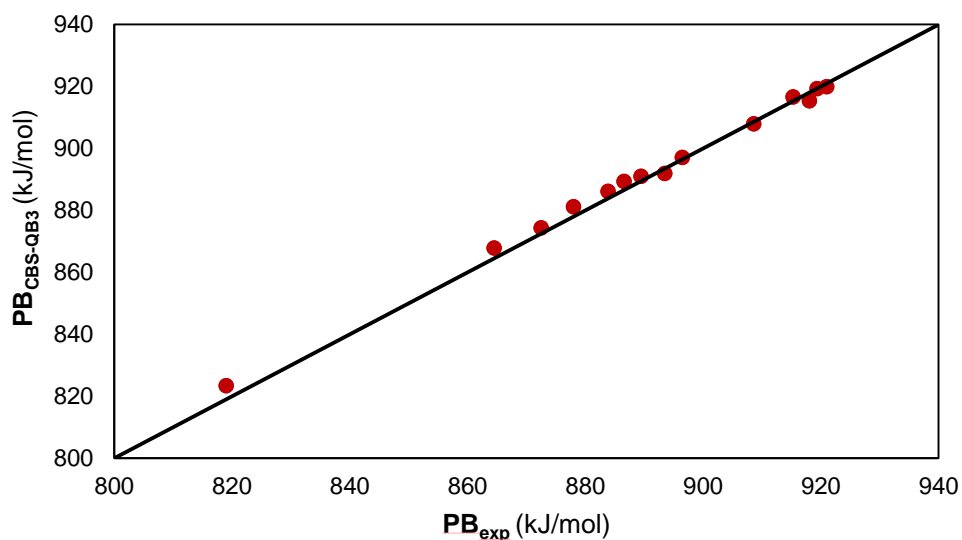


Figure A-3: comparison of the gas-phase experimental proton basicity (PB) by Hunter and Lias⁶ for the amines displayed in Figure A-1, compared to the gas-phase PB values calculated with the CBS-QB3 model chemistry, at 298.15 K and 1 atm.

A.2 TMB complexation geometry

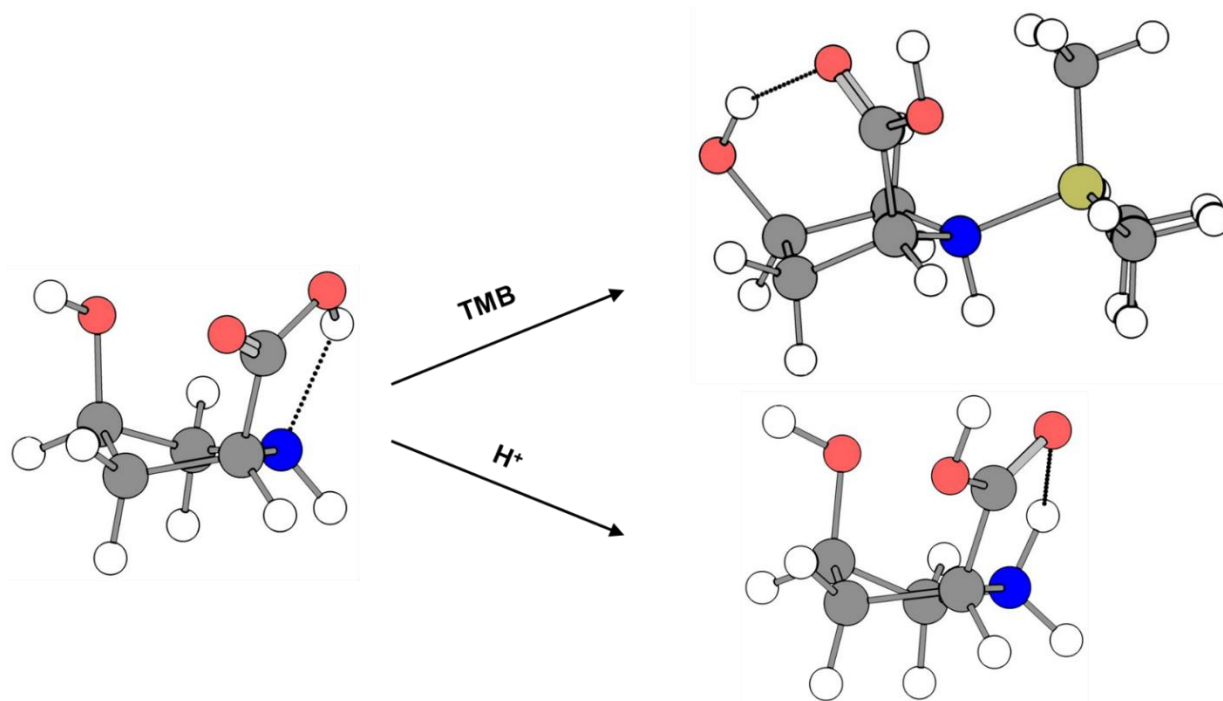


Figure A-4: 4R-4-hydroxy-D-proline complexation with trimethylborane (TMB) and protonation (H^+). The hydrogen-bond between the carboxylic acid and the amine is lost upon TMB complexation and a new hydrogen-bond between the hydroxyl group and the carboxylic acid is formed.

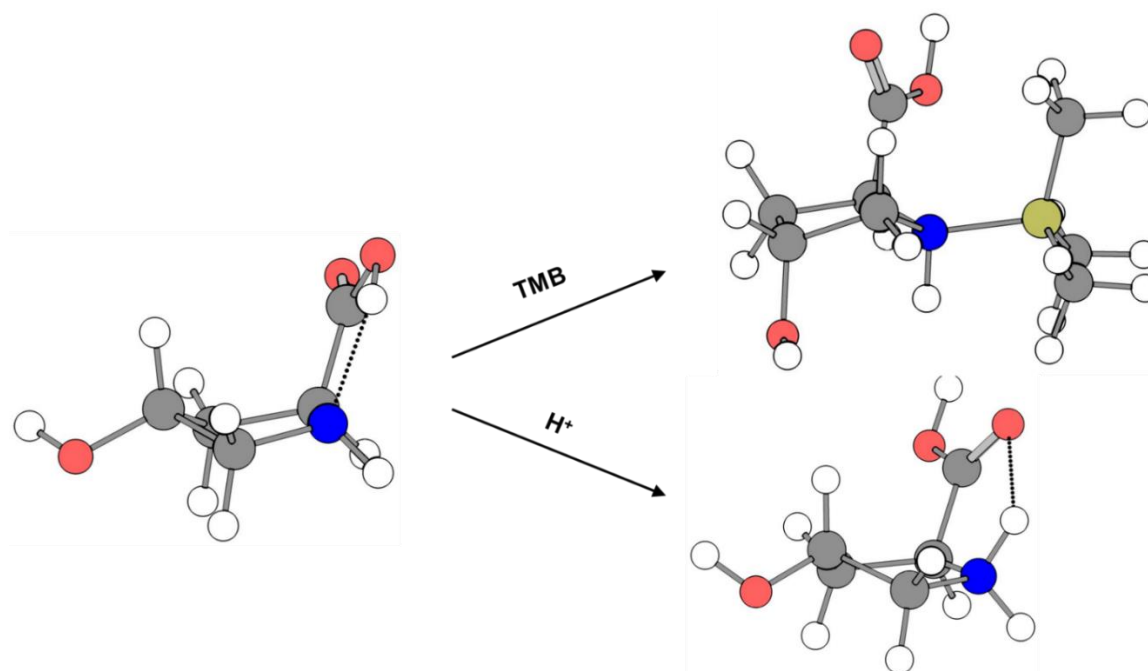


Figure A-5: 4S-4-hydroxy-L-proline complexation with trimethylborane (TMB) and protonation (H^+). The hydrogen-bond between the carboxylic acid and the amine is lost upon TMB complexation.

A.3 References

1. Brown, H. C.; Taylor, M. D.; Sujishi, S., Dissociation of the Addition Compounds of Trimethylboron with the Normal Primary Aliphatic Amines; the Straight-chain Anomaly. *Journal of the American Chemical Society* **1951**, *73* (6), 2464-2467.
2. Brown, H. C.; Gerstein, M., Acid-base studies in gaseous systems. VII. Dissociation of the addition compounds of trimethylboron and cyclic imines; I-strain. *Journal of the American Chemical Society* **1950**, *72* (7), 2926-2933.
3. Brown, H. C.; Taylor, M. D., Dissociation of the Addition Compounds of Trimethylboron with the Ethylamines; Configuration of the Ethylamines. *Journal of the American Chemical Society* **1947**, *69* (6), 1332-1336.
4. Brown, H. C., Studies in Stereochemistry. VII. The Effect of F-Strain on the Relative Base Strengths of Ammonia and the Ethylamines. *Journal of the American Chemical Society* **1945**, *67* (9), 1452-1455.
5. Brown, H. C., Studies in Stereochemistry. VI. The Effect of F-Strain on the Relative Base Strengths of Ammonia and the Methylamines. *Journal of the American Chemical Society* **1945**, *67* (3), 378-380.
6. Hunter, E. P.; Lias, S. G., Evaluated gas phase basicities and proton affinities of molecules: an update. *Journal of Physical and Chemical Reference Data* **1998**, *27* (3), 413-656.

Appendix B

B.1 Additional characterization figures and data

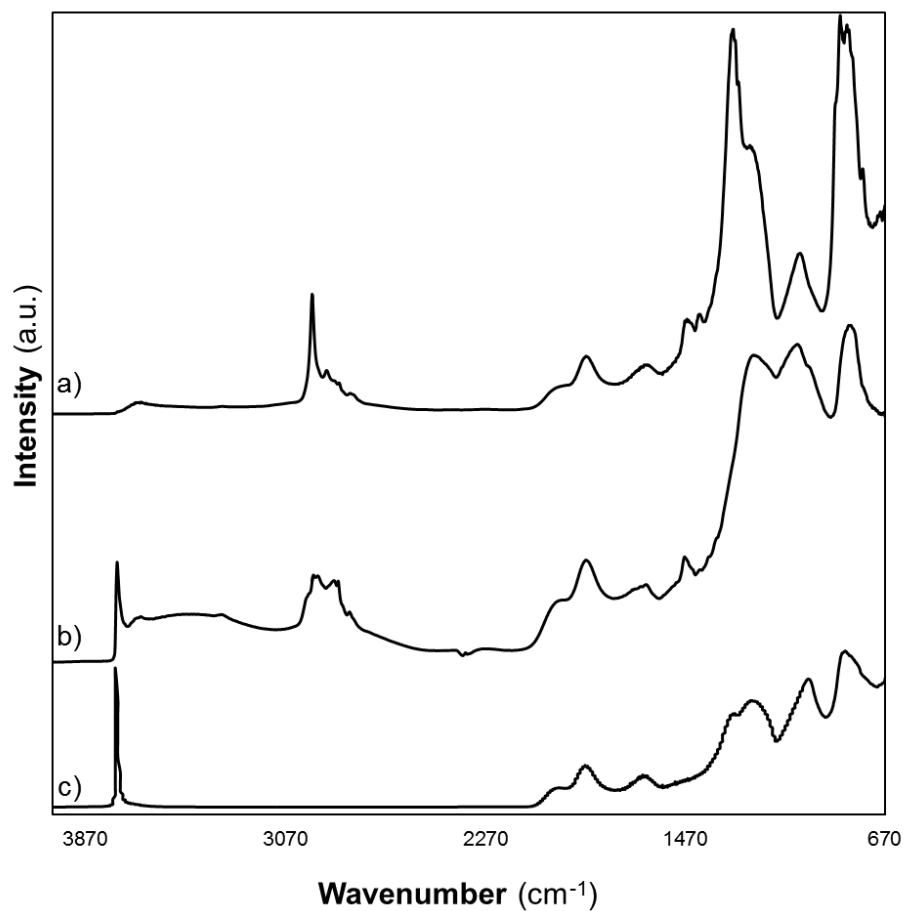


Figure B-1. DRIFT spectrum of the monofunctional base catalyst (a), acid-base cooperative catalyst (b) and the pristine silica gel support material (c).

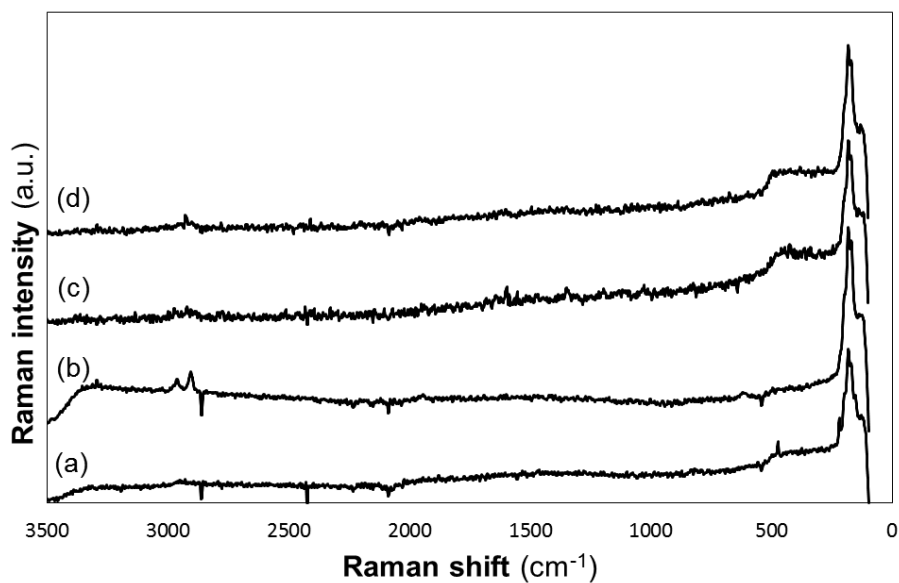


Figure B-2: Raman spectroscopy of (a) fresh cooperative acid-base catalyst, (b) fresh monofunctional base catalyst (trimethyl groups at 2900 cm^{-1} and 2960 cm^{-1}), (c) cooperative acid-base catalyst exposed to a mixture of 55 g DMSO and 45 g acetone, (d) cooperative acid-base catalyst exposed to 0.45 wt% 4-nitrobenzaldehyde dissolved in DMSO

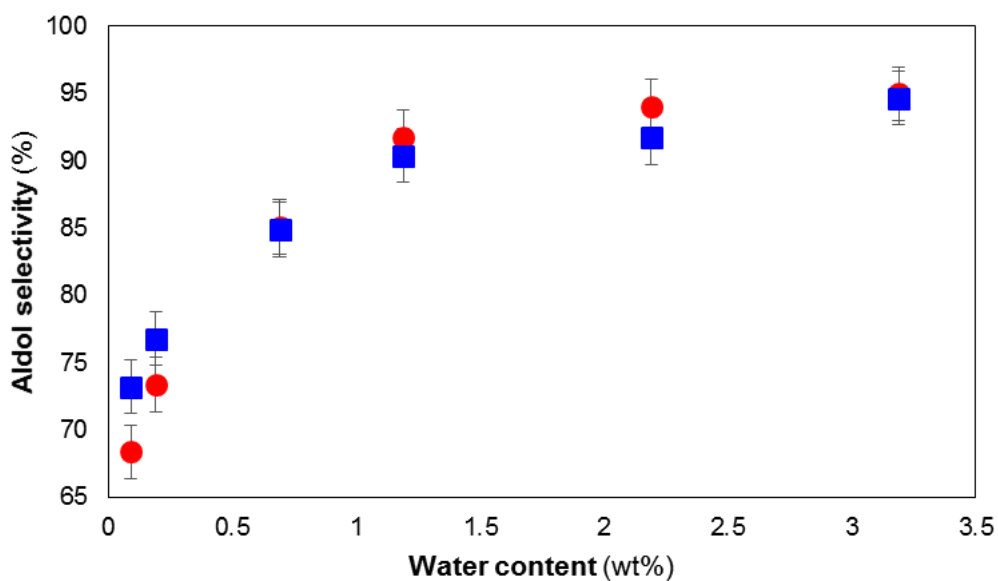


Figure B-3. Effect of water on the selectivity to the aldol product for the cooperative acid-base catalyst (●, red) and the monofunctional base catalyst (■, blue).

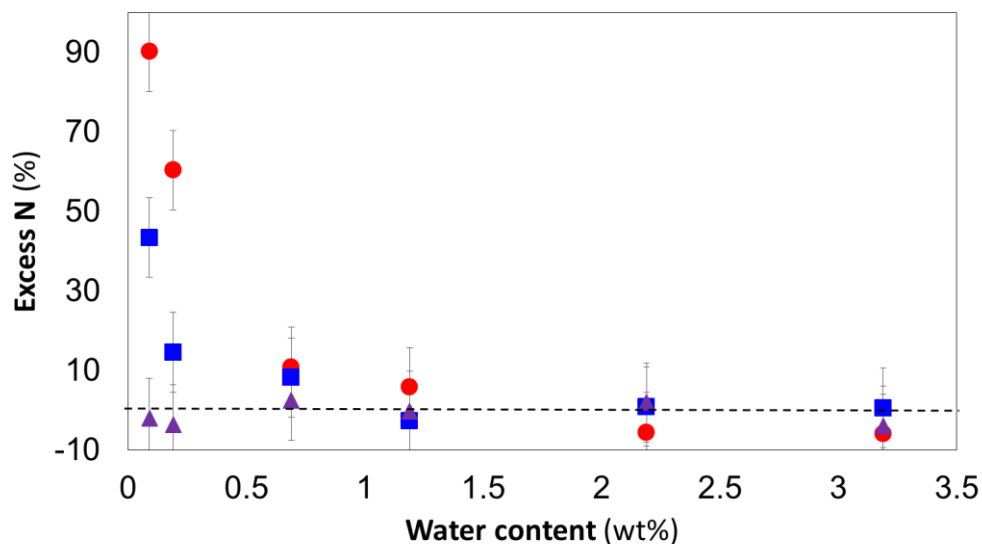


Figure B-4. CHNS elemental analysis of the spent cooperative acid-base catalyst (●, red) and the spent monofunctional base catalyst (■, blue), relative to the amount of amine sites on the catalyst, as a function of the water content in the reactor. CHNS results for the experiments performed with 4-chlorobenzaldehyde instead of 4-nitrobenzaldehyde (▲, purple).

Table B-1. Properties of the spent cooperative catalysts in the batch reactor

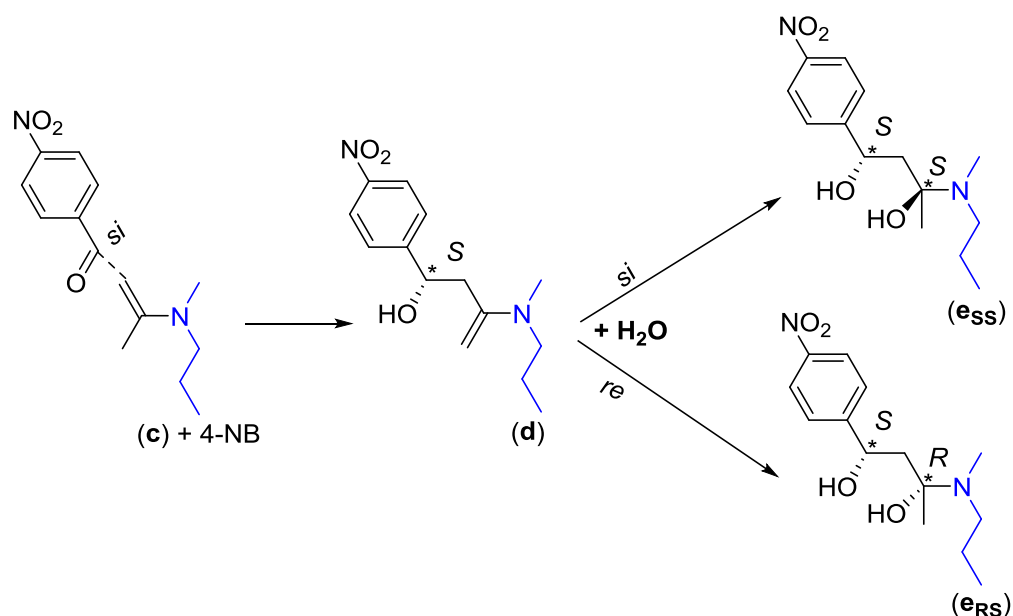
Water (wt%)	BET surface area ± 30 (m ² /g)	Pore size ±0.3 (nm)	Pore volume ±0.04 (cm ³ /g)
0.09	315	5.0	0.49
0.19	296	5.6	0.48
0.69	288	5.3	0.48
1.19	287	5.2	0.47
2.19	286	5.0	0.46
3.19	292	5.1	0.47

Table B-2. Properties of the spent monofunctional catalysts in the batch reactor

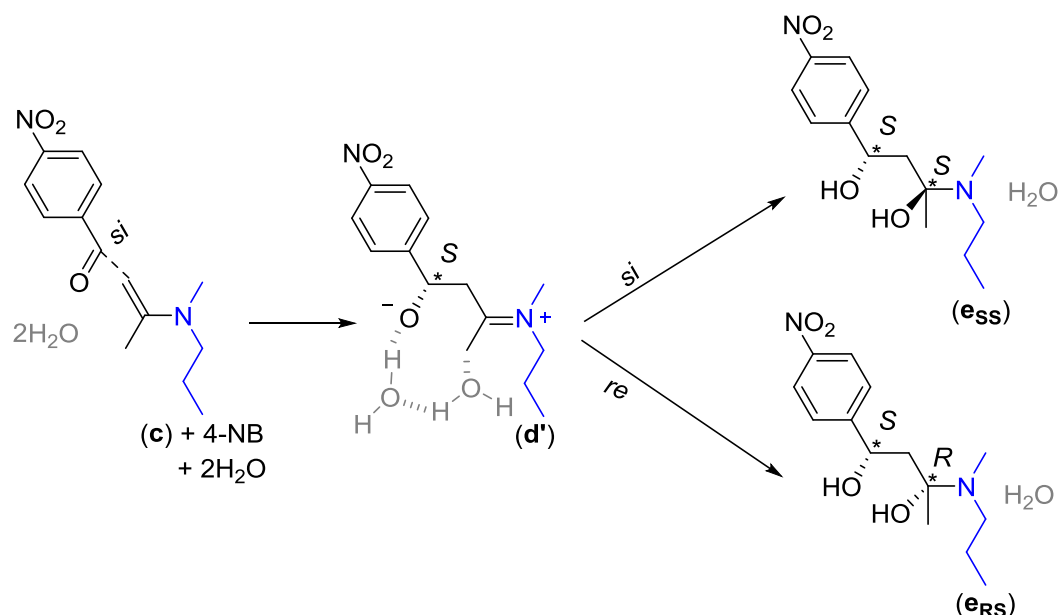
Water (wt%)	BET surface area ± 30 (m ² /g)	Pore size ±0.3 (nm)	Pore volume ±0.04 (cm ³ /g)
0.09	276	4.8	0.43
0.19	280	5.2	0.44
0.69	273	5.1	0.44
1.19	274	4.8	0.44
2.19	268	5.0	0.42
3.19	276	5.1	0.44

Appendix C

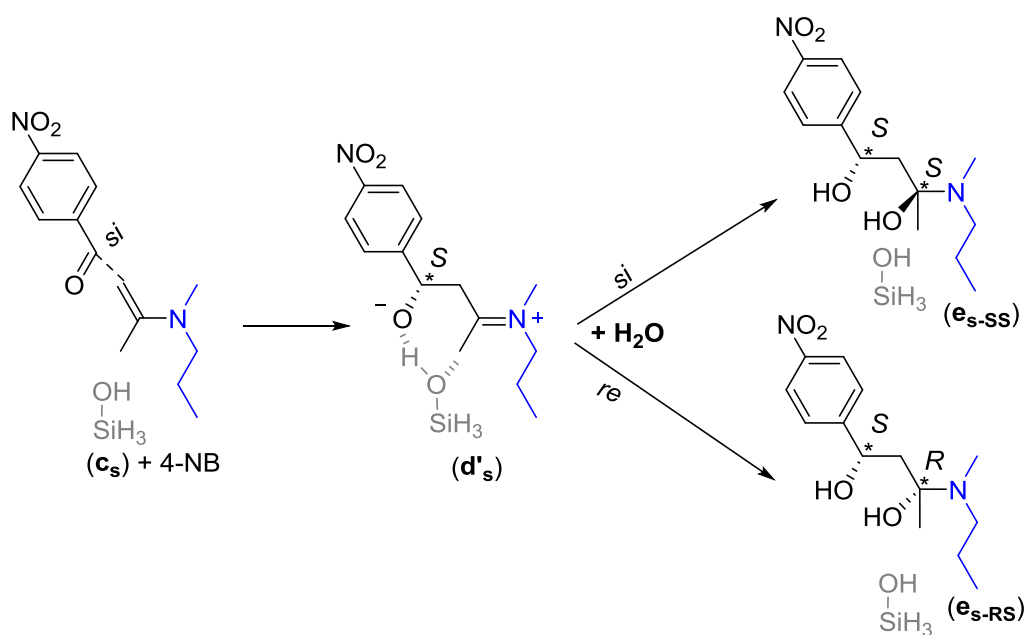
C.1 Reactions towards (S,S) diastereomer



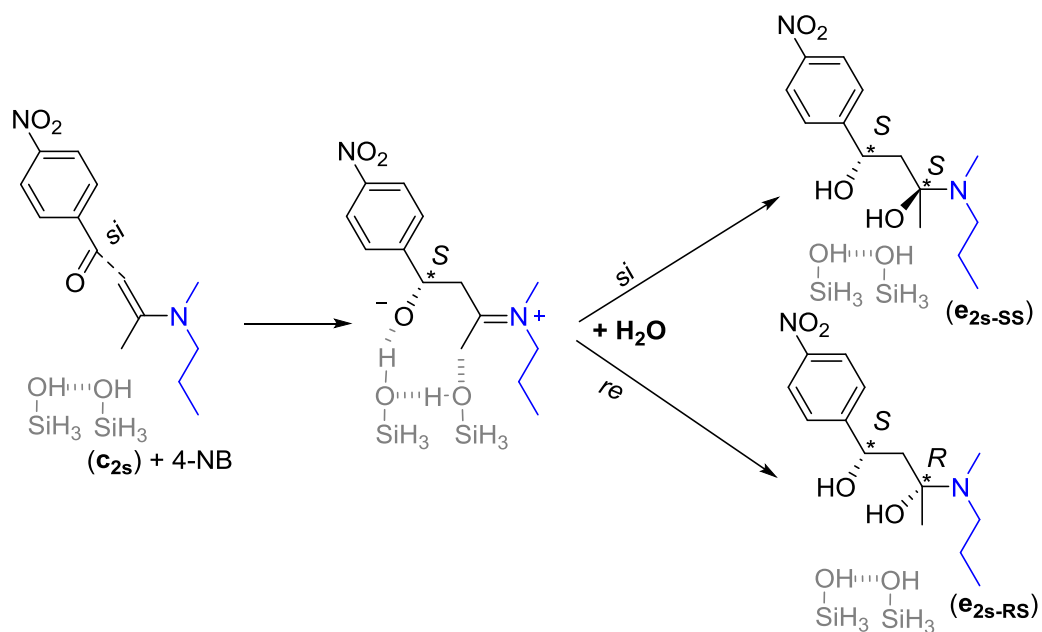
Scheme C-1: *si*-faced attack of 4-nitrobenzaldehyde on the enamine of acetone (c) leading to the enamine intermediate (d). Hydration of (d) occurs either *si*-faced, towards the *S,S*-diastereomer (e_{SS}) or *re*-faced towards the *R,S*-diastereomer (e_{RS})



Scheme C-2: *si*-faced attack of 4-nitrobenzaldehyde on the enamine of acetone (c), assisted by two water molecules, leading to iminium ion (d'). Hydration of (d'), with two water molecules, occurs either *si*-faced, towards the *S,S*-diastereomer (e_{SS}) or *re*-faced towards the *R,S*-diastereomer (e_{RS}) with the release of a water molecule



Scheme C-3: si-faced attack of 4-nitrobenzaldehyde on the enamine of acetone (*c*), assisted by one silanol group, leading to iminium ion (*d'*_s). Hydration of (*d'*_s), occurs either si-faced, towards the *S,S*-diastereomer (*e*_{ss}) or re-faced towards the *R,S*-diastereomer (*e*_{rs}).



Scheme C-4: si-faced attack of 4-nitrobenzaldehyde on the enamine of acetone (*c*), assisted by two silanol groups, leading to iminium ion (*d'*_{2s}). Hydration of (*d'*_{2s}), occurs either si-faced, towards the *S,S*-diastereomer (*e*_{ss}) or re-faced towards the *R,S*-diastereomer (*e*_{rs}).

The reaction barriers, and thermodynamic stability, of the pathway along the (R,S) diastereomer is reported in the manuscript. The same information for the pathway along the (S,S) diastereomer is reported in Table C-1 and Table C-2. Differences between both pathways are minor and do not lead to different conclusions regarding the promoting effect of water or silanol groups.

Table C-1: reaction barriers for the pathway along the (S,S) diastereomer

		50 vol% DMSO			50 vol% HEXANE		
		$\Delta^\ddagger H_{\text{liq}}^{328\text{K}}$ kJ mol ⁻¹	$\Delta^\ddagger S_{\text{liq}}^{328\text{K}}$ J K ⁻¹ mol ⁻¹	$\Delta^\ddagger G_{\text{liq}}^{328\text{K}}$ kJ mol ⁻¹	$\Delta^\ddagger H_{\text{liq}}^{328\text{K}}$ kJ mol ⁻¹	$\Delta^\ddagger S_{\text{liq}}^{328\text{K}}$ J K ⁻¹ mol ⁻¹	$\Delta^\ddagger G_{\text{liq}}^{328\text{K}}$ kJ mol ⁻¹
TS3							
Assisted by	H ₂ O	21.1	-214.7	91.5	8.2	-234.0	85.0
	2H ₂ O (2)	43.0	-5.0	44.7	38.7	-13.5	43.1
TS4							
	-	149.9	50.0	133.5	139.8	26.9	131.0
	H ₂ O	88.0	-11.8	91.8	67.4	-46.9	82.8
	2H ₂ O	74.0	-27.2	82.9	31.3	-108.2	66.8
	3H ₂ O	75.9	-82.6	103.1	27.7	-162.6	81.0
	H ₃ SiOH	49.5	53.3	32.0	33.8	9.0	30.8
	2H ₃ SiOH	-0.8	-40.7	12.5	-6.7	-26.8	2.1
hydr							
(d)	-	127.0	-105.4	161.6	126.0	-107.6	161.3
(d)	H ₂ O	71.9	-129.9	114.5	57.4	-149.3	106.4
(d _s ')	H ₃ SiOH	39.3	-39.5	52.3	19.9	-75.6	44.7
(d _s ')	2H ₃ SiOH	44.7	-39.6	57.7	25.9	-75.2	50.5

Table C-2: Thermodynamic stability of the intermediates in the reaction path along the (S,S) diastereomer

	50 vol% DMSO			50 vol% HEXANE		
	$\Delta_r H_{\text{liq}}^{328\text{K}}$ kJ mol ⁻¹	$\Delta_r S_{\text{liq}}^{328\text{K}}$ J K ⁻¹ mol ⁻¹	$\Delta_r G_{\text{liq}}^{328\text{K}}$ kJ mol ⁻¹	$\Delta_r H_{\text{liq}}^{328\text{K}}$ kJ mol ⁻¹	$\Delta_r S_{\text{liq}}^{328\text{K}}$ J K ⁻¹ mol ⁻¹	$\Delta_r G_{\text{liq}}^{328\text{K}}$ kJ mol ⁻¹
d + H₂O → e(SS)	-44.7	-116.1	-6.6	-48.1	-116.2	-10.0
d' → e(SS) + H₂O	-78.0	-35.3	-66.4	-62.1	-8.3	-59.3
d_s' + H₂O → e_s(SS)	-43.2	-98.6	-10.8	-49.9	-96.3	-18.3
d_{2s}' + H₂O → e_{2s}(SS)	-2.3	0.5	-2.5	-20.6	-53.5	-3.1
e(SS) → a + aldol	57.8	257.0	-26.5	49.4	236.8	-28.3
e_s(SS) → a_s + aldol	33.9	253.7	-49.3	26.5	234.0	-50.3
e_{2s}(SS) → a_{2s} + aldol	30.5	176.1	-27.3	31.8	210.7	-37.3

C.2 Transition states TS1 and TS2 with zero, one or two assisting water molecules

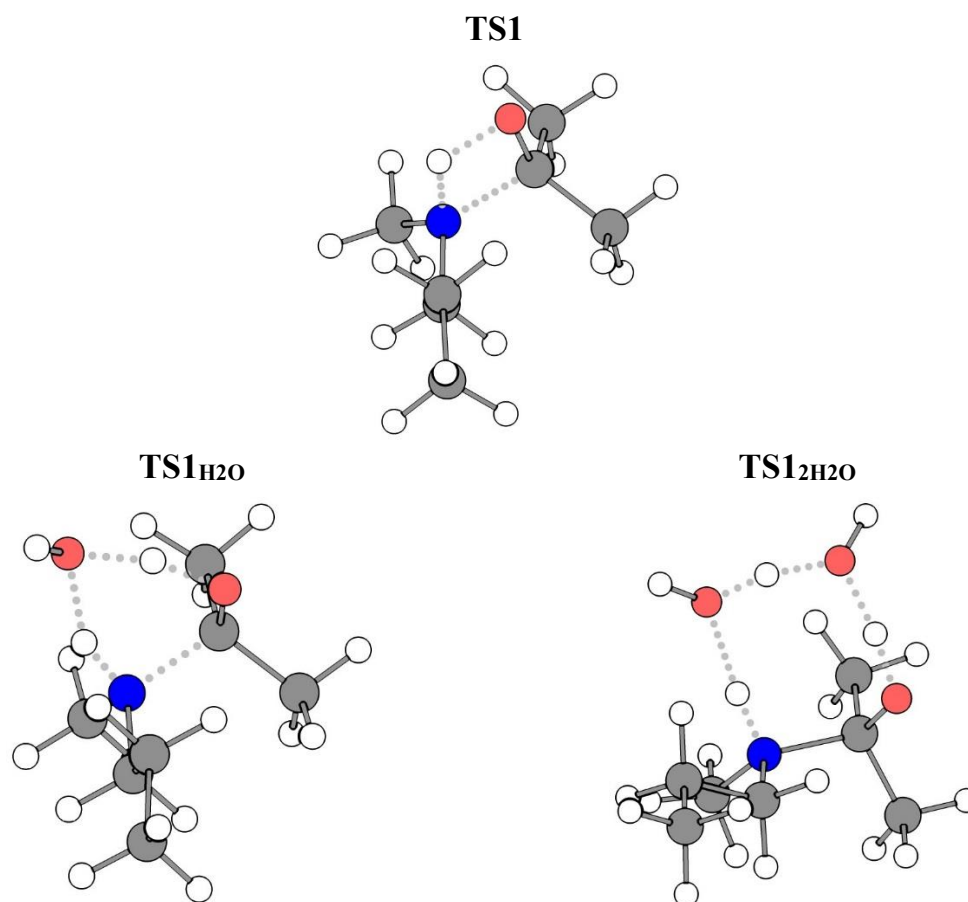


Figure C-1: Transition state for the addition of acetone with N-methylpropylamine with respectively zero (TS1), one (TS1_{H2O}) or two (TS1_{2H2O}) assisting water molecules.

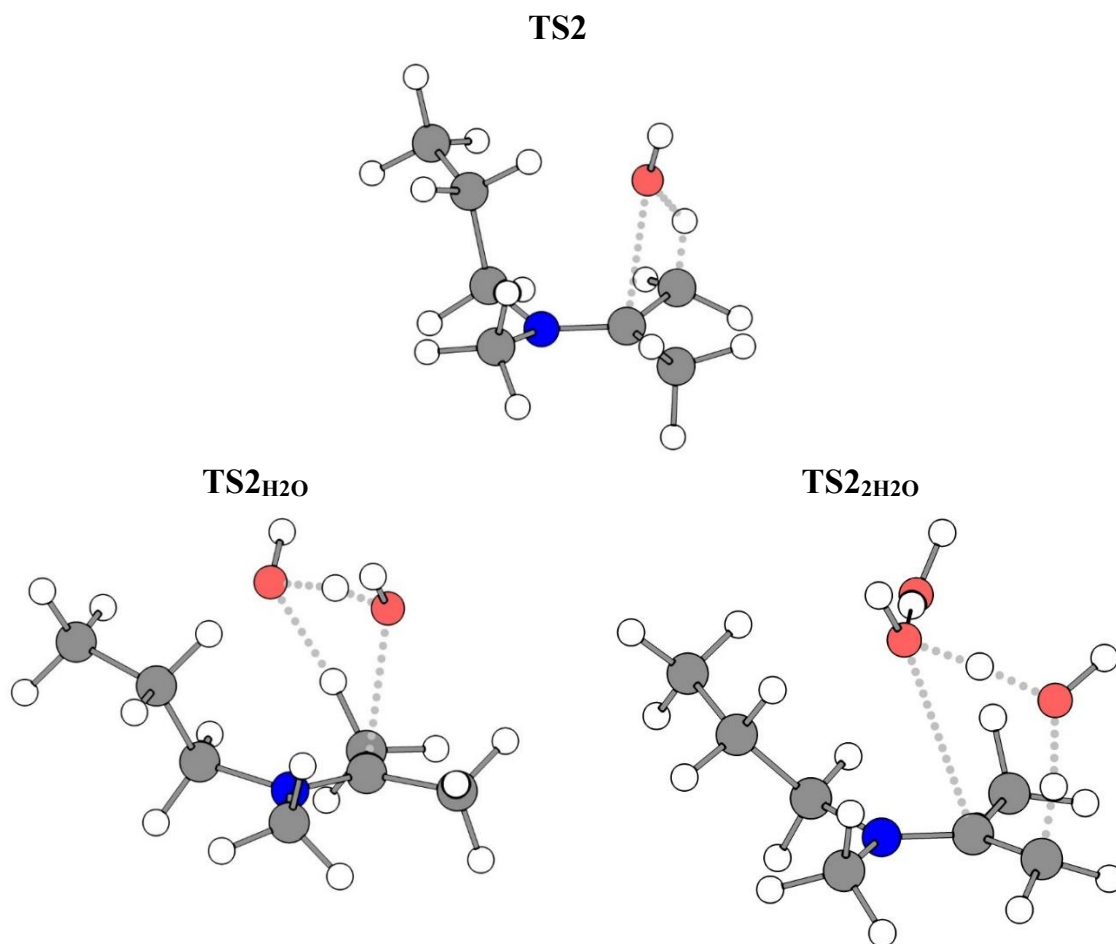


Figure C-2: Transition state for the carbinolamine dehydration towards the enamine with respectively zero (TS2), one (TS_{2H2O}) or two (TS_{2_{2H2O}}) assisting water molecules.

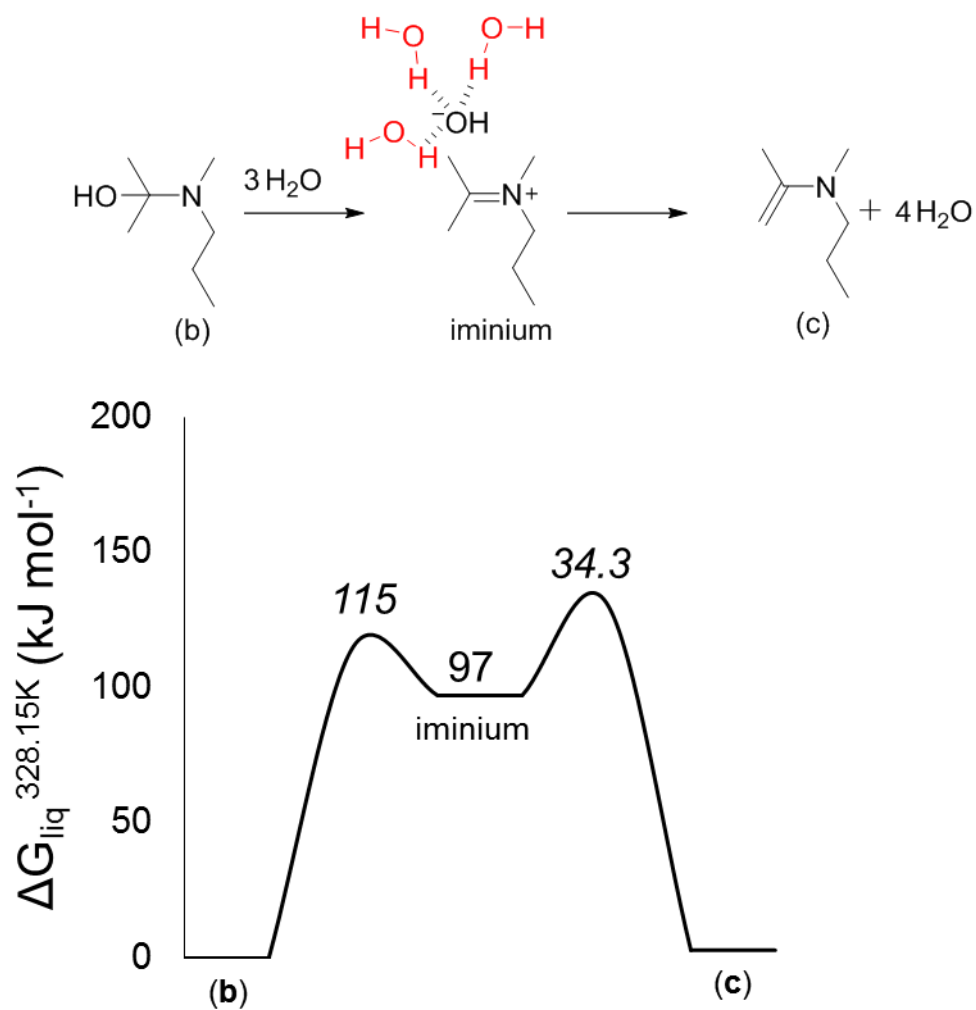


Figure C-3: carbinolamine dehydration, assisted by three water molecules, passing through the unstable iminium intermediate. Values are ΔG_{liq} in kJ mol^{-1} , relative to the previous stable state. Composite barrier is $131.3 \text{ kJ mol}^{-1}$.

C.3 Reaction coordinate scan in gas phase and DMSO

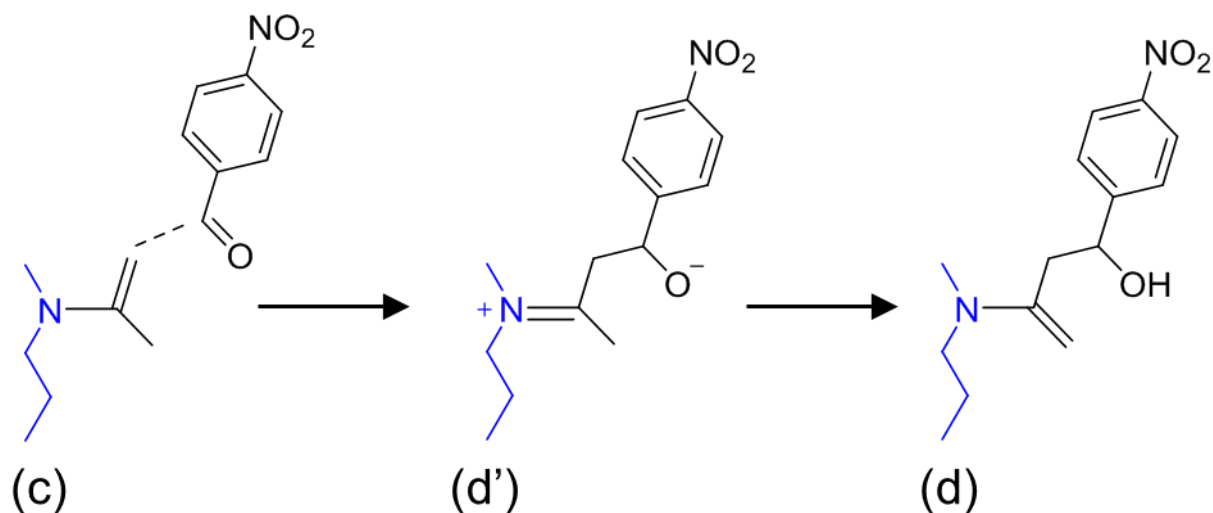


Figure C-4: reaction of 4-nitrobenzaldehyde with the enamine intermediate (c) (TS3) towards the aldol product enamine (d), passing through the iminium intermediate (d').

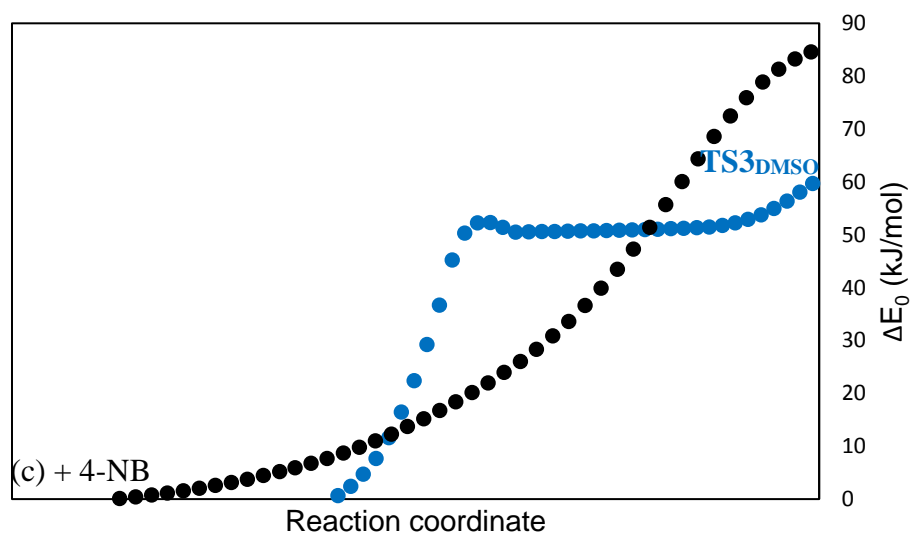


Figure C-5: Bond scan of 4-nitrobenzaldehyde reaction with enamine (Figure 3S), in vacuum (black) and in DMSO (blue). Vacuum calculations are performed with B3LYP/CBSB7, solvent phase calculations have been performed on the same level of theory and an SMD Polarizable Continuum Model of DMSO ($\epsilon = 46.826$). The electronic energy is calculated relative to the separated reactants.

C.4 Comparison of minimal cluster model with periodic silica surface model

Validation of the geometric positioning of the silanol groups relative to each other and the amine function in the minimal cluster model is performed using VASP 5.4.4 with two different periodic surface slabs of silica. While the mesoporous silica catalysts are amorphous in nature, periodic surface models have often been used to simulate the local environment of an amorphous silica¹⁻⁴. The first model is based on the (111) surface of β -cristobalite and is representative for patches of isolated silanols found on amorphous silica⁵. The second model is the (100) surface of α -quartz, representing the patches of vicinal silanols on amorphous silica⁴. Geminal silanols are not modeled due to their relatively lower occurrence on the experimentally investigated material⁶. Both models are 4-layer slabs, where the bottom two layers are fixed and the upper two layers are allowed to relax during geometry optimization. All VASP surface calculations are performed using the revised Perdew–Burke–Ernzerhof (RPBE) exchange–correlation functional. Dispersion corrections were implemented with the Grimme D3 method using Becke-Johnson damping. A plane wave basis set and the projector-augmented wave (PAW) method with a cut-off energy of 600 eV was used. No electron smearing was used. Geometries were optimized until the maximum force on the relaxed atoms was less than 0.05 eV Å⁻¹. All energies were sampled at gamma point.

C.4.1 Isolated silanols

The N-methylpropylaminemethoxysilane (MAPTMS) group is attached with one linker to the β -cristobalite surface, as is expected when grafting on isolated silanols. This renders the methylaminopropane group very flexible and thereby allows the functional group to assume a geometric positioning relative to the surface silanols that is remarkably similar to the minimal cluster employed.

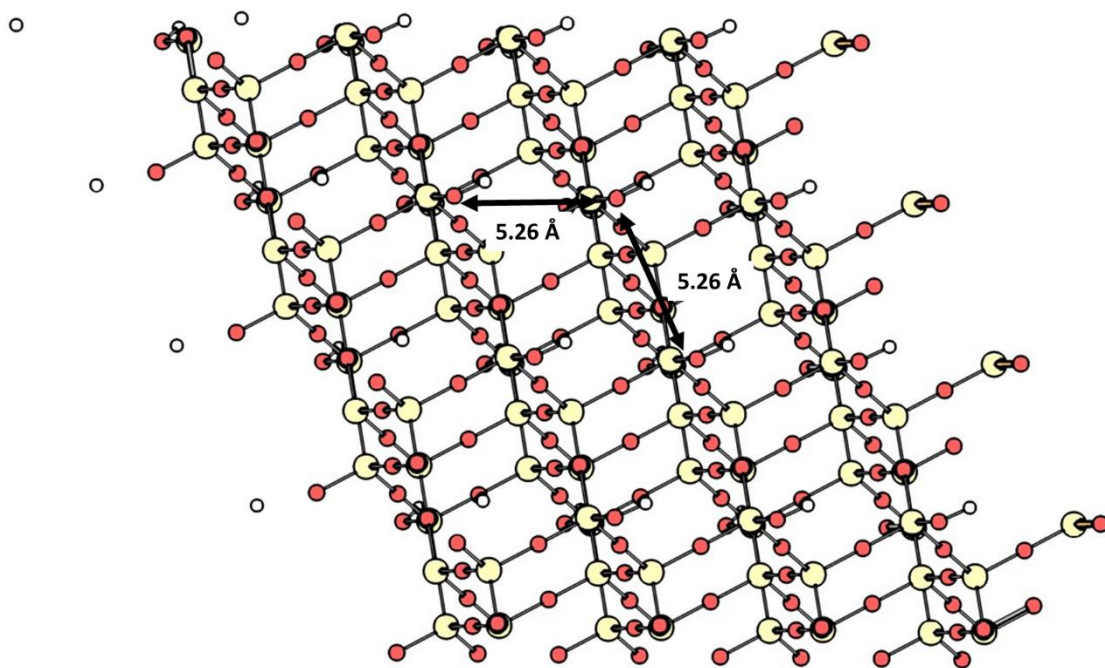


Figure C-6: Top view of the (111) β -cristobalite surface with isolated silanols 5.26 Å apart.

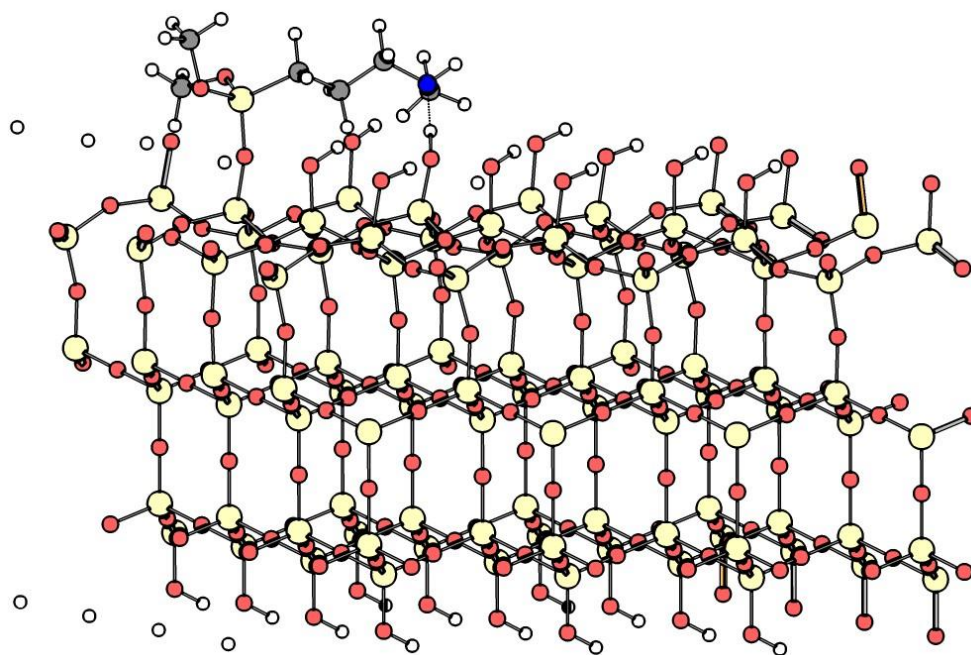
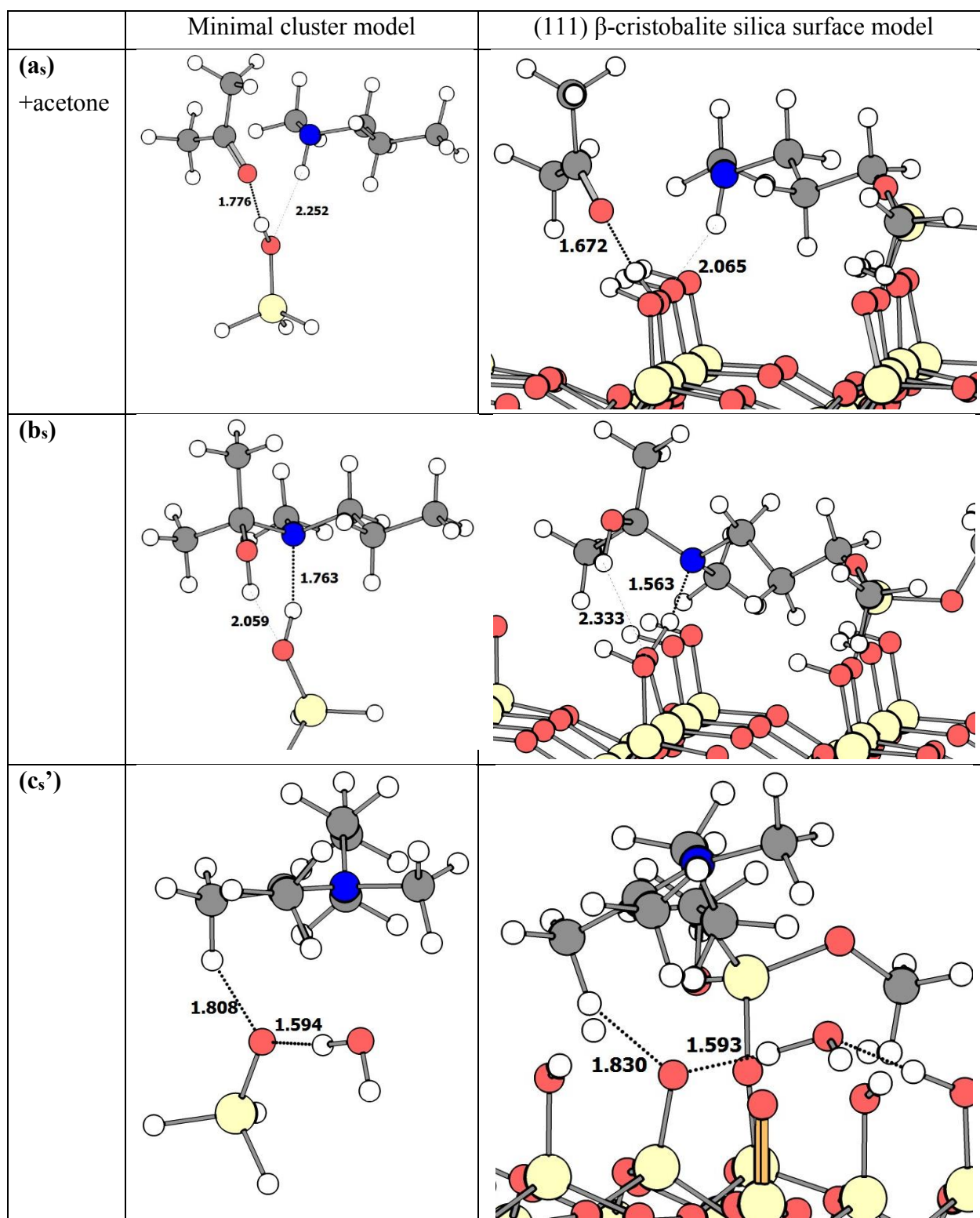
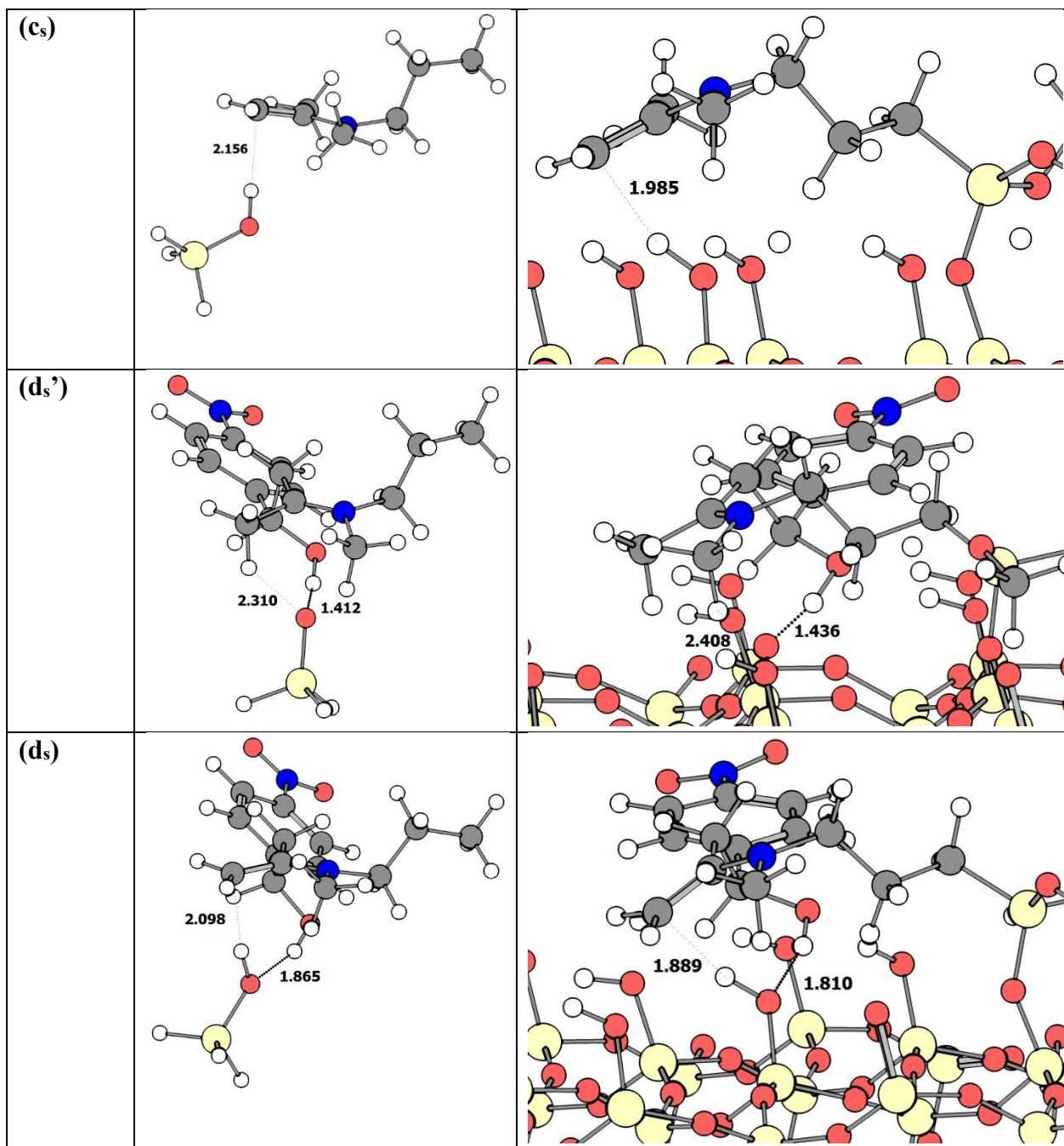
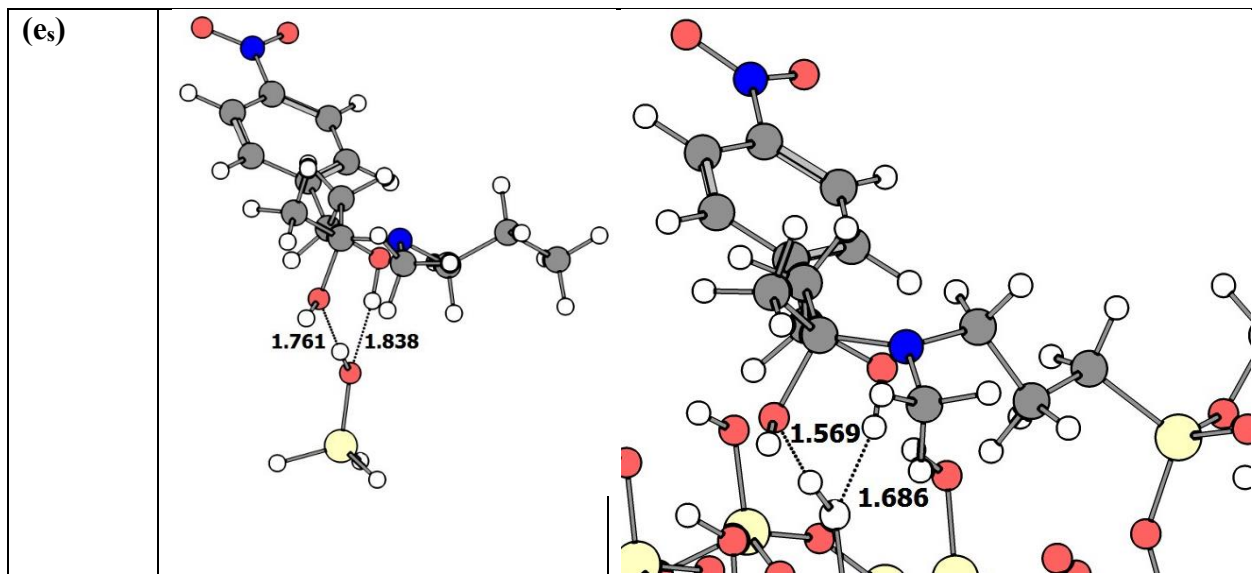


Figure C-7: grafted N-methylpropylaminemethoxysilane on the (111) β -cristobalite surface with isolated silanols. Connected with one linker.







C.4.2 Vicinal silanols

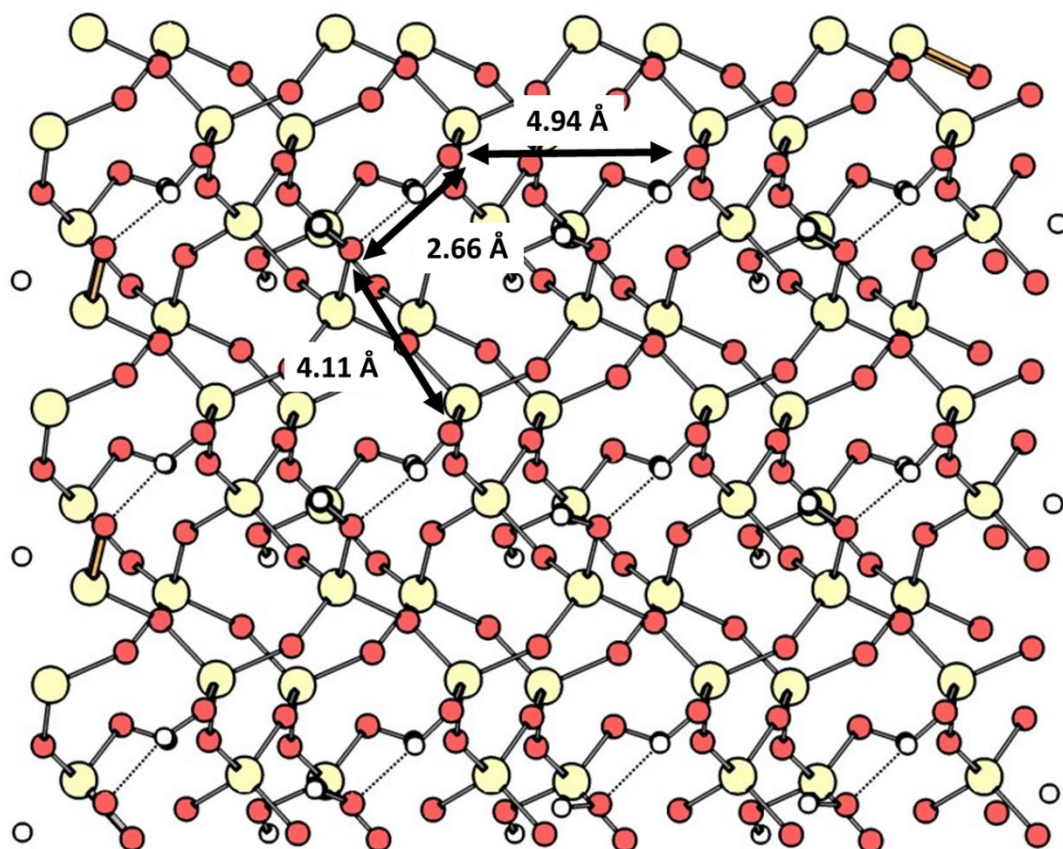


Figure C-8: The (100) α -quartz surface with vicinal silanols (2.66 Å apart from each other)

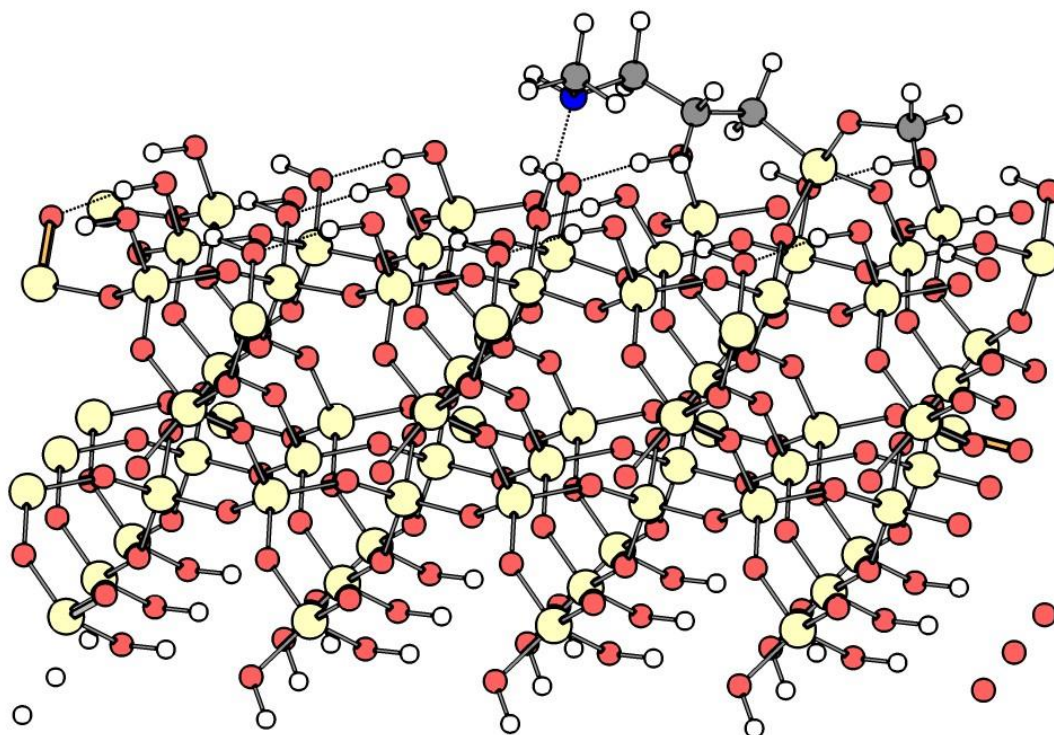
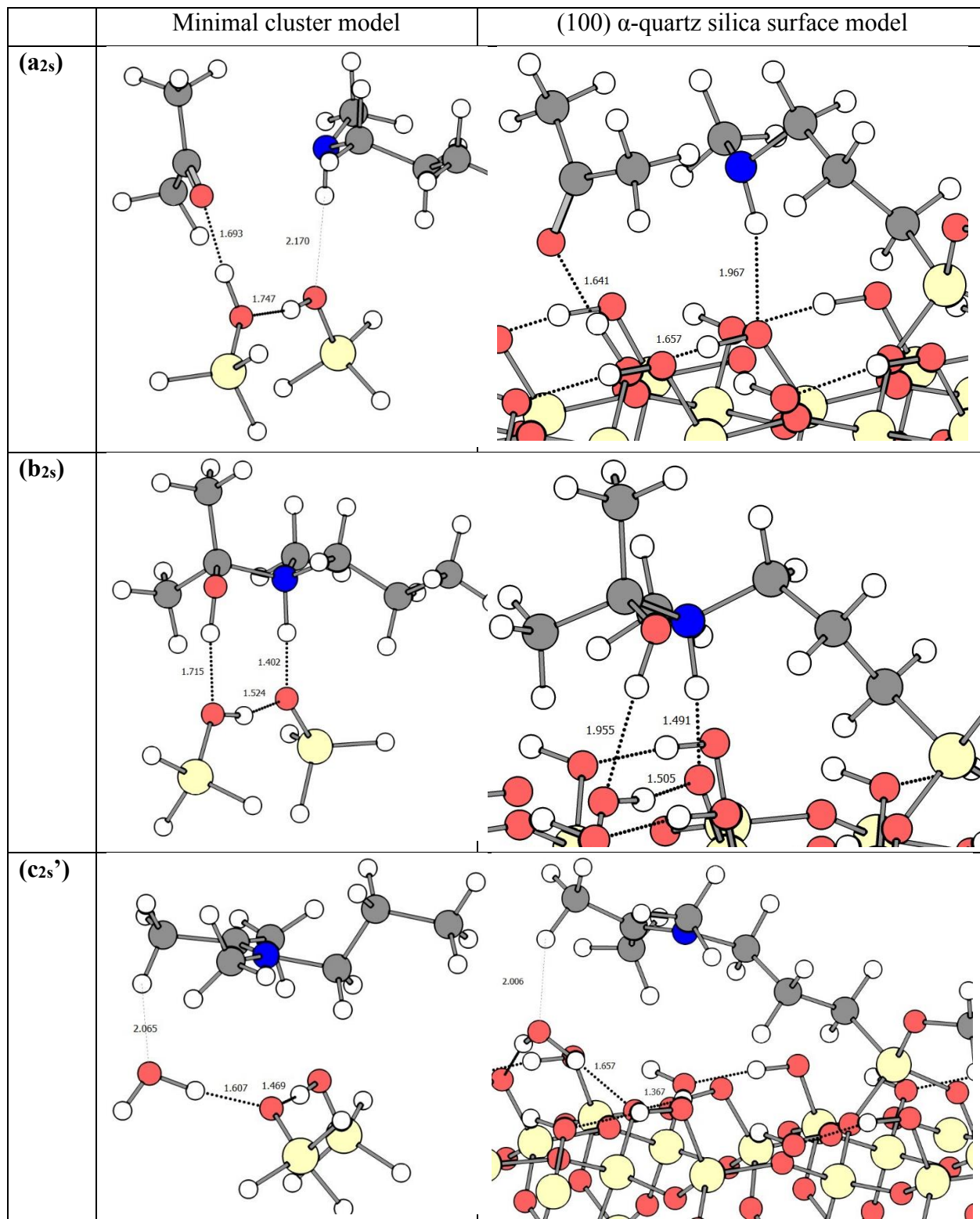
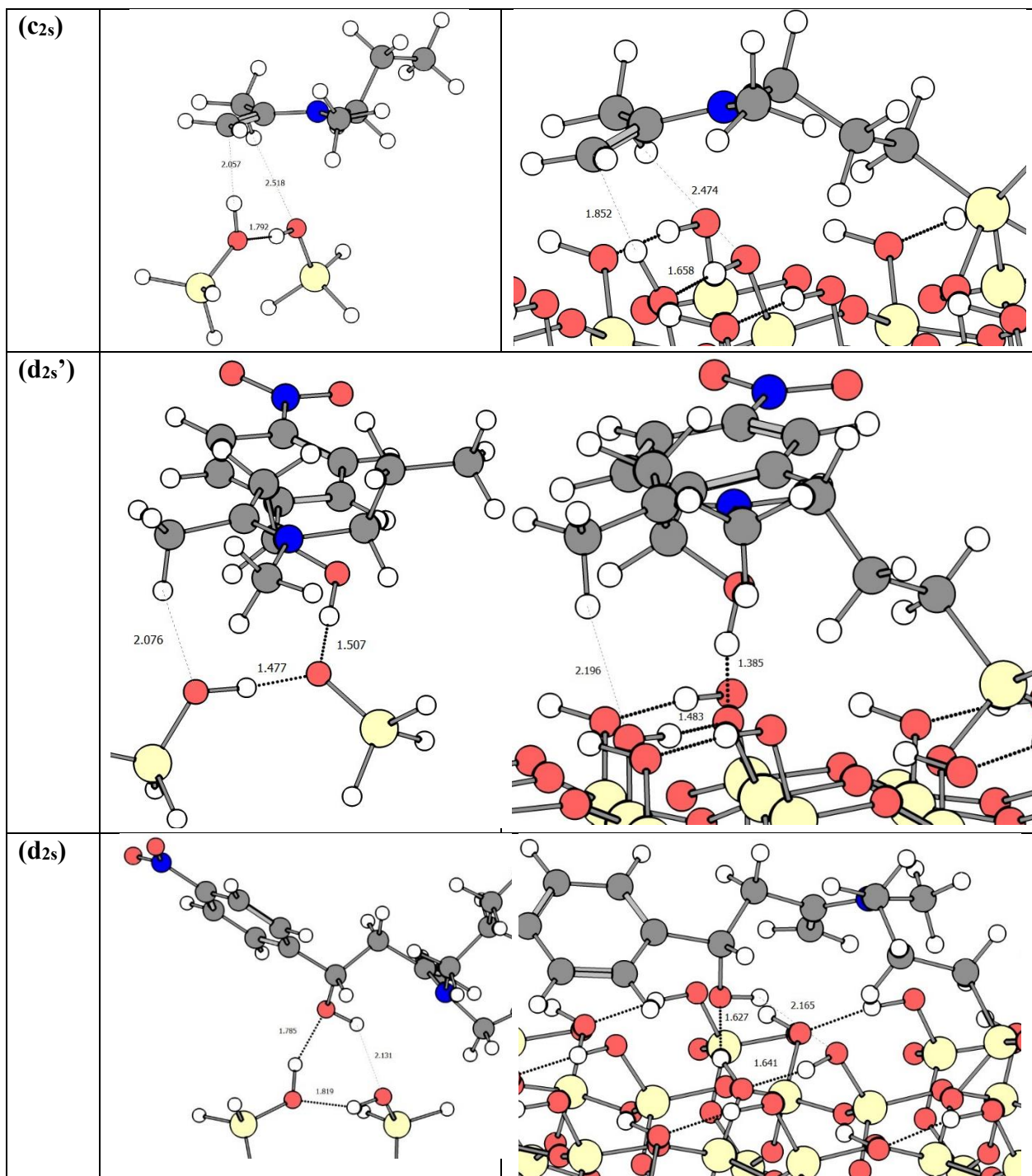


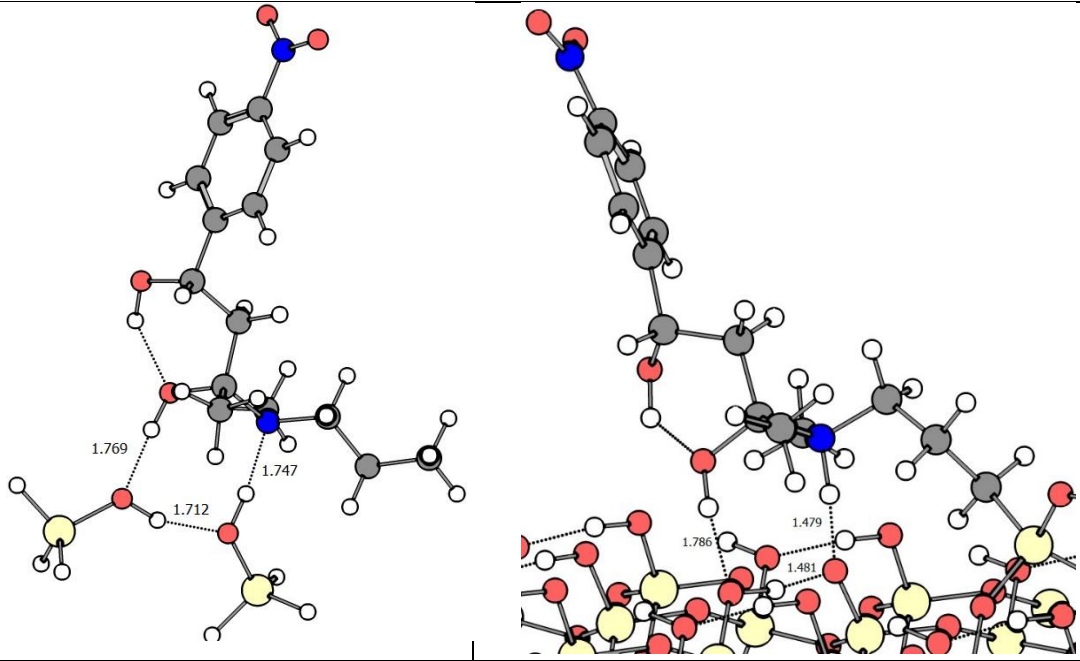
Figure C-9: N-methylpropylaminemethoxysilane grafted on the (100) α -quartz surface with vicinal silanols, connected with two linkers.

The N-methylpropylaminemethoxysilane (MAPTMS) group is attached with two linkers to the α -quartz surface, as was determined previously by Cho et al.⁷ for amine functionalized α -quartz. While two linkers restrict the movement of the amine group more than one linker, still the optimal silanol configurations found in the minimal cluster model are found. A minor difference is found for the position of the proton between the silanol group and the amine group in the product carbinolamine (**e_{2s}**). On the surface model, this proton is closer to the amine, rendering this product carbinolamine a zwitterionic intermediate, such as is the case for the carbinolamine of acetone (**b_{2s}**).

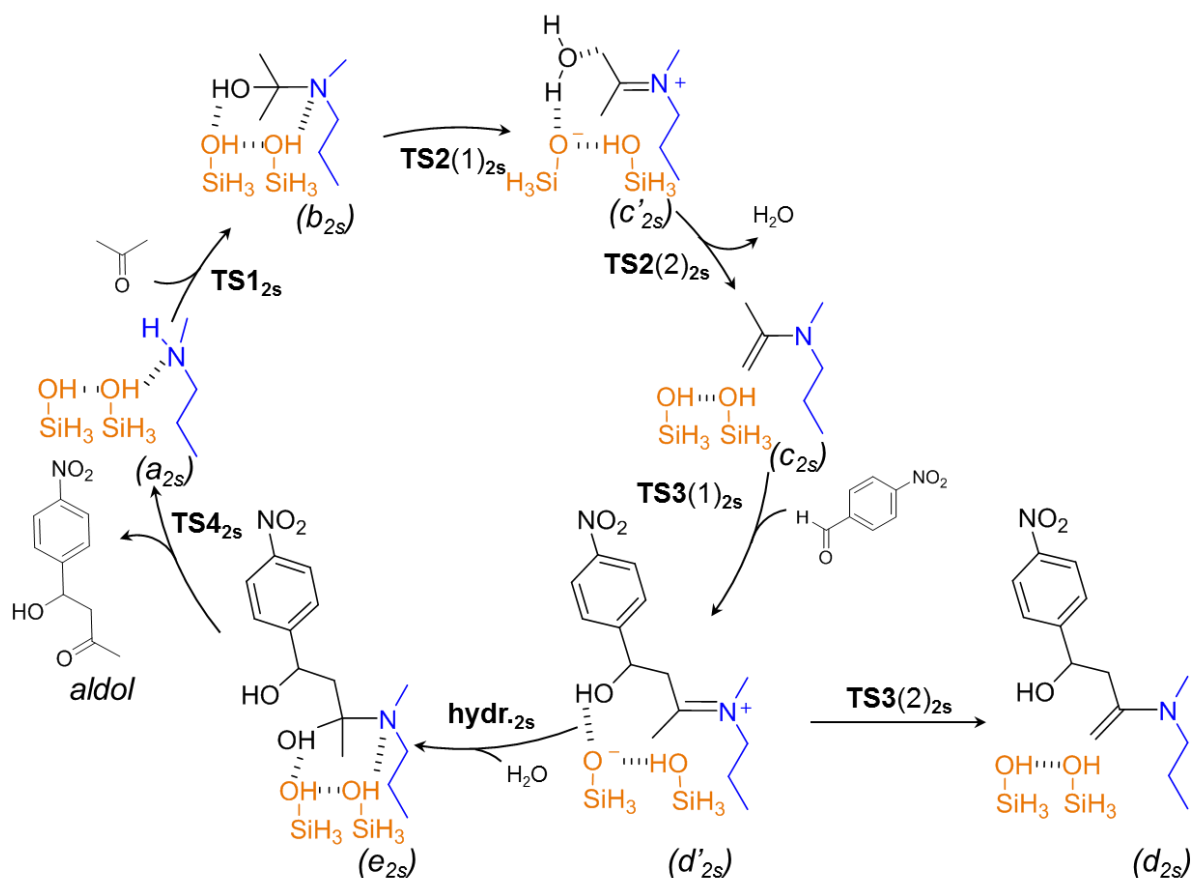




(e_{2s})



C.5 Mechanism of the aldol reaction promoted by two vicinal silanol groups



Scheme C-2: Reaction mechanism of the aldol reaction of acetone with 4-nitrobenzaldehyde catalyzed by N-methylpropylamine, promoted by two vicinal silanol groups

C.6 Activity coefficients in kinetic rate coefficients

The Gibbs free energy in gas phase is expressed as:

$$G = G^{\circ}_{\text{gas}} + RT \ln \frac{p}{p^{\circ}} \quad (\text{D.1})$$

where G°_{gas} is the standard Gibbs free energy in the gas phase, referenced to a standard state of 1 atm, R is the gas constant ($8.314 \text{ J mol}^{-1} \text{ K}^{-1}$), T the temperature and p the pressure (in atm), p° is the reference pressure (1 atm).

Using the law of Henry for infinitely diluted solutions:

$$H c = p \quad (\text{D.2})$$

where c is the concentration (in mol L^{-1}) and H is the Henry coefficient (in L atm mol^{-1}). We come to the following expression (putting c° in nominator and denominator):

$$G = G^{\circ}_{\text{gas}} + RT \ln \frac{H c c^{\circ}}{p^{\circ} c^{\circ}} \quad (\text{D.3})$$

Which we can write as a function of c , in order to go to the Gibbs free energy in solution:

$$G = G^{\circ}_{\text{gas}} + RT \ln H \frac{c^{\circ}}{p^{\circ}} + RT \ln \frac{c}{c^{\circ}} \quad (\text{D.4})$$

which means that we get an expression of the solution Gibbs free energy as follows:

$$G^{\circ}_{\text{sol}} = G^{\circ}_{\text{gas}} + RT \ln \frac{H c^{\circ}}{p^{\circ}} \quad (\text{D.5})$$

The difference between G°_{sol} and G°_{gas} is ΔG_{solv} .

Thus:

$$\Delta G^{\circ}_{\text{solv},i} = RT \ln \frac{H_i c^{\circ}}{p^{\circ}} \quad (\text{D.6})$$

This is the Gibbs-free energy change for one species i going from gas to liquid in an infinite dilution. The value for the Henry coefficient H_i is obtained from a COSMO-RS calculation. Care should be taken that the correct units for H_i are selected, or the appropriate corrections are performed.

Moreover, Gaussian computes the thermochemistry for an ideal gas, where the standard state is a pressure of 1 atm (symbol $^{\circ}$). Because the solvation free energies are computed for a 1 mol/L standard state (symbol *), the Gibbs free energy must be corrected accordingly⁸:

$$\Delta G^* = \Delta G^{\circ} + \Delta G^{\circ \rightarrow *}$$

$$\Delta G^{\circ \rightarrow *} = RT \ln \left(\frac{V^*}{V^{\circ}} \right)$$

With V the volume of 1 mol of gas in the reference state.

C.7 References

1. Kim, K. C.; Moschetta, E. G.; Jones, C. W.; Jang, S. S., Molecular Dynamics Simulations of Aldol Condensation Catalyzed by Alkylamine-Functionalized Crystalline Silica Surfaces. *Journal of the American Chemical Society* **2016**, *138* (24), 7664-7672.
2. de Lima Batista, A. P.; Zahariev, F.; Slowing, I. I.; Braga, A. A. C.; Ornellas, F. R.; Gordon, M. S., Silanol-Assisted Carbinolamine Formation in an Amine-Functionalized Mesoporous Silica Surface: Theoretical Investigation by Fragmentation Methods. *The Journal of Physical Chemistry B* **2016**, *120* (8), 1660-1669.
3. Nedd, S.; Kobayashi, T.; Tsai, C.-H.; Slowing, I. I.; Pruski, M.; Gordon, M. S., Using a reactive force field to correlate mobilities obtained from solid-state ^{13}C NMR on mesoporous silica nanoparticle systems. *The Journal of Physical Chemistry C* **2011**, *115* (33), 16333-16339.
4. Cho, M.; Park, J.; Yavuz, C. T.; Jung, Y., A catalytic role of surface silanol groups in CO_2 capture on the amine-anchored silica support. *J Physical Chemistry Chemical Physics* **2018**, *20* (17), 12149-12156.
5. Ceresoli, D.; Bernasconi, M.; Iarlori, S.; Parrinello, M.; Tosatti, E., Two-membered silicon rings on the dehydroxylated surface of silica. *Physical review letters* **2000**, *84* (17), 3887.
6. Der Voort, P. V.; Vansant, E., Silylation of the silica surface a review. *Journal of liquid chromatography & related technologies* **1996**, *19* (17-18), 2723-2752.
7. Cho, M.; Park, J.; Yavuz, C. T.; Jung, Y. J. P. C. C. P., A catalytic role of surface silanol groups in CO_2 capture on the amine-anchored silica support. **2018**, *20* (17), 12149-12156.
8. Jensen, J. H., Predicting accurate absolute binding energies in aqueous solution: thermodynamic considerations for electronic structure methods. *Physical Chemistry Chemical Physics* **2015**, *17* (19), 12441-12451.

Appendix D

Intrinsic kinetics assessment (LS)² reactor

Reactions on heterogeneous catalysts consist of multiple sequential steps¹, as displayed in Figure D-1. These steps include mass transfer of the reactant(s) from the bulk phase to the catalyst (1), mass transfer of the reactant(s) inside the pellet (2), adsorption of the reactant on the active sites (3), reaction on these active sites (4), desorption of the product(s) (5), mass transfer of the products out of the pellet (6) and towards the bulk phase (7).

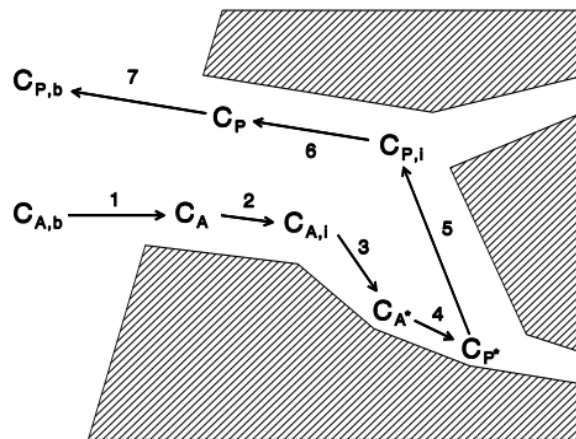


Figure D-1: Transport and reaction of reactant (A) and product (P) species inside the pores of a heterogeneous catalyst¹.

Experimentally, only bulk properties can be measured. To adequately assess catalyst performance based on the measured experimental data, it is thus important to operate the reactor in the intrinsic kinetics regime², i.e. the regime where the kinetics describe the chemical behavior of the system, unaffected by heat or mass transfer limitations.

D.1 Theoretical background

Transfer limitations generally appear when the rate of mass, or heat, transfer from the bulk phase towards the catalyst active sites, or vice versa, is on a similar timescale as the rate of reaction on the active sites. These heat and mass transfer limitations can occur at two levels: externally in the film around the catalyst pellet, and internally inside the pores of the pellet. In

bench scale reactors, due to the small pellet diameters, usually internal concentration gradients and internal heat transfer limitations are relatively unimportant compared to external heat and external concentration gradients².

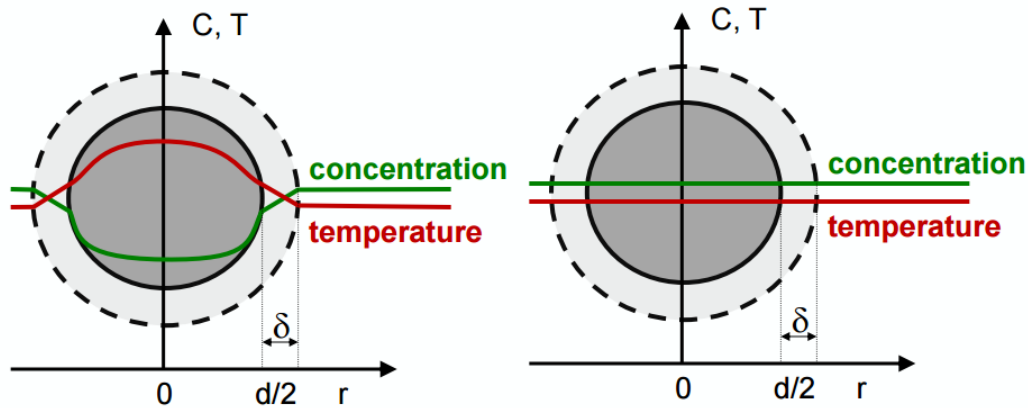


Figure D-2: Left: concentration and temperature gradients in a catalyst pellet with an exothermic reaction. Right: gradientless pellet required for intrinsic kinetic measurements².

The goal of this paragraph is to discuss the reaction conditions under which the gradients of Figure D-2 (left) do not appear. When this is achieved, the concentration and temperature inside the pellets is equal to the bulk conditions, as in Figure D-2 (right), and the observed reaction rate is equal to the intrinsic reaction rate. For the following paragraph, a deviation of maximum 5 % is allowed in the rate (D-1) and in the concentration gradient (D-2).

$$\frac{R_{\text{obs}} - R_{\text{intr}}}{R_{\text{intr}}} < 0.05 \quad (\text{D-1})$$

$$\frac{C_{A,\text{bulk}} - C_{A,\text{surface}}}{C_{A,\text{bulk}}} < 0.05 \quad (\text{D-2})$$

D.1.1 Plug flow criterion and maximal bed dilution

Two criteria should be met to achieve plug flow which verify the effect of the reactor inlet, outlet and wall on the flow pattern. Ideal plug flow satisfies the following criteria:

- The velocity profile in the direction of flow is flat
- There is no mixing in the axial direction
- There is complete mixing in the radial direction

The radial criterion (D-3) tests whether the wall effects cause a radial velocity profile. The axial criterion (D-4) determines whether the residence time distribution may be neglected.

$$\frac{d_t}{d_p} > 8 \quad (\text{D-3})$$

$$\frac{L_B}{d_p} > 8 \frac{n}{\text{Pe}} \ln\left(\frac{1}{1-x}\right) \quad (\text{D-4})$$

With:

d_p	Pellet diameter [m]
d_t	Tube diameter [m]
L_B	Bed length [m]
n	Reaction order [-]
x	Conversion [mol mol ⁻¹]

The modified Peclet number is given by:

$$\text{Pe} = \frac{u_0 d_p}{D_{ea}} \quad (\text{D-5})$$

With:

u_0	Linear liquid velocity [m s ⁻¹]
D_{ea}	Effective axial diffusion coefficient [m ² s ⁻¹]

Increasing the bed length and decreasing the particle diameter seems to have a beneficial effect on the above criteria. However, also criteria exist for the maximal pressure drop and the maximal bed dilution. A maximal bed dilution is specified via the correlation (D-6), which is an upper bound for the size of the catalyst bed.

$$b_{\max} = \frac{0.004 L_B \epsilon d_p}{1 + 0.004 L_B \epsilon d_p} \quad (\text{D-6})$$

With:

ϵ	Bed porosity [-]
------------	------------------

A maximal pressure drop is specified via (D-7) and (D-8) which represent a lower limit for the pellet diameter.

$$\Delta p < 0.2 \frac{p_{\text{tot}}}{n} \quad (\text{D-7})$$

$$\frac{\Delta p}{h_{\text{bed}}} = \frac{f_m \rho_L u_0^2}{d_p} \quad (\text{D-8})$$

With:

p_{tot}	Total pressure [Pa]
n	Reaction order [-]
f_m	Modified friction factor from the Ergun equation [-]
ρ_L	Liquid density [kg m^{-3}]
u_0	Superficial liquid velocity [m s^{-1}]
h_{bed}	Bed height [m]

D.1.2 Mass transfer limitations

The external mass transfer limitation is expressed using the Carberry number³ (Ca), defined in (D-9). This dimensionless group expresses the fractional concentration difference between the concentration of component A in the bulk phase, $C_{A,b}$ and the concentration of component A at the external surface, $C_{A,s}$:

$$\text{Ca} = \frac{C_{A,b} - C_{A,s}}{C_{A,b}} = \frac{R_{v,A}^{\text{obs}}}{k_L a_v C_{A,b}} < \frac{0.05}{n} \quad (\text{D-9})$$

With:

$R_{v,A}^{\text{obs}}$	Observed volumetric rate [$\text{mol m}_{\text{pellet}}^{-3} \text{s}^{-1}$]
k_L	External mass transfer coefficient [-]
a_v	Specific external surface area of the catalyst [$\text{m}^2 \text{m}_{\text{pellet}}^{-3}$]
$C_{a,b}$	Bulk concentration of reactant A [mol m^{-3}]
$C_{a,s}$	Concentration of reactant A at the external pellet surface [mol m^{-3}]

The mass transfer coefficient k_L is calculated using equation (D-10).

$$k_L = \frac{\text{Sh } D_{L,i}}{d_p} \quad (\text{D-10})$$

With:

Sh	Sherwood number [-]
D_L	Molecular diffusion coefficient of component i in the liquid phase [$\text{m}^2 \text{s}^{-1}$]
d_p	Pellet diameter [m]

The Sherwood number can be calculated using equation.

$$\text{Sh} = j_m \text{Re} \text{Sc}_1^{1/3} \quad (\text{D-11})$$

$$\text{Re} = \frac{\rho_{\text{mix}} u_0 d_p}{\mu_{\text{mix}}} \quad (\text{D-12})$$

$$\text{Sc}_1 = \frac{\mu_{\text{mix}}}{\rho_{\text{mix},l} D_{L,i}} \quad (\text{D-13})$$

With:

- j_m Chilton and Colburn mass transfer factor
- ρ_{mix} Density of the liquid mixture [kg m^{-3}]
- u_0 Characteristic velocity [m s^{-1}]
- μ_{mix} Dynamic viscosity of the liquid mixture [Pa s]

The molecular diffusion coefficient ($D_{L,i}$) of a component is calculated using Wilke and Chang's relation⁴:

$$D_L = \frac{2.34 \cdot 10^{-13} T_b \overline{MM_i \varnothing_i}}{\mu_{l,\text{mix}} V_{m,i}^{0.6}} \quad (\text{D-14})$$

With:

- T_b Temperature bulk [K]
- MM_i Molecular mass of component i [g mol^{-1}]
- \varnothing_i Association factor for the solvent [-]
- $V_{m,i}$ Molar volume of the solute at its boiling point estimated from group contribution method [$\text{m}^3 \text{kmol}^{-1}$]

The association factor \varnothing_i depends on the solvent that is used, Table D-1 shows some values for frequently used solvents.

Table D-1: Association factors of frequently used solvents

Solvent	Association factor
Water	2.26
Ethanol	1.9
Methanol	1.5
Propanol	1.2
Others	1.0

The internal mass transfer limitation is expressed using the Weisz-Prater criterion:

$$\Phi = \eta\phi^2 = \frac{n+1}{2} \frac{R_{v,A}^{obs} \frac{d_p}{6}}{D_{A,eff} C_{a,s}} < 0.08 \quad (D-15)$$

With:

- $D_{a,eff}$ Effective diffusivity inside the catalyst particles [$m^2 s^{-1}$]
- η Effectiveness factor defined as the ratio of the observed production rate to the intrinsic rate [-]
- ϕ Thiele modulus [-]

The effective diffusion coefficient of a component is calculated using equation (D-16).

$$D_{A,eff} = \frac{\varepsilon_p D_{L,A}}{\tau} \quad (D-16)$$

With:

- ε_p Porosity of the catalyst particle [$m^3 m^{-3}$]
- τ Tortuosity of the catalyst [$m m^{-1}$]
- $D_{L,A}$ Molecular diffusion coefficient for component A [-]

The deviation caused by internal diffusion limitations is less than 5 %, if Φ is lower than 0.08.

D.1.3 Heat transfer limitations

A criterion can be derived for respectively **external** (D-17) and **internal** (D-18) temperature gradients.

$$\frac{R_{w,A}^{obs} \rho_p d_p |\Delta_r H|}{6 \alpha T_b} \frac{E_a}{R T_b} < 0.05 \quad (D-17)$$

$$\frac{R_{w,A}^{obs} \rho_p d_p^2 |\Delta_r H|}{60 \lambda_p T_b} \frac{E_a}{R T_b} < 0.05 \quad (D-18)$$

With:

- $R_{w,A}^{obs}$ Observed reaction rate per unit of catalyst mass [$mol kg^{-1} s^{-1}$]
- $\Delta_r H$ Reaction enthalpy [$J mol_D^{-1}$]
- α Heat transfer coefficient inside the film [$W m^{-1} K$]
- T_b Bulk temperature [K]
- E_a Activation energy of the reaction [$J mol^{-1}$]

λ_p Catalyst pellet heat conductivity [$\text{W m}^{-1} \text{K}$]

ρ_p Particle density [$\text{kg m}_{\text{pellet}}^{-3}$]

The heat transfer coefficient is calculated using equation.

$$\alpha_p = \frac{\text{Nu } \lambda_{l,\text{mix}}}{d_p} \quad (\text{D-19})$$

$$\text{Nu} = j_h \text{Re } \text{Pr}_l^{1/3} \quad (\text{D-20})$$

$$\text{Pr}_l = \frac{\mu_{\text{mix}} c_{p,\text{mix}}}{\lambda_{l,\text{mix}}} \quad (\text{D-21})$$

With:

$\lambda_{L,\text{mix}}$ Thermal conductivity of the liquid mixture [$\text{W m}^{-1} \text{K}^{-1}$]

j_h Chilton and Colburn heat transfer factor [-]

$c_{p,\text{mix}}$ Heat capacity of the liquid mixture [$\text{J kg}^{-1} \text{K}^{-1}$]

Radial heat transport limitations

$$\Delta T = \left| \frac{R_{w,A}^{\text{obs}} |\Delta_r H| (d - d_t)^2 (1 - \varepsilon)(1 - b)}{32\lambda_{\text{er}}} \right| < \frac{0.05RT_b^2}{E_a} \quad (\text{D-22})$$

With:

ΔT Temperature difference between center of the reactor and the inside of the wall
[K]

λ_{er} Effective thermal conductivity [$\text{W m}^{-2} \text{K}^{-1}$]

d_t External diameter thermocouple [m]

ε Bed voidage [$\text{m}^3 \text{m}^{-3}$]

b Volumetric dilution degree [$\text{m}^3 \text{m}^{-3}$]

Axial heat transport limitations

Due to the nature of a tubular reactor, axial temperature profiles are always the case. Typically, its effect is much smaller and at maximum only approximately equal to the radial temperature gradient.

D.2 Evaluation of criteria

Using the correlations as described above, the criteria for intrinsic kinetics were verified for the aldol reaction of acetone with 4-nitrobenzaldehyde, catalyzed by a silica supported secondary amine using either hexane, DMSO or acetone as solvent. The highest measured reaction rate in a batch reactor for each solvent is always selected, as well as the lowest flowrate, in order to ensure the most ‘severe’ reaction conditions where transfer limitations can occur.

Table D-2: Reactor properties for the Liquid-Solid Lab-Scale (LS)² reactor and catalyst properties for the amine functionalized silica material.

L_r	Length of the reactor	0.3 m
d	Internal reactor diameter	0.008 m
T	Temperature	328.15 K
P_{tot}	Pressure in the reactor	180 kPa
d_t	External diameter internal thermocouple	0.001 m
u₀	Flow velocity	$7.62 \cdot 10^{-4} \text{ m s}^{-1}$
L_B	Length of the catalyst bed	0.15 m
d_p	Catalyst particle diameter	0.000375 m
ε	Void fraction of bed	0.38
ε_p	Porosity of the catalyst particle	0.6
τ	Tortuosity of the catalyst	4
k_l	Mass transfer coefficient	0.0002 m s^{-1}
a_v	Specific external surface area	$16\,000 \text{ m}^{-1}$

D.2.1 Hexane as solvent

Table D-3: Properties of the reaction mixture for the aldol reaction between acetone and 4-nitrobenzaldehyde using a 50/50 vol% hexane/acetone liquid mixture.

$D_{L,A}$	Molecular diffusion coefficient of A in the liquid phase	$6.17 \cdot 10^{-9} \text{ m}^2 \text{ s}^{-1}$
n	Reaction order	1
x	Conversion	0.2
D_{ea}	Effective axial diffusion coefficient	$2.86 \cdot 10^{-7} \text{ m}^2 \text{ s}^{-1}$
μ_{mix}	Viscosity of the liquid mixture	$2.8 \cdot 10^{-4} \text{ kg m}^{-1} \text{ s}^{-1}$
ρ_{mix}	Density of the liquid mixture	746.9 kg m^{-3}
$R_{v,A}$	Observed reaction rate of A	$2.5 \cdot 10^{-4} \text{ mol}_A \text{ kg}_{\text{cat}}^{-1} \text{ s}^{-1}$
TOF	Turnover frequency	$1.0 \cdot 10^{-3} \text{ s}^{-1}$
$D_{A,\text{eff}}$	Effective diffusion coefficient of A	$9.26 \cdot 10^{-10} \text{ m}^2 \text{ s}^{-1}$
$\Delta_r H$	Reaction enthalpy	$-52 \cdot 1000 \text{ J mol}_D^{-1}$
α_p	Heat transfer coefficient	$897.9 \text{ W m}^{-2} \text{ K}^{-1}$
E_a	Activation energy	$33 \cdot 800 \text{ J mol}^{-1}$
λ_p	Catalyst pellet thermal conductivity	$0.22 \text{ W m}^{-1} \text{ K}^{-1}$
λ_{er}	Effective radial thermal conductivity	$0.37 \text{ W m}^{-1} \text{ K}^{-1}$
j_m	Transfer factor for mass	3.80
j_h	Transfer factor for heat	2.15
$\lambda_{l,\text{mix}}$	Thermal conductivity of the liquid mixture	$0.14 \text{ W m}^{-1} \text{ K}^{-1}$
$c_{p,\text{mix}}$	Heat capacity of the liquid mixture	$2257 \text{ J kg}^{-1} \text{ K}^{-1}$
M_A	Molecular weight of component A	$151.12 \text{ g mol}^{-1}$
Φ_{solvent}	Association factor of solvent	1
$V_{m,A}$	Molar volume of component A	$112.9 \cdot 10^{-6} \text{ m}^3 \text{ mol}^{-1}$

Table D-4: Criteria for intrinsic kinetics of the aldol reaction between acetone and 4-nitrobenzaldehyde using a 50/50 vol% hexane/acetone liquid mixture in the (LS)² reactor.

<i>Criterion</i>	<i>Value</i>	<i>Limit</i>
Ca	$2.1 \cdot 10^{-3}$	<5 10^{-2}
ϕ	$2.3 \cdot 10^{-2}$	<8 10^{-2}
ΔT_{ext}	$5.3 \cdot 10^{-4}$	<1.32 K
ΔT_{rad}	$1.9 \cdot 10^{-2}$	<1.32 K
ΔT_{int}	$7.9 \cdot 10^{-5}$	<1.32 K
ΔT_{ax}	$4.2 \cdot 10^{-2}$	<1.32 K
d/d_p	9.3	>8
L_B/d_p	400	>1.6
$\Delta P/P$	108.4	<36 000 Pa

D.2.2 DMSO as solvent

Table D-5: Properties of the reaction mixture for the aldol reaction between acetone and 4-nitrobenzaldehyde using a 50/50 vol% DMSO/acetone liquid mixture.

$D_{L,A}$	Molecular diffusion coefficient of A in the liquid phase	$2.32 \cdot 10^{-9} \text{ m}^2 \text{ s}^{-1}$
n	Reaction order	1
x	Conversion	0.2
D_{ea}	Effective axial diffusion coefficient	$2.9 \cdot 10^{-7} \text{ m}^2 \text{ s}^{-1}$
μ_{mix}	Viscosity of the liquid mixture	$7.6 \cdot 10^{-4} \text{ kg m}^{-1} \text{ s}^{-1}$
ρ_{mix}	Density of the liquid mixture	908.5 kg m^{-3}
$R_{v,A}$	Observed reaction rate of A	$2.3 \cdot 10^{-4} \text{ mol}_A \text{ kg}_{\text{cat}}^{-1} \text{ s}^{-1}$
TOF	Turnover frequency	$9.0 \cdot 10^{-4} \text{ s}^{-1}$
$D_{A,\text{eff}}$	Effective diffusion coefficient of A	$3.48 \cdot 10^{-10} \text{ m}^2 \text{ s}^{-1}$
$\Delta_r H$	Reaction enthalpy	$-52 \cdot 1000 \text{ J mol}_D^{-1}$
α_p	Heat transfer coefficient	$833.3 \text{ W m}^{-2} \text{ K}^{-1}$
E_a	Activation energy	$33 \cdot 800 \text{ J mol}^{-1}$
λ_p	Catalyst pellet thermal conductivity	$0.24 \text{ W m}^{-1} \text{ K}^{-1}$
λ_{er}	Effective radial thermal conductivity	$0.18 \text{ W m}^{-1} \text{ K}^{-1}$
j_m	Transfer factor for mass	6.97
j_h	Transfer factor for heat	4.05
$\lambda_{l,\text{mix}}$	Thermal conductivity of the liquid mixture	$0.16 \text{ W m}^{-1} \text{ K}^{-1}$
$c_{p,\text{mix}}$	Heat capacity of the liquid mixture	$2132 \text{ J kg}^{-1} \text{ K}^{-1}$
M_A	Molecular weight of component A	$151.12 \text{ g mol}^{-1}$
ϕ_{solvent}	Association factor of solvent	1
$V_{m,A}$	Molar volume of component A	$113 \cdot 10^{-6} \text{ m}^3 \text{ mol}^{-1}$

Table D-6: Criteria for intrinsic kinetics of the aldol reaction between acetone and 4-nitrobenzaldehyde using a 50/50 vol% DMSO/acetone liquid mixture in the (LS)² reactor.

<i>Criterion</i>	<i>Value</i>	<i>Limit</i>
Ca	4.9 10 ⁻³	<5 10⁻²
ϕ	6.2 10 ⁻²	<8 10⁻²
ΔT_{ex}	6.0 10 ⁻⁴	<1.32 K
ΔT_{rad}	2.0 10 ⁻²	<1.32 K
ΔT_{int}	7.7 10 ⁻⁵	<1.32 K
ΔT_{ax}	3.8 10 ⁻²	<1.32 K
d/d_p	9.3	>8
L_B/d_p	400	>2.7
ΔP/P	177.8	<36 000 Pa

D.2.3 Acetone as solvent

Table D-7: Properties of the reaction mixture for the aldol reaction between acetone and 4-nitrobenzaldehyde using a 100 vol% acetone liquid mixture.

$D_{L,A}$	Molecular diffusion coefficient of A in the liquid phase	$5.95 \cdot 10^{-9} \text{ m}^2 \text{ s}^{-1}$
n	Reaction order	1
x	Conversion	0.2
D_{ea}	Effective axial diffusion coefficient	$2.0 \cdot 10^{-7} \text{ m}^2 \text{ s}^{-1}$
μ_{mix}	Viscosity of the liquid mixture	$3.0 \cdot 10^{-4} \text{ kg m}^{-1} \text{ s}^{-1}$
ρ_{mix}	Density of the liquid mixture	791 kg m^{-3}
$R_{v,A}$	Observed reaction rate of A	$2.3 \cdot 10^{-4} \text{ mol}_A \text{ kg}_{\text{cat}}^{-1} \text{ s}^{-1}$
TOF	Turnover frequency	$9.0 \cdot 10^{-4} \text{ s}^{-1}$
$D_{A,\text{eff}}$	Effective diffusion coefficient of A	$8.93 \cdot 10^{-10} \text{ m}^2 \text{ s}^{-1}$
$\Delta_r H$	Reaction enthalpy	$-52 \cdot 000 \text{ J mol}_D^{-1}$
α_p	Heat transfer coefficient	$850 \text{ W m}^{-2} \text{ K}^{-1}$
E_a	Activation energy	$33 \cdot 800 \text{ J mol}^{-1}$
λ_p	Catalyst pellet thermal conductivity	$0.24 \text{ W m}^{-1} \text{ K}^{-1}$
λ_{er}	Effective radial thermal conductivity	$0.18 \text{ W m}^{-1} \text{ K}^{-1}$
j_m	Transfer factor for mass	4.31
j_h	Transfer factor for heat	2.50
$\lambda_{l,\text{mix}}$	Thermal conductivity of the liquid mixture	$0.15 \text{ W m}^{-1} \text{ K}^{-1}$
$c_{p,\text{mix}}$	Heat capacity of the liquid mixture	$2239 \text{ J kg}^{-1} \text{ K}^{-1}$
M_A	Molecular weight of component A	$151.12 \text{ g mol}^{-1}$
ϕ_{solvent}	Association factor of solvent	1
$V_{m,A}$	Molar volume of component A	$113 \cdot 10^{-6} \text{ m}^3 \text{ mol}^{-1}$

Table D-8: Criteria for intrinsic kinetics of the aldol reaction between acetone and 4-nitrobenzaldehyde using a 100 vol% acetone liquid mixture in the (LS)² reactor.

<i>Criterion</i>	<i>Value</i>	<i>Limit</i>
Ca	$2.7 \cdot 10^{-3}$	<5 10^{-2}
ϕ	$2.6 \cdot 10^{-2}$	<8 10^{-2}
ΔT_{ex}	$5.3 \cdot 10^{-4}$	<1.32 K
ΔT_{rad}	$1.8 \cdot 10^{-2}$	<1.32 K
ΔT_{int}	$7.0 \cdot 10^{-5}$	<1.32 K
ΔT_{ax}	$3.7 \cdot 10^{-2}$	<1.32 K
d/d_p	9.3	>8
L_B/d_p	400	>2.7
$\Delta P/P$	80.4	<36 000 Pa

D.3 References

1. Marin, G.; Yablonsky, G. S., *Kinetics of chemical reactions*. John Wiley & Sons: 2011.
2. Berger, R. J.; Stitt, E. H.; Marin, G. B.; Kapteijn, F.; Moulijn, J. A., Eurokin. Chemical reaction kinetics in practice. *Cattech* **2001**, 5 (1), 36-60.
3. Carberry, J. J., *Chemical and catalytic reaction engineering*. Courier Corporation: 2001.
4. Wilke, C.; Chang, P., Correlation of diffusion coefficients in dilute solutions. *AIChE Journal* **1955**, 1 (2), 264-270.

Appendix E

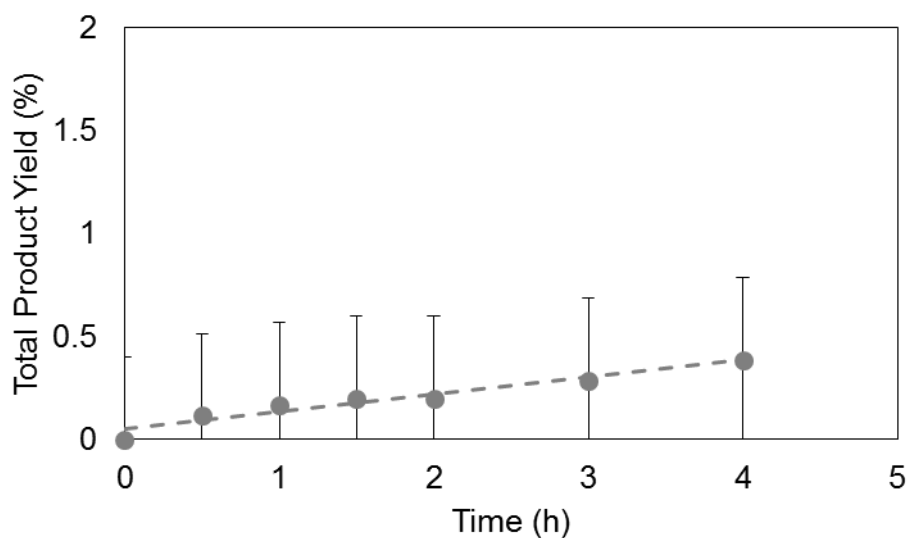


Figure E-1: measured total product yield versus reaction time when no catalyst is used. ($T = 55\text{ }^{\circ}\text{C}$, $m_{\text{acetone}} = 45\text{ g}$, $m_{4\text{NB}} = 0.45\text{ g}$, $m_{\text{water}} = 55\text{ g}$)

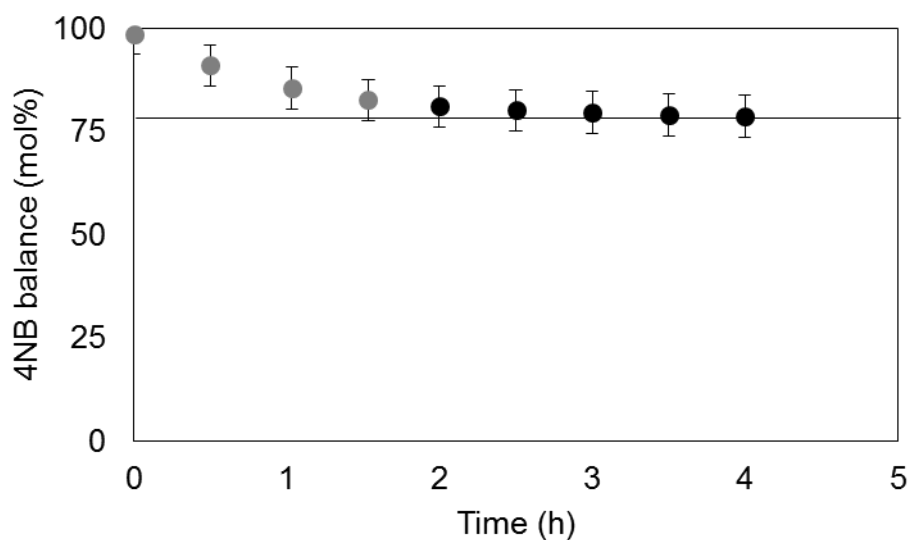


Figure E-2: 4-nitrobenzaldehyde molar balance versus reaction time for crude low-molecular weight chitosan as catalyst in the aldol reaction of acetone with 4-nitrobenzaldehyde. ($T = 55\text{ }^{\circ}\text{C}$, $m_{\text{acetone}} = 45\text{ g}$, $m_{4\text{NB}} = 0.45\text{ g}$, $m_{\text{water}} = 55\text{ g}$, $m_{\text{cat}} = 0.26\text{ g}$)

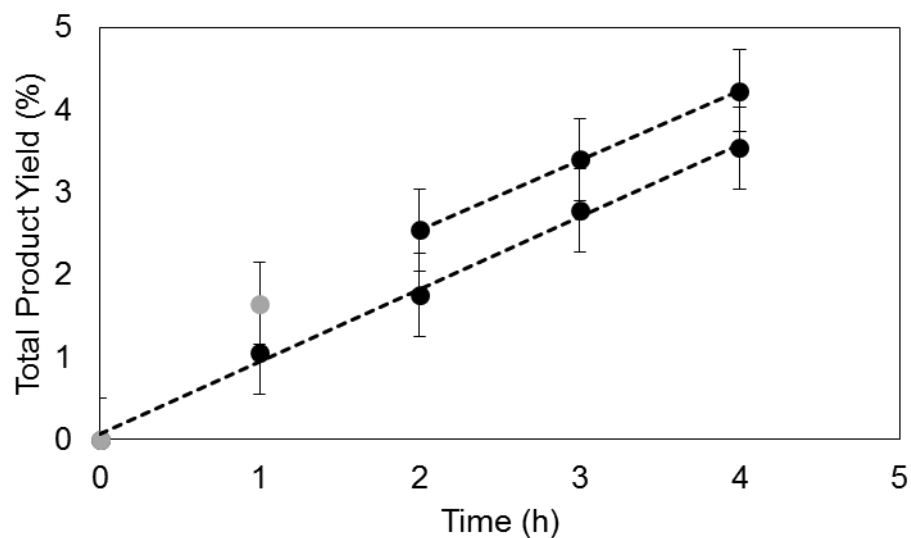


Figure E-3: measured total product yield versus reaction time for low-molecular weight chitosan hydrogel as catalyst in the aldol reaction of acetone with 4-nitrobenzaldehyde in a small scale reaction. ($T = 55\text{ }^{\circ}\text{C}$, $m_{\text{acetone}} = 22.5\text{ g}$, $m_{4\text{NB}} = 0.225\text{ g}$, $m_{\text{water}} = 27.5\text{ g}$, $m_{\text{chitosan}} = 0.05\text{ g}$)

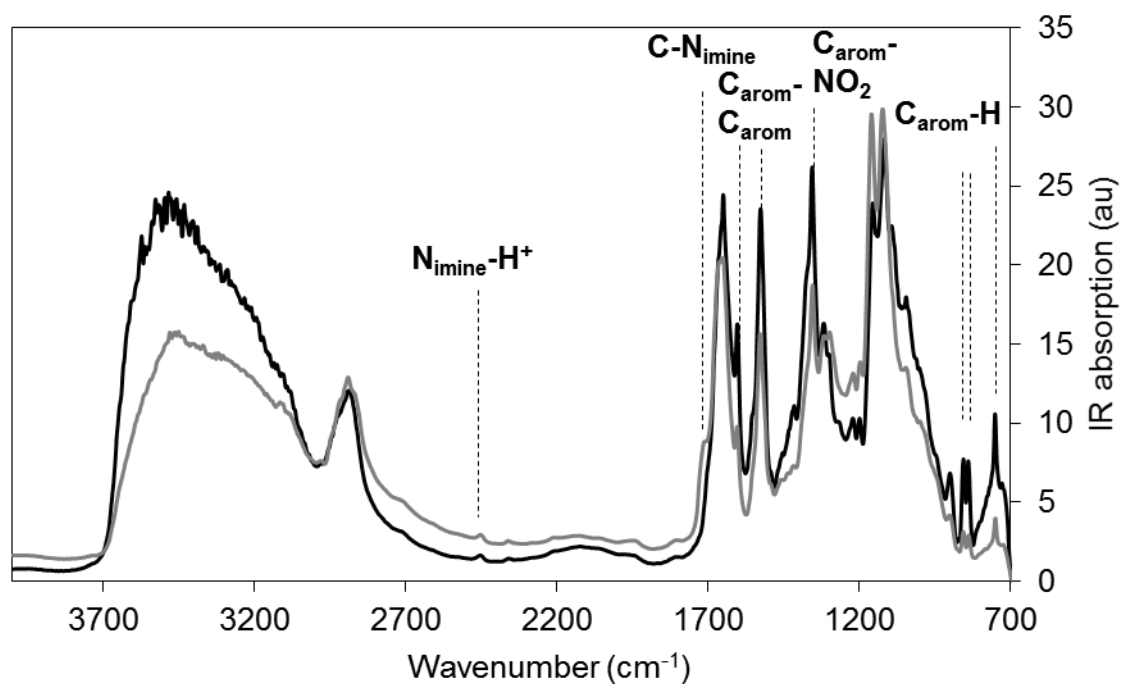


Figure E-4: DRIFTS spectrum of chitosan reacted with 4-nitrobenzaldehyde in a 45g DMSO, 55g water mixture at $55\text{ }^{\circ}\text{C}$ (black) compared to the catalyst spent in the aldol reaction (grey).

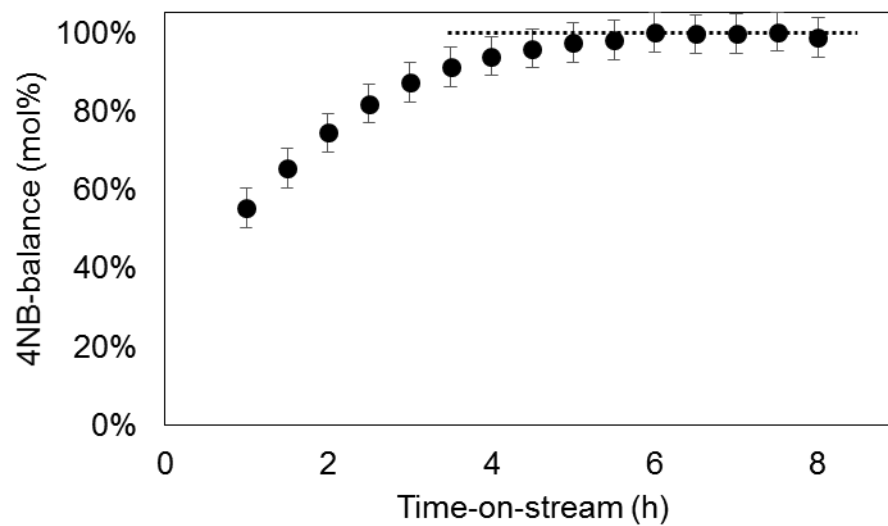


Figure E-5: 4-nitrobenzaldehyde molar balance as a function of time-on-stream in the continuous-flow reactor using chitosan as catalyst.

Appendix F

F.1.1 PMO materials

F.1.1.1 100% Ethane-bridged PMO

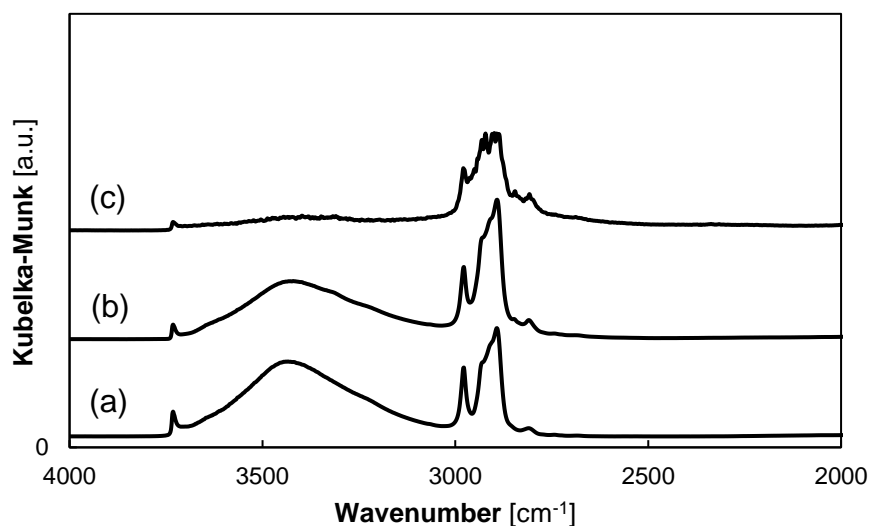


Figure F-1: DRIFTS spectrum of the 100% Ethane-bridged PMO (a), Amine-Ethane-PMO (b) and HMDS-Amine-Ethane-PMO (c).

F.1.1.2 100% Ethylene-bridged-PMO

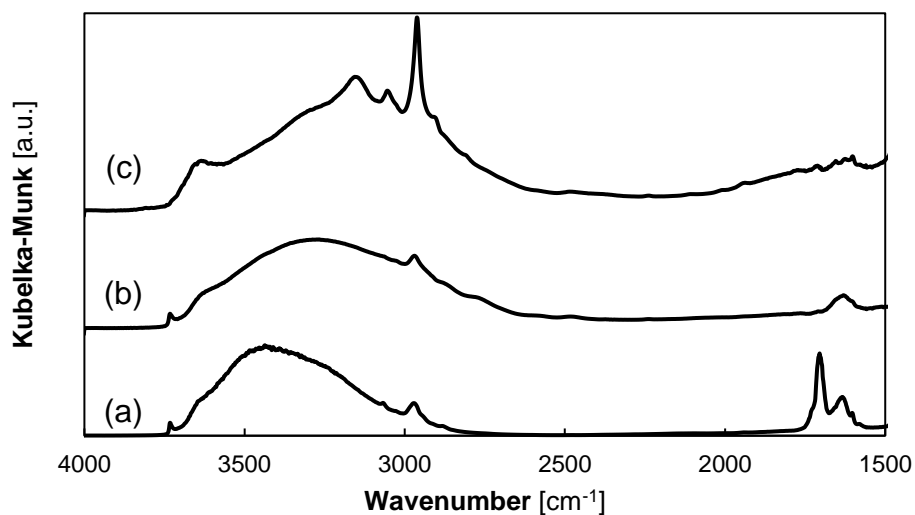


Figure F-2: DRIFTS spectrum of the 100% Ethylene-bridged PMO (a), Amine-Ethylene-PMO (b) and HMDS-Amine-Ethylene-PMO (c).

F.1.2 PEGMA materials

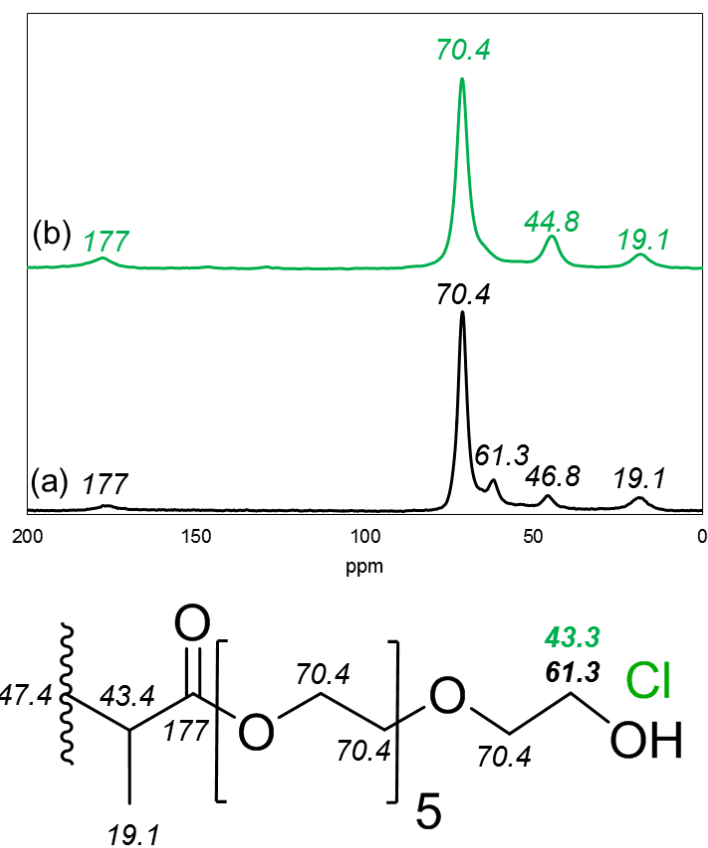


Figure F-3: DP ^{13}C -NMR at 60 °C for the pristine PEGMA hydrogel (a) and the 100% chlorine functionalized PEGMA material (b) and the corresponding peak assignments.

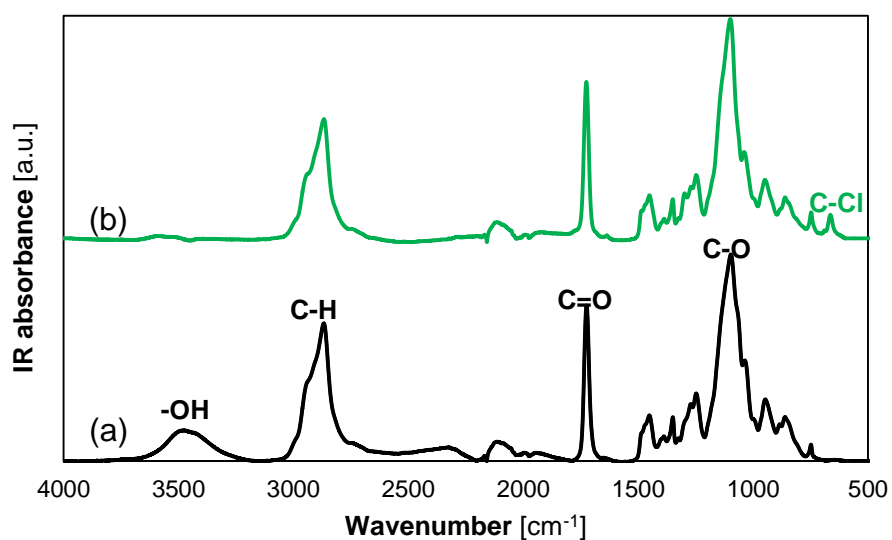


Figure F-4: FT-IR spectrum of pristine PEGMA hydrogel (a) and fully chlorine functionalized PEGMA-Cl (b).

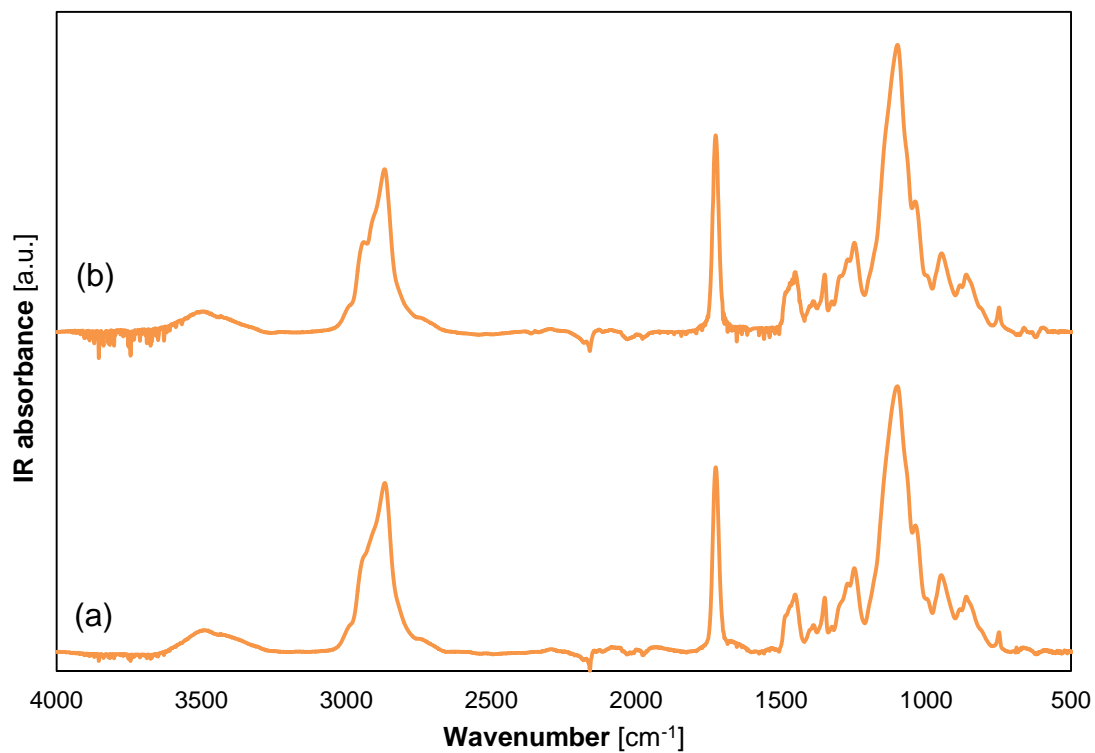


Figure F-5: FT-IR spectrum PEGMA-EDA (a) and PEGMA-DED (b).

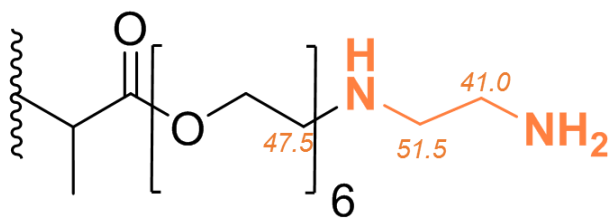
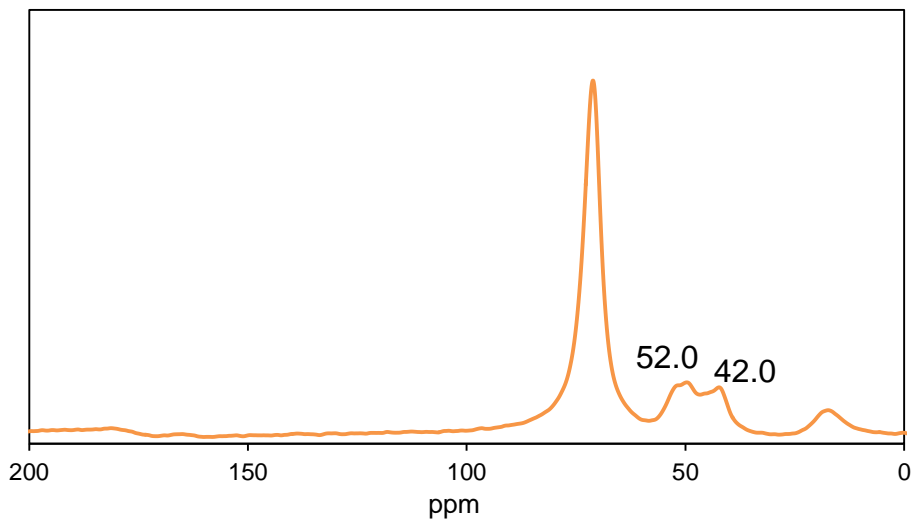


Figure F-6: DP ^{13}C -NMR at 60 °C for high loading PEGMA-EDA (2.1 mmol_{diamine} g⁻¹)

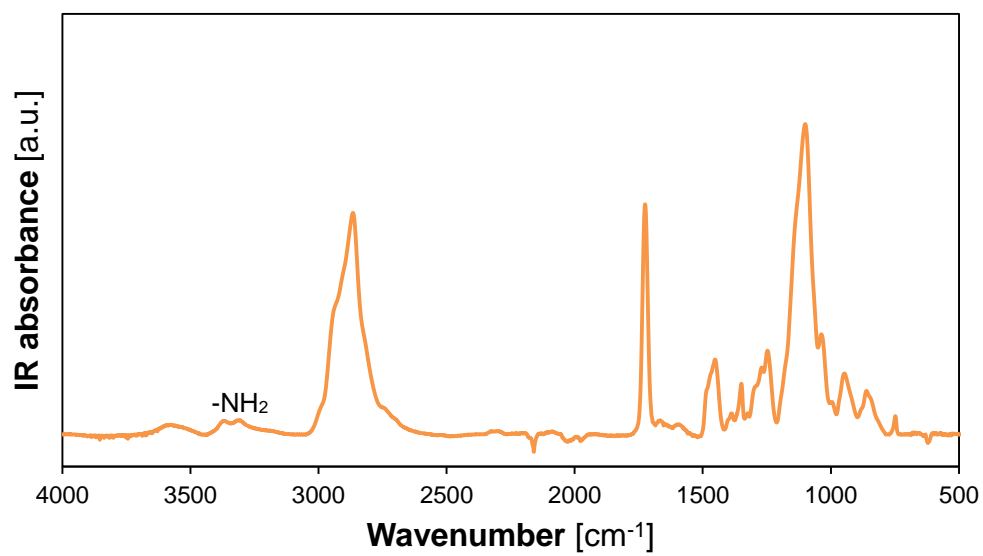


Figure F-7: FT-IR spectrum of high loading PEGMA-EDA (2.1 mmol_{diamine} g⁻¹).

List of publications

A1 publications

Okonkwo, C. N., Lee, J. J., De Vylder, A., Chiang, Y., Thybaut, J., & Jones, C. W. (2020). Selective removal of hydrogen sulfide from simulated biogas streams using sterically hindered amine adsorbents. *Chemical Engineering Journal*, In Press

De Vylder, A., Lauwaert, J., De Clercq, J., Thybaut, J.W. (2019). Catalyst Stability Assessment in a Lab-Scale Liquid Solid (LS)² Plug-Flow Reactor. *Catalysts*, 9(9), 755

De Vylder, A., Lauwaert, J., De Clercq, J., Van Der Voort, P., Stevens, C.V., Thybaut, J.W. (2019). Kinetic evaluation of chitosan-derived catalysts for the aldol reaction in water. *Reaction Chemistry & Engineering*, In Press

De Vylder, A., Lauwaert, J., Sabbe, M., Reyniers, M.-F., De Clercq, J., Van Der Voort, P., Thybaut, J. W. (2019). Rational design of nucleophilic amine sites via computational probing of steric and electronic effects. *Catalysis Today*, 334, 96-103

Seghers, Sofie, Lefevere, J., Mullens, S., De Vylder, A., Thybaut, J. W., Stevens, C. (2018). Enhancing zeolite performance by catalyst shaping in a mesoscale continuous-Flow Diels-Alder process. *ChemSusChem*, 11(10), 1686–1693.

De Vylder, A., Lauwaert, J., Esquivel, D., Poelman, D., De Clercq, J., Van Der Voort, P., Thybaut, J. W. (2018). The role of water in the reusability of aminated silica catalysts for aldol reactions. *Journal Of Catalysis*, 361, 51–61.

Huybrechts, Ward, Lauwaert, J., De Vylder, A., Mertens, M., Mali, G., Thybaut, J. W., Van Der Voort, P., Cool, P., (2017). Synthesis of L-serine modified benzene bridged periodic mesoporous organosilica and its catalytic performance towards aldol condensations. *Microporous and Mesoporous Materials*, 251, 1–8.

Conference contributions

Oral presentations

De Vylder, A., Lauwaert, J., Sabbe, M., Reyniers, M.-F., De Clercq, J., Van Der Voort, P., Thybaut, J. W. (2019). A Quantitative Understanding of the Water Effect on the Amine Catalyzed Aldol Reaction. *Presented at the North American Symposium for Chemical Reaction Engineering (NASCRE 4)*

De Vylder, A., Lauwaert, J., De Clercq, J., Van Der Voort, P., Thybaut, J. W. (2017). The effect of water on the reusability of aminated mesoporous silica catalysts for Aldol condensations. *Presented at the 2017 AIChE Annual meeting (AIChE)*.

De Vylder, A., Bouriakova, A., Toch, K., Thybaut, J. W. (2017). Training Our Upcoming Chemical Engineers By Simulating an Industrial Setting : A Classroom Case-Study on Waste Cellulose Valorization. *Presented at the 2017 AIChE Annual Meeting (AIChE)*.

Poster presentations

De Vylder, A., Lauwaert, J., Sabbe, M., Reyniers, M.-F., De Clercq, J., Van Der Voort, P., Thybaut, J. W. (2018). Rational design of supported amine organocatalysts via computational probing of steric and electronic effects. *Presented at the 12th International symposium on the Scientific Bases for the Preparation of Heterogeneous Catalysts (PREPA-12)*.

De Vylder, A., Lauwaert, J., Moens, E., Seghers, S., Stevens, C., Van Der Voort, P., De Clercq, J., Thybaut, J.W. (2018). Shrimp cocktails in the reactor as renewable catalyst. *Presented at the FEA Research Symposium 2018 (FEARS2018)*.

De Vylder, A., Lauwaert, J., De Clercq, J., Van Der Voort, P., Thybaut, J. W. (2017). Tuning the reusability of cooperative aminated silica catalysts for continuous-flow aldol condensations. *Presented at the 18th Netherlands' Catalysis and Chemistry Conference (NCCC XVIII)*.

De Vylder, A., Lauwaert, J., Moens, E., Seghers, S., Stevens, C., Van Der Voort, P., De Clercq, J., Thybaut, J.W. (2017). Chitosan as a sustainable heterogeneous catalyst for aqueous aldol condensation. *Presented at the 4th International Congress on Catalysis and Biorefineries (CatBior 2017)*.

De Vylder, A., Lauwaert, J., De Clercq, J., Van Der Voort, P., Thybaut, J. W. (2016). Exploring the reusability of aminated silicas for aldol condensations. *Presented at the Chemical Research in Flanders (CRF-1)*.

Nalli, H., Lauwaert, J., De Vylder, A., Van Der Voort, P., Thybaut, J. W. (2016). Continuous flow investigation of “green” aldol condensations. *Presented at the 17th Netherlands' Catalysis and Chemistry Conference (NCCC XVII)*.

